Dynamics meets Morphology - towards Dymorph Computation

Dissertation

submitted to the Faculty of Engineering, Kiel University,

in fulfilment of the requirements for the degree of

Doctor of Engineering (Dr.-Ing.)

submitted by

Tom Birkoben

Kiel 2021

Reviewer of the doctoral thesis:

Prof. Dr. Hermann Kohlstedt
Prof. Dr. Rainer Adelung
Prof. Dr. Simon Brown

Disputation examination committee (14 January 2022):

Prof. Dr. Lorenz Kienle (Chairman)
Prof. Dr. Hermann Kohlstedt
Prof. Dr. Rainer Adelung
Prof. Dr. Robert Rieger

Erklärung

Hiermit erkläre ich, dass die Dissertation mit dem Titel:

"Dynamics meets Morphology - towards Dymorph Computation"

abgesehen von der Beratung durch meinen Betreuer, nach Inhalt und Form, meine eigene Arbeit ist und ohne unzulässige Hilfe Dritter angefertigt wurde. Diese Arbeit ist unter Einhaltung der Regeln guter wissenschaftlicher Praxis der Deutschen Forschungsgemeinschaft entstanden. Weiterhin hat diese Arbeit weder ganz noch zum Teil schon an einer anderen Stelle im Rahmen eines Prüfungsverfahrens vorgelegen und wurde auch noch nicht veröffentlicht oder zur Veröffentlichung eingereicht.

Kiel, den 29.04.2021

(Tom Birkoben)

Acknowledgement

First, I would like to thank Hermann Kohlstedt, not just for the opportunity to work in his lab and for the supervision of my dissertation, but for his ongoing support and inspiring questions and discussions during the last years. He managed to create an environment in which, despite all the ups and downs of science, working was enjoyable.

I would also like to thank my office colleagues Nick and Henning for the great atmosphere in our office and the exchange of experience. Besides them, other people have also contributed to the wonderful atmosphere at the chair of Nanoelectronics and have always supported me with suggestions and comments in the daily lab routine. Thank you, Mirko, Sandra, Nico, Finn, Richard, Adrian and Christoph. A special thanks goes to Thora who guided me through so many administrative tasks.

My thanks also goes to Serhiy Yanchuk, Vladimir Klinshov and Philipp Hövel for the fruitful discussions on chaotic dynamics and the insight to delayed pulse feedback in relaxation type oscillators.

I would also like to thank Moritz, Marie, Michelle, Maximiliane, Alexander, Jonas, Lisa, Arthur, and all the other students who I was able to accompany during their theses and who actively supported me.

I am grateful for the working atmosphere and the stimulating discussions with my colleagues in Research Group 2093. In particular, I would like to thank Rainer Adelung and Franz Faupel as well as Alexander Vahl, Niko Carstens, Maik-Ivo Terasa and Ole Gronenberg for their productive cooperation and open ears.

Furthermore, I gratefully acknowledge the financial support of the Deutsche Forschungsgemeinschaft (DFG, German Research Foundation) through FOR 2093 “Memristive Devices for neural Systems” and through – Project-ID 434434223 – SFB 1461. Moreover, I would like to thank for the graduate scholarship of the state of Schleswig-Holstein.

But I would especially like to thank my family, my parents Annegret and Waldemar, as well as my beloved wife Fabia for their never-ending support.

Abstract

English

In recent years, a rapid advance in biologically inspired information processing systems could be observed. The progress in this area could not only be achieved by the constant progress of digital computer technology, but also by the development of novel components for the emulation of fundamental neuronal principles. In this dissertation, approaches are presented for both technically using and investigating biological principles with oscillators in the context of electrical engineering, in particular neuromorphic engineering. Thereby, dynamics as well as morphology as important neuronal principles were explicitly selected, which shape the information processing in the human brain and distinguish it from other technical systems. The aspects and principles selected here are adaptation during the encoding of stimuli, the comparatively low signal transmission speed, the continuous formation and elimination of connections, and highly complex, partly chaotic, dynamics. The selection of these phenomena and properties has led to the development of a sensory unit that is capable of encoding mechanical stress into a series of voltage pulses by the use of a MOSFET augmented by AlScN. The circuit is based on a leaky integrate and fire neuron model and features an adaptation of the pulse frequency with respect to the excitation strength and duration. Furthermore, the slow signal transmission speed of biological systems was the motivation for the investigation of a temporal delay in the feedback of the output pulses of a relaxation oscillator. Therefore, different approaches to generate a temporal delay in the lower Hertz range were investigated. After selecting a suitable delay line based on a field programmable gate array (FPGA), stable pulse patterns which form due to so-called jittering bifurcations could be observed. In particular, switching between

different stable pulse patterns was possible to induce. In the further course of the work, the first steps towards time-varying coupling of dynamic systems are investigated. In the course of this investigation, it was shown that in a system consisting of dimethyl sulfoxid (DMSO) and zinc acetate, oscillators can be used to force the formation of filaments. The resulting filaments then lead to a change in the dynamics of the oscillators, so that full and partial synchronisation could be observed in a group of three oscillators. Finally, it is shown that in a system with chaotic dynamics, the extension of it with a memristive device can lead to transient stabilisation of the dynamics. Through a theoretical analysis and experimental realisation of the system, this behaviour can be identified as a repeated pass of Hopf bifurcations.

German

In den vergangenen Jahren konnte eine rasante Weiterentwicklung der biologisch inspirierten informationsverarbeitenden Systeme beobachtet werden. Die Fortschritte in diesem Bereich wurden nicht nur durch die stetige Verbesserung der digitalen Computertechnik erreicht, sondern auch durch die Entwicklung von neuartigen Bauelementen zur Emulation fundamentaler neuronaler Prinzipien. In der hier vorliegenden Dissertationsschrift werden Möglichkeiten und Wege präsentiert um mit Oszillatoren im Rahmen der Elektrotechnik, insbesondere des Neuromorphic Engeneerings, biologische Prinzipien technisch sowohl zu nutzen als auch zu untersuchen. Dazu wurden explizit sowohl dynamische als auch morphologische neuronale Prinzipien ausgewählt, die die Informationsverarbeitung im menschlichen Gehirn prägen und von anderen technischen Systemen unterscheiden. Dies sind erstens die Adaption während der Codierung von Stimuli, zweitens die vergleichsweise geringe Signalübertragungsgeschwindigkeit biologischer Systeme, drittens das kontinuierliche Entstehen und Wegfallen von Verbindungen, sowie viertens hochkomplexe, teilweise chaotische Dynamiken. Die Auswahl dieser Phänomene und Eigenschaften führte zur Entwicklung einer Sensoreinheit, welche dazu in der Lage ist, mittels eines um eine AlScN-Schicht erweiterten MOSFETs mechanischen Spannung in eine Reihe von elektrischen Pulsen zu kodieren. Die Schaltung orientiert sich dabei an einem Leaky Integrate and Fire Neuronen-Modell und weist eine Adaption der Pulsfrequenz hinsichtlich der Anregungsstärke und -dauer auf. Weiterhin dient die langsame Signalübertragungsgeschwindigkeit biologischer Systeme als Motivation für die Untersuchung einer zeitlichen Verzögerung bei der Rückkopplung der Ausgangspulse eines Relaxationsoszillators. Hier wurden verschiedene Ansätze zur Generierung einer zeitlichen Verzögerung im unteren Hertz-Bereich untersucht. Nach der Auswahl einer auf einem FPGA basierenden Verzögerungsleitung konnten stabile Pulsmuster auf Basis sogenannter Jittering Bifurcations in einem Relaxationsoszillator erzeugt und manipuliert werden. Insbesondere war ein Schalten zwischen verschiedenen stabilen Pulsmustern möglich. Im weiteren Verlauf der Arbeit wurden erste Schritte zur zeitlich variierenden Kopplung von dynamischen Systemen untersucht. Im Rahmen dieser Untersuchung konnte gezeigt werden, dass in einem System aus DMSO und Zinkacetat Oszillatoren genutzt werden können, um die Entstehung von Filamenten zu forcieren. Die entstanden Filamente führten zu einer Änderung der Dynamik der

Oszillatoren, sodass eine vollständige und eine teilweise Synchronisation in einer Gruppe von drei Oszillatoren beobachtet werden konnte. Abschließend wird gezeigt, dass in einem System mit einer chaotischen Dynamik die Erweiterung des selbigen mit einem memristiven Bauelement zur transienten Stabilisierung der Dynamik führen kann. Mit Hilfe einer theoretischen Analyse und experimentellen Realisation des Systems, lässt sich dieses Verhalten als ein sich wiederholender Durchlauf von Hopf-Bifurkationen identifizieren.

Contents

List of abbreviations

ADC	analogue to digital converter
AlScN	$Al_xSc_{1-x}N$
AMPA	α-amino-3-hydroxy-5-methyl-4-isoxazolepropionic acid
ANN	artificial neural network
ASIC	application-specific integrated circuit
BCM	Bienenstock, Cooper, and Munro
BGA	ball grid array
Bi-CMOS	bipolar CMOS
CMOS	complementary metal-oxide-semiconductor
DAC	digital to analogue converter
DBMD	double barrier memristive device
DMSO	dimethyl sulfoxid
ENIG	electroless nickel immersion gold

EPSC	excitatory post synaptic current
EPSP	excitatory post synaptic potential
FPGA	field programmable gate array
HRS	high resistance state
INIC	negative impedance converter
IPSP	inhibitory post synaptic potential
ISI	interspike interval
I-V	current-voltage
LGS	langasite
LIF	leaky integrate and fire
LRS	low resistance state
LSODA	livermore solver for ordinary differential equations
LTD	long-term depression
LTP	long-term potentiation
MRI	magnetic resonance imaging
MOSFET	metal-oxide-semiconductor field-effect transistor
NMDA	N-methyl-D-aspartate

PCB	printed circuit board
PiezoFET	piezoelectric field effect transistor
POSFET	piezoelectric oxide semiconductor field effect transistor
PRC	phase response curve
PUJT	programmable unijunction transistor
PVDF-TrFE	polyvinylidene fluoride trifluoroethylene copolymer
PZT	$PbZr_xTi_{1-x}O_3$
SPI	serial peripheral interface
STDP	spike timing dependent plasticity
TSS	transient silent state
VHDL	very high speed integrated circuit hardware description language
QRC	charge response curve
Zinc Acetate	$Zn(CH_3CO_2)_2$

1 Introduction

The attempt to fathom the foundations of our mind and thus the basis of our mental performance has fascinated mankind since a long time. Although some fundamental insights into the structural properties of the human brain were already gained at the turn from the 19th to the 20th century, its functioning is far from being fully understood.[1–6] This becomes obvious when one considers that the brain forms a highly complex network of approximately 10^{11} nerve cells. Each of these nerve cells has an average of 10^3 connections, which results in the entire brain becoming a highly complex structure with 10^{14} interconnections.[7,8]

A closer study of how the brain works has revealed that individual functions can be distinguished and localised in specific areas. This is exemplified by the famous Broca's and Wernicke's areas, which are responsible for the formation and understanding of language, or the hippocampus and its importance for the formation of long-term memory.[8–11] Although the overall functionality of the brain is based on parallel processing of information, so that within certain limits the role of dysfunctional areas can be compensated by fully functional areas. In addition to this highly parallel computing structure, however, the memory does not exist separately, but is present in the path of information exchange between the individual units of the network. This contrasts strongly with the classical von Neuman architecture that forms the backbone of our modern computer technology.[8,12] Therefore, it is hardly surprising that the first approaches to the construction of biologically engineered systems date back several decades. At that time, it was scientists such as Warren McCulloch, Walter Pitts, Donald Hebb, Carver Mead and John Hopfield, among others, who have coined terms such as neuromorphic engineering and artificial neural network (ANN).[13–20] However, in particular the increase in computing power, which became known as Moore's Law,[21] has accelerated the development of increasingly powerful neural networks in recent

years. Nowadays, it is hard to imagine everyday life without the application of neural networks, be it in the use of facial or speech recognition, in the operation of digital devices or the quick glance at a translation programme. Especially in the recent past, ANNs have received a large amount of media attention for their victory over human opponents in the game show Jeopardy! or the ancient Asian board game Go.[22,23] Although the latter is based on very few rules, it is considered to be one of the most difficult classical board games for an artificial intelligence to master, because of the huge number of possible moves and game length.[23]

Despite all the euphoria, however, it should be noted that most of these technical systems are only designed to solve individual, clearly defined tasks. Humans, for example, have the ability to adapt quickly to changing conditions, even if the rules of the task, or the environment itself, change. A human opponent would be able to react quickly without having to tediously learn new behaviours or be fed with vast amounts of data for supervised or even unsupervised learning. Furthermore, humans possess an immense variety of learned behaviours. For example, a knowledgeable Go player probably would be able to play Shōgi or Mill at an above average level, but certainly at least averagely well, even with little experience. Moreover, if one thinks of everyday life, in many situations there are no rigid rules to follow. Thus, a high degree of transfer of knowledge and behaviour to different contexts is necessary.

In this regard, it is interesting to note that the current algorithms may not represent the learning of a single animal during its lifetime, at least if the algorithms start on a blank sheet. The detection and extraction of statistical regularities would then rather refer to evolutionary processes and a connection to a system that learns on the smaller time scale, i.e. during lifetime, is missing. In this context, an approach based on a mixture of inert information due to a general set of rules given by evolution and additional knowledge gained during lifetime could be promising.[24,25]

Nevertheless, the successes of artificial neural systems are considerable but they came at a high price if their power consumption is taken into account. The technical systems need many kilowatts of power to keep up with their human counterparts, although the latter are commonly quoted to as consuming only about 20 watts. There is no doubt, that this superiority of the brain over man made systems is based on efficient computing and a low energy consumption of actions potentials. This basic units of information in the brain are estimated to consume energy in the range of pJ to nJ.[26–30] This

energy efficiency is remarkable. But what else distinguishes the neuronal information processing in addition to its highly parallel architecture? Where is the secret that needs to be deciphered? Even if these questions have not yet been answered, there are some aspects that stand out.

First of all, it is striking that all information processing in the brain seems to be analogue and binary. It is binary with regard to the generation of action potentials and analogue if one looks at the interaction with the environment.[7,8] Physical quantities such as temperature, light or force, are encoded by specialised cells into neuronal signals and transmitted to the central nervous system for further processing. Although this is the first information reduction, the underlying neuronal code is extremely powerful. It is able to encode the essential information in the form of action potentials on the basis of a multitude of different cells and a sophisticated interconnection of these cells into a spatio-temporal pattern. The neural response varies gradually with time and stimulus strength in an analogue way.[7,8,31,32] Furthermore, the excitation and inhibition of adjacent cells uses neurotransmitters and ion influx and is analogue as well.[7,8]

Second, the transmission of information in the brain differs from modern digital computation. In contrast to the digital computer, the human brain "calculates" much more slowly. This means, that in contrast to transmission at almost the speed of light in a vacuum in a digital computer, an action potential in the biological system travels at speeds of a few to a hundred metres per second.[8] This results in an exchange of information which is far from instantaneous. Furthermore, the information exchange is based on an electrical and a chemical component. In addition to utilising ion-based voltage transmission of signals, the additional neurotransmitter-based, this is the chemical component, signal conduction also introduces a significant time delay.[8] This can result in significant changes in the overall dynamics of a dynamical system.[33,34]

Third, with regard to the brain structure, other interesting features of the brain can be found. It is striking, that the overall organisation of the brain differs from man made systems like the internet or electronic circuits, if network measures like heterogeneity, modularity and randomness are considered. Even biological networks like the proteome or food webs do not match the high degrees of randomness and modularity of cortical maps.[35,36] Here, it should be emphasised, that cortical maps show a high complexity, something which is connected to an intermediate state in between disorder and order or randomness and regularity.[36]

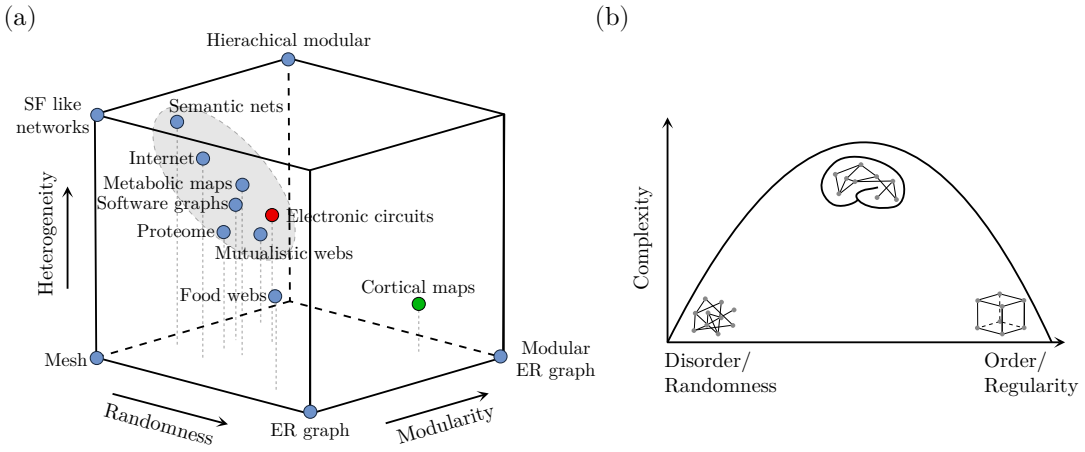

Fig. 1.1: Difference between biological and technical systems in terms of network measures. (a) The difference between technical systems such as the internet and electronic systems and cortical maps is shown qualitatively (graphic adapted from Solé and Valverde (2004)[35]). (b) The complexity increases for an intermediate level of order and disorder (graphic adapted from Sporns (2011)[36]).

In addition, there are indications that the network is self-organised in a way, that the dynamics are at a point of criticality, a point at the beginning of a phase transition. In this respect, there are similarities between the organisation of the brain and other non artificial networks, if properties like scale free dynamics and organisation of brain structures and even chaotic sequences are considered.[37–45]

Inspired by this remarkable creation of nature, alternative computing approaches came into focus in recent years. The driving force behind this development is not only the performance of biological systems, but also the fact that the scaling of components on a chip as predicted by Gordon E. Moore is becoming increasingly difficult and could soon end.[21,46–48] Particular attention is given to oscillators, which can be seen as an abstraction of both local and global activity patterns in neural networks. Furthermore, oscillations and oscillatory dynamics are present in the brain and mechanisms such as synchronisation seem to be important for the cognitive performance of the brain.[34,49–54] Inspired by biology, this has led to significant progress in the development of technical systems based on oscillators. Starting from the purely theoretical considerations of

using oscillators to realise pattern recognition and associative networks, research has accelerated and a plethora of demonstrators have been developed, that can perform a variety of different tasks. Nowadays, even the first nanoscale systems have been successfully realised, proving their feasibility.[55–64]

With today's knowledge it is already possible to develop novel technical systems, that are able to solve problems, in some cases for the first time and in other cases in a different way. However, still not everything is known about the brain and there is much to discover left.

The nervous system of each living being is in an ongoing interaction with the environment. In addition to this loop of sensory reception of information and reaction to it through the manipulation of matter, the dynamics[65] and morphology of the nervous system itself is also in a constant state of interaction.

Where the dynamics are influenced by a change in morphology through phenomena such as plasticity or growth, this does not remain without trace in the structure, and thus morphology. Both areas are mutually connected and individual aspects span a wide parameter space that needs to be investigated in order to find new powerful computing approaches. An attempt to combine both areas could be called *Dymorph Computation*, derived from both fundamental aspects: Dynamics and Morphology. Under certain circumstances, this could lead to new technical systems that are closer to cortical maps in terms of their network properties, such as modularity, randomness and heterogeneity, thus maximising their complexity.

A guiding idea and measure could be to find a path from the red dot to the green dot in Fig. 1.1 (a) and investigate the influences of different system aspects on the parameter space depicted.

In the context of this work, some of the above-mentioned aspects that distinguish neuronal information processing in the human brain from the familiar digital silicon technology will be examined in more detail and used as a motivation.

Inspired by the famous expression *"What I cannot create I do not understand"** this is done with the help of experiments and model systems.

Initially, general and basic chapters on neurobiology, dynamic systems, network theory

*This much-quoted sentence was written on the blackboard of the famous physicist Richard Phillips Feynman at the California Institue of Technolgy in Pasedena shortly before he passed away in 1988. Feynman's thought is complemented by the expression *"Know how to solve every problem that has been solved"*, which can also be found on the board and underlines how fundamental he seemingly considered a profound understanding to be.

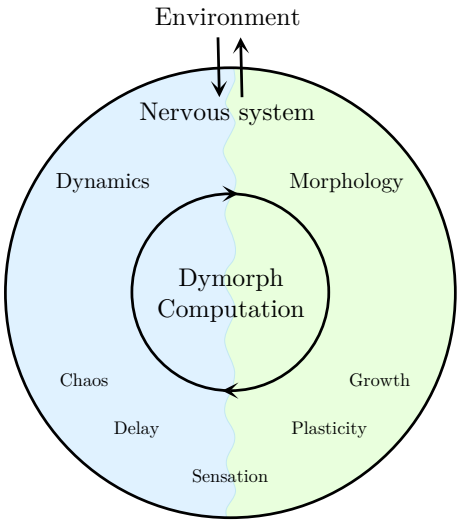

Fig. 1.2: There is an ongoing interaction between environment and nervous system as well as dynamics and morphology. The unification of dynamics and morphology should lead to a Dymorph computational approach. In the course of this work, individual aspects such as chaos, delay, touch, plasticity, and growth are addressed.

and selected technical systems and phenomena are presented. The following chapters of the work are oriented towards and inspired by the path, that an imaginary external stimulus would take to the central nervous system.

In this sense, first a system is presented that uses a force-sensitive component to convert a mechanical voltage into a sequence of pulses of variable frequency. This system is based on a metal–oxide–semiconductor field-effect transistor which is augmented with a piezoelectric material.

In the following, this work focuses on a system which has a pulsatile feedback loop with a finite time delay. The design of the system and the integrated delay line lead to stable firing patterns of the underlying oscillator. In addition, the firing pattern is switchable between different stable states in response to an external stimulus.

Furthermore, first results regarding the short-term and variable coupling of several oscillators are presented. These are based on a liquid electrolyte and filamentary

connections that form. Finally, inspired by network criticality and deterministic chaos, the influence of a memory element on a chaotic system is examined in more detail. Here, Chua's oscillator is used as a model system for a chaotic system. The memristive element for this study is a strongly asymmetric double barrier memristive device with an interface-based switching mechanism.

2 Biological foundations

2.1 Basic structure of a neuron

Already with the change from the 18th to the 19th century, more than 100 years ago, enormous progress was made in understanding the human brain. This is all the more fascinating as the imaging techniques that are common today did not exist at that time.[1,2,4,66]

With an increasing knowledge about the neural structure of the brain and its cells, it seems clear that they can be divided into two main classes. On the one hand, there are the neurons, which are responsible for processing and transmitting information, and on the other hand, there are the glial cells, which are thought to support the structure and functionality of the neurons.[7,8]

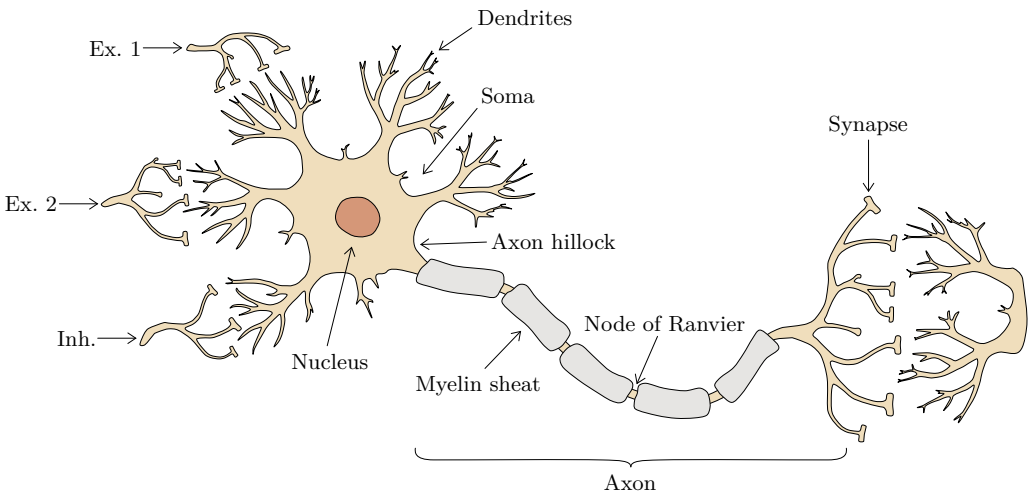

Fig. 2.1: Schematic representation of the basic structure of a multipolar myelinated nerve cell. The incoming synaptic connections are marked as Ex. 1, Ex. 2 and Inh. and refer to potential excitatory or inhibitory connections to the nerve cell.

The basic structure of a multipolar nerve cell is depicted in Fig. 2.1. The nucleus is in the middle of the soma or cell body of the neuron and contains the genetic information. The endoplasmic reticulum, which is omitted in this sketch, is also connected to it and responsible for the synthesis of cell proteins.[8] Another structure present in a cell but not depicted is the Golgi apparatus, which is involved in packaging proteins into vesicles. Several structures extend from the soma. The extensions with a tree like

shape are the dendrites and responsible for the collection of the incoming stimuli, as for example from other neurons.[7,8]
The incoming signals propagate wave-like through the cell body and are integrated at the so-called axon hillock.[7] This part marks the transition from the soma to the axon. It is this tube-like structure that acts as the transmission line for information in the form of action potentials to other neurons. To increase the speed of transmission, the axons of the majority of neurons in vertebrates are coated with myelin.[8] The small segments of the axon which are not coated by myelin are called nodes of Ranvier. Synapses, which connect one cell to another cell, are present at the end of the axon.[7,8]
Furthermore, neurons can be divided into unipolar, bipolar and multipolar neurons with regard to their physiological appearance. The unipolar neurons are most common in invertebrates and are characterised by a single extension with separate functional areas for input and output.[7,8] Bipolar cells have two extensions. One extension serves as an input and one extension as an output for the cell. Many sensory cells are of this type.[7,8] However, the most prevalent group of cells in the nervous system of vertebrates are the multipolar cells. Characteristic for this sort of cells are a single axon and multiple extensions which form the dendrites.[8]
Regardless of the structure of a single neuron, information is transmitted in action potentials. Action potentials are small changes in ionic concentration which lead to a measurable voltage change. However, the information propagation is not solely ionic but also chemical due to the release of neurotransmitters.
It should be emphasised that the form of the action potentials does not differ between cells or between different pieces of information. This means that the manipulation of information and computing power of the nervous system is based on a connection of neurons, their interaction, and in result the path the information travels through and goes to.[8]
The influence one neuron can have on another neuron is based on the type of neurotransmitter released. It is important to note, that different influences can not be mixed regarding a single cell. This means, that each cell is either exciting or inhibiting and in return increase or decrease the firing probability of the subsequent cell.[7,8]

2.2 Information propagation

The information processing in the nervous system is based on changes in ionic concentrations which propagate through the inner cell and neurotransmitters influencing other cells. Together, a complex interplay between dynamics and structure takes place and gives rise to perception and consciousness. In the following, the basic electrical impulse, the action potential, and the local structure that connects nerve cells through neurotransmitters, the synapse, are discussed.

2.2.1 Action potential

In the nervous system, a universal measure of information transmission is the action potential. It is omnipresent and has the same characteristics in magnitude and time between different cells and neural circuits.[7,8,67,68] If the neuron is at rest, that is, in the absence of an action potential, there is a measurable voltage difference between the intracellular and extracellular space which is called resting potential. This voltage potential can be explained in terms of concentration gradients of ions.[7,8]
The build-up of the resting potential is based on a semi-permeable membrane and different concentration gradients. If, for example, there is a high number of K^+ ions and an equal number of organic anions A^- inside the cell, the interior of the cell is initially neutrally charged. However, if the semi-permeable membrane is only permeable to K^+, these ions begin to diffuse into the extracellular space according to the concentration gradient. Since the negatively charged A^- remain inside the cell, a potential difference builds up between the inside and the outside of the cell. This potential difference counteracts the concentration gradient, so that in the case of equilibrium the outflowing and inflowing ion currents balance each other out.[7,8] It was Walther Nernst and his seminal work on electrochemistry who gave rise to the following equation which allows the calculation of the voltage in dependence on different ion concentrations:[69]

$$V = \frac{RT}{zF} \ln\left(\frac{C_e}{C_i}\right). \tag{2.1}$$

It states, that the voltage between the extra- and intracellular space is proportional to the logarithm of ion concentrations outside C_e and inside C_i of the cell. Here, R is not to be confused with an electrical resistance but refers to the gas constant, T to the temperature and F to the Faraday constant. The variable z is the electrical charge of the ion. For example, would z be $+1$ or -1 if one considers K^+ and A^- .[7,8]
Regarding biology, the most common ions in- and outside of the nerve cell are K^+, Na^+, Cl^-, and A^-. During rest, K^+ and A^- have their highest concentration inside the neuron and Na^+ and Cl^- outside of the neuron.[7,8] Thus it is clear, that the equation 2.1 must be further generalized to account for different ions, leading to the Goldman equation:[70]

$$V = \frac{RT}{F} \ln \left(\frac{p_{K^+} C_e^{K^+} + p_{Na^+} C_e^{Na^+} + p_{Cl^-} C_i^{Cl^-}}{p_{K^+} C_i^{K^+} + p_{Na^+} C_i^{Na^+} + p_{Cl^-} C_e^{Cl^-}} \right). \tag{2.2}$$

In addition to equation 2.1, the ion concentrations are weighted by the permeability p of the membrane for each individual type of ion. Normally, the outside of the cell is treated as having a zero potential. Following this convention, the equilibrium voltage of the nerve cell is in the range of $-60\,\mathrm{mV}$ to $-70\,\mathrm{mV}$.[7,8]

Fig. 2.2 (a) shows a schematic of a non-myelinated and a myelinated axonal membrane. Although not depicted, the cell membrane does contain various ionic channels.[8] These channels are built by proteins which give them certain properties, such as specificity for certain types of ions, voltage controlled or neurotransmitter controlled on and off conduction.[7,8,71]
Gene analysis has led to the assumption that there are at least 70 different potassium channels, 9 different sodium channels and a variety of calcium, chlorine and unspecified cation channels.[71] However, for the general qualitative description of the dynamics of an action potential propagating through an axon, it is sufficient to consider the sodium and potassium channels only.[7,8,71] Usually, an action potential of a neuron at rest is triggered by the influence of a depolarizing current. This means that the membrane voltage increases either directly due to the influence of a stimulus injected during an experiment or due to an ion influx as a result of synaptic transmission. The latter is usually based on neurotransmitters which open specialized ion channels

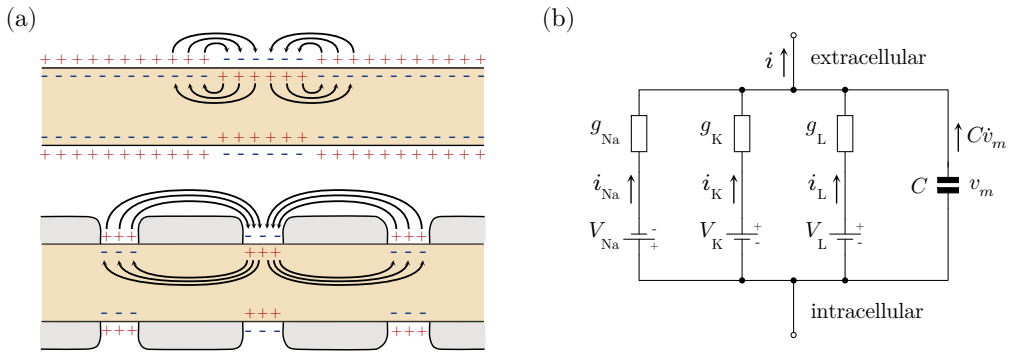

Fig. 2.2: Basic principle behind the dynamics of action potentials and equivalent circuit of the conductance based model. (a) Schematic of a non-myelinated (top) and myelinated (bottom) axon following Purves *et al.* (2004) and Kandel *et al.* (2013).[7,8] The charges of the membrane are marked symbolically with a + and −. The arrows represent the local ionic currents which are responsible for the spread of the depolarization. (b) Equivalent circuit of conductance based membrane model. V_i refer to the single potentials. The conductances of the membrane to specific ions are represented by the conductances g_i. The index "L" refers to the leakage.

in the cell membrane. An increase in membrane voltage will activate more and more voltage gated channels, which increase the membrane voltage further. After a delay, the opened channels start to close again and other voltage gated channels open, causing the membrane voltage to decrease again. One action potential ends with a decrease in membrane voltage below the resting state which is the so-called phase of hyperpolarization.[7,8,71]

The previous considerations and observations are largely based on the patch clamp method.[72–74] The patch clamp method allows the measurement of ionic currents by fixating, thus the name "clamping", the voltage of the membrane. Although the first experiments were carried out on the giant squid axon, these findings also apply to other neurons. As a result, the experiments have lead to the famous Hodgkin-Huxley neuron model.[73] Fig. 2.2 (b) presents the equivalent circuit in which the basic assumptions are shown. In the first model only the sodium, potassium and leakage conductances were used. However, even an increase in ionic currents does not change the basic mechanism behind the generation of action potentials, which makes the Hodgkin-Huxley Model one of the most recognized models.[53] Following the equivalent circuit in Fig. 2.2 (b) it

is clear that:

$$i = C\dot{v}_m + i_{\mathrm{Na}} + i_{\mathrm{K}} + i_{\mathrm{L}}, \tag{2.3}$$

with C as the capacitance of the cell membrane. The variables g_i refer to the conductance of the ion channels. As the conductances are not static, meaning that the resistances are not ohmic, Hodgkin and Huxley introduced so called gating variables, m, n and h.[53,73] As a result, the evolution of the membrane voltage can be modelled as a differential equation, leading to the famous Hodgkin-Huxley model of the squid giant axon.[73] Because

$$i_i = g_i(v_m - V_i) \tag{2.4}$$

for the membrane voltage v_m follows:[73]

$$\dot{v}_m = \frac{1}{C}\left(-\hat{g}_{\mathrm{Na}} m^3 h\,(v_m - V_{\mathrm{Na}}) - \hat{g}_{\mathrm{K}} n^4\,(v_m - V_{\mathrm{K}}) - g_{\mathrm{L}}\,(v_m - V_{\mathrm{L}})\right). \tag{2.5}$$

The intention behind these variables is to introduce a measure of the proportion of open or closed ionic channels in the membrane. The variables m and n refer to the proportion of the activated channels. Here the deactivated state refers to $m, n = 0$ and the activated refers to $m, n = 1$. A value between zero and one refers to a state where just a proportion of the channels is activated.[53]
Besides the activation gates, inactivation gates are also present. These gates are described by h. An inactivated channel refers to $h = 0$, whereas a deinactivated channel is described by $h = 1$.[53] The variables $\hat{g}_i$ are the maximum conductances for the specific ions. Only the leakage current $g_{\mathrm{L}}\,(v_m - V_{\mathrm{L}})$ is modelled as ohmic. The evolution of

the gating variables is described by[53] :

$$\dot{m} = \frac{m_\infty(v) - m}{\tau_m(v)} \tag{2.6a}$$

$$\dot{n} = \frac{n_\infty(v) - n}{\tau_n(v)} \tag{2.6b}$$

$$\dot{h} = \frac{h_\infty(v) - h}{\tau_h(v)} \tag{2.6c}$$

with:

$$m_\infty(v) = \frac{\alpha_m(v)}{\alpha_m(v) + \beta_m(v)} \tag{2.7a}$$

$$n_\infty(v) = \frac{\alpha_n(v)}{\alpha_n(v) + \beta_n(v)} \tag{2.7b}$$

$$h_\infty(v) = \frac{\alpha_h(v)}{\alpha_h(v) + \beta_h(v)} \tag{2.7c}$$

$$\tau_n = \frac{1}{\alpha_n(v) + \beta_n(v)} \tag{2.7d}$$

$$\tau_m = \frac{1}{\alpha_m(v) + \beta_m(v)} \tag{2.7e}$$

$$\tau_h = \frac{1}{\alpha_h(v) + \beta_h(v)} \tag{2.7f}$$

The exact values of the parameters can be found by experimental measurements, making the model highly biologically valid and accurate.[7,8,53,73]

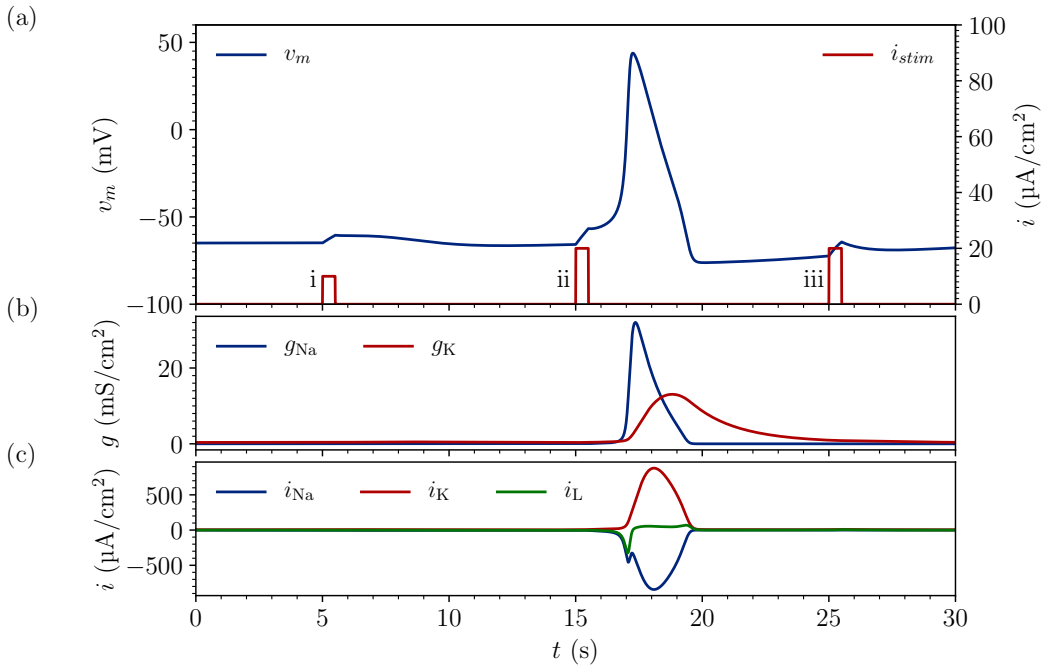

Fig. 2.3: Time evolution of the Hodgkin-Huxley membrane model as described by the equations (2.5)-(2.7f). (a) Evolution of the membrane voltage (blue) under the influence of different input currents (red). (b) The conductance of the Na^+ and K^+ channels. The successive rise and fall of the conductance values that generate the action potential is clearly visible. (c) The resulting ionic currents, which show the net inflow of Na^+ and the outflow of K^+. Additional information about the used parameters and model can be found in A.1.

The results obtained by solving the system which is described by the equations (2.5)-(2.7f) (please refer to A.1 for an overview of the used parameters for this simulation) are presented in Fig. 2.3.

In the partial figure (a) the evolution of the membrane voltage is depicted in blue under the influence of different stimuli which are shown in red ((i)-(iii)). Depending on the timing of the stimulus and the stimulus strength the influence on the membrane dynamics differs. For example, as a result to the stimulus (ii) an action potential is generated. During an action potential the increase and successive decrease in membrane voltage is well visible.

The changing conductances for different ions of the membrane are depicted in Fig.

2.3 (b). The onset of the action potential is connected to a steep increase in g_{Na} due to an opening of voltage gated Na^+ channels.[7,8,71] After a short period of time, the sodium channels start to close again due to deactivation and are inactivated for periods from milliseconds (fast inactivation) to seconds (slow inactivation).[7,8,71,75] Delayed to the onset of the sodium conductance open the potassium channels. This opening is significantly slower and leads to an inward flow of K^+. As a result, the membrane voltage decreases again. This decrease leads to a voltage below the resting potential which is normally referred to as hyperpolarization.[7,8,71]

Although three input currents are presented to the system, just one action potential is generated. This happens because the input must raise the membrane voltage above the threshold at which an action potential is triggered at the axon hillock. It can be seen, that the stimulus (i) is not strong enough to excite the cell. This is the so-called all or nothing principle of neural excitability.[7,8,53] However, even if the stimulus would be strong enough to excite a resting neuron, during the period of hyperpolarization the excitability of the neuron is decreased (compare stimulus (iii) in Fig. 2.3 (a)).[7,8,53] The Fig. 2.3 (c) shows the resulting ionic currents during the generation of an action potential and successive stimulation. Besides the active components of the membrane, its passive properties also have a significant influence on the speed by which the generated action potentials are transmitted. The moment the action potential is generated, the ionic concentrations change. The resulting current depolarizes the adjacent membrane areas of the neuron.[8] Thus, the current has to charge the membrane capacitor. If it is the case, that the membrane is non-myelinated, this is slow, because the membrane capacitance his high.[8] Thus, by decreasing the membrane capacitance the velocity of the action potential can be increased significantly. This happens in the segments of the membrane that are wrapped by the myelin.[8] The small capacitance at the insulated parts of the membrane lead to the observation, that an action potential seems to skip the myelinated parts of the axon. This is the so-called saltatory conduction from the latin word *saltare*.[8] In result, the velocity of the action potential is increased significantly to speeds of about $100\,\mathrm{m\,s^{-1}}$.[7,8]

Indeed, the above considerations and simulations are based on Hodgkin and Huxleys original considerations.[73] However, the model is the most accepted one for neuronal dynamics to date with a high degree of biological plausibility.[53] To name but a few examples for more information on different models and more sophisticated modelling,

the reader might refer to Dayan *et al.* (2001),[67] Izhikevich (2006),[53] Pospischil *et al.* (2008),[76] Haken (2008)[77] or Gerstner (2014).[68]

2.2.2 Synapse

The huge number of nerve cells in the human brain form a dense network. These connections between individual nerve cells are established via so-called synapses. It is thought, that each neuron can have up to a thousand connections to other neurons.[8] Although there are distinct types of synapses present, as for example electrical so-called gap junctions and chemical synapses, the following discussion will be restricted to chemical synapses. It is here, that a conversion from an electrical signal to a chemical signal and back to an electrical signal takes place, and in this process the action potentials, which are identical in each neuron, can have different influences on the postsynaptic cell, depending on the type of neuron, strength of neuronal connection, and type of released neurotransmitters.[7,8,71] The chemical transmission of information is based to a large extend on the release of neurotransmitters into the synaptic cleft. This process is depicted in Fig. 2.4. The neurotransmitters are encapsulated in vesicles for controlled release.[7,8] Their synthesis takes place in advance either in the soma, the synapse, or within the vesicles. Thereby, the cytoskeleton with its microtubules plays a decisive role in the transport of large membranous organelles such as the vesicles. They built a track on which molecular motors transport substances which were formed in the cell body to the synapses.[8]

As soon as an action potential reaches the synapse, voltage-controlled calcium ion channels are opened in the cell membrane of the synapse. This causes the vesicles to connect to the cell membrane and release their content into the synaptic cleft. This process of merging with the cell membrane and distribution of neurotransmitters into the synaptic cleft is known as exocytosis. In contrast, the pinching off of excessive membrane and its absorption back into the cell is called endocytosis.[7,8,71]

After the release of the neurotransmitters, they connect to receptors at the membrane of the postsynaptic cell, among others. Here, depending on the type of neurotransmitter ligand gated ion channels open for specific ions leading to an inflow of ions and change of the membrane voltage of the postsynaptic cell.[7,8,71]

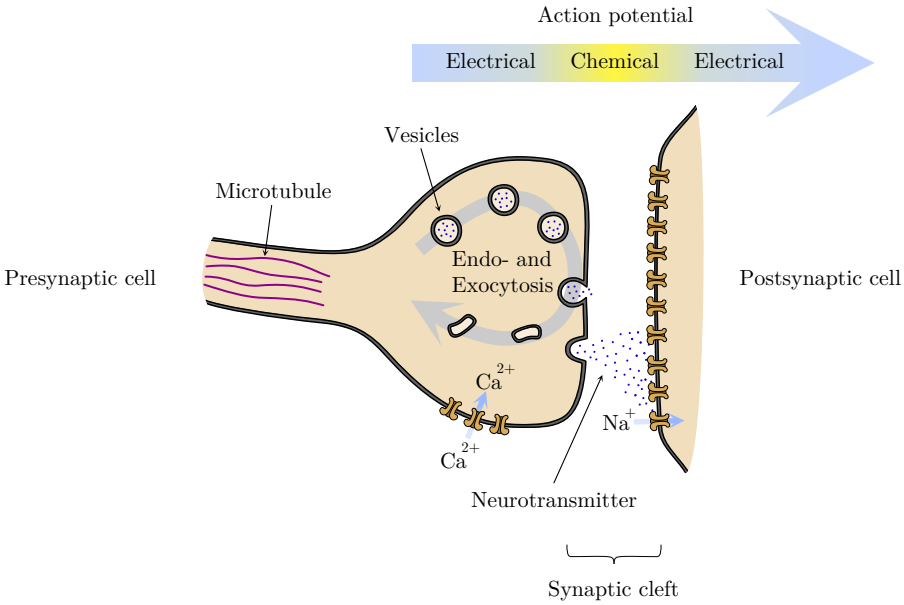

Fig. 2.4: Schematic of synaptic transmission at a chemical synapse. The arrival of an action potential leads to the release of neurotransmitters and influences the next cell.

In general, this direct influence on the membrane voltage is said to be either excitatory or inhibitory and called with respect to the postsynaptic cell an excitatory post synaptic potential (EPSP) or inhibitory post synaptic potential (IPSP). During an EPSP the membrane voltage is depolarized, which increases the probability to generate an action potential, because the membrane voltage is closer to the firing threshold of the cell. In contrast, the membrane voltage during an IPSP becomes hyperpolarized, thus decreasing the firing propability of the cell.[7,8]
It is said that excitatory synapses, which are referred to as Typ I synapses are more likely to be connected to dendrites and Typ II synapses, which act inhibitive, are more likely to be connected to the soma of the postsynaptic cell. The most common representatives of neurotransmitters which generate an EPSP and IPSP are glutamate and γ-aminobutyric acid (GABA), respectively. Here, glutamate typically opens ion channels which are conductive for Na^+ and K^+, whereas GABA opens typically Cl^- conductive channels.[7]

The general capability of computation shall be illustrated by the single and combined occurrence of EPSPs and IPSPs as shown in Fig. 2.5. Depicted is the membrane voltage of the postneuron and a potential influence a transmitter release at the preneuron can have. The red part of the curve shows an increase in the membrane voltage due to a presynaptic synapse. For EPSP 1, the increase in membrane voltage is not sufficient to initiate an action potential. In contrast, the EPSP 2 elevates the membrane voltage over the threshold voltage. As a result, an action potential is generated. The green part of the curve depicts a possible influence of an inhibitory synapse which leads to a decrease in firing probability.
The summation of postsynaptic potentials shall be illustrated by the orange part of the curve. Although EPSP 2 (red dotted line) alone would be strong enough to trigger an action potential, the combination with the IPSP (green dotted line) is not strong enough. The resulting influence on the membrane voltage is depicted in

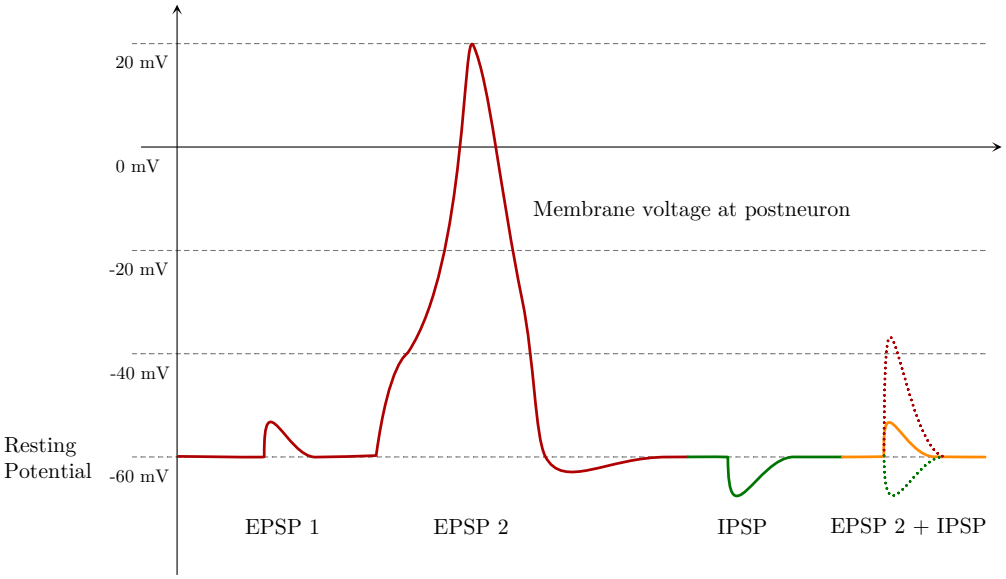

Fig. 2.5: Potential influence of different combinations of EPSPs and IPSPs on the membrane voltage of the postsynaptic neuron schematised. Although the EPSP 1 is not strong enough to trigger an action potential, the EPSP 2 is. However, the combination of an EPSP and an IPSP (EPSP 2 + IPSP) may result in no action potential being generated (modified from Purves *et al.* (2004)[7]).

orange.[7] It should be said that the synaptic transmission is not instantaneous, because the exocytosis, diffusion of neurotransmitters and their binding to receptors at the postsynapse take time. Although a chemical synapse can be as fast as 0.3 ms, usually a transmission delay of 1 ms to 5 ms is present.[8]

2.3 Plasticity and memory

Most likely, the ability of a life form to adapt to its environment during its lifetime, and not just through reproduction, is advantageous for success of the species. In this context the possibility to collect information and use it in later situations drastically improves chances of survival. It is this collection and processing of information for later use which is understood as memory. Memory can be categorized into two different kinds. For instance, consciously remembering a person's name is an example of explicit memory. Whereas the unconscious remembering of the motions required to ride a bicycle is an example of implicit memory.[78]

It were the early studies conducted on the famous patient H. M. by Scoville and Milner[11] which unravelled the importance of certain neuronal circuits for specific memory functions. The patient H. M. was a young man who had already developed epilepsy as a boy. Over the years, the disease became more and more severe, until it was no longer possible to carry out his profession. At this point a bilateral medial temporal-lobe resection was done. In result, he lost his Hippocampus and parts of his Amygdala.[11] Although his recovery from the operation went very well and even his results on the Wechsler-Bellevue intelligence scale were at the same level as before, with the loss of parts of his brain, he has also lost the ability to transfer factual knowledge from the short- to the long-term memory.[11]

Actually, the function of his explicit memory was disturbed, because it relies on the integrity of the Temporal Lobe, Hippocampus, Subiculum, and Entorhinal Cortex, whereas implicit memory needs the integrity of the Cerebellum and Basal Ganglia.[8, 78, 79]

Although the cellular and molecular basis of learning and memory has been suspected earlier in the strength of connection between neurons,[80] it took several years before plasticity could be observed experimentally in mammals, in precisely one of the parts of the brain which were removed from H. M. years ago.[81–83]

2.3.1 Long term depended plasticity

In 1973, Timothy Bliss and Terje Lømo presented, that the activation of specific pathways in the hippocampus can result in an increase in the synaptic transmission along this neuronal pathway. More specifically, it was synapses of the perforant pathway connected to the dentate granule cells. That they observed was, that the response in the second cell increased after the activation by a train of stimuli.[81–83] Today, this behavior is called long-term potentiation (LTP). In contrast, the weakening of neuronal connections is known as long-term depression (LTD). Both mechanisms are often referred to as Hebbian plasticity, named after Donald Hebb, who postulated the modification of neuronal connections as a result of evoked firing.[80,84] The three main

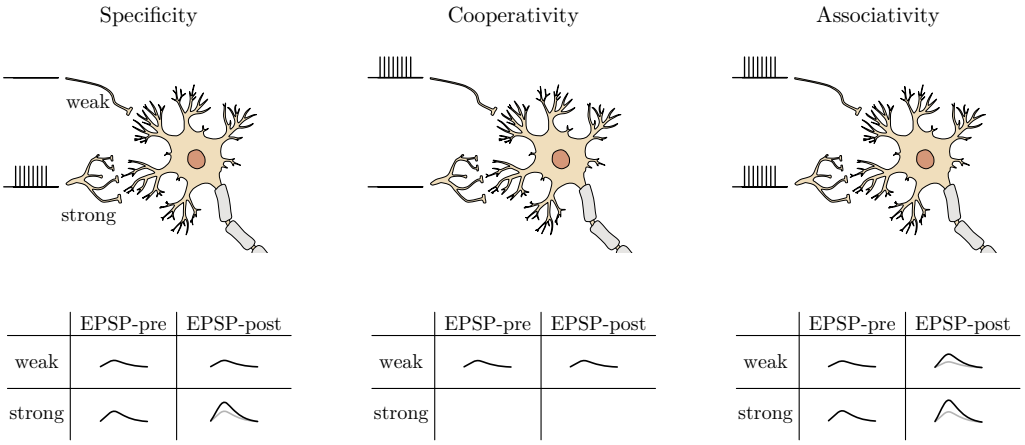

Fig. 2.6: Different properties of long-term potentiation in the hippocampus. Three basic principles of long-term potentiation in the hippocampus, if multiple synapses are involved in the excitation, are specificity, cooperativity, and associativity. Graphic adapted from Nicoll *et al.* (1988).[85]

characteristics of LTP regarding the stimulation by multiple pathways, are shown in Fig. 2.6. In the example presented, a neuron of the hippocampus is stimulated by two different signal pathways. One pathway symbolizes a weak connection and one pathway a strong connection to the cell. The weak connection is drawn at the top and the strong connection at the bottom. Depending on the stimulation, different synaptic connections are increased. It is said that the neuronal connection shows specificity,

cooperativity, and associativity.[8,71,85]

The first property, specificity, refers to the characteristic of synaptic connections that only the stimulated synapses increase in connection strength (Fig. 2.6 left).[8,71] The second property, cooperativity was discovered as soon as the strength needed to evoke LTP was investigated.[71] It states, that the exciting stimulus has to overcome a certain threshold to induce LTP.[8,71] The third property, is associativity and results from cooperativty. Even if the stimulation of the synaptic connection alone would not be sufficient to induce LTP, simultaneous stimulation does evoke LTP (Fig. 2.6 right).[8,71]

Today, the shadows over the molecular and cellular mechanisms of LTP start to vanish. It appears that LTP is decisively caused by an increase in the calcium levels of the postsynaptic nerve cell. The increase in calcium as a result of an increase in firing is mostly supported through the activation of N-methyl-D-aspartate (NMDA) receptors.[8,78]

Besides their importance for the plasticity in the brain, the NMDA receptors have some distinguishing features from other glutamate sensitive receptors, like α-amino-3-hydroxy-5-methyl-4-isoxazolepropionic acid (AMPA) receptors. Whereas, the EPSP evoked by the stimulation of an AMPA receptor is short in time and high in magnitude, the EPSP evoked by a NMDA receptor is usually longer and lower in magnitude due to the tighter binding of the neurotransmitters to the receptor.[71] Moreover, NMDA receptors are blocked by an extracellular magnesium ion, which is removed by a depolarization of the postsynaptic membrane voltage. Thus, a conduction of the NMDA receptor is only possible, if Mg^{2+} is removed and glutamate is present.[71]

However, it should be noted that the exact mechanisms of LTP can vary considerably between different areas of the brain, even within the hippocampus. For example, LTP at the Schaffer collaterals projecting on CA1 is induced through the activation of NMDA receptors. Whereas the initiation of LTP at the direct perforant pathway, which also stimulates region CA1 of the hippocampus, depends only partially on NMDA receptors but also voltage gated Ca^{2+} channels. Furthermore, just a small distance away at the Mossy fibre pathway which stimulates CA3, LTP functions without NMDA receptors, but depends on protein kinase A.[8]

Of course, the mere strengthening of synaptic connections would probably lead to a reduced brain functionality, because the synaptic transmissions might saturate and a further strengthening is not possible.[8] Thus, LTD seems to act as a counterweight and

is important for balance. Unlike LTP, the mechanisms and implications of LTD are less well investigated. However, interestingly LTD does depend on an activation of NMDA receptors and Ca^{2+} channels as well.[8,71,86,87]
In contrast to LTP, different patterns of stimulation are used to trigger LTD. Whereas the stimulus for LTP is usually high in frequency, the stimulus for LTD is low in frequency which leads to a lower depolarization at the postsynaptic cell.[87] The resulting lower levels of Ca^{2+} in the cell activate different enzymes and a different signal pathway.[8]
The first results showing the importance of LTD were obtained using genetically modified mice which had deficits in NMDA depended LTD.[8] During the experiment, the mice had to learn and remember the position of an underwater platform, a task which is known as Morris water maze.[88] Although the mice with a deficit in LTD did learn the location of the platform, they had problems to learn a new location, when the platform was moved. These findings underline the importance of a well-dosed balance between the strengthening and weakening of connections.[8]

2.3.2 Spike timing dependent plasticity

Recently, a rather new model which connects the strengthening and weakening of synaptic connections and correlates both to the exact spike times, has risen.[89] This rather new model is referred to as spike timing dependent plasticity (STDP), which highlights the idea that the causality of firing has an influence on the sign and strength of synaptic change.[90–92] The concept of STDP dates back mainly to the work of Markram *et al.* (1997)[90] and Bi and Poo (1998).[91] In the Fig. 2.7 the original experimental results for the measurement of changed excitatory post synaptic currents (EPSCs) in a solution of dissolved hippocampal cells from Bi and Poo (1998) are shown as blue circles.[91] As mentioned above, the basic concept of STDP lies in the dependence of plasticity on the spike times and causality. Thus, the experimental findings are based on the activation of a pre neuron and a post neuron. The time at which the spike was emitted at the pre-neuron is termed t^{pre} and the time the post-neuron fires is termed t^{post}. Depending on the sequence of firing, the evoked synaptic changes vary significantly.[90,91]

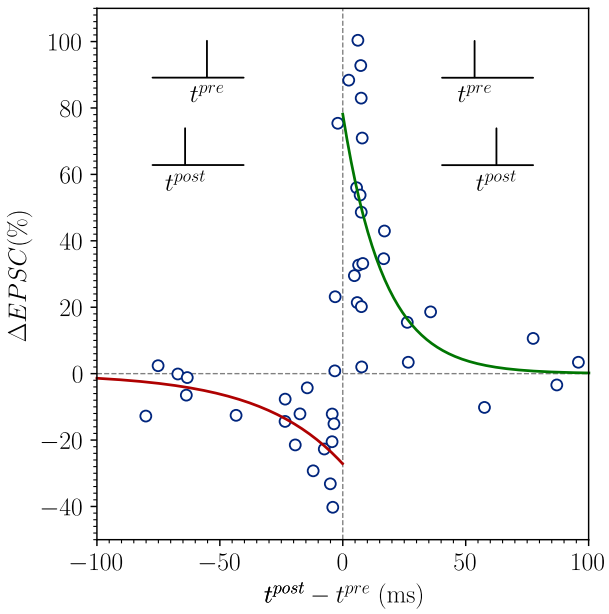

Fig. 2.7: Basic principle of spike timing depend plasticity. The timing of action potential generation at the pre- and post-neurons changes the amplitude of the evoked excitatory postsynaptic current. The open circle refer to the original measurements of Bi and Poo (1998)[91] at dissolved hippocampal neurons. The solid lines are fit functions (please refer to A.2 for additional information about the fit functions and used parameters).

The abscissa of Fig. 2.7 refers to the difference in the action potential generation. Here, a negative value corresponds to the case, that the post neuron fires before the pre neuron has fired. Therefore, this excitation pattern is anticausal, since the supposedly triggering signal occurs after the reaction. By contrast, positive values refer to a causal excitation pattern. Whereas the anticausal case diminishes the evoked EPSC in the post synaptic cell, the causal case increases it.[91]

However, until now the exact cellular and molecular mechanism behind STDP have not been clarified. Nevertheless, this model has some very interesting implications like spike-spike correlation, reduced latency, temporal coding and rate normalization.[89] Additionally it should be noted, that a stabilizing functionality was also proposed through the Hebb-like Bienenstock, Cooper, and Munro (BCM) plasticity theory.[93] Interestingly, the BCM theory follows from STDP if poission like spike trains are considered, although the BCM theory was formulated earlier.[93,94]

2.4 Sensation of mechanical stimuli

The ubiquitous struggle for survival in nature rewards those creatures that have developed an efficient and effective way to collect and process information about their environment. Early on, perceived environmental stimuli were abstracted into different categories. For the human being, this results in the five classical senses: vision, hearing, taste, touch, and smell. Today, the list could be extended to include the modularities: thermal sense, pain, balance and proprioception.[8] In this context sensation is defined as the evoked neural activity in specific parts of the body as a result of a certain physical quantity and thus distinguished from the perception of them.[8]
Following the aforementioned categorisation, the different cells can be divided into classes, such as photoreceptors, thermoreceptors, chemoreceptors and mechanoreceptors. The photoreceptors are part of the visual system with their well-known representatives rod and cone cells which are located in the retina.[7,8] Pain can be sensed by thermoreceptors which are part of the somatosensory system as well as mechanoreceptors and chemoreceptors. Whereas chemoreceptors are also part of the olfactory and gustatory system, mechanoreceptors occur in the vestibular and auditory system.[7,8]
The sensation of touch is part of the somatosensory system and related to the mechanoreceptors.[8] This system can be subdivided further into proprioception, exteroception and interoception, depending on the areas which are covered. It is the exteroception which describes the interaction with the external world in contrast to the sense of oneself and state of the own organs which are described as proprioception and interoception.[8]

The four essential mechanoreceptor cells in the glabrous skin are Meissner corpuscles, Merkel cells, Pacinian corpuscles, and Ruffini endings.[7,8,95] Although all of them respond to mechanical stimulation their response properties differ significantly.
In Fig. 2.8 the typical responses to stepwise mechanical stimuli are shown. Whereas Merkel cells respond to a stepwise excitation by a spiking, which correlates solely by the intensity of the stimulus (Fig. 2.8(i)), the response of Ruffini endings shows an additional activity after the response has ended (Fig. 2.8(ii)), which is in contrast to the response of Meissner and Pacinian corpuscles.[95] Here, the neural response is typically restricted to a change in stimulus strength (Fig. 2.8(iii)).[95]
This results in a certain specificity of each cell type. Therefore, each type of cell has

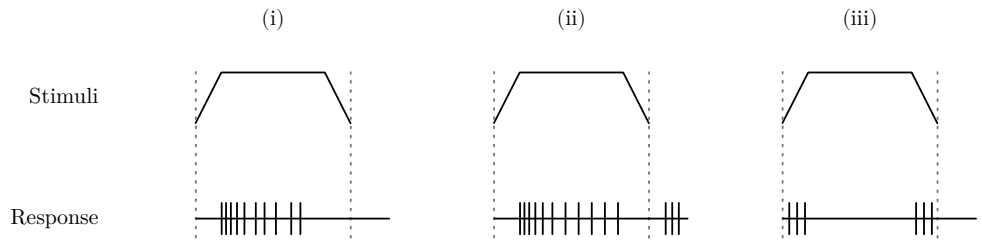

Fig. 2.8: Responses associated to the four principle classes of mechanoeceptors. The inset (i) shows the typical response of Merkel cells. The inset (ii) represents Ruffini endings and inset (iii) shows the response property of Meissner and Pacinian corpuscles. The upper row shows a potential mechanical stimulus and the resulting neural answer is depicted below (adapted from Abraira and Ginty (2013)[95]).

a certain stimulus to which it responds slightly better, such as indentation, stretch, skin movement and vibration.[95] Depending on the response to a constant stimulus, a further differentiation between slow and fast adapting receptors is possible.[7,8,95]

2.5 Spike frequency adaptation

From early on, studies have shown this adaptation of sensory neurons. Here, the work of Adrian *et al.* should certainly be emphasised.[31,32,96] With a series of seminal papers E. D. Adrian formulated and formed the firing rate hypothesis as well as the theory of adaptation in neural signal processing.[32,96] During one of his experiments E. D. Adrian and his colleague Y. Zotterman conducted experiments on the paw of cats. With the help of his experimental set-up the researchers were able to apply a defined pressure to a certain area of the paw and measure simultaneously the neuronal response. The results allowed them to create diagrams showing the frequency in dependence on the stimulus intensity as well as the time course of the neural activity in response to continuous and repeated stimulation.[32] Their results showed, that a constant input results in a sharp increase in neural activity which is followed by an exponential decrease. It can further be observed, that not just the frequency during a continuous stimulation decreases but also the peak frequency, if multiple stimuli are presented in short succession.[32]

The adaptation of the spike firing seems to be an omnipresent functionality which has its roots in both cellular and network induced mechanisms and is not just restricted to receptor cells.[7,97–101]

2.6 Network behaviour and criticality

Up to this point, the nerve cells have only been considered as a single unit. Even the exception, the consideration of plasticity, does not do justice to the complexity that results from the interaction of many nerve cells. Today, it is assumed that the human brain consists of a combination of 85 billion neurons and just as many non-neuronal cells.[102] Besides the pure number of nerve cells, each of them has up to several thousand synapses which result in an enormous interconnected network.[7,8]
Whereas the dynamics of single cells are somewhat well understood, the complex interplay of a multitude of single units is still an open question. Various phenomena can be observed in this highly complex network of nerve cells, which differ significantly depending on the size scale.[8,51,68]
If, for example, only a few cells are considered, dynamics such as bursting or oscillations can already occur even in this small network of neurons.[53] With an increase in the size of the network under consideration, the complexity of the phenomena also increases further. This becomes even clearer when phenomena such as adaptation and plasticity are considered.
The sheer amount of different network configurations as well as the constant exchange between the system and its environment further complicates the picture.[8,34,51,53]
With the consideration of the entire network and the underlying highly complex structure, criticality has come into focus in recent years. There is increasing evidence that the brain as a complex network is self organised at a critical point.[103–106] This critical point is found, for example, at a phase transition from order to disorder or in the context of percolation theory, when, for example, surface coverage increases. Common to the different concepts is a parameter that reaches a critical size. It should be noted, that criticality is not restricted to neuronal systems but can be found in a variety of different models and systems.[106–108]

A well-known model in which criticality becomes visible is the Ising model[109] which can be used to describe ferromagnetism in solids. In this model, the transition from order to disorder can be illustrated by temperature as a parameter. Within the model, the individual spins are coupled to their respective neighbours. The temperature is given as a parameter and has an influence on the spins present. Without an external magnetic field and at a temperature of 0 K, the presence of a common spin direction is most likely. In the model, this would mean that all spins would be up or down, for example. Far above the critical temperature, the system loses its order, so that the spins separate macroscopically. However, at the critical point the fluctuations are scale invariant, and the spatial distribution of the spins show power-law correlations.[104]
Furthermore, criticality is very interesting for the application. It was shown that criticality is a possibility to increase the computing power in recurrent neural networks. This type of networks became known in the context of liquid state machines or echo state networks.[110,111] Instead of changing all internal weights, in this class of networks only the weights of the linear classifier at the output are adjusted during the learning process. If such a network is in a critical state near a phase transition, the performance of the network increases. Here, the separation of input information was used as a measure. As a result, even simple linear classifiers show a higher performance in mapping complex functions in a network organized in such a way.[112,113]

3 Technical foundations

3.1 Dynamical systems

With regard to the analysis of the chaotic system in section 4.4, a brief overview of dynamic systems and some important mathematical concepts will be given below. In general, a dynamical system describes the change of its states in time depending on the initial conditions. A way of describing such systems mathematically is by using differential equations of the form:[114,115]

$$\begin{aligned} \dot{x}_1 &= f_1(x_1, ..., x_n) \\ &... \\ \dot{x}_n &= f_n(x_1, ..., x_n). \end{aligned} \tag{3.1}$$

Here, the variable x_i describes the state of a system and $\dot{x}_i$ its derivative in time.[114,115] The states can have a physical meaning like a position, velocity, current or voltage. If the function $f(x)$ does not explicitly depend on time, the system is said to be autonomous.[115] By using vector notation this system can be written in a more compact fashion:

$$\dot{\mathbf{x}} = \mathbf{f}(\mathbf{x}) \tag{3.2}$$

with $\mathbf{x} = (x_1, ..., x_n)$ and $\mathbf{f}(\mathbf{x}) = (f_1(\mathbf{x}), ..., f_n(\mathbf{x}))$. The point $\mathbf{x}$ refers to one point in the phase plane and its derivative $\dot{\mathbf{x}}$ to the velocity of the point in the phase plane. Tracing the evolution of this system for a given set of initial conditions in the phase plane will give a trajectory of the system.[114,115] An example for a 1-dimensional system could be the reproduction of a bacterial population. It clearly depends on the size of the population at the start and a constant which resembles the rate of cell division.[33]

Thus a potential equation reads to:

$$\dot{x} = \alpha x \tag{3.3}$$

Here, x is the population size and $\dot{x}$ the change with respect to time.[33] It is clear, that this equation can be solved by integration over time:

$$\int_0^t \frac{1}{x} \mathrm{d}x = \int_0^t \alpha \mathrm{d}t \tag{3.4}$$

leading to:

$$ln\left(\frac{x(t)}{x(0)}\right) = \alpha t. \tag{3.5}$$

This is this the well known formula for exponential growth of the form:[33]

$$x(t) = x(0)e^{\alpha t}. \tag{3.6}$$

Note that in equation (3.3) the variable x has the first power only, unlike in nonlinear systems. In nonlinear systems higher orders, multiplications of several variables or trigonometric functions of these occur.[114,116]

A rough classification of problems and observable phenomena, such as chaos or oscillations, is shown in Fig 3.1. The classification is made with regard to the linearity or nonlinearity of the system and the number of independent variables n.
For example, chaos only occurs in a system with three or more independent variables.[114] Whereas a solution to ordinary linear differential equations can be found by solving the characteristic equation, this is generally not possible for nonlinear differential equations.

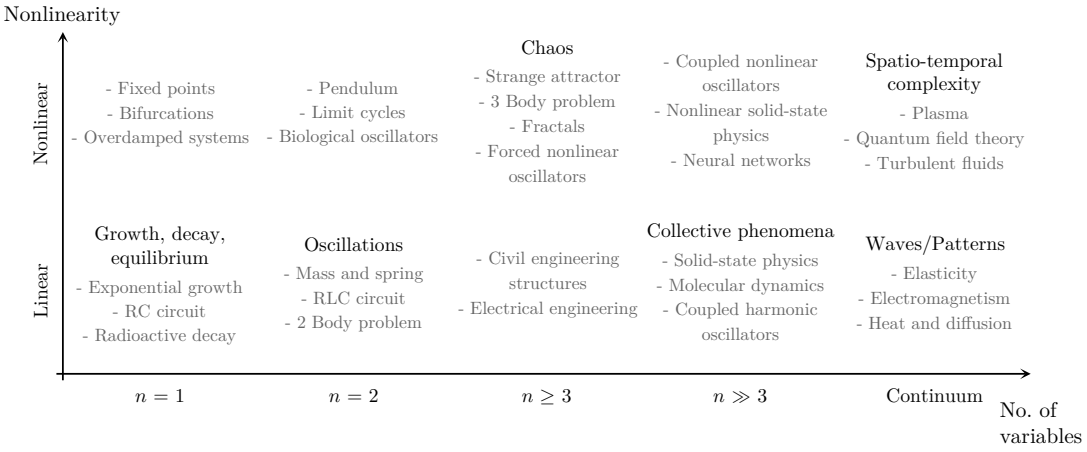

Fig. 3.1: Qualitative classification of dynamic systems based on the number of variables and their nonlinearity. Examples of the individual areas are given in grey (graphic adapted from Strogatz (1994)[114]).

However, an analysis of the stability of fixed points can reveal overall dynamics and an estimation of the system behaviour in the long-term. A fixed point or equilibria of the system satisfies $f(x*) = 0$.[114,116]

For multidimensional systems the dynamics of even nonlinear systems can be approximated in the vicinity of the fixed points by linearisation at these points. By examining the eigenvalues of the linearised system, the fixed points can be classified to be stable or unstable. If for example all eigenvalues are real and negative, the fixed point is said to be stable. In contrast, the fixed point is unstable if the values are real and positive. However, due to different combinations of eigenvalues as well as imaginary parts, further classifications are needed. For example, a two dimensional system with complex eigenvalues and zero real parts can show stable oscillations, but if the real parts increase or decrease the oscillations can turn into unstable or stable spirals, respectively.[33,114–116]

3.1.1 Oscillator

In a mathematical sense the most basic oscillator refers to a trajectory forming a stable periodic orbit in the phase space. Each particle trapped to this orbit passes through the same recurring states in a self-sustained fashion.[34,114,117] Thus, an example of a physical system following this kind of behaviour would be the successive charging of a capacitor and the subsequent discharging due to a nonlinear resistance. The nonlinear resistance could be, for example, a tetrode or tunnel diode which together with an inductance leads to the well known van der Pol oscillator.[118]
From the mathematical definition it is clear, that oscillators are not restricted to electrical systems, but also present in areas such as chemistry (e.g. Belousov-Zhabotinsky reaction[119]), economics (e.g. business cycle model[120,121]) or biology (e.g. circadian rhythm[122]) to name just a few.

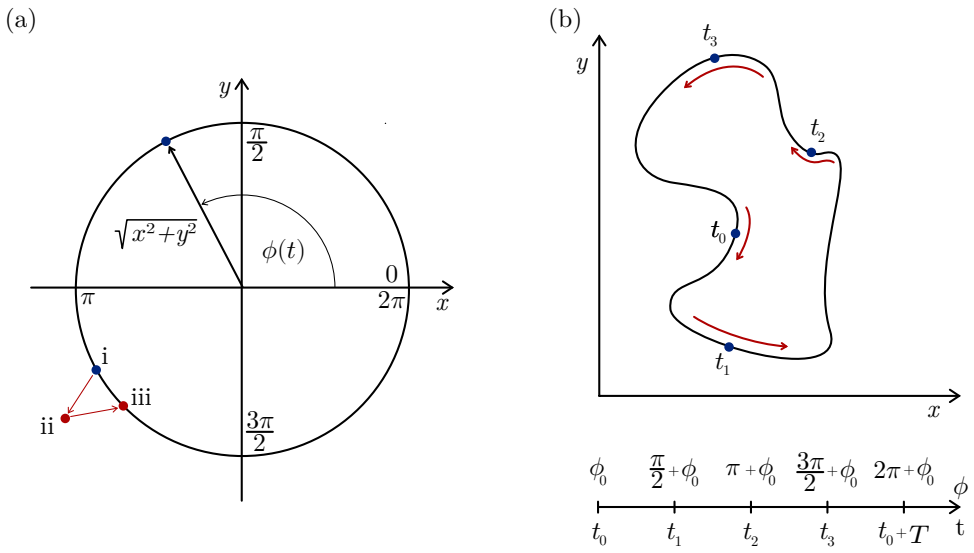

Fig. 3.2: Possible interpretation of an oscillator in the phase space. (a) The state (blue circle) changes and moves uniformly in a circle in the euclidean distance $\sqrt{x^2+y^2}$ to the center. In the third quadrant an example of a perturbation to the system is given. From the initial state (i) the system is perturbed into the state (ii) and converges back on the limit cycle (iii). (b) The definition of a self sustained oscillation is shown, where the state follows a trajectory of arbitrary shape. In general, the movement around the limit cycle is non uniform. The phase $\phi(t)$ is considered as a fraction regarding the period, with a $\phi(t) = \phi(t) + 2\pi k, k \in \mathbb{Z}$ periodicity (graphics in reference to Pikovsky *et al.* 2003[34]).

In Fig. 3.2 (a) the limit cycle of a quasilinear oscillator is shown. In the case of quasilinear oscillators, the periodic orbit in the phase space is nearly circular. For each moment in time, the system is in a certain state which is shown as the blue dot and its underlying function can be taken as a sine function of the following form:[34]

$$x(t) = \hat{x}sin(\omega t + \phi_0). \tag{3.7}$$

Here, ω refers to the angular frequency of the oscillator as a multiple of 2π and f, and ϕ_0 is the initial phase of the oscillator. The distance from the center can be measured as the euclidean distance and is the amplitude of the oscillation. The phase changes with time and equals the angle between the vector pointing to the state of the system and the origin with regard to the coordinate system. Thus, the phase of the oscillator is periodic with $\phi(t) = \phi(t) + 2\pi k, k \in \mathbb{Z}$, as well.[34] The time needed for the state to fulfil one rotation is the period of the oscillation and connected to the angular frequency by:[34]

$$T = \frac{2\pi}{w}. \tag{3.8}$$

In the third quadrant of the coordinate system in Fig. 3.2 (a) an example for a geometrical interpretation of a perturbation is given. An external stimulus will change the state of the system (i) to a new state (ii). In result, the system will converge back to the limit cycle (iii). It is important to note, that the time needed for the system to relax back to the limit cycle might be different from the time which would be necessary for the system to move directly from the point (i) to the point (iii). This leads to a persistent phase difference, although the amplitude converges back to its original value.[34]

Usually, the limit cycle of an oscillator does not have the shape of a circle. In Fig. 3.2 (b) a general case is shown. There, the limit cycle is arbitrarily shaped. Here, the starting point of the oscillation can be chosen randomly. While the oscillator passes through all states in T, ϕ and T can be defined as connected linearly. Therefore, it is clear that the velocity on the limit cycle is not distributed necessarily uniformly.[34]

Furthermore, a limit cycle on which the velocities alternate between slow and fast in short distance is a so-called relaxation type oscillator. The example of a slowly charging and quickly discharging capacitor would be a classical example of such a system.[34,118]

3.1.1.1 Phase response curve

In neural systems the neurons are interconnected in a highly complex way and in an ongoing interaction with each other. Through the interpretation of single neurons or neuronal ensembles as neural oscillators, the possibility to quantify the interaction between single units is highly interesting for the prediction of network behaviour. One tool to gain insight into this interaction is the so-called phase resetting or phase response curve (PRC), which defines the change in phase in response to an external perturbation at a certain phase.[123]

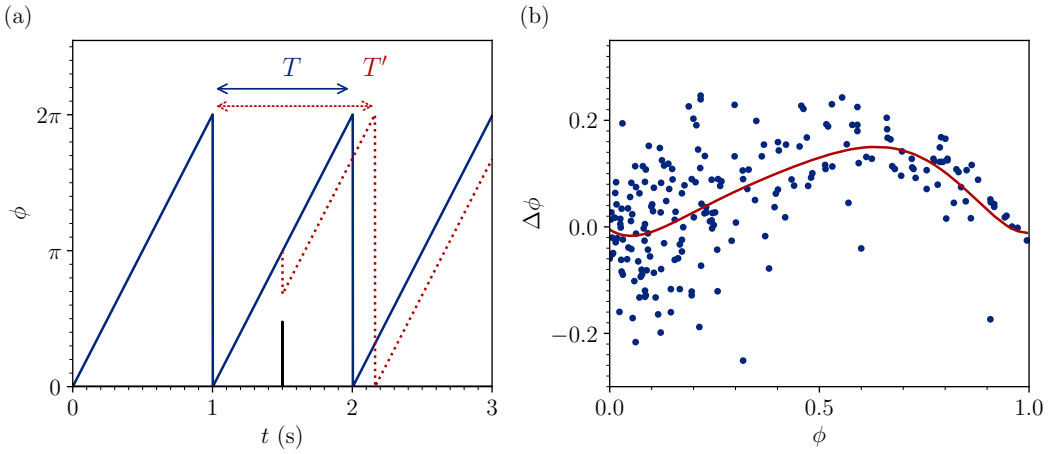

Fig. 3.3: Example of the influence of an external perturbation signal on an oscillator and an experimentally obtained PRC. (a) Possible inhibitory influence of an external perturbation to the phase of an oscillator and resulting change in period. (b) Measured Phase Response Curve from a stellate cell in the medial entorhinal cortex (data from Netoff *et al.* 2005,[124] for the curve fit a sextic polynomial was used, values in A.3).

In Fig. 3.3 (a) the possible time evolution of a phase oscillator is shown. The blue line represents the evolution of the phase of the unperturbed oscillator in time, whereas

the red dotted line depicts the perturbed oscillator. A perturbing signal (black) is applied at 1.5 s in this example. The phase of the oscillator changes in reaction to the perturbation signal. The trajectory is set to an earlier phase and in result the period of the oscillator is prolonged. In this case the interaction is said to be inhibitory. In contrast, an acceleration of the trajectory or shortening of the period refers to an excitatory connection (please see EPSP and IPSP in section 2.2.2 for biological excitatory and inhibitory connections). From the influence of a short perturbing signal on the phase of an oscillator the PRC can be calculated using[123] :

$$\Delta\phi = 1 - \frac{T'(\phi)}{T}. \tag{3.9}$$

The resulting PRC $\Delta\phi$ depends on the modulated period T' normalized by the intrinsic, unperturbed period T. From the definition it is easy to see, that $\Delta\phi < 0$ for inhibitory connections and $\Delta\phi > 0$ for excitatory connections.
Due to the definition of a changing period as the response of the system to a small and short perturbation, the PRC can be determined experimentally. This was done by Netoff *et al.* 2005[124] on stellate cells in the medial entorhinal cortex. The resulting PRC as a fit to the measured values is presented in Fig. 3.3 (b). Although, the main influence of the perturbation is an advancement of the period, pulses presented at the beginning of the phase do have a delaying influence.
It is possible to make predictions regarding network behaviour by distinguishing PRCs qualitatively. For example, a PRC with only positive values is called Typ I, whereas a PRC with positive and negative values is called Typ II PRC. Simulations with different neuron models have shown, that a Typ I PRC can prevent synchronization. Whereas, a Typ II PRC can promote a synchronization.[125] Besides network behaviour an exactly known PRC can be used to predict firing patterns in oscillators with a defined time delay.[126,127] Thus, knowledge of the PRC is a useful tool for the analysis of the dynamics of coupled oscillators.

3.1.1.2 Delayed feedback and jittering bifurcations

When thinking about the influence of time delays on dynamical systems, an example could be an old shower where time delays cause oscillating instabilities.[128] In the beginning the water might be too cold. However, the moment one starts to regulate the amount of hot or cold water, the system needs time to change the temperature. Therefore, one might be tempted to regulate the temperature even further beyond the point of a comfortable temperature, which means that one has to change the water temperature again after the new temperature is finally set. As a result, the point of a comfortable temperature can be missed completely.[128]
In biological systems the information propagation is not instantaneous and far from speeds comparable to the clock speed of modern computers (please refer to chapter 2.2.2 for more information about the signal transmission between neurons). Therefore, studying the influence of a time delay on the dynamics of oscillators is obviously desirable. In recent times, tremendous progress was made regarding pulsatile feedback loops and their impact on the dynamics of phase oscillators. A research on neurons of the sea slug *Aplysia* with an artificial feedback loop revealed multistable solutions in the firing patters in dependence on the delay, initial conditions and external perturbations.[129]
Furthermore, a time delay influences the synchronization behaviour of coupled oscillators and gives rise to complex spike patterns and interactions.[130–133] This can even lead to the phenomenon of amplitude death in a system of coupled identical oscillators.[128,134] By changing the time delays in networks of interconnected oscillators, complex patterns can be stored in the phase relationships of the oscillators.[135]

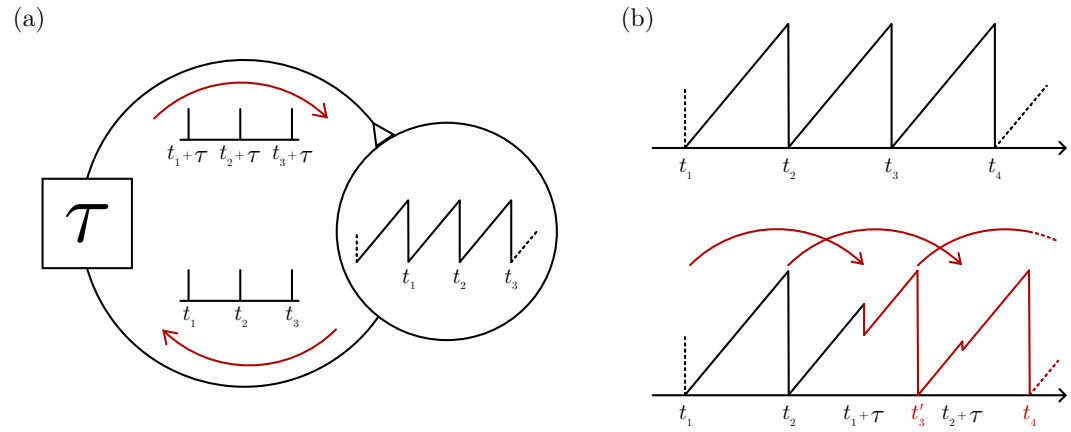

Fig. 3.4: Schematic representation of a pulsatile feedback loop with finite time delay of an oscillator and its self-influence. (a) Working principle of a basic loop. The times of phase reset are treated as pulses which are delayed. (b) Influence of an activated delayed feedback at t_1 on the phase evolution in time. The red trace corresponds to the change in the trajectory due to a pulsatile delayed feedback.

The basic principle of an oscillator with a pulsatile feedback and finite time delay is depicted in Fig. 3.4 (a). Here, a pulse refers to the time the phase of the oscillator is reset to 0. These pulses are delayed and feed back to the oscillator. Depending on the coupling, the influence can be excitatory, inhibitory or any combination of both depending on the specific phase in which the delayed pulse influences the oscillator as described by the underlying PRC.

In Fig. 3.4 (b) an example for the on-switch of a delayed feedback on a phase oscillator is given. In the upper part of the diagram a possible time course of an unperturbed oscillator is shown, the spike times are marked as t_1 to t_4. After the onset of the pulsatile delay at $t = t_1$ the pulse is delayed by $\tau > t_2 - t_1$. In return, it influences the phase between t_2 and the original spike time t_3.

In the example given, the influence is set to be inhibitory but not constant, which leads to a reset of the phase at the time point $t_1 + \tau$. In response to the perturbation the spike time changes to t'_3. As the time delay is longer than one intrinsic period of the oscillator, the next delayed pulse arrives at a different phase which leads to a different change in phase (depending on the shape of the PRC). This underlines the potential complex solutions which might arise from long delays and complex PRCs. Depending

on the slope of the PRC, multiple stable solutions can arise, which will be shown in the following by means of an example.

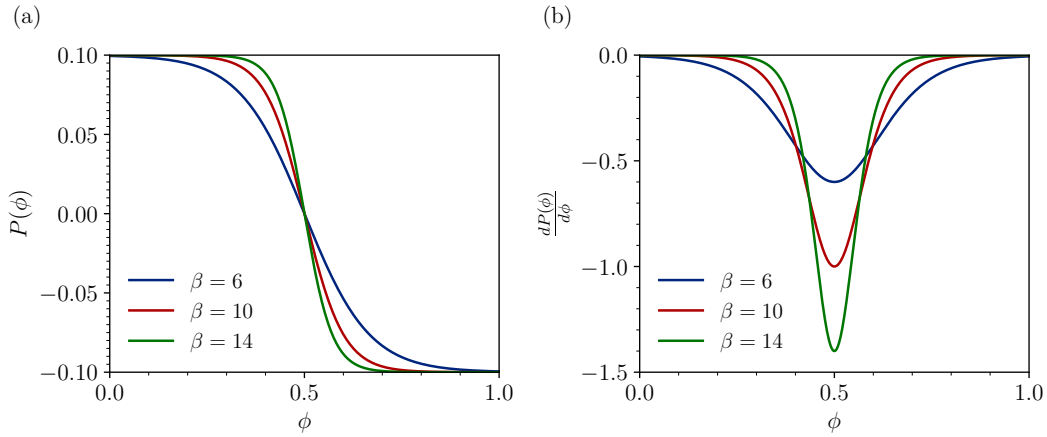

Fig. 3.5: An example of a PRC following the function $P(\phi) = \alpha \tanh(\beta(\phi - 0.5))$ with $\alpha = -0.1$ under variation of β. (a) Resulting PRC for different values of β. (b) Slope of the PRCs shown in (a).

A given PRC $P(\phi)$ of the form presented in Fig. 3.5 (a) is used. The underlying function reads to:

$$P(\phi) = \alpha \tanh(\beta(\phi - 0.5)). \tag{3.10}$$

The PRC changes from advancing to delaying the intrinsic period of the oscillator in the interval [0,1]. The slope can be calculated by differentiating the PRC which leads to:

$$\frac{dP(\phi)}{d\phi} = \alpha\beta \operatorname{sech}^2(\beta(\phi - 0.5)). \tag{3.11}$$

As the function $P(\phi)$ has it highest slope at $\phi - 0.5 = 0$ and the hyperbolic secant

equals 1 at this point, the maximum slope of the PRC reduces further to:

$$\frac{dP(\phi = 0.5)}{d\phi} = \alpha\beta. \tag{3.12}$$

Different magnitudes of the slope which result from a variation of β are depicted in Fig. 3.5 (b). As stated by Klinshov *et al.* 2015,[126,127] multijitter bifurcations can occur at systems with an underlying PRC which has an interval with a slope < -1. In the given example, this is the case for $\alpha = -0.1$ and $\beta > 10$.

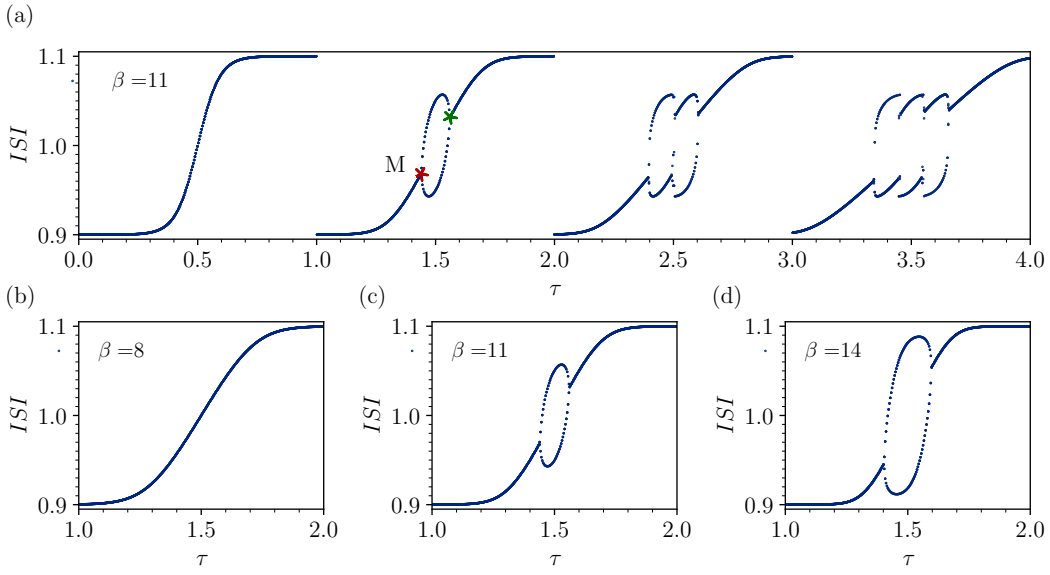

Fig. 3.6: Resulting interspike interval (ISI) for a delayed feedback loop of an oscillator with the PRC presented in 3.9 ($\alpha = -0.1$). The points of multijitter bifurcations are marked red and green, respectively. (a) ISI with for the first four periods and a fixed β. (b) - (d) ISI for $1 \leq \tau \leq 2$ under variation of β.

From the PRC defined in eq. 3.10 the resulting ISIs for a self sustained oscillator under the influence of a delayed pulsatile self feedback can be calculated. With a given intrinsic period of one for the underlying oscillator, the Fig. 3.6 depicts the resulting periods for different sets of parameters. Subfigure (a) shows the ISIs for $0 \leq \tau \leq 4$ for a fixed β. For $\tau \leq 1$ the resulting points have the same shape as the mirrored underlying

PRC (compare Fig. 3.3). The behaviour of the oscillator changes with increasing delay time. While for $0 \leq \tau \leq 1$, only one stable solution exists, the ISIs split up for $\tau > 1$. The points at which several ISIs exist for a constant τ are in the area of the largest negative slope, this is around $\tau = k + 0.5$ with $k \in \mathbb{N}_0$.
The transition from regular spiking, this is the change from only one ISI into the regime of alternating spiking, is called multijitter bifurcation. It should be noted, that in this regime multiple stable solutions for the sequence of long and short ISIs exist.[126,127]
Fig. (b) - (d) show the influence of the changing slope on the system behaviour. Only with the transition from $\beta < 10$ to $\beta > 10$, which refers to a slope < -1, for the fixed α, does the ISI over τ curve split up.

3.1.2 Deterministic chaos

To investigate the potential influence of a memory element on highly chaotic dynamics, a model system was chosen. Because of the good mathematical treatment of the base system and the use of just a few basic passive components, besides the nonlinear one, the model system is the well known Chua's Circuit. In Fig. 3.7 (a) the equivalent circuit of Chua's System is shown. The basic circuit consists of one passive ohmic resistance, three energy storing elements and a nonlinearity, the so-called Chua's Diode. Both the circuit and the diode are named after their inventor Leon Chua.[136,137]
The fundamental differential equations which describe the system can be derived easily from the circuit. It is clear, that for the state variables v_1, v_2 and i_l follows:

$$\dot{v}_1 = \frac{\dot{i}_1}{C_1} \tag{3.13a}$$

$$\dot{v}_2 = \frac{\dot{i}_2}{C_2} \tag{3.13b}$$

$$\dot{i}_l = -\frac{v_2}{L}. \tag{3.13c}$$

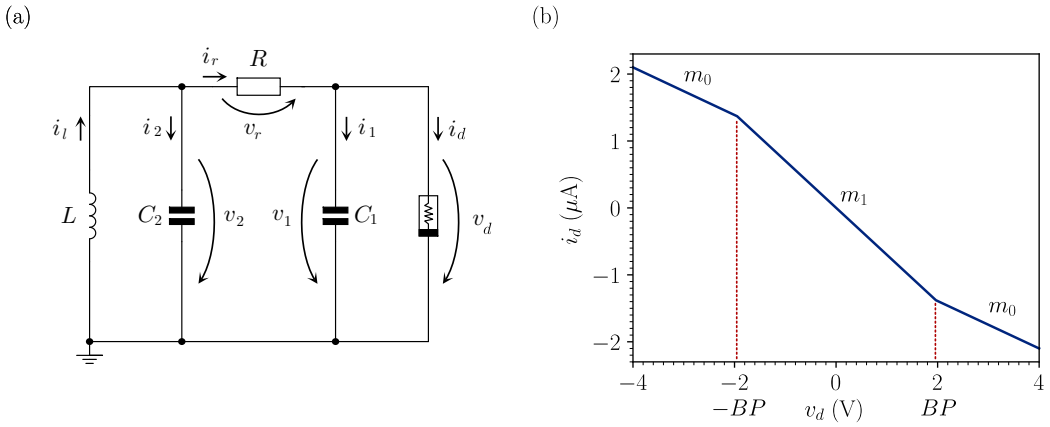

Fig. 3.7: Chua's Circuit and current-voltage (I-V) curve of Chua's Diode. (a) Equivalent circuit of the system, the three state variables are the voltages over the capacitors and the current through the inductance. (b) Piecewise linear function showing the current-voltage characteristics of Chua's Diode. The slopes are marked by m_0 and m_1, the symmetry breaking points are $-BP$ and BP.

Using Kirchoff's first law, the currents can be expressed as:

$$i_1 = i_r - i_d(v_1) \tag{3.14}$$

and

$$i_2 = i_l - i_r. \tag{3.15}$$

The voltage over the resistance R using Kirchoff's second law reads to:

$$v_r = v_2 - v_1. \tag{3.16}$$

Because:

$$i_r = \frac{v_2 - v_1}{R}, \tag{3.17}$$

a system of differential equations describing Chua's Oscillator can be derived by inserting (3.14) and (3.15) in (3.13a) - (3.13c) together with (3.17). Thus, the overall system reads to:

$$\dot{v_1} = \frac{1}{C_1}\left(\frac{v_2 - v_1}{R} - i_d(v_1)\right) \tag{3.18a}$$

$$\dot{v_2} = \frac{1}{C_2}\left(\frac{v_1 - v_2}{R} + i_l\right) \tag{3.18b}$$

$$\dot{i_l} = -\frac{v_2}{L}. \tag{3.18c}$$

The current $i_d(v_1)$ refers to the current through Chua's Diode. Normally the diode is modelled as a piecewise linear function as shown in Fig. 3.7 (b). The diode is crucial for the functioning of the chaotic oscillator, because of the polarities of the current-voltage characteristics. When a positive voltage is applied, the resulting current is negative in relation to the passive sign convention and vice versa. This means, that the resonant circuit, which is build by L, C_1, and C_2, is supplied by energy through this active component.
An additional function of Chua's Diode is the symmetry breaking property of its I-V curve. The points where the slopes change are called symmetry breaking points. At $-BP$ the slope changes from m_0 to m_1 and at BP back to m_0. A function of the current voltage characteristics of the diode is normally expressed as:

$$i_d(v_1) = m_0 v_1 + \frac{m_1 - m_0}{2}\left(|v_1 + BP| - |v_1 - BP|\right). \tag{3.19}$$

Besides the original definition in equation (3.19), cubic functions can be used to model Chua's Diode resulting in chaotic oscillations as well.[138,139] A first stability analysis of the system can be made in regard to the stationary solutions using the Jacobian:

$$J_0 = \begin{pmatrix} \frac{\partial f_1}{\partial x_1} & \cdots & \frac{\partial f_1}{\partial x_n} \\ \vdots & \ddots & \vdots \\ \frac{\partial f_n}{\partial x_1} & \cdots & \frac{\partial f_n}{\partial x_n} \end{pmatrix} \Bigg|_{x=x_0} . \tag{3.20}$$

This leads to the following trivial solution for the system (3.18a)-(3.19):

$$J_0 = \begin{pmatrix} -\frac{1}{RC_1} - \frac{m_1}{C_1} & \frac{1}{RC_1} & 0 \\ \frac{1}{RC_2} & -\frac{1}{RC_2} & \frac{1}{C_2} \\ 0 & -\frac{1}{L} & 0 \end{pmatrix}, \tag{3.21}$$

because the first derivative for the piecewise linear function $i_d(v_1)$ equals the slope m_1 at the evaluation point. A statement about the stability can be made using the determinant of the Jacobian. Using the Rule of Sarrus the determinant of the matrix reads to:

$$\begin{aligned} det(J_0) &= -\left(-\frac{1}{L} \cdot \frac{1}{C_2} \cdot \left(-\frac{1}{RC_1} - \frac{m_1}{C_1}\right)\right) \\ &= -\frac{1}{LC_1C_2}\left(\frac{1}{R} + m_1\right) \end{aligned} \tag{3.22}$$

This point is unstable if:

$$-\frac{1}{LC_1C_2}\left(\frac{1}{R} + m_1\right) > 0, \tag{3.23}$$

because a real-valued positive eigenvalue exists. This condition is true, as long as:

$$\frac{1}{R} + m_1 < 0, \tag{3.24}$$

and therefore it follows for the control parameter:

$$R > -\frac{1}{m_1}. \tag{3.25}$$

For the set-up used in this work, this is given for values of $R > 1.423\,\mathrm{M\Omega}$ (see A.4 for more information about the used parameters), which were used during the entire experimental and theoretical work.
Further information about the dynamics of the Chua System can be obtained by setting the vector field given by (3.18a)-(3.19) to zero. From (3.18c) the first solution $v_2 = 0$ can be obtained easily. By inserting $v_2 = 0$ into (3.18b) it follows:

$$0 = \frac{1}{C_2}\left(\frac{v_1}{R} + i_l\right), \tag{3.26}$$

which leads to:

$$i_l = -\frac{v_1}{R}. \tag{3.27}$$

Thus, equation (3.18a) is left to solve. It is:

$$0 = \frac{1}{C_1}\left(-\frac{v_1}{R} - i_d(v_1)\right) \tag{3.28}$$

and thus:

$$v_1 = -Ri_d(v_1). \tag{3.29}$$

For the evaluation of the piecewise linear function $i_d(v_1)$ only positive values greater than the symmetry breaking point are considered. Therefore, it follows:

$$v_1 = -R\left(m_0 v_1 + BP\left(m_1 - m_0\right)\right). \tag{3.30}$$

Solving this leads to:

$$v_1 = \frac{BP(m_0 - m_1)}{\frac{1}{R} + m_0}. \tag{3.31}$$

Again the Jacobian can be evaluated at that stationary state:

$$J_{12} = \begin{pmatrix} -\frac{1}{RC_1} - \frac{m_0}{C_1} & \frac{1}{RC_1} & 0 \\ \frac{1}{RC_2} & -\frac{1}{RC_2} & \frac{1}{C_2} \\ 0 & -\frac{1}{L} & 0 \end{pmatrix}, \tag{3.32}$$

with a change in the slope from m_1 to m_0 an upper bound at $R = 2.817\,\mathrm{M\Omega}$ for the real eigenvalue can be obtained.
Numerical studies show, that the stationary solutions are unstable over almost the entire range of the explored resistance values. The change of the sign of the complex eigenvalues real parts hints at the existence of a Hopf Bifurcation. Treating the coupling resistance R between C_1 and C_2 as a control parameter a bifurcation diagram can be obtained as a helpful tool to visualize the changes in the dynamics.

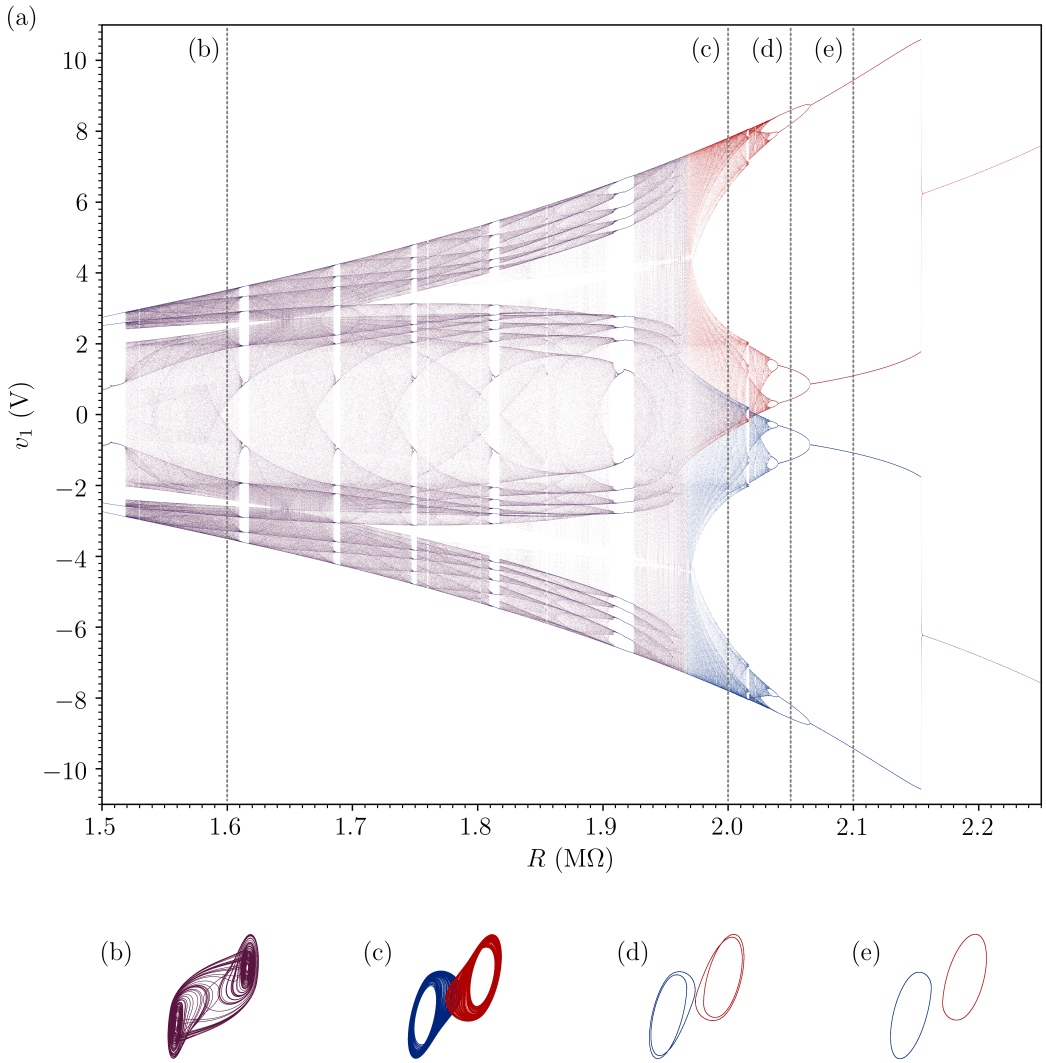

Fig. 3.8: Bifurcation diagram of v_1 with R as the control parameter. (a) Bifurcation diagram of the equilibrium point of v_1 of Chua's Circuit with R as a control parameter for two different initial conditions (red: $v_{10} = 1, v_{20} = 0, i_{l0} = 0$, blue: $v_{10} = -1, v_{20} = 0, i_{l0} = 0$). The simulation was carried out by a continuous decrease in R, with $\Delta R = 100\,\Omega$ using an algorithm with an automatic switch between implicit Adams and backward differentiation formulas (livermore solver for ordinary differential equations (LSODA), as integrated in scipy which is based on Hindmarsh (1983)[140] and Petzold (1983)[141]). The single simulated time windows are 200 s. Shown are the local minima and maxima of v_1. (b)-(e) Sections of the time evolution of the system variables v_1, v_2 and i_l for different values of R. With a decrease in R, the dynamics traverse from periodic solutions ((e): $R = 2.1\,\mathrm{M}\Omega$ and (d): $R = 2.05\,\mathrm{M}\Omega$) to a chaotic one scroll attractor ((c): $R = 2.002\,\mathrm{M}\Omega$) and the well known double scroll attractor ((b): $R = 1.6\,\mathrm{M}\Omega$). The dynamics are repeatedly interrupted by periodic windows (refer to A.4 for an overview of the used parameters).

The diagram depicted in 3.8 (a) was obtained by varying the resistance in steps of $\Delta R = 100\,\Omega$ starting from certain initial conditions. For every step of R, the state of the system from the previous value of the bifurcation parameter is conserved. This keeps the trajectory near the attractor which minimizes possible transients.
For each step of the control parameter a time window of 200 s is simulated. Then, for each time window the local minima and maxima of the state variable v_1 are determined and plotted with their corresponding value of R. The simulations are done with two different initial conditions. One run starts at a positive value of v_1 (red) and one at a negative value of v_1 (blue). It can be seen that the stable equilibrium in both cases vanishes in a Hopf Bifurcation ($R \approx 2.155\,\mathrm{M}\Omega$), which gives rise to a periodic solution (3.8 (e)). From this the system undergoes the well known period doubling (3.8 (d)) route to chaos (3.8 (c), (b)).
The time courses for certain characteristic parameters are shown in 3.8 (b)-(e). Here the merging of the two trajectories into one chaotic double scroll attractor and the underlying symmetry of the system is clearly visible. During the experiments, the values for R were chosen in the regime of a double scroll attractor at $R = 1.6\,\mathrm{M}\Omega$ to exploit the positive and negative dynamics as well as minimizing the maximum voltages of the system to magnitudes beneath critical values for the memristive device. The chaotic double scroll attractor shown in (b) is also called strange attractor. Although the trajectories at the attractor are bound to this region in the phase space, they separate exponentially from each other.[114]
There exist a variety of different strange attractors. Besides the attractor from Chua's circuit, among the most popular ones there are the Lorenz,[142] the Rösler,[143] and the Hénon[144] attracors. In Fig. 3.9 the time evolution of the system at $R = 1.6\,\mathrm{M}\Omega$ is shown. The characteristic oscillations of Chua's Oscillator are clearly visible. Although the underlying dynamics are based on deterministic chaos, the change in polarity seems to be randomly driven. After each polarity change of the state variable v_1, the local oscillations increase until v_1 switches its polarity again. This change of polarity is visible as a change between the scrolls of the attractor of the momentary state in the phase space.

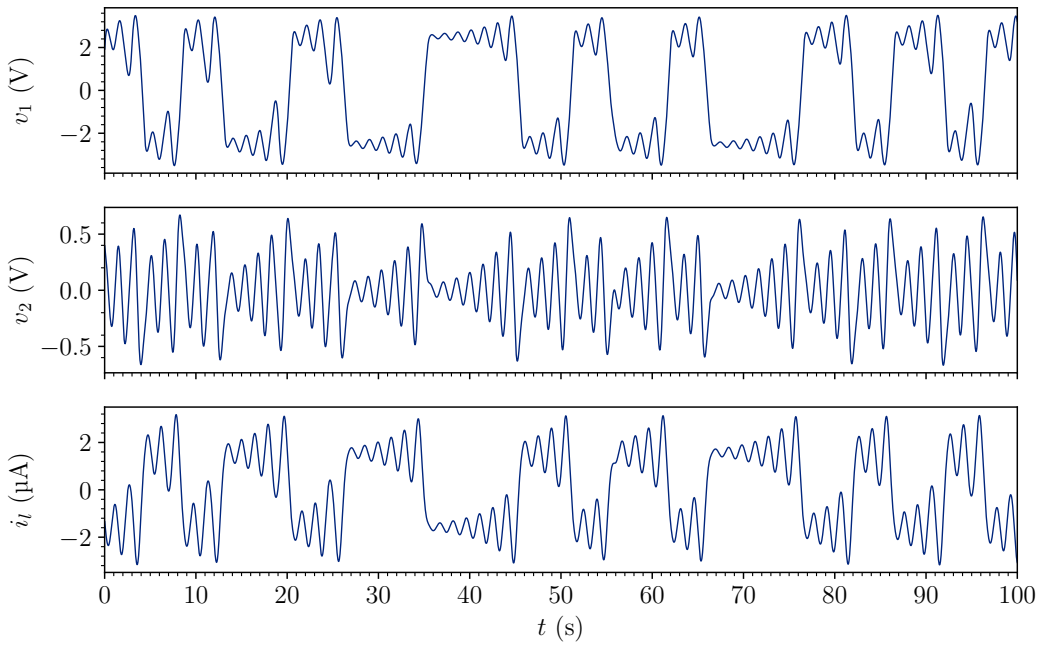

Fig. 3.9: Time series of the system described by equations (3.18a) -(3.19). The used values can be found in A.4. The control parameter R was set to 1.6 MΩ. Well visible is the local increase in the oscillation amplitude before changing the polarity of the voltage. This switching occurs chaotically.

3.2 Networks and network measures

As already mentioned, the human brain forms an extremely complex network. It consists not only of a multitude of cells, but also of a wide variety of cell types with different dynamics and morphologies. The idea of representing physical and abstract dependencies as a network dates back at least to the 18th century. Leonhard Euler is credited with solving the Königsberg bridge problem at this time with the help of a network.[40] This problem is about the question of whether there is a walk through the city so that all of its seven bridges are crossed exactly once. With the help of network theory, this question could be answered in the negative.[40] In the description of the city, the individual city districts form nodes and the bridges form the edges between them.

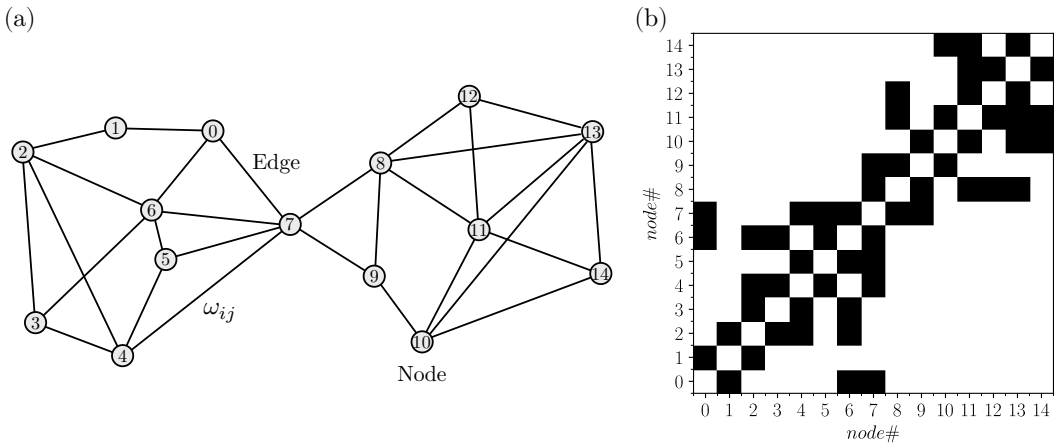

Fig. 3.10: Example of an arbitrary undirected and binary network and its associated adjacency matrix. (a) Shown is an undirected and binary network. The nodes and edges can represent a variety of very different networks, such as the internet, power grids, neural networks or food web. (b) Adjacency matrix associated with the network presented in (a). A black entry in the diagram indicates a connection between two nodes.

Today, the concept of networks is almost omnipresent, it can be thought of different networks which refer to the interaction between webpages, generators, neurons or species and thus are models of the internet, the power grid, neural networks or food webs, respectively.[145]

Fig. 3.10 refers to an example network. It consists of 15 nodes and 29 edges. The connection between each two nodes i and j is called an edge and a connection strength ω_{ij} can be assigned. The network is called binary if the connection strength is either zero or one, which means that there is no connection in the case of zero or an existing connection in the case of one. Besides the connection strength, a differentiation into directed an undirected graphs is usually done.[40,145]

For the visualization of the connection and calculation of different network measures the so called adjacency matrix A_{ij} is used. The matrix is exemplarily illustrated in Fig. 3.10 for the network also shown there. In recent years and with regard to the progress in neuroscience, the graph theoretical analysis of networks has gained momentum. In this context the term "connectome" was established for the network of single elements and their connections which together form the human brain.[146]

At this point in time, a variety of different measurements are used to unravel the human connectome which range from optical imaging technologies to functional connectivity measures based on magnetic resonance imaging (MRI).[40,145,147] Besides different technologies, the functional connectivity analysis is based on the statistical dependence between measured time series.[40] In order to characterise and compare different networks several different metrics were developed.

Today, a variety of network measures exist, as for example: the degree, shortest path length, characteristic path length, clustering coefficient, transitivity, modularity, betweenness centrality, and many more.[148] In order to conserve the scope of this work, the description of networks is limited to the characteristics: degree, clustering coefficient, the shortest path length, network motifs, and hubs which will be used during the analysis of a time varying network.

It should be noted, that it is usually necessary to relate the network measures to a null-hypothesis network in order to interpret the results properly, because the basic characteristics of a network can have a strong influence. Thus, a randomly generated network with the same size, density and binary degree distribution is often used.[148] However, in order to give an overview, different concepts will be explained in greater detail in the following.

3.2.1 Node degree

The node degree is probably one of the most straightforward and widely used measures in network analysis.[40,145] If the adjacency matrix A_{ij} is known, the degree d_i of node i

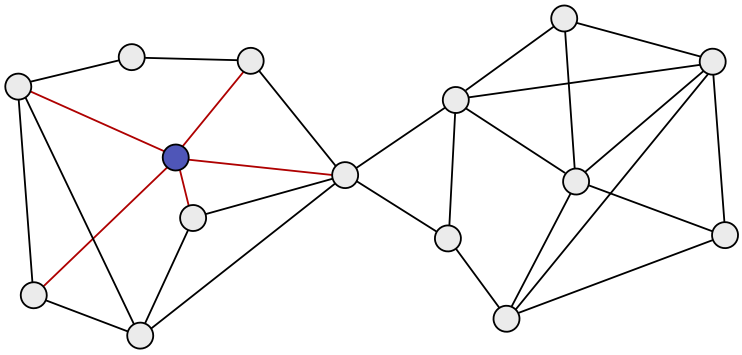

Fig. 3.11: The degree of the blue node equals five. The highest degree in the above network is six for the node in the centre and the lowest degree degree is two for the node in the upper left.

equals:[40,145,148]

$$d_i = \sum_{j \neq i} A_{ij}. \tag{3.33}$$

Thus, the degree is the number of links a node has to other nodes. Here, one speaks from a regular network if all nodes have the same degree.[145]
From the degrees at the single node level, the probability to find a connection between any two randomly chosen nodes of a network with the size N can be determined as the

mean degree $\mathfrak{D}$:[40]

$$\mathfrak{D} = \frac{1}{N} \sum_{i=1}^{N} d_i. \tag{3.34}$$

$\mathfrak{D}$ is also known as the wiring cost of the total network.[148] In directed graphs a distinction between the incoming connections and outgoing connections is made.[40] From the mean degree the density $\mathfrak{p}$ follows as:[145]

$$\mathfrak{p} = \frac{1}{N\,(N-1)} \sum_{i=1}^{N} d_i. \tag{3.35}$$

In the limit case of an infinitely large network, a sparse network refers to a network where $\mathfrak{p} = 0$ for $N \to \infty$ and a dense network to the case that $\mathfrak{p} > 0$ for $N \to \infty$.[145] It is obvious that the inclusion of weights is important for the meaningfulness of the indicator if the networks are not binary. In this context, the node strength s is defined by:[40,148]

$$s_i = \sum_{j \neq i} w_{ij}. \tag{3.36}$$

The degree can be used to visualize and compare different networks. In this context, the degree distribution is commonly used. If the probability of one node to connect to d other nodes $P(d)$ follows a power law, this is:

$$P(d) \sim d^{-\gamma}. \tag{3.37}$$

Thus, the network is said to be scale free, a feature which distinguishes networks such as the world wide web from randomly generated networks.[37] That means that a

completely random mechanism for the generation of such networks is not sufficient but the growth and attachment of new nodes are crucial. It has turned out, that it is more likely that new nodes are connected to other nodes which are highly connected instead of being connected completely randomly, something which can be called a "rich get richer" phenomenon.[37]
Furthermore, the power law property of networks and thus criticality seems to be a property and condition of complex processes in efficient neuronal structures (compare 2.6).[38, 40, 104, 149, 150]

3.2.2 Motifs

A lot of insights can be gained about certain characteristics of a graph, if its subgraphs are analysed. This can be done in terms of network motifs and their occurrence in the network in relation to a randomly generated graph.[40] Possible motifs for a directed

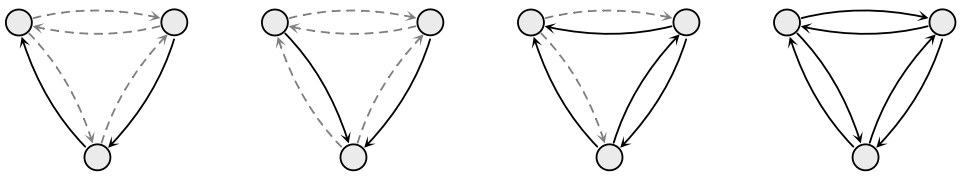

Fig. 3.12: Motifs on the node level for a directed network which consists of three nodes. From all existing 13 possibilities of the digraph are shown four. The dashed lines refer to possible connections and the solid black lines to existing connections.

network of three nodes are shown in Fig. 3.12. The dashed lines refer to the possible connections and the solid line to the established connections. While the possible connections for a network with three nodes are manageable with 13 possibilities, the possibilities increase rapidly with increasing network size. There exist already 199 possibilities for a network with four nodes and for a network of five nodes there are 9364. With a size of eight nodes, the different motifs in a digraph already reach more than $1.79 \cdot 10^{12}$ possibilities.[40, 151]

Certain statements and especially differences to randomly determined networks can be observed with motifs. For example shows the nematode *Caenorhabditis elegans* a larger number of feed forward associated motifs than a randomly generated network.[152]
In network analysis the occurrence of a high number of triangles in neural networks is associated with the ability of the network for specialized processing in densely interconnected groups of neurons. This is a characteristic known as functional segregation.[148]

3.2.3 Clustering coefficient

When considering individual motifs, it is obvious that different distributions of individual motifs are also associated with different connection densities.
Even if this does not necessarily apply universally, a measure for a local and also global tendency to cluster together is the clustering coefficient $\mathfrak{C}$. On the node level,

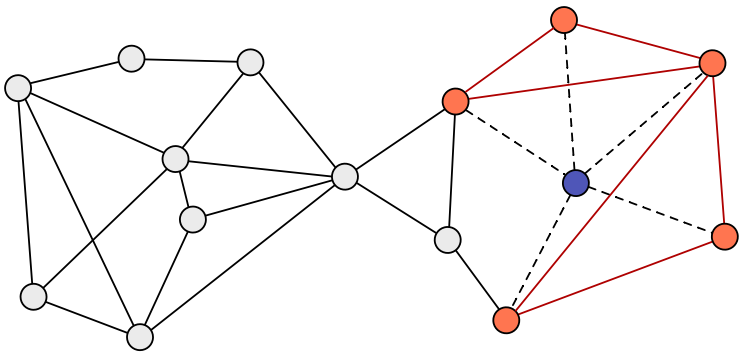

Fig. 3.13: Example network illustrating the definition of the clustering coefficient. The blue node is directly connected to five different nodes. Thus its degree is equal to five. Because there are six connections between the direct neighbours of the blue node the clustering coefficient $\mathfrak{C}_i = \frac{2 \cdot 6}{5 \cdot (5-1)} = \frac{3}{4}$.

$\mathfrak{C}_i$ describes the level to which the neighbours of one node i are also neighbours of each other.[148,153] In an undirected and binary network, the cluster coefficient can be calculated by counting the connections between the neighbours of one node. In

the following, this value is normalized by the total number of possible connections, irrespective whether they are connected or not.[40]
It is clear, that this is connected to considerations regarding network motifs because the established connection between two neighbours of i forms a fully connected triangle, whereas a missing link forms an open triangle. Additionally, through the normalization, the clustering coefficient is between zero and one and reflects the probability to find a connection between two neighbours of the node i.[40] Mathematically, one can define this local clustering coefficient $\mathfrak{C}_i$ of node i as follows:[40,145]

$$\mathfrak{C}_i = \frac{2n_i}{d_i\,(d_i - 1)}. \tag{3.38}$$

The value n_i is the number of connected pairs and d_i the degree of i which equals the number of neighbours. The number of possible connections in an undirected graph equals $\frac{d_i}{2}\,(d_i - 1)$, which leads to the previous formula.[145] This definition is based on graphs without weights. For the application on weighted graphs, the measure of the local clustering coefficient can be adapted by defining:[154]

$$\tilde{\mathfrak{C}}_i = \frac{2}{d_i\,(d_i - 1)} \sum_{j,k} \left(\tilde{w_{ij}} \tilde{w_{jk}} \tilde{w_{ki}}\right)^{\frac{1}{3}}. \tag{3.39}$$

Here, $\tilde{w_{ij}}$ refers to the respective weight which is normalized by the largest weight $\max\left(w_{ij}\right)$ of the network. For binary networks $\tilde{\mathfrak{C}}_i = \mathfrak{C}_i$ which is a necessary requirement for the definition of a weighted clustering coefficient.[154] A natural definition for a global clustering coefficient can be the average over the local coefficients:[40,145]

$$\mathfrak{C} = \frac{1}{N} \sum_{i \in N} \mathfrak{C}_i \tag{3.40}$$

with N being the number of nodes in the network.

3.2.4 Path length

By considering the path lengths in a network, the distances between two nodes i and j of the network are measured. In contrast to walks and trails, it is prohibited for a path to traverse a node more than once.[40] The shortest paths a network includes are from

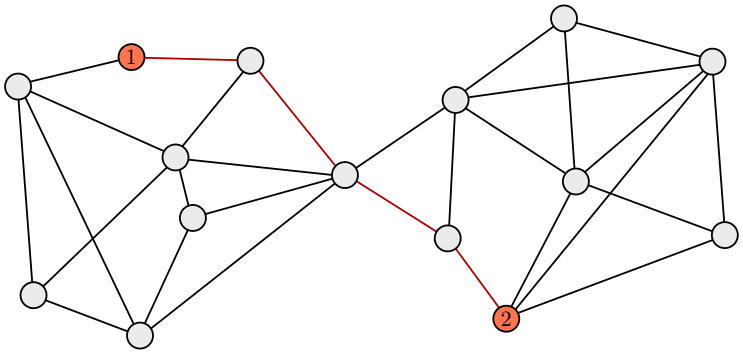

Fig. 3.14: Example network which visualizes the shortest path between two nodes.

interest for the analysis of the network, for example, in a network with many short paths, the nodes can interact more strongly. A more efficient exchange of information could take place, a disease could spread more quickly, or a set of oscillators might be able to synchronize.
An example for the shortest path is given in Fig. 3.14. By averaging over all shortest paths in a network the characteristic path length of the network can be obtained. This is:[40,148,153]

$$\mathfrak{L} = \frac{1}{N\,(N-1)} \sum_{i \neq j} l_{ij}. \tag{3.41}$$

Here, N refers to the network size and l_{ij} to the shortest path between the node i and j. The inverse of the $\mathfrak{L}$ is sometimes named global efficiency.[148,155]

The characteristic path length is of interest with regard to the capability of the network to integrate information from different parts of the network. This characteristic is called functional integration.[148] It should be noted that an adaptation to digraphs and weighted graphs can be easily done by including the edge weights or determine the shortest path regarding the direction of the respective edges.[40]
Although it seems obvious that a minimisation of the characteristic path length is always accompanied by a reduction in clustering, it has been impressively shown by Watts and Strogatz (1998)[153] that these changes occur at different rates. In their experiment, they rewired a ring lattice and thus explored the transition from a regular to a random network. Upon this process, the characteristic path length of the network started to drop immediately, whereas the clustering coefficient remained high before it dropped in value. These transitional networks between regular and random which exhibit a short characteristic path length and a high clustering coefficient is what they named small world networks.[153]

3.2.5 Hubs

A hub is meant to be a highly connected node. However, a measure which is based on the degree distribution only is too arbitrary to gain any functional insight. Therefore, a more detailed set of criteria was proposed. Following this, a hub is defined as having a high connectivity and betweenness centrality and low average path length as well as clustering.[40,156] For the identification of hubs in the network, the betweenness centrality can be used. This term refers to the ratio between the shortest paths and all paths that pass through the node in question. Mathematically, this is:[40,157,158]

$$\mathfrak{C}_B = \frac{1}{(N-1)\,(N-2)} \sum_{h\neq i, h\neq j, j\neq i} \frac{l_{hj}(i)}{l_{hj}}. \tag{3.42}$$

Here, $l_{hj}(i)$ refers to the number of shortest paths which exist between node h and node j and include the node i. The variable l_{hj} is the total number of shortest paths regardless if i is part of it and $(N-1)(N-2)$ is the number of pairs of different node

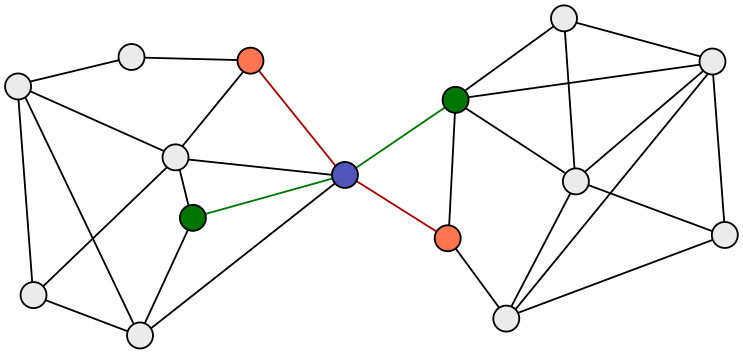

Fig. 3.15: Example of an hub in a network, which connects connectivity, betweenness centrality, path length and clustering to identify hub nodes.

without i in a directed graph.[40] By looking at aggregation of high degree nodes so called rich clubs are formed, which seem to play an important role for the hierarchical organisation of complex networks as they were found to be at the highest level of connectional hierarchy.[147]

3.3 Devices and technical systems

In the following, the basic oscillator circuit which is used during this work, as well as the underlying physical effects and phenomena which have been exploited are examined in more detail. This should enable a better classification of the presented experiments, as well as describe the basics and models of the respective phenomena.
In addition to the effects of piezoelectricity and piezoresistivity, the concept of memristive devices is also introduced. Due to its importance for the present work, a focus lies on the double barrier memristive device (DBMD).
On the circuit side, a relaxation oscillator based on a programmable unijunction transistor (PUJT) is presented. This device exhibits a negative differential resistance for certain input voltages, which allows for the generation of sustained oscillations with a suitable circuit.

3.3.1 Piezoresistivity

Today the piezoresistive effect is exploited in semiconductors and widely used in technical applications.[159] From the model perspective, a way to explain the piezoresistive phenomenon is the so called many valley model.[160,161] This is a type of quantum physical explanation for the measured change in resistance in response to a mechanical compression or tensile force.
In solid state physics the position of atoms in the crystal is considered as periodically arranged. Thus, the energy function of free electrons is described by periodicity as well. Here, the intersects of the single energy curvatures in the reciprocal space give rise to forbidden states, which lead to the well known band gabs in semiconductors.[162,163]

The principle of the many valley model as the basic quantum physical model behind piezoresistivety is shown in Fig. 3.16.[160,161] It is thought, that mechanical stress leads to strain that changes the distances between the atoms in the crystal. Because Bragg's law still holds true, the energy levels and shape of the energy landscape changes in the lattice. The model describes the piezoresistive effect as this change in the energy level

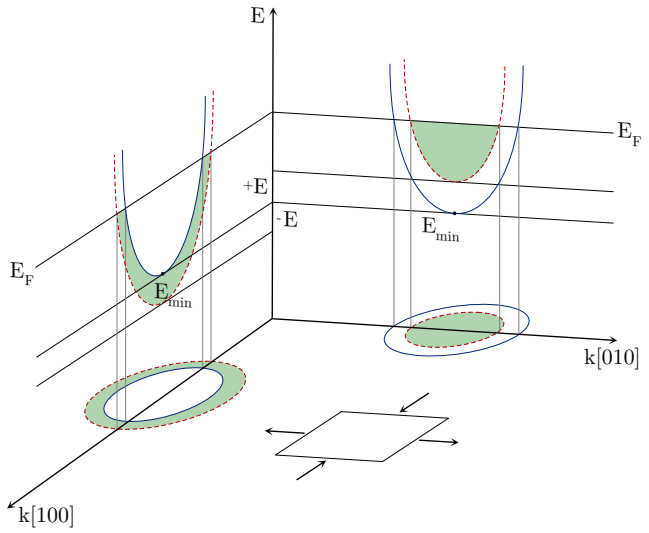

Fig. 3.16: Schematic representation of the energy landscape in k-space of n-type silicon. The band edge points are marked by E_{min}. Strain changes the energy curvature which is highlighted by the red dashed lines. Graphic adapted from Sze (1994).[161]

of the valence and conductance band in the semiconductor.[160,164–168]

In Fig. 3.16 the directions k[100] and k[010] are depicted. In the case of compression in the [100] direction, which would be a traction in the [010] direction, the band energy changes as highlighted by the red dashed line. In result, the band edge energy E_{min} is lowered in the [100] direction by -E and increased by +E in the [010] direction, which leads to a change in the average mobility of the electrons.[163]

This model points to two things which are important in order to exploit the resulting change in carrier mobility μ efficiently. First, the crystallographic orientation with regard to the applied stress and direction of current flow has to be aligned. For a given material and its crystallographic orientation this is described by the transversal and longitudinal coefficients. And second, the significant change in the energy landscape should affect the majority charge carriers and therefore manifest as a change in the valence or conduction band.

3.3.2 Piezoelectricity

A different effect which is based on pressure is the piezoelectric effect. The discovery of piezoelectricity dates back to the Curie brothers who conducted experiments on different materials.[169]
Today, mostly materials like ZnO, AlN, $PbZr_xTi_{1-x}O_3$ (PZT) or $BaTiO_3$ are used.[163] Although the piezoelectric effect, like the piezoresistive effect, depends on the crystalline structure, the mechanisms differ considerably. While the piezoresistive effect is essentially based on the change in mobility of the majority charge carriers, the piezoelectric effect is based on a polarisation of the material.[163,170]

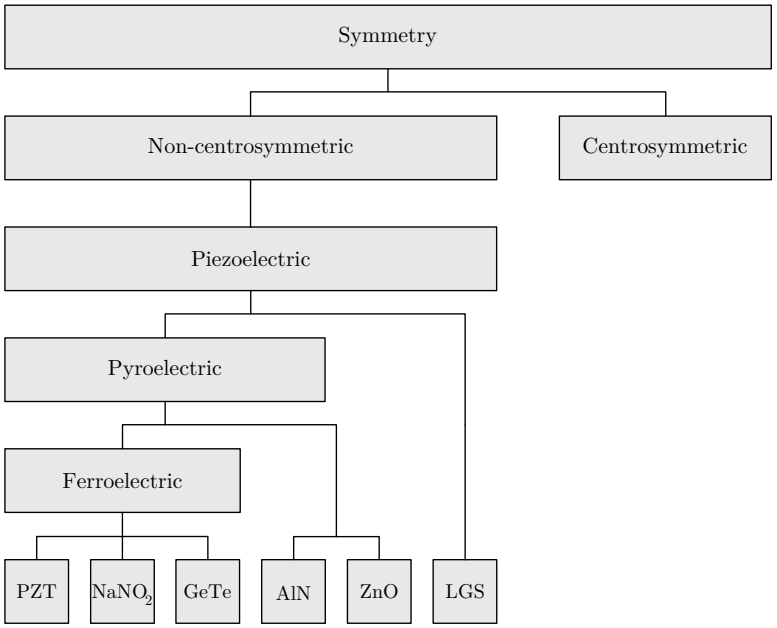

Fig. 3.17: Classification of different materials into piezo-, pyro- and ferroelectric based on the symmetry of their crystal structure. Schema adapted from Haertling (1999),[171] additional material examples are based on:.[162,172–174]

In Fig. 3.17 a classification of different materials into piezoelectric, pyroelectric and ferroelectric is shown. The polarization due to stress depends strongly on the crystalline structure. For example, in symmetrical crystals there is no polarisation, whereas in asymmetrical structures polarisation can occur both parallel and perpendicular to the voltage.[163]
Considering all possible point groups of crystalline materials, 20 of all the 32 possible groups are piezoelectric.[171] From the diagram it is clear, that a ferroelectric material is always piezoelectric, but a piezoelectric material is not necessarily ferroelectric, because not all piezoelectric materials exhibit a spontaneous polarization.[171]

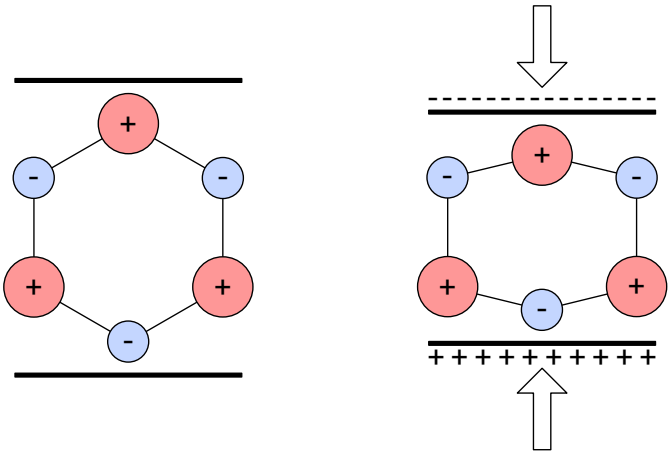

Fig. 3.18: Schematic which shows compression of a quartz crystal with positive silicon and negative oxygen atoms. The deformation results in a displacement of the charges which results in surface charges. Adapted from Tränkler and Obermeier (1998)[170]

The basic principle behind the piezoelectric effect is shown in Fig. 3.18. The picture shows a unit cell of a quartz crystal without (left) and with (right) mechanical deformation. The occurring force is depicted by big arrows. The positions of the charges of the crystal atoms change as a result to the force. This leads to a polarisation inside of the crystal and a surface charge, which is measurable.[170] Thus, the importance of the crystalline structure for piezoelectric properties is underlined.[163,171]

The generation of a polarization due to mechanical stress is called the direct piezoelectric effect. It follows for the displacement D in dependence on the electric field E:[171,175]

$$D = dE + \epsilon^{\sigma} E. \tag{3.43}$$

It should be noted that the permittivity ϵ^{σ} is defined with regard to a constant stress σ. Here, the variable d is called the piezoelectric coefficient connecting the displacement or polarization to the applied electric field. For the strain S in dependence on the stress follows:[171]

$$S = s^{E}\sigma + dE \tag{3.44}$$

with the elasticity s^{E} under a constant electrical field. This relation is also known as the converse effect.[162,171,175] Again, does d refer to the piezoelectric coefficient. Although the direct effect is typically exploited for the design of sensors, the converse effect is no less important as it is used for the design of mechanical actuators.[162] Physically, the dependence on the crystal structure makes it necessary to consider the individual directions so that the equations (3.43) and (3.44) in matrix notation are as follows:[176]

$$\begin{aligned}\begin{pmatrix} D_1 \\ D_2 \\ D_3 \end{pmatrix} = &\begin{pmatrix} d_{11} & d_{12} & d_{13} & d_{14} & d_{15} & d_{16} \\ d_{21} & d_{22} & d_{23} & d_{24} & d_{25} & d_{26} \\ d_{31} & d_{32} & d_{33} & d_{34} & d_{35} & d_{36} \end{pmatrix} \begin{pmatrix} E_1 \\ E_2 \\ E_3 \\ E_4 \\ E_5 \\ E_6 \end{pmatrix} \\ &+ \begin{pmatrix} \epsilon^{\sigma}_{11} & \epsilon^{\sigma}_{12} & \epsilon^{\sigma}_{13} \\ \epsilon^{\sigma}_{21} & \epsilon^{\sigma}_{22} & \epsilon^{\sigma}_{23} \\ \epsilon^{\sigma}_{31} & \epsilon^{\sigma}_{32} & \epsilon^{\sigma}_{33} \end{pmatrix} \begin{pmatrix} E_1 \\ E_2 \\ E_3 \end{pmatrix},\end{aligned} \tag{3.45}$$

and

$$\begin{pmatrix} S_1 \\ S_2 \\ S_3 \\ S_4 \\ S_5 \\ S_6 \end{pmatrix} = \begin{pmatrix} s_{11}^E & s_{12}^E & s_{13}^E & s_{14}^E & s_{15}^E & s_{16}^E \\ s_{21}^E & s_{22}^E & s_{23}^E & s_{24}^E & s_{25}^E & s_{26}^E \\ s_{31}^E & s_{32}^E & s_{33}^E & s_{34}^E & s_{35}^E & s_{36}^E \\ s_{41}^E & s_{42}^E & s_{43}^E & s_{44}^E & s_{45}^E & s_{46}^E \\ s_{51}^E & s_{52}^E & s_{53}^E & s_{54}^E & s_{55}^E & s_{56}^E \\ s_{61}^E & s_{62}^E & s_{63}^E & s_{64}^E & s_{65}^E & s_{66}^E \end{pmatrix} \begin{pmatrix} \sigma_1 \\ \sigma_2 \\ \sigma_3 \\ \sigma_4 \\ \sigma_5 \\ \sigma_6 \end{pmatrix} + \begin{pmatrix} d_{11} & d_{12} & d_{13} \\ d_{21} & d_{22} & d_{23} \\ d_{31} & d_{32} & d_{33} \\ d_{41} & d_{42} & d_{43} \\ d_{51} & d_{52} & d_{53} \\ d_{61} & d_{62} & d_{63} \end{pmatrix} \begin{pmatrix} E_1 \\ E_2 \\ E_3 \end{pmatrix}. \tag{3.46}$$

The tensor directions are usually defined as 1 and 2 being perpendicular to each other in the horizontal plane, with direction 3 being perpendicular to both and thus aligned in the vertical. The directions 4, 5, and 6 are the shear stress, which is often denoted by τ.[161,176]

Depending on the crystalline structure of the material, the above equations simplify, so that significantly fewer variables have to be taken into account.[176]

In this context, it should be pointed out, that it is possible to generate a voltage perpendicular or aligned to the direction of stress.[170] Thus, for the calculation of the voltage perpendicular to the stress follows:[171,177]

$$v_{31} = \sigma_{xx} t \frac{d_{31}}{\epsilon_0 \epsilon_r}, \tag{3.47}$$

with t as the thickness of the material. It is for the voltage aligned to the stress:[171,177]

$$v_{33} = \sigma_{xx} L \frac{d_{33}}{\epsilon_0 \epsilon_r}. \tag{3.48}$$

Here, L denotes to the length of the respective material and σ_{xx} to the stress perpendicular to the tensor in the direction 3.

3.3.3 Memristive devices and systems

Recently, a lot of research interest is attracted by so called memristors or memristive devices. A memristor is a term which is a mixture of the words memory and resistor, which should indicate the duality of the component. Actually, the theoretical prediction of a fourth elemental electronic device was made by Leon Chua as early as the year 1971, but it took almost 40 years until a connection between his theoretical predictions and an experimental observation was made.[178]
In the year 2008 a system of Pt-TiO_2-Pt, in which scientist observed the characteristic current-voltage loop of a memristor, was presented.[179] Although this was not the first publication showing switchable memory effects (see for example: Gibbons and Beadle (1964),[180] Simmons and Verderber (1967),[181] Liu *et al.* (2000),[182] and Seo *et al.* (2004)[183]), the scientific response to this component was enormous.
However, it should be noted, that there are also critical voices about the connection of the proposed device and the originally postulated memristor.[184–186]
In the following, the term memristor or memristive device will be used synonymously for those systems that are used today primarily in the field of alternative computing concepts, such as neuromorphic engineering, and are characterised by a type of resistive switching. Today, the well accepted signature of a memristive device, is a so-called pinched hysteresis loop.[187] This observation formed the nucleus for the further discovery of various material systems that show a pinched I-V curve.

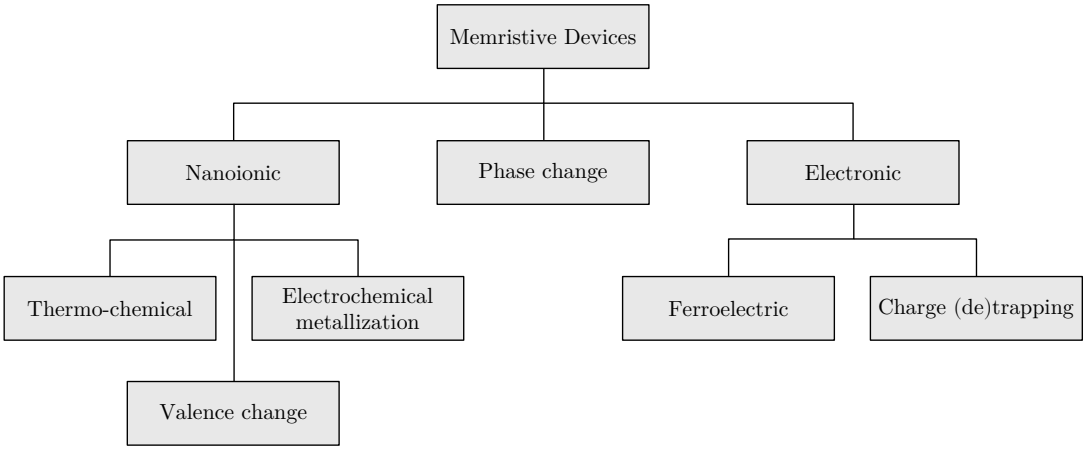

Fig. 3.19: Possible classification of non mechanical memristive devices based on their working principle. Adapted from Tetzlaff (2014)[188]

One way of categorising this multitude of different systems is shown in Fig. 3.19. One can distinguish between memristive devices which are based on nanoionic, electronic and phase change effects. Known representatives of nanoinic devices are electrochemical metallisation cells, valence change or thermo-chemical devices. Memristors which are based on ferroelectric or charge trapping and detrapping are considered as electronic principles. Nevertheless, today a lot of different observations are reported. Originally, the definition of a charge controlled memristor is:[178]

$$v(t) = M\left(q(t)\right) i(t) \tag{3.49}$$

where

$$M(q) = \frac{d\varphi(q)}{dq} \tag{3.50}$$

is the so-called memristance. It is also possible to define a flux controlled memristor,

which reads to:[178]

$$i(t) = W\left(\varphi(t)\right) v(t) \tag{3.51}$$

where

$$W(\varphi) = \frac{dq(\varphi)}{d\varphi} \tag{3.52}$$

is called a memductance. The variable φ is called flux linkage and connected to the voltage with $\varphi(t) = \int_{-\infty}^{t} v(\tau)\mathrm{d}\tau$, which is a kind of analogy to the connection between charge q and current i.[178] Nowadays the original definition is expanded and includes systems of switchable resistances as well. Which leads to the more general definition of memristive systems:[189]

$$v(t) = R\left(w(t), i(t)\right) i(t) \tag{3.53}$$

where

$$\frac{dw(t)}{dt} = f(w(t), i(t)). \tag{3.54}$$

In these systems the change of resistance is a function of some internal state which is described by $w(t)$. For example, in the memristive device, which was presented in 2008 by HP, this internal state is related to the drift of the dopants across the device.[179] To underline the basic dynamics of a memristive device, consider a simple dimensionless

system of the form:

$$y = \gamma x \tag{3.55}$$

with

$$\dot{\gamma} = \alpha x. \tag{3.56}$$

Thus, γ is proportional to $\int_{-\infty}^{t} x(t)\mathrm{d}t$. It can be seen, that the system dynamics follow the proposed memristive system determined by the equations (3.53) and (3.54). Fig. 3.20 shows the basic dynamics for $x = sin(\omega t)$ and $\alpha = 5$. The typical pinched hysteresis is clearly visible in the xy-plane. Besides the characteristic shape, an increase in frequency leads to a decrease in the opening of the hysteresis loop. Another observation is, that for $x = 0$ is $y = 0$ as well. However, even if these properties are associated to memristive devices, they are not necessarily true for an ideal memristor.[184]

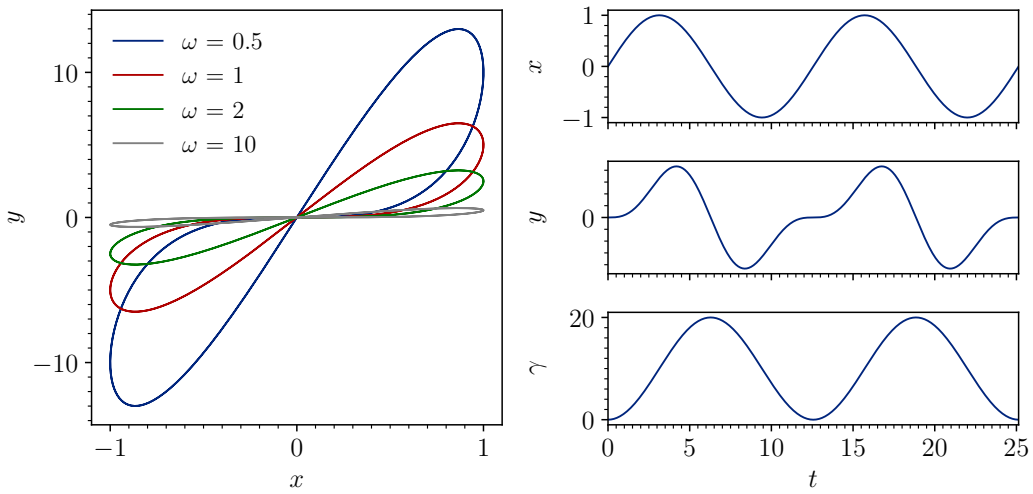

Fig. 3.20: Solution to the system described by the equations (3.55) and (3.56), with $x = sin(\omega t)$ and $\gamma(t = 0) = 0$ under variation of ω.

3.3.4 Double barrier memristive device

In 2015, Hansen *et al.* reported on a memristive device for nonvolatile memory and alternative computing designs.[190] This so-called DBMD and its switching properties between a high resistance state (HRS) and a low resistance state (LRS) will be discussed in greater detail in the following. The basic structure of the device is shown in Fig.

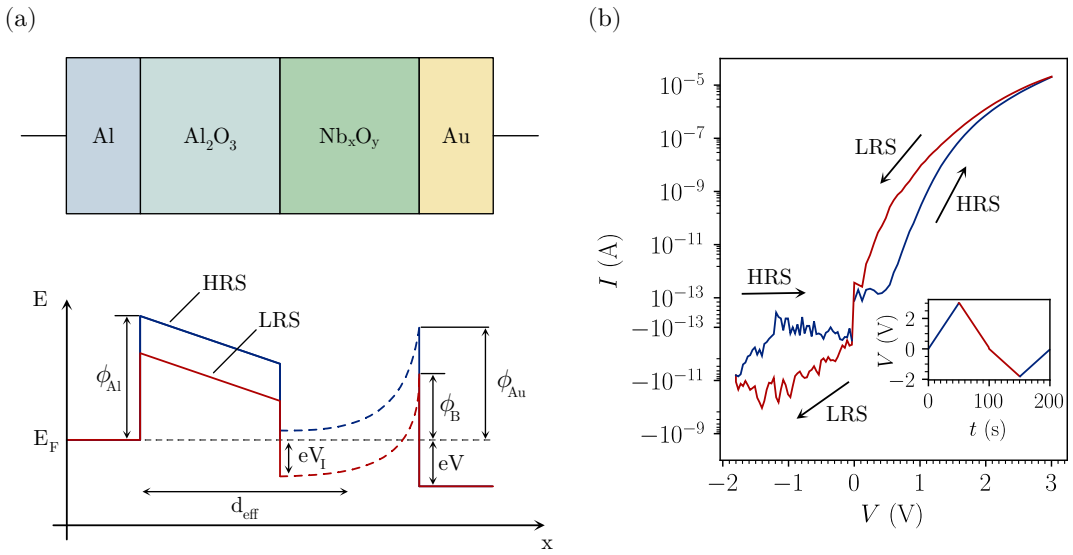

Fig. 3.21: Structure, proposed working principle, and typical I-V curve of the DBMD. (a) The original structure of the DBMD is depicted at the top. Below is a schematic band diagram which shows the lowering of the effective barrier heights as a result of the switching process. Graphic adapted from Hansen *et al.* (2015).[190](b) Typical I-V curve of the memristive device. The inset shows the applied voltage. The switching between a HRS and LRS as well as the pinched hysteresis loop is demonstrated (the scale is linear and scaled to a half division for $-10^{-13}\,\mathrm{A} < I < 10^{-13}\,\mathrm{A}$).

3.21 (a). The sequence of the used materials for the different thin films reads to $Al/Al_2O_3/Nb_xO_y/Au$. Beneath the basic structure of the device, the band diagram is shown schematically.

The basic working principle of the device appears to be influenced by the filling of traps with charge carriers and the movement of oxygen vacancies towards the Au layer.[190] In the schematic band diagram, the change in resistance is associated with a decrease

in the barrier height ϕ_B of the Schottky contact. However, due to the thin layers, both interfaces are effected by the charge movements. As a result, the barrier height ϕ_{Al} decreases as well.[190] Although the underlying working principle can be explained by both electron trapping and oxygen vacancy diffusion, the latter seems to be the dominant mechanism on the larger time scale.[190,191]
The DBMD has some advantages over other concurring concepts, because there is no initial forming step necessary. Furthermore, the interface based switching allows for an analogue like change in the resistances in contrast to binary switches based on filaments.[190]
In Fig. 3.21 (b) a typical I-V curve is shown. The applied triangular voltage is depicted in the insert. The amplitude of the measuring voltage varies between 3 V and −2 V and is connected to the Au layer. The Al layer refers to the ground potential. Starting at $V = 0\,\mathrm{V}$, the current through the device increases exponentially. However, at the beginning the device is in the HRS. After reaching the maximum voltage, the applied voltage decreases, which is highlight red in the diagram. It can be seen, that the resulting current is higher if equal voltage values are considered. This behaviour is associated to the switching between the HRS and the LRS. Only after passing through the negative voltage, the resistance increases again which is associated to the switch back from the LRS to a HRS. As a result, the I-V curve displays the pinched hysteresis loop common to memristive devices (please compare to Fig. 3.20). The DBMDs which are used during the course of this work were fabricated by Finn Zahari from the chair of nanoelectronics.

3.3.5 Programmable unijunction transistor and relaxation oscillator

For the technical realization of a leaky integrate and fire neuron model either a PUJT or its electrically equivalent interconnection between a npn- and pnp bipolar junction transistor was used.[163,192,193] Although the use of bipolar junction transistors in neuromorphic circuits can probably be considered unusual today, it has advantages for research, as rapid prototyping is possible without problems. It should also be noted, that bipolar CMOS (Bi-CMOS) processes make it possible to integrate bipolar junction transistors and complementary metal-oxide-semiconductor (CMOS) gates.[194]

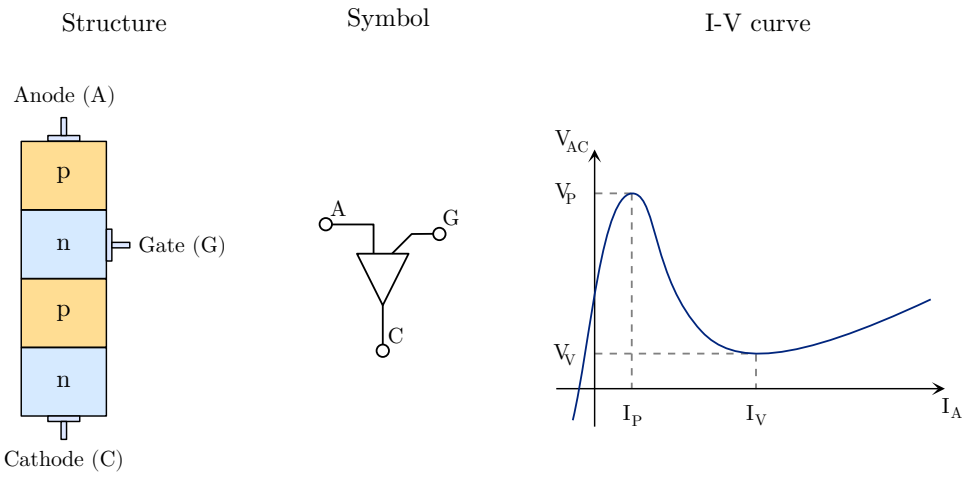

Fig. 3.22: Structure, symbol and typical voltage current characteristic of the PUJT. Graphic after Floyd (2012).[195]

The PUJT belongs to the class of four-layer diodes and is depicted in Fig. 3.22. Its structure is shown on the left side of the figure. The PUJT consists of two layers of p-doped and n-doped silicon. This distinguishes the programmable unijunction transistor from its ancestor, the unijunction transistor, which consists of a bar of doped material with a doped inlet. Clearly visible is the gate connection at the n-region which differentiates the device from other thyristors.[195]
Common to both is a strongly non-linear I-V curve which is depicted on the right side of the Fig. 3.22. With an increase in the anode-cathode voltage V_{AC} increases the anode current I_A only minimally. However, with a further increase of the voltage, the behaviour changes and the current increases by leaps and bounds. This voltage is called peak voltage V_P. Even with a reduction in voltage, the current flow remains high. Thus, the component has changed its state. The change can only be reversed when the current drops below the valley current I_V. It is precisely this behaviour that can be exploited to build an oscillator.[195]

A typical realisation of a relaxation oscillator using a PUJT is shown in Fig. 3.23 (a). Although the charging current can certainly be generated in different ways, the simplest option is probably a series resistor R_1 to charge a capacitance C. The charging current

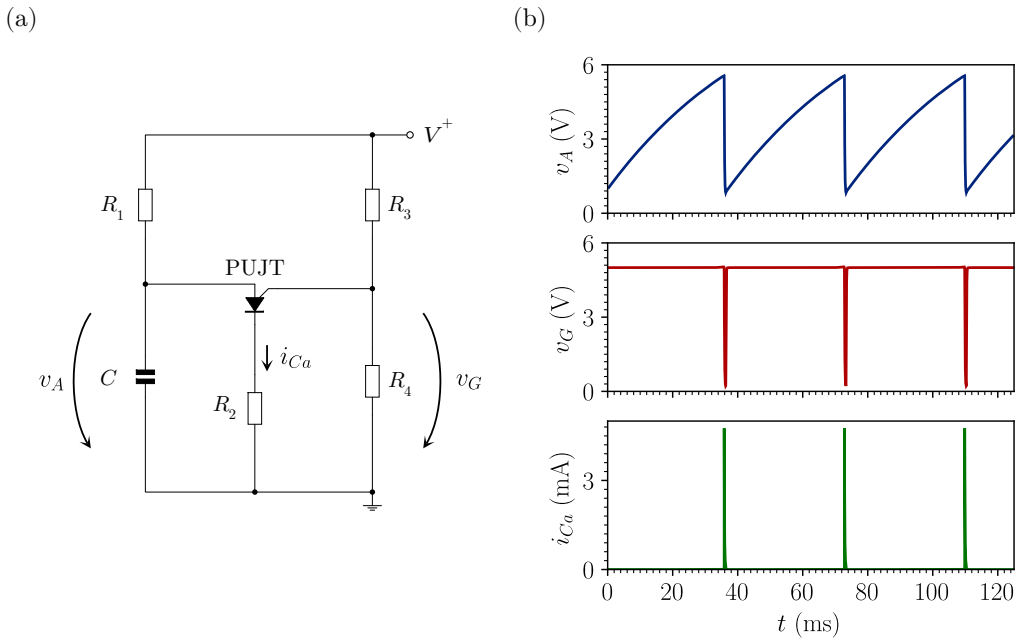

Fig. 3.23: Equivalent circuit and time evolution of the main voltages and discharge current of a relaxation type oscillator based on an PUJT. (a) Equivalent circuit of an oscillator, which is built based on a PUJT. (b) Typical voltage and current traces of such an oscillator. The time transients are based on simulations (please refer to A.5 for further information about the parameters.)

increases the capacitor voltage. As a result, the anode-cathode voltage increases as well. If the voltage over the capacitor exceeds the peak voltage, the current through the PUJT increases abruptly.[195]

In this way the capacitor voltage decreases again. The fast discharge leads to a short voltage pulse over R_2. A big gain for the versatility of the circuit is the possibility to program the peak voltage. This is done with the help of the voltage divider formed by the resistors R_3 and R_4.[195]

The typical time courses of the main voltages and current are shown in partial figure (b). The successive charging represented by the sawtooth-like charging behaviour of voltage v_a. The abrupt discharge process is accompanied by a voltage drop of v_g due to the reduction of the resistance of the component. During this voltage drop, the capacitor discharges through the cathode, which results in i_{Ca}. By generalizing the

voltage drop over the pn-region to 0.7 V, it can be approximated that:[195]

$$V_P = V^+ \frac{R_3}{R_3 + R_4} + 0.7\,\mathrm{V}. \tag{3.57}$$

Therefore, it is clear, that the accessible voltage divider built by R_3 and R_4 is analogous to the standoff ratio of the non programmable unijunction transistor.
If the circuit is initialized without any charge on the capacitance, the first period of the oscillation will be longer, because the succeeding periods will not discharge the capacitor completely, which is determined by the valley current of the PUJT. However, if the relaxation oscillator is simplified and assumed to be ideal, the frequency can be estimated, if the charging process of an RC element is considered. With:

$$V_C = V^+ \left(1 - e^{-\frac{t}{R_1 C}}\right) \tag{3.58}$$

an approximation of the frequency can be made by neglecting the time needed to discharge the capacitance. Thus, it follows for the time t which is necessary to reach a certain capacitor voltage V_C:

$$t(V_C) = -R_1 C \ln\left(1 - \frac{V_C}{V^+}\right). \tag{3.59}$$

For the sustained oscillation, the capacitor voltage changes between the peak and the valley voltage. Thus it is:

$$F = \frac{1}{T} = \frac{1}{t(V_C = V_P) - t(V_C = V_V)}. \tag{3.60}$$

It follows for the period T accordingly:

$$T = R_1 C \left(\ln\left(1 - \frac{V_V}{V^+}\right) - \ln\left(1 - \frac{V_P}{V^+}\right)\right). \tag{3.61}$$

Using the calculation rules with logarithms and inserting (3.57), it follows for the frequency:

$$F \approx \frac{1}{R_1 C \ln\left(\frac{V^+ - V_V}{V^+\left(1 - \frac{R_3}{R_3+R_4}\right) - 0.7\,\mathrm{V}}\right)}. \tag{3.62}$$

4 From sensory input to network behaviour

4.1 Spiking and adapting mechanical sensor

It is clear that living species do not exist separately from their surrounding, but in a constant exchange of information between them. In order to process information, it must first be collected. Here, the sensory system has the task to pre-process and transfer stimuli from the environment to the central nervous system.
Classically, senses are subdivided into vision, audition, gustation, olfaction and touch. The latter does not just include the classical sensation of touch but pain and temperature perception as well as proprioception and viszeroception. Proprioception refers to the ability to percept the position and movement of the body and viszeroception to the perception of the organs.[8]
Here, the perception of an external stimulus is not just a function of its intensity, but also of its duration. Normally, the perception decreases with time and eventually vanishes completely. This behaviour is called adaptation.[7,8] The first experiments discovering the principle of adaptation were conducted by Edgar Douglas Adrian, who published a series of seminal papers and formulated the firing rate hypothesis (please refer to chapter 2.4 for an overview of the responses of some mechanical sensors).[31,32,96] Today, adaptation is not just restricted to the sensation of stimuli, but a basic principle in neurons and networks of neurons, even in those not involved in the sensory system.[97,98,100,101]
In contrast to vision, audition, gustation and the sense of balance, the cells of the somatosensory system as well as the olfactory system are nerve cells. They combine the coding and transfer of information into one cell.[8] These biological findings served as a guideline for the development of a highly bio-inspired sensing device based on $Al_xSc_{1-x}N$ (AlScN), a field effect transistor and a negative differential resistance based leaky integrate and fire (LIF) circuit.[196,197]
It should be noted, that besides the following concept, a variety of approaches exists. These range from the use of different materials as for example the ceramics PZT[198] or $BaTiO_3$[199] to sensors which are based on graphene[200–203] or polymers.[204–208] Even more advanced concepts, as for example the capacitively coupling of field-effect transistors with nanowires[209,210] and use of fluids[211] are exploited.
One approach which is also based on a polymer stands out due to its similarity to the here presented piezoelectric field effect transistor (PiezoFET). This is the piezoelectric

oxide semiconductor field effect transistor (POSFET), which is used in tactile sensors as well and is based on the ferroelectric copolymer polyvinylidene fluoride trifluoroethylene copolymer (PVDF-TrFE).[205,212–214] As in the PiezoFET, the co-polymer is located in the gate stack of the POSFET and modulates the channel current through interfacial charges generated by mechanical stress.
However, in contrast to AlScN, the polymer has a few distinguishing characteristics. First, PVDF-TrFE is not compatible with Si-CMOS technology. Second, usually it needs a wake-up procedure which consists of the application of an electric field in the order of $80 - 100\,\mathrm{V\,\mu m^{-1}}$.[212,213] Both shortcomings make the integration of this mechanical sensor into dense interconnected arrays more difficult, compared to the use of AlScN.
Besides the research regarding the development of a mechanical sensitive device, which converts mechanical stress into a current response, a tremendous progress in the development of integrated circuits was made. These circuits are highly biologically inspired, as for example the adaptive exponential integrate and fire neuron[215,216] or other mixed signal circuits which are used for visual information processing.[217–220] In the following the working principle of the PiezoFET as well as the readout circuit will be discussed. Both together lead to a spiking and adapting sensory unit based on the piezoelectric stress sensing capabilities of the enhanced field effect transistor as well as the LIF unit, which relies on a negative differential resistance.[197]

4.1.1 Piezoelectrically enhanced metal–oxide–semiconductor field-effect transistor

As Fig. 4.1 shows, the basis of the piezoelectrically enhanced field effect transistor is a standard metal-oxide-semiconductor field-effect transistor (MOSFET). The layer sequence of the gate stack of the device is: Pt (300 nm), AlScN (500 nm), Pt (100 nm), AlN (20 nm), and SiO_2 (13 nm). The PiezoFET was fabricated by Henning Winterfeld from the chair of nanoelectronics and the AlScN was deposited by Simon Fichtner from the materials and processes for nanosystem technologies chair.[197]
The AlN functions as an adhesion layer for the Pt which is the structural seed and ensures the c-oriented growth of the AlScN. The influence of the adhesion layer can be

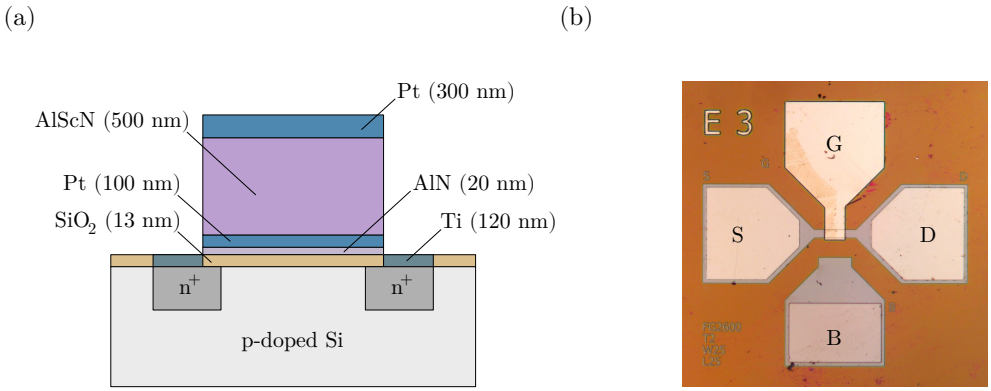

Fig. 4.1: Structure of the PiezoFET. (a) Schematic of the structure of the augmented field effect transistor. AlN functions as an adhesion layer for the Pt which is used to ensure the c-oriented growth of AlScN. (b) Photography of a typical PiezoFET. The channel is oriented in the [100] direction of the substrate.

neglected, because it is sputter deposited directly on the amorphous dielectric. Even if the AlN is not amorphous the piezoelectric parameters are less pronounced with regard to the thick AlScN film. It should be noted, that the PiezoFET is built on a (100) oriented p-type Si wafer. Thus, the channel orientation of the device is in [110] direction. The PiezoFET is based on an n-MOSFET, which leads to electrons as the majority charge carriers. The orientation, together with electrons as the majority charge carriers, minimises possible influence of the piezoresistive effect.[164,165,221,222] The used AlScN was chosen because it has a higher piezoelectric coefficient compared to AlN and a lower leakage current compared to most perovskite piezoelectric materials.[223–225]

In Fig. 4.2 the current voltage characteristic of the PiezoFET is shown. In subfigure (a) the output characteristic of the PiezoFET for a small set of devices is depicted. Besides the mean values, the standard error is shown as the shaded area around the curves.
Additionally, the partial figure (b) shows a typical transfer curve of the device. The exponential increase in the drain source current I_{DS} when the gate source voltage V_{GS} exceeds approximately 1 V is clearly visible. This is the so called subthreshold regime, which extends to about 2 V and is used as the working point of the device. The subthreshold swing is 300 V decade^{-1}. The red line shows a fit using the following equation:[163]

$$I_{DS} = I_s e^{\left(\frac{V_{GS}}{mV_T}\right)} \left(1 - e^{\left(-\frac{V_{DS}}{V_T}\right)}\right). \tag{4.1}$$

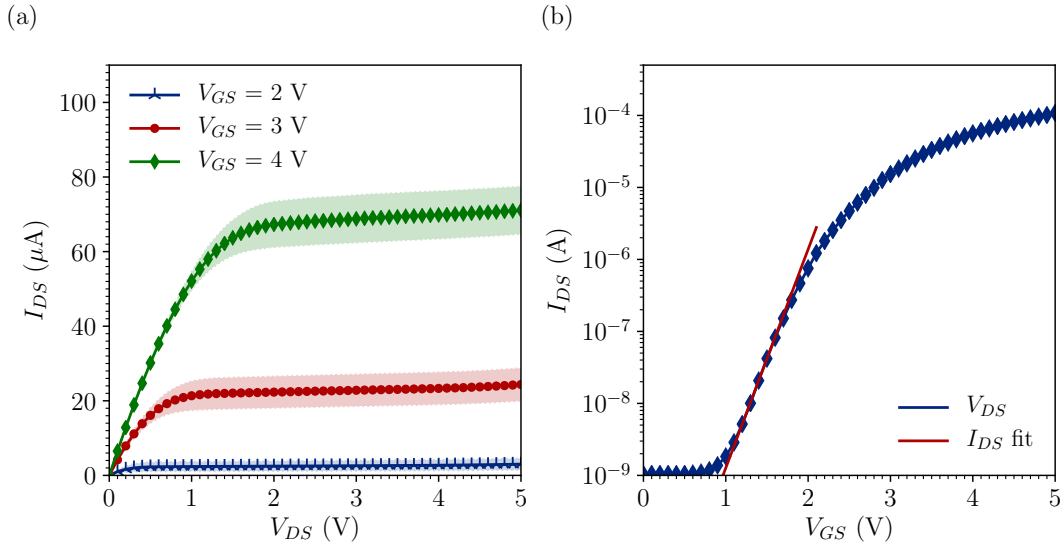

Fig. 4.2: Electrical characteristics of the PiezoFET. (a) The output characteristic of the PiezoFET. Shown are the mean values for a small set of devices and the standard error (N = 3). (b) A typical transfer curve of the augmented field effect transistor. The subthreshold regime can be modelled by the exponential function (4.1).

Besides, V_T, which is the thermal voltage, the current is a function of the input voltages V_{GS} and V_{DS}, as well as the reverse current I_s and the slope factor m. The generated voltage of the piezoelectric layer which is perpendicular to the applied stress, can be calculated with:[177]

$$V_{31} = \sigma_{11} g_{31} h_{AlScN}. \tag{4.2}$$

Besides the stress σ_{11}, the voltage is a function of the thickness of the piezoelectric layer h_{AlScN} and the piezoelectric voltage constant g_{31}, which connects stress and voltage perpendicular to each other. For the piezoelectric layer, the equivalent circuit is modelled as a capacitance in parallel to a leakage resistance. Thus, a differential equation for the time evolution of the generated voltage over the piezoelectric layer can be derived and reads to:

$$\dot{v}_p = \dot{\sigma}_{11} g_{31} h_{AlScN} - \frac{v_p}{\tau_{AlScN}}, \tag{4.3}$$

with $\tau_{AlScN} = R_{AlScN} C_{AlScN}$ as the characteristic time constant of the piezoelectric. For the defined generation of stress, a defined force has to be applied to the device. The resulting set-up is shown in Fig. 4.3. The basic concept for the defined generation of positive and negative forces and thus a movement in two directions is based on a cantilever, a permanent magnet and an electric coil. The cantilever is fixed on one side. On the other side, a permanent magnet is attached. The magnetic field of the permanent magnet B_1 and controllable field of the electric coil B_2 leads to a force at the tip of the cantilever (please refer to Fig. 4.3 (b) for an overview of the variables and coordinate system). It is assumed with simplifications that the resulting force is:

$$F = \frac{B_1 B_2 A_1 A_2}{4\pi r^2 \mu_0}. \tag{4.4}$$

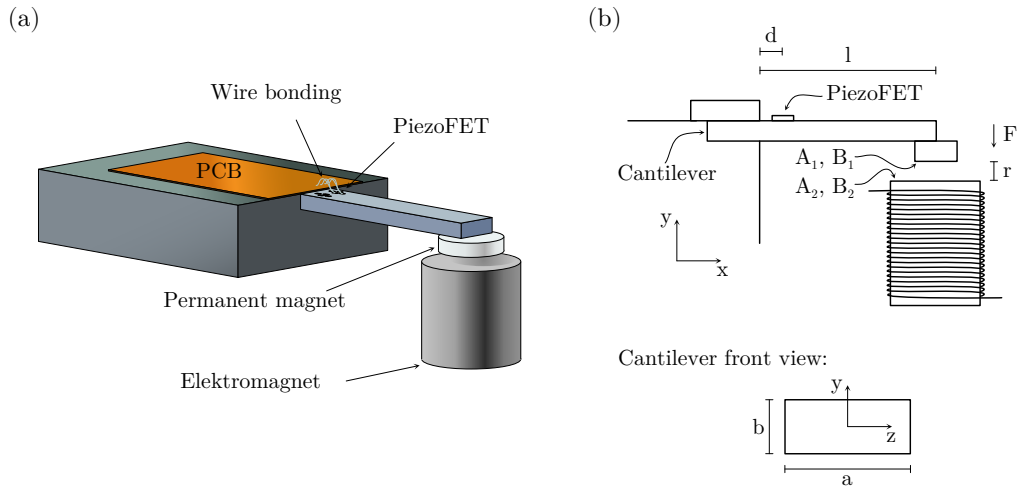

Fig. 4.3: Experimental set-up for the application of stress to the PiezoFET. (a) 3D image of the set-up. The cantilever is fixed on one side, the other side is used for the bending. At the tip is a permanent magnet, beneath which an electromagnet is located. (b) Schematic of the set-up. Besides the variables, also the used coordinate system is depicted.

To determine the stress over the component, it is necessary to consider the geometry of the cantilever. It is:

$$\sigma_{11}(x, y) = \frac{M(x)y}{I_z}. \tag{4.5}$$

The stress scales to the distance between the PiezoFET and the tip of the cantilever due to the bending moment $M(x)$, and the second moment of intertia I.[226] For the beam, the necessary second moment of inertia can be calculated as the area integral of the cross section:

$$
\begin{aligned}
I_z &= \iint y^2 \mathrm{d}A \\
&= \int_{-\frac{a}{2}}^{\frac{a}{2}} \int_{-\frac{b}{2}}^{\frac{b}{2}} y^2 \mathrm{d}y\mathrm{d}z \\
&= \frac{1}{3}\frac{b^3}{4}a = \frac{ab^3}{12}.
\end{aligned} \tag{4.6}
$$

together with the bending moment $M(x) = F(l - x)$, the stress is:

$$
\sigma_{11}(x, y) = \frac{12F(l - x)y}{ab^3}. \tag{4.7}
$$

Because the PiezoFET is located at the surface of the cantilever and the thickness of the device is much smaller compared to the thickness of the silicon beam, the distance from its center is assumed to be equal to half the distance. Thus, with $y = \frac{b}{2}$, it follows:

$$
\sigma_{11}(x = d, y = \frac{b}{2}) = \frac{6F(l - d)}{ab^2}. \tag{4.8}
$$

By inserting (4.8) in (4.3), the differential equation describing the generated voltage at the PiezoFET on a one side fixed cantilever in dependence of an external force reads to:

$$
\dot{v}_p = \frac{6g_{31}h_{AlScN}\,(l - d)}{ab^2}\dot{F} - \frac{v_p}{\tau_{AlScN}}. \tag{4.9}
$$

Because the piezoelectric voltage is generated in the gate stack, it is assumed for the simulation, that the resulting channel voltage will be a superposition of the gate source

voltage and the piezoelectrically generated voltage. Thus, equation (4.1) changes to:

$$I_{DS} = I_s e^{\left(\frac{V_{GS}+v_p}{mV_T}\right)} \left(1 - e^{\left(-\frac{V_{DS}}{V_T}\right)}\right). \tag{4.10}$$

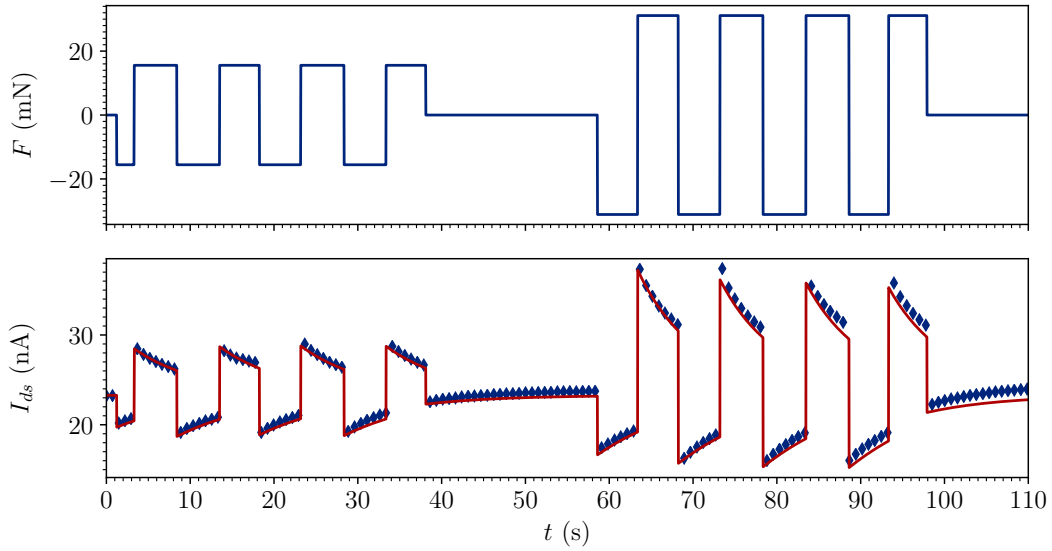

Fig. 4.4: Numerical results for the drain source current as proposed in equation (4.1). The measured values are shown as diamonds. The solid line refers to the numerical results, obtained by solving the differential equation (4.9) with an rectangular force as the system input ($I_s = 1.216 \cdot 10^{-12}, m = 5.646$). Please refer to chapter A.6 for an overview of the used parameters.

As Fig. 4.4 shows, the equations (4.9) and (4.10) fit the experimental data. The top graph shows the input force F to the system, together with a fit of the transfer curve in the subthreshold regime, the resulting current can be calculated. The match of the magnitudes as well as the general discharging behaviour under a constant stress are apparent, although the overall change in current is not represented by this simple model. However, to assist the experiment and demonstrate the feasibility of the approach, this simplified model is sufficient.

4.1.2 Spike coding based on a negative differential resistance

For the readout of the stress sensitive device, a bio-inspired approach based on spikes in the low Hz range is chosen. This might make the output directly compatible to spiking neural networks, which might prove superior to conventional deep neural networks regarding energy consumption and computational capability without the need for analogue to digital converter.[227]

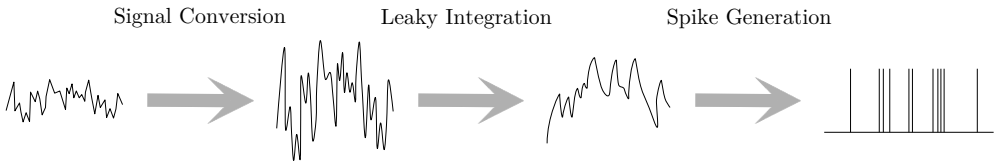

Fig. 4.5: Schematic of the basic working principle of the touch sensitive sensory unit with adaptive capabilities. Shown are the single functional steps. The *Signal Conversion* stage converts the mechanical quantity into an electrical quantity. This is followed by the processing of the signal in form of an integration. Then, this integrated signal is converted into a series of spikes.

The neuronal model which is used for the spike generation with regard to the sensor signal, is based on a LIF neuron model. This model is based on an ongoing integration of incoming information and their coding into a series of spikes.[67,68] The normal form of a LIF model is as follows:[68]

$$\dot{x} = \frac{1}{\tau}\left(-x + \gamma i\right). \tag{4.11}$$

Here, the state variable increases by an input current i and decreases by itself. The latter is the leakage part of the model. Overall, the system is scaled by the intrinsic time constant τ. In contrast to the biological system, a spike is not modelled as a steep increase of the membrane voltage, rather it is determined by the time of reaching the

threshold voltage. This is:

$$t^s : x(t^s) = x_\vartheta. \tag{4.12}$$

For a higher biological plausibility, the spike time can be incorporated as a necessary time until the state variable x is reset:

$$x(t^s + t_\epsilon) = x_r. \tag{4.13}$$

Using the timings of two successive spikes, a measure for the instantaneous frequency can be found.

$$ISI = t^s_{n+1} - t^s_n \tag{4.14}$$

This is the so-called ISI, which can be used to gather information about population dynamics and synchrony in small and big populations of neurons.[228–230] However, to get an output signal based on spikes, comparable to nerve cells, the spikes can be defined as Dirac pulses which are shifted by the corresponding spike times:[68]

$$S(t) = \sum_i \delta\left(t - t^s_i\right). \tag{4.15}$$

It should be noted, that a general solution for equation (4.11) can be found, if a constant input current is assumed. This solution reads to:

$$x = \gamma i + (x_0 - \gamma i)e^{-\frac{t}{\tau}}. \tag{4.16}$$

From here the frequency can be calculated. It is:

$$f = \frac{1}{T} = \frac{1}{t + t_\epsilon}, \tag{4.17}$$

which leads to:

$$f = \frac{1}{t_\epsilon - \tau \ln\left(\frac{x_\vartheta - \gamma i}{x_r - \gamma i}\right)}. \tag{4.18}$$

Therefore, the frequency f is reciprocally proportional to the logarithm of the quotient of the firing threshold x_ϑ and the reset value x_r of the system. Besides the continuous frequency f of the system, it is possible to calculate an instantaneous estimate $\mathcal{F}$ of the firing frequency, which depends on the difference of two following pulses. Thus, it is:

$$\mathcal{F} = \frac{1}{t^s_{n+1} - t^s_n} = \frac{1}{\mathcal{I}}. \tag{4.19}$$

4.1.2.1 Equivalent circuit of sensory unit

The integration of the PiezoFET into a compact circuit results in a sensory unit which generates voltage pulses in dependence on the stress applied to the device. The Fig. 4.6 shows the equivalent circuit of the resulting sensory unit. The circuit can be subdivided into three functional stages, each with a certain functionality, as described in Fig. 4.5. The first stage is responsible for the signal conversion, which is carried out by PiezoFET. In response to a change in stress, the channel current i_{DS} changes, which results in a change in the potential at node 'A'. Due to the change in the base current of the transistor T_1, the current i_c changes. After this, the leaky integration takes place. The current i_c charges the capacitor C_2. Finally, the spike generation is done by reaching the fixed threshold voltage V_{th} and exploiting the non linearity of the positive feedback

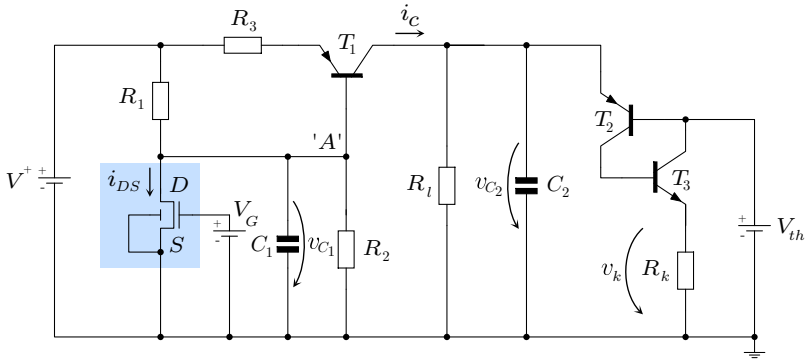

Fig. 4.6: Equivalent circuit of the PiezoFET with a spike based readout. The PiezoFET is located on the left of the circuit diagram (blue). A change in current i_{DS} leads to a change in current i_c, which modulates the spiking frequency of the LIF circuit. Thus, the force coding takes place as the generation and modulation of voltage pulses v_k at the cathode resistance R_k.

loop of two transistors (please refer to 3.3.5 for further information on a relaxation type oscillator based on a negative differential resistance).
For the simulation of the resulting circuit, a mathematical model is needed. Following functional steps stated above, the circuit can be analysed in more detail. The channel current of the PiezoFET discharges the voltage v_{c1} by influencing the voltage divider built by R_1 and R_2 directly (see Fig. 4.6). Thus, it is:

$$\dot{v}_{C_1} = \frac{1}{C_1}\left(\frac{V^+ - v_{C_1}}{R_1} - \frac{v_{C_1}}{R_2} - i_{DS}(v_p, v_{C_1})\right). \tag{4.20}$$

For a positive force, the channel current i_{DS} increases. This decreases the voltage v_{C_1}. As a result, the current i_c increases:

$$i_c = I_{T_1 s}\left(e^{\left(\frac{v_{EB}}{V_T}\right)} - 1\right). \tag{4.21}$$

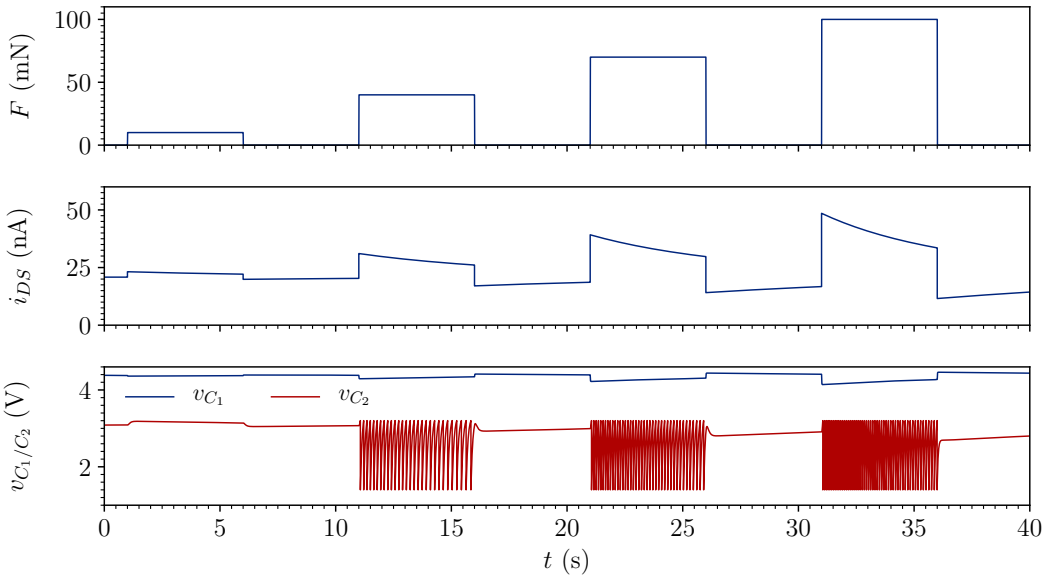

Fig. 4.7: Time evolution of the system variables of the spike based readout circuit for the PiezoFET. The numerical solution was obtained by forward integration of the system equations. The input force F to the system is varied stepwise (top). As a result, the channel current of the PiezoFET changes. A positive force increases the current, which decreases exponentially despite a constant input force (middle). The channel current results in a decrease in v_{C_1}, which in return increases the voltage over the second capacitor v_{C_2}. If this voltage reaches the threshold, the circuit starts to oscillate and in return generates voltage pulses (bottom). Please refer to chapter A.6 for an overview of the used parameters.

This is due to the transistor T_1 which is from the pnp-type. Thus, the decrease in v_{C_1} increases the voltage from transistor emitter to base v_{EB}. The resulting collector current of the transistor is the input to the leaky integrator of the circuit. It is:

$$\dot{v}_{C_2} = \frac{1}{C_2}\left(i_c - \frac{v_{C_2}}{R_l}\right). \tag{4.22}$$

Accordingly, an increase in i_c increases the voltage v_{C_2} over the capacitor C_2. Furthermore, equation (4.22) is equal to the normal form of the LIF (4.11) model ($\gamma = R_l, \tau = C_2 R_l$). Using the voltage of the capacitor, the last functional stage,

which consists of a pair of transistors (T_2 and T_3), is connected. Both transistors form a positive feedback loop with a negative resistance region. This design is equal to the use of a four layer silicon diode for the generation of spikes.[163, 193]
In Fig. 4.7 a numerical solution for the overall system is depicted. The top trace shows four rectangular forces with different magnitudes, which serve as an input to the system. The range of the pulses are between 10 mN and 100 mN. The resulting channel current of the PiezoFET is depicted in the middle.
The different magnitudes in response to the different forces as well as the falling edges during constant forces due to the leakage current are evident. Moreover, the quiescent current is reduced, which is caused by the compensation current during excitation. The resulting voltages at the capacitors are depicted at the bottom. The voltage at the capacitor v_{C_1} discharges beneath its resting potential. As a result the voltage at the capacitor v_{C_2} increases due to the higher charging current. The threshold behaviour of the system is apparent, when comparing the first pulse with the last three pulses. The first pulse is not strong enough to trigger the oscillation, whereas the last three pulses are.
The resulting pulses are depicted in Fig. 4.8 (a). Besides the resulting spikes, the instantaneous frequency is depicted. The magnitude of the force is encoded in a high frequency response to the onset of the stimulus, which is followed by an exponential decrease in frequency. This decrease is the adaptation to the system input. The adaptation proceeds to the point where there is no more system performance, i.e. no more spikes are generated, as shown in Fig. 4.8 (b). The input-output characteristic of the system under variation of the forces is depicted in Fig. 4.8 (c). The values of the frequency are obtained by a variation of the input force strength. The values refer to the maximum of the generated pulses, which is usually the onset of pulse generation. For the used parameters, the oscillation will start at approximately 13 mN. After a short transition, the onset frequency scales linearly with the applied force.

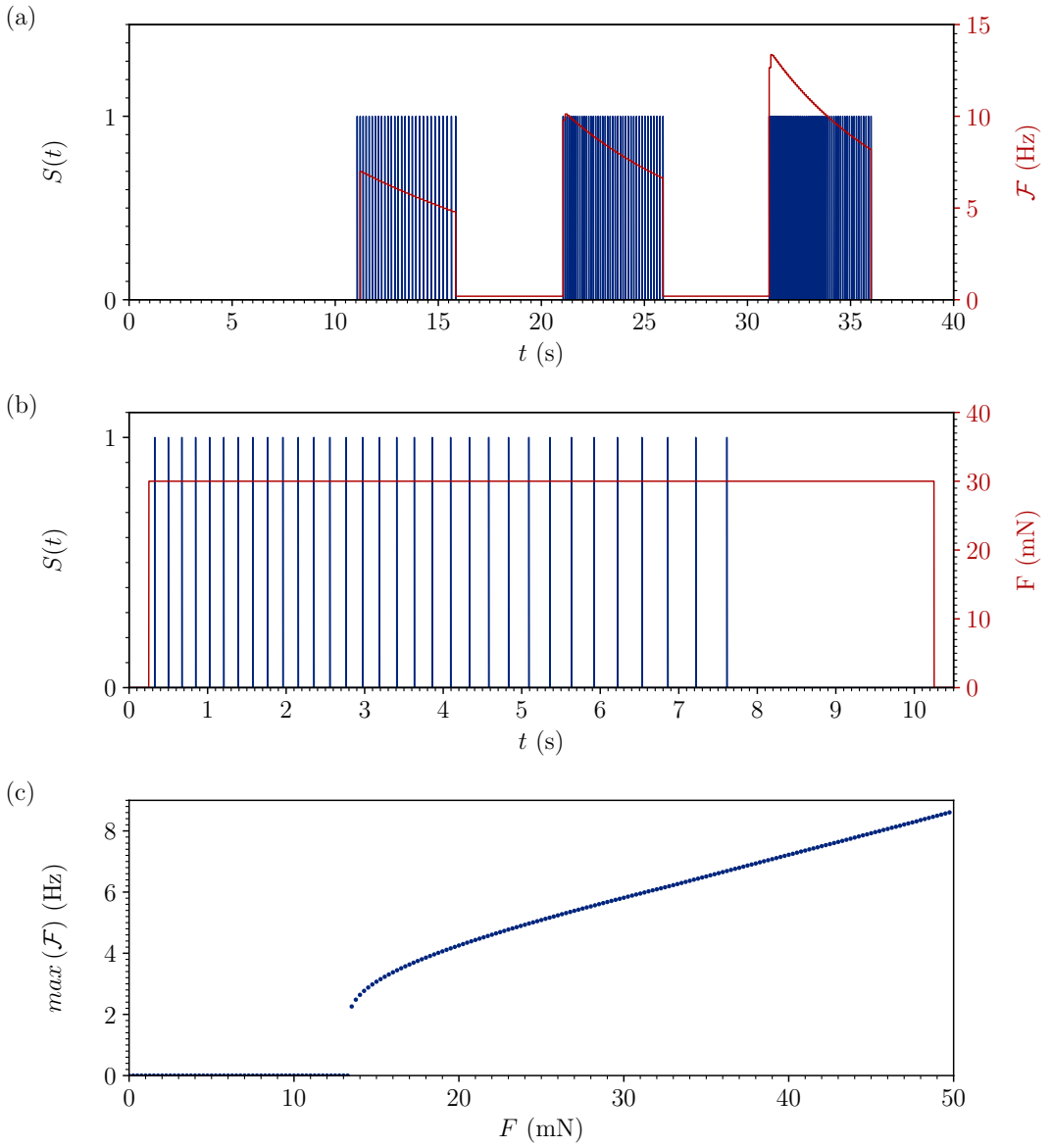

Fig. 4.8: System output of the touch sensitive sensory unit with a spike based readout. (a) System output under the influence of various pulses with different height. The magnitudes of the forces are equal to the ones shown in Fig. 4.7 top. (b) Decrease in firing frequency during the application of a constant force. The frequency decreases until the oscillation stops completely. (c) Maximum instantaneous frequency under variation of the applied force magnitude. After reaching the threshold at approximately 13.3 mN, the system starts to settle into a regime showing a linear frequency/force response. Please refer to A.6 for further information about the used parameter.

4.1.2.2 Experimental verification

For verification, the system was build and measured experimentally. Therefore, the PiezoFET was fixed in a plastic holder. On top of the plastic holder sits a printed circuit board (PCB) (please see C.1 for the layout) containing the oscillator circuit, as can be seen in Fig. 4.3 (a). The force was applied using an electromagnet. To calculate the applied forces, the electromagnet was characterised under constant operation. Then, the force was calculated using equation (4.4). Because of the small pulses in comparison to the sampling frequency, a software filter was used to visualise the output pulses. Thus, for the output pulse train follows:

$$\sigma(t) = \begin{cases} 1, & \text{for } (v_k - \theta) \geq 0 \\ 0, & \text{for } (v_k - \theta) \leq 0. \end{cases} \tag{4.23}$$

The results for the dynamic application of stress to the PiezoFET is shown in Fig. 4.9 (a) and (b). In (a) the results obtained by an application of rectangular shaped force pulse with increasing magnitude are depicted. Although the first two pulses are not strong enough to trigger a pulse response of the system, the voltage at the capacitor does decrease. In subfigure (b) a close up of the last force pulse between 70 s and 80 s is shown. After a steep increase in the firing frequency to approximatly 14.1 Hz, the frequency decreases exponentially. This shows, that the frequency of the pulse response of the PiezoFET based touch sensor adapts to a constant input. This behaviour is based on the exploitation of the leakage current of the PiezoFET. This is the adaptation to the input stimulus, as Fig. 4.10 illustrates. In (a), the system is excited by a long force pulse of approximately 62 s. The system responds with continuous oscillations until it stops after approximately 48 s at 50 s. In subfigure (b) the decrease in firing frequency of the output is shown for 10 s of adaptation. As can be seen by the red line, an exponential fit follows the experimental data.

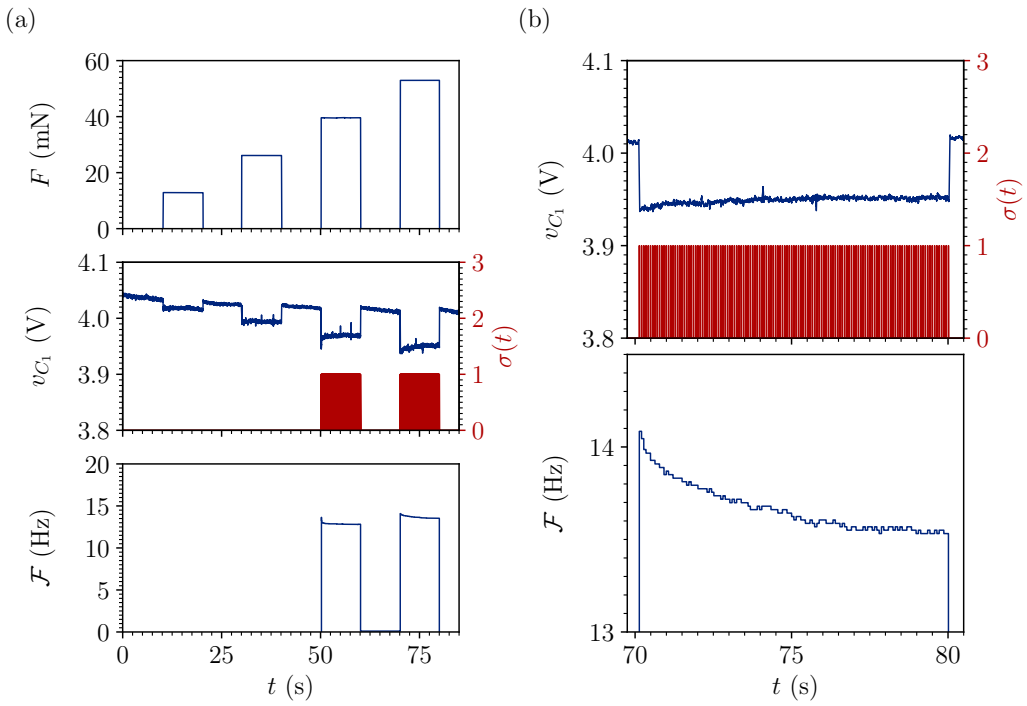

Fig. 4.9: Results of experiments with the touch sensor based on a PiezoFET by stimulation with a series of pulses. (a) Dynamic excitation of the PiezoFET with a series of rectangular force pulses at the tip of the cantilever, shown by the upper trace. The resulting change of the capacitor voltage and the spiking output is shown at the middle. The resulting frequency which is obtained from the ISIs is depicted at the bottom. (b) Close up of the system output for the last force pulse in (a) between 70 s and 80 s.

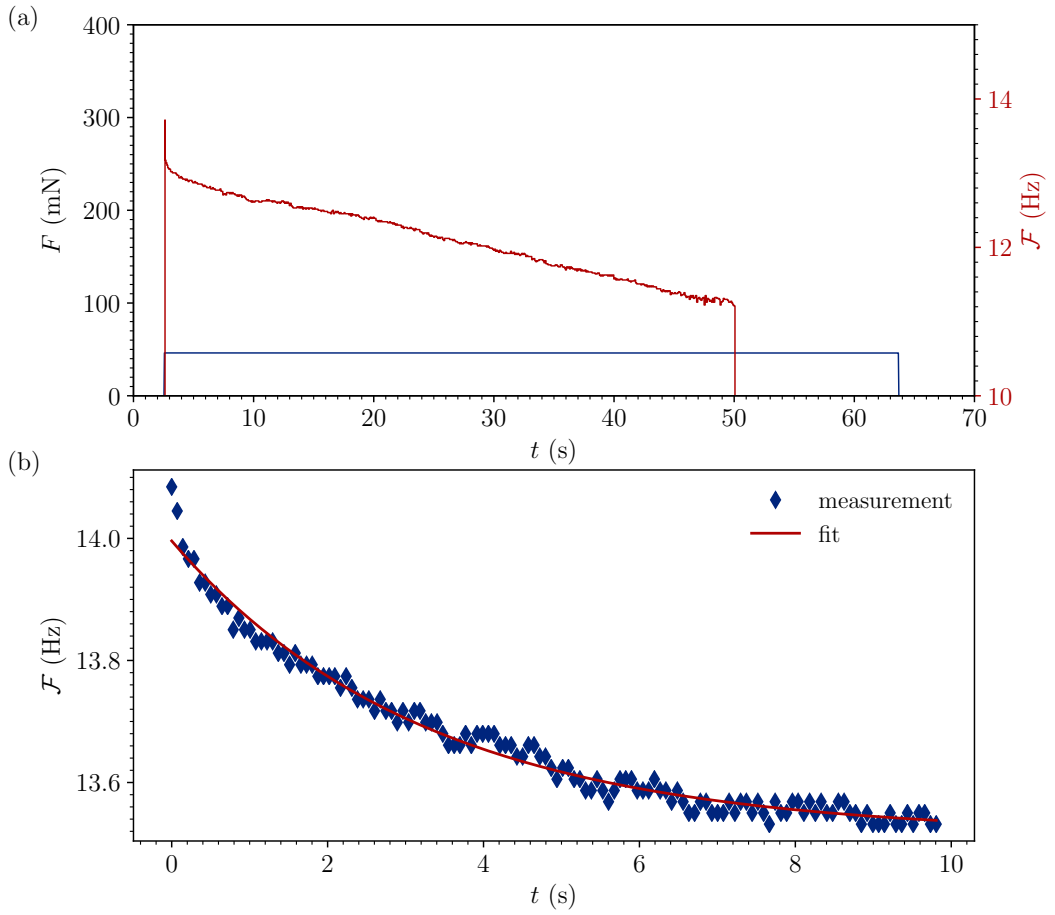

Fig. 4.10: Results of experiments with the touch sensor based on a PiezoFET by stimulation with a single long pulse. (a) Excitation with one long force pulse. After the steep onset of firing, the frequency decreases until it stops completely after approximately 48 s of continuous spiking. (b) Fit of the firing frequency during the adaptation to the input force. The decrease in firing frequency follows an exponential function (red line, $f(t) = \alpha e^{-\beta t} + \gamma$ with $\alpha = 0.481, \beta = 0.309$, and $\gamma = 13.515$).

4.2 Delayed feedback

Indeed, biological neural systems usually work in the range of a couple of Hertz.[7,8,51] Therefore, in terms of speed, they are way behind modern computers, which relay on a precise clock rate in the gigahertz range. However, besides the speed and certain specialised tasks, until today the human brain is unbeaten in robust speech and visual pattern recognition. All the more, if the low power consumption is considered, where the human brain excels the technical systems.[27,29,231]
Nonetheless, besides the low frequencies, also the transmission of information does not even come close to the speeds electric signals reach in modern computer systems. The transmission of action potentials is in the order of several tens of meter per second, and even the delay at the synapses are in the millisecond range.[8]
Furthermore, the neuronal structure of higher vertebrates is characterised through a complex network of interconnected nerve cells. Thus, besides feedback, reentry mechanisms are present during procession of information.[36,147,232–234]
It is known, that the occurrence of time delays in the transmission of spikes can have a tremendous impact on the generation of stable patterns in polysynaptic feedback loops as investigated in the *Aplysia*.[129] In the following, a methodology for the derivation of a charge response curve (QRC) from a measured PRC in the context of a relaxation type oscillator will be given. After this, different approaches for the experimental generation of time delays in the millisecond range are discussed followed by measurements of multijitter bifurcations and pattern switching phenomena.

4.2.1 From phase to charge response curve of a relaxation type oscillator

The measurement of a PRC has a pure observational character, since the effect of an external pulse on the phase of an oscillator is measured, but not the underlying phenomenon. In the following, a QRC will be derived from a PRC as an example of a change of a fundamental electric quantity.
It is important to note, that a QRC relates the change in phase to the dynamics of the underlying system. In the here presented QRC, the change in phase becomes a change

of charge in response to a perturbation. The following considerations are strongly oriented on a relxation type oscillator based on a negative differential resistor and a charging capacitor.

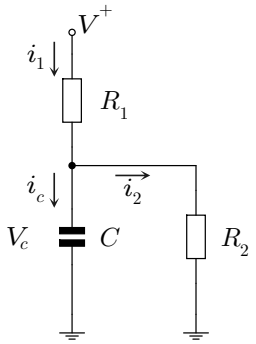

Fig. 4.11: Electric equivalent circuit of a charging capacitor with a leakage resistance.

Considering Fig. 4.11 as the equivalent circuit of a leaky charging capacitor, which is also present in a relaxation type oscillator as depicted in Fig. 3.23 under consideration of non ideal components or if a leakage is intentionally added, it is clear, that from Kirchhoffs current law follows:

$$i_1 = i_c + i_2. \tag{4.24}$$

Thus:

$$i_c = \frac{V^+ - V_c}{R_1} - \frac{V_c}{R_2}. \tag{4.25}$$

Because $Q = CV$:

$$\frac{dQ_c}{dt} = \frac{CR_2V^+ - Q_cR_1 - Q_cR_2}{R_1R_2C}. \tag{4.26}$$

This equation can be solved by integration:

$$\int_0^{Q_c(t)} \frac{1}{Q_c(R_1+R_2) - CR_2V^+} \mathrm{d}Q_c = \int_0^t -\frac{1}{R_1R_2C} \mathrm{d}t. \tag{4.27}$$

This is:

$$\ln\left(\frac{Q_c(t)(R_1+R_2) - R_2CV^+}{-R_2CV^+}\right) = -\frac{t\,(R_1+R_2)}{R_1R_2C}. \tag{4.28}$$

By resolving the logarithm:

$$V_c(t)\,(R_1+R_2) = R_2V^+\left(1 - e^{-\frac{t(R_1+R_2}{R_1R_2C}}\right). \tag{4.29}$$

Introducing eta as the ratio between leakage resistance and series resistance, this is $\eta = \frac{R_2}{R_1+R2}$, the equation (4.29), which describes the charging of a capacitor under the influence of a static and constant leakage resistance reads to:

$$V_c(t) = \eta V^+\left(1 - e^{-\frac{t}{\eta R_1C}}\right). \tag{4.30}$$

Thus, the time t can be expressed as:

$$t = -\eta R_1 C \ln\left(\frac{\eta V^+ - V_c}{\eta V^+}\right). \tag{4.31}$$

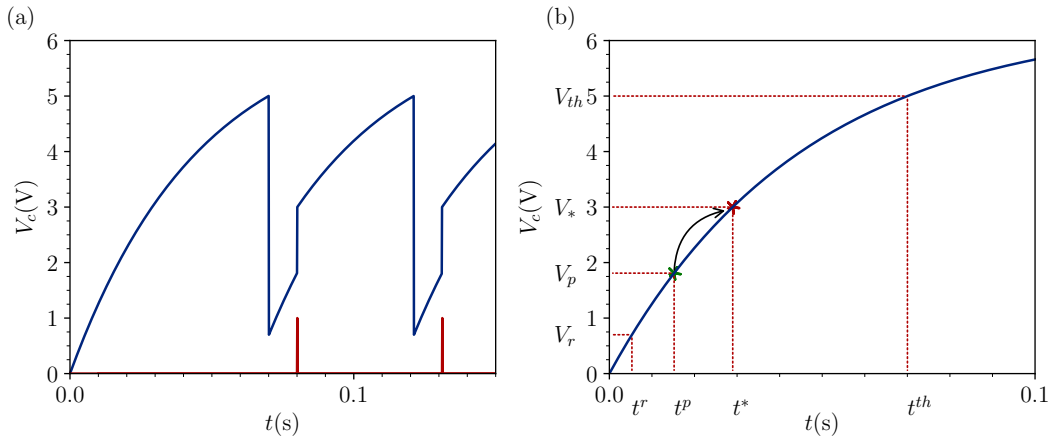

Fig. 4.12: Definition of key times during ongoing oscillations. (a) Evolution of the capacitor voltage of a successively spiking relaxation type oscillator with time delay. (b) Charge curve of an RC element without reset ($V_c = \eta V^+ \left(1 - e^{-\frac{t}{\eta RC}}\right)$). The pulse arrives at t^p and changes the voltage from V_p (green star) to V_* (red star), which is equal to the charge time t^* ($\eta = 0.909$, see A.8 for the parameters used).

In Fig. 4.12 (b), the relevant points in time for an unperturbed charging of a capacitor are depicted. Here, t^r refers to the time needed to reach the reset voltage V_r and t^{th} equals the point in time where the threshold voltage V_{th} is reached.
If a pulse arrives at a certain point t^p in time, the voltage V_p (green star) of the capacitor changes and is transferred to the new voltage V_* (red star). This equals the time t^*, which would have been necessary to charge the unperturbed capacitor to the same voltage.
The PRC measures the change in period $T'(\phi)$ with respect to the phase in which the perturbation occurs. Therefore, the times have to fulfil:

$$t^p - t^r + t^{th} - t^* = T'(\phi). \tag{4.32}$$

With the definition of the PRC:

$$P(\phi) = 1 - \frac{T'(\phi)}{T_0} \tag{4.33}$$

the duration of the changed period $T'(\phi)$ can be calculated as:

$$T'(\phi) = T_0 \left(1 - P(\phi)\right). \tag{4.34}$$

The intrinsic period can be expressed with the same time points used in equation (4.32). This is:

$$T_0 = t^{th} - t^r. \tag{4.35}$$

By inserting (4.35) in (4.34) the influenced period in dependence on the time points from Fig. 4.12 reads to:

$$T'(\phi) = t^{th} - t^{th}P(\phi) - t^r + t^r P(\phi). \tag{4.36}$$

Inserting 4.36 in 4.32 leads to:

$$t^* = t^p + t^{th}P(\phi) - t^r P(\phi). \tag{4.37}$$

From the equation (4.31), the time needed for the capacitor to charge to a certain

voltage V_c can be calculated. Together with equation (4.37) it follows for the time t^*:

$$t^* = -\eta RC \ln\left(\frac{\eta V^+ - V_p}{\eta V^+}\right) + P(\phi)\eta RC\left(\ln\left(\frac{\eta V^+ - V_r}{\eta V^+}\right) - \ln\left(\frac{\eta V^+ - V_{th}}{\eta V^+}\right)\right). \tag{4.38}$$

This can be simplified to:

$$t^* = P(\phi)\eta RC \ln\left(\frac{\eta V^+ - V_r}{\eta V^+ - V_{th}}\right) - \eta RC \ln\left(\frac{\eta V^+ - V_p}{\eta V^+}\right). \tag{4.39}$$

From the definition of t^* the corresponding voltage V_* can be expressed as:

$$V_* = \eta V^+\left(1 - e^{\ln\left(\frac{\eta V^+ - V_p}{\eta V^+}\right) - P(\phi)\ln\left(\frac{\eta V^+ - V_r}{\eta V^+ - V_{th}}\right)}\right). \tag{4.40}$$

Alternatively, instead of calculating the new voltage by V_p, one can express the actual voltage by its phase. Because:

$$\phi = \frac{t^p - t^r}{t^{th} - t^r}, \tag{4.41}$$

one can write:

$$\phi = \frac{\ln\left(\frac{\eta V^+ - V_p}{\eta V^+}\right) - \ln\left(\frac{\eta V^+ - V_r}{\eta V^+}\right)}{\ln\left(\frac{\eta V^+ - V_{th}}{\eta V^+}\right) - \ln\left(\frac{\eta V^+ - V_r}{\eta V^+}\right)}. \tag{4.42}$$

By extending and transforming (4.42) it follows:

$$e^{\left(\phi \ln\left(\frac{\eta V^+ - V_{th}}{\eta V^+ - V_r}\right) + \ln\left(\frac{\eta V^+ - V_r}{\eta V^+}\right)\right)} = \frac{\eta V^+ - V_p}{\eta V^+}, \tag{4.43}$$

which leads to an expression for V_p as a function of the phase:

$$V_p = \eta V^+ \left(1 - e^{\left(\phi \ln\left(\frac{\eta V^+ - V_{th}}{\eta V^+ - V_r}\right) + \ln\left(\frac{\eta V^+ - V_r}{\eta V^+}\right)\right)}\right). \tag{4.44}$$

By defining the QRC $\Delta Q(\phi)$ as the difference between the actual charge on the capacitor $Q_c(\phi)$ and the charge Q^* the capacitor is transferred to in dependence on the phase ϕ:

$$\Delta Q(\phi) = Q_* - Q_c(\phi), \tag{4.45}$$

it follows from(4.40) and (4.44), with $Q = VC$:

$$\begin{aligned}\frac{\Delta Q(\phi)}{C} =& \eta V^+ \left(1 - e^{\left(\ln\left(\frac{\eta V^+ - \eta V^+ \left(1 - e^{\left(\phi \ln\left(\frac{\eta V^+ - V_{th}}{\eta V^+ - V_r}\right) + \ln\left(\frac{\eta V^+ - V_r}{\eta V^+}\right)\right)}\right)}{\eta V^+}\right) - P(\phi) \ln\left(\frac{\eta V^+ - V_r}{\eta V^+ - V_{th}}\right)\right)}\right) \\ & - \eta V^+ \left(1 - e^{\left(\phi \ln\left(\frac{\eta V^+ - V_{th}}{\eta V^+ - V_r}\right) + \ln\left(\frac{\eta V^+ - V_r}{\eta V^+}\right)\right)}\right).\end{aligned} \tag{4.46}$$

This equation can be reduced. For the first part of the exponent of the first exponential function in equation (4.46) it is:

$$\ln\left(\frac{\eta V^+ - \eta V^+\left(1 - e^{\left(\phi \ln\left(\frac{\eta V^+ - V_{th}}{\eta V^+ - V_r}\right) + \ln\left(\frac{\eta V^+ - V_r}{\eta V^+}\right)\right)}\right)}{\eta V^+}\right) = \phi \ln\left(\frac{\eta V^+ - V_{th}}{\eta V^+ - V_r}\right) + \ln\left(\frac{\eta V^+ - V_r}{\eta V^+}\right). \tag{4.47}$$

Thus, the complete exponent of the first exponential function reads to:

$$\phi \ln\left(\frac{\eta V^+ - V_{th}}{\eta V^+ - V_r}\right) - P(\phi) \ln\left(\frac{\eta V^+ - V_r}{\eta V^+ - V_{th}}\right) + \ln\left(\frac{\eta V^+ - V_r}{\eta V^+}\right). \tag{4.48}$$

This can be simplified to:

$$(\phi + P(\phi)) \ln\left(\frac{\eta V^+ - V_{th}}{\eta V^+ - V_r}\right) + \ln\left(\frac{\eta V^+ - V_r}{\eta V^+}\right). \tag{4.49}$$

By rewriting equation (4.46) with equation (4.49), the function for the charge reads to:

$$\begin{aligned}\Delta Q(\phi) = {} & C\eta V^+ \left(e^{\phi \ln\left(\frac{\eta V^+ - V_{th}}{\eta V^+ - V_r}\right) + \ln\left(\frac{\eta V^+ - V_r}{\eta V^+}\right)}\right) \\ & - C\eta V^+ \left(e^{(\phi + P(\phi)) \ln\left(\frac{\eta V^+ - V_{th}}{\eta V^+ - V_r}\right) + \ln\left(\frac{\eta V^+ - V_r}{\eta V^+}\right)}\right).\end{aligned} \tag{4.50}$$

Because the logarithm is defined as $a^x = b^{x \log_b(a)}$ equation (4.50) equals:

$$\frac{\Delta Q(\phi)}{\eta C V^+} = \left(\frac{\eta V^+ - V_r}{\eta V^+}\right)\left(\frac{\eta V^+ - V_{th}}{\eta V^+ - V_r}\right)^{\phi} - \left(\frac{\eta V^+ - V_r}{\eta V^+}\right)\left(\frac{\eta V^+ - V_{th}}{\eta V^+ - V_r}\right)^{\phi + P(\phi)}. \quad (4.51)$$

And in result the QRC can be written in a more compact form as follows:

$$\Delta Q(\phi) = C\left(\eta V^+ - V_r\right)\left(k^{\phi} - k^{\phi + P(\phi)}\right) \quad (4.52)$$

with

$$k = \frac{\eta V^+ - V_{th}}{\eta V^+ - V_r}. \quad (4.53)$$

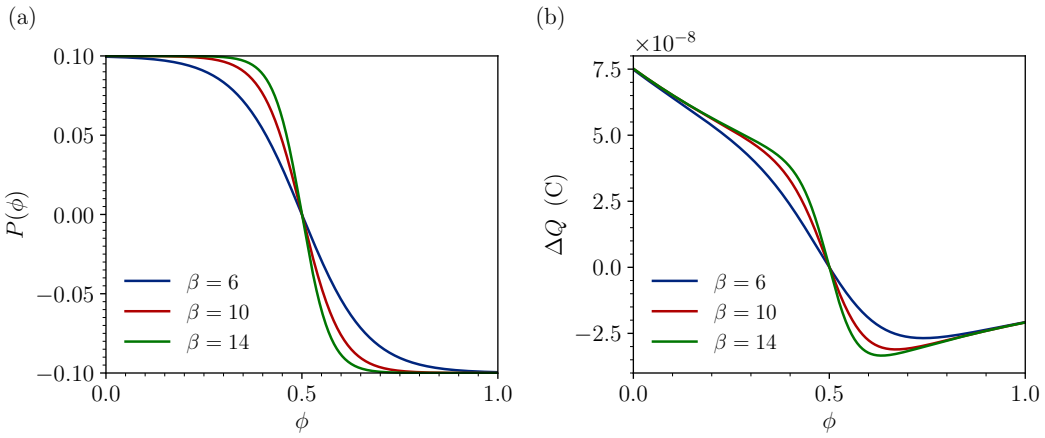

Fig. 4.13: Comparison between PRC and underlying QRC. (a) PRC based on the hyperbolic tangent (see 3.1.1.2 for further information on the PRC). (b) QRC calculated from the PRC shown in (a) (see A.8 for a list of the used parameters).

In Fig. 4.13 a comparison between a PRC and QRC is shown. Although the PRC shows the symmetric shape of a tangent hyperbolic, the QRC differs slightly. This is a

result of the underlying dynamics. In the presented example, the basis is an integrator circuit as can be used in a relaxation type oscillator. Thus, the nonlinear influence of a perturbation on the charge is a result of the current voltage relation of the charging capacitor. This dependence could be completely different, depending of the underling system.

4.2.2 Generation of a finite time delay

For the generation of a finite time delay, different approaches can be used. However, different to studies using high frequency systems, as for example delays in photonic systems, the signal propagation time in relation to the delay needed is not suitable for the realisation of the system.
In biological neural systems, the intrinsic frequency of the neurons is usually less than 1 kHz.[7] This, together with the ability to change the delay dynamically in order to scan a certain parameter space, makes the use of digital or at least mixed signal systems necessary.
Although the experiments were carried out using a field programmable gate array (FPGA), which is programmed to represent a structure of multiple adders driven by a synchronous clock, two more approaches will be presented in the following. Each of them has certain advantages and disadvantages over the chosen approach, which might make them interesting for different bio-inspired systems.

4.2.2.1 Shift register

The first and probably most natural approach is the use of shift registers for the signal delay, which can interpreted as analogous to the transmission of the action potential along the axon. The basic principle is shown in Fig. 4.14. Based on a clock signal, the

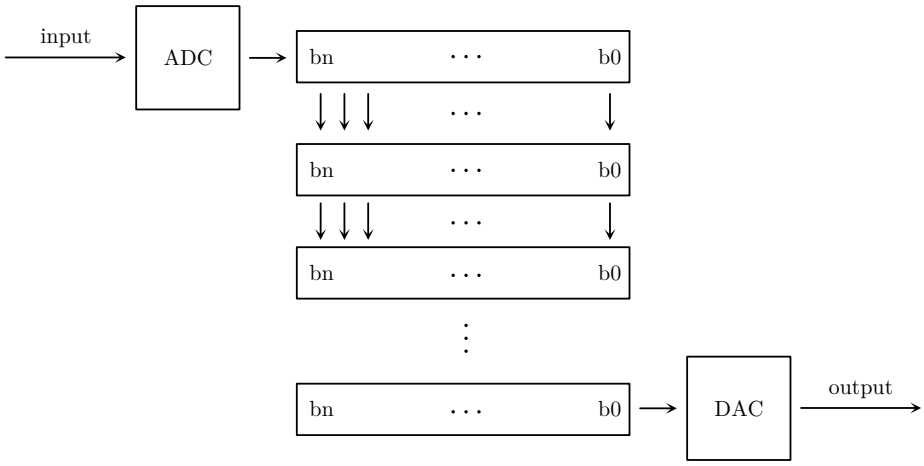

Fig. 4.14: Block diagram of a delay line based on shift registers.

input signal is converted to a digital number by an analogue to digital converter (ADC). In this example, the serial output of the ADC is fed into a shift register. From the serial input and parallel output register, the number is shifted one step further with each cycle. With each successive clock cycle, the number is shifted by parallel in- and parallel out-register, until the intended delay is reached. Here, the intended delay needs to be corrected by the input, output and signal conversion times.
The last stage includes a parallel input and serial output to a digital to analogue converter (DAC). The number is converted back to an analogue value and fed back to the system. It is clear, that a high sampling rate is necessary for the system to gather the small pulses reliably. With regard to the long periods without any information, this is the time between pulses, the system is quite resource consuming.

All in all, the system has the advantage of delaying the pulse shape with a resolution depending on the used number of bits. However, the shortcomings are the use of an analogue to digital converter, a digital to analogue converter, and a high amount of registers depending on the pulse duration and thus sampling rate as well as the time delay needed.

4.2.2.2 Software based ring buffer

Another approach is based on microcontrollers, which are programmed to store the delayed pulse times in a ring buffer and give an output pulse as soon as the desired delay time is reached.

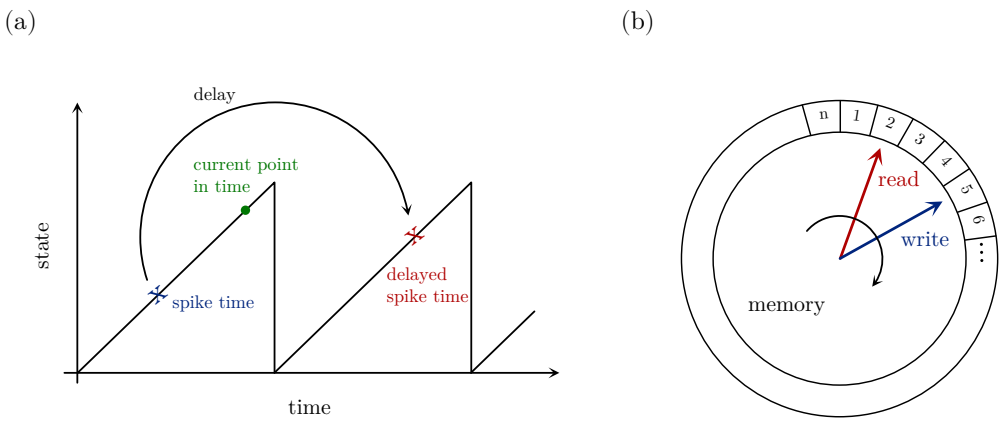

Fig. 4.15: Possible basic principle behind a software based delay line which utilizes a ring buffer. (a) The internal state of the counter is shown. Marked blue and red are the time points which refer to the occurrence of a pulse and the projected output of the delayed pulse. The green dot illustrates the current point in time, which is between both. (b) The ring buffer is illustrated. Every time a pulse is sensed, the write head stores the pulse time plus the delay and moves to the next address. The read head just moves one address further, if the state of the counter is equal to the stored value.

As Fig. 4.15 (a) shows, the delay line is based on the calculation of the new pulse time, which results from adding the delay to the sensed time.
Inside of the microcontroler a counter increases continuously. From the point in time a pulse is sensed (blue cross), the delayed pulse time is calculated (red cross). The moment the state of the counter equals the calculated time, the output of the microcontroller generates an output pulse.
In order to allow for the delay of multiple pulses, which is necessary when the pulse period is shorter than the delay time, the system needs a memory. This is built through a ring buffer. In this, the calculated time is stored in one address and as a result the write head increases to the following address in the memory. The read head refers to the next output pulse time.
In summary, this approach is based on the conventional von Neuman architecture, which is to be overcome by neuromorphic computing schemes. Moreover, the maximum delay is based on the counter and clock of the used system, thus lacking variability in the generation of time delays. Furthermore, regarding experimental work, the change in the delay is rather static, because each change normally needs a new compilation of the software code. However, there are also strong advantages. The use of an approach based on basic programming languages makes it flexible in terms of fast adaptation to different systems. In addition, the use of multiple delay lines is easy to implement, due to the availability of low budget microcontroller.

4.2.2.3 Delay line based on a parallel adder structure

The generation of an in operando programmable, fixed signal delay was done using a FPGA. FPGAs are versatile tools for the representation of various functions. These integrated circuits can be adjusted in their functionality by hardware description languages. Therefore they are in between application-specific integrated circuits (ASICs) and general purpose processors in terms of specificity and efficiency. The internal structure is depicted in Fig. 4.16. The working principle is based on a series and parallel connection of different blocks, which are based on adder structures. The first block Ad_1 has the function to detect a positive edge of an input pulse. In case the logic threshold at the input of Ad_1 is exceeded, the output is set to a high level for one

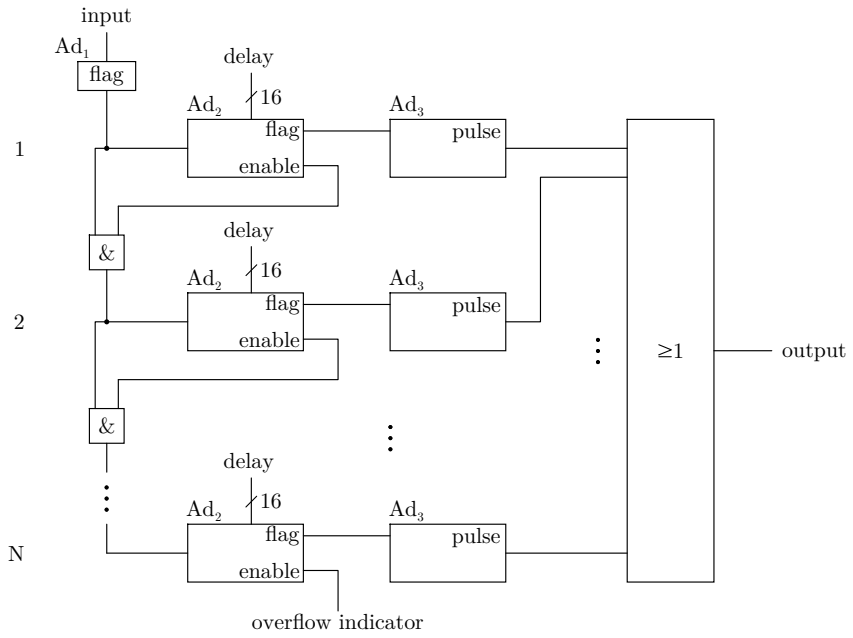

Fig. 4.16: Block diagram of the delay line as implemented in the FPGA. The basic structure consists of a parallel and series connection of multiple adder blocks Ad_i, which are interconnected with AND gates. Each line is capable of delaying one pulse at a time. The OR gate at the end generates the output. For the very high speed integrated circuit hardware description language (VHDL) code of the respective entities, please refer to the chapter D.

clock cycle. To prevent an input pulse from causing the output to be high for several clock cycles, a refractory time at Ad_1 follows.

After the detection of an input pulse, the high level output of Ad_1 is the input to the actual delay blocks, for example line number 1. A high input at Ad_2 starts a counter whose cap is set by an external 16 bit number. As long as the block counts up, the enable output is set to high. After the cap is reached, the flag is set to high for one output cycle.

This triggers Ad_3, which gives a high output for a certain, programmed amount of time, that is programmed and usually based on the width of the delayed input pulse. If a second input arrives, although the first is still delayed, the next line starts to count up, because the enable output of block Ad_2 sets the second input to the AND gate to high. The last block is an OR gate, which will output the high pulses, if at least one of the third level blocks Ad_3 has a high output. Due to the 16 bit input, a change in the

time delay can be made without the need of a new compilation. Thus, the time needed to conduct experiments which are based on delay sweeps is reduced significantly. Even dynamically changing delays can be represented by the system shown in Fig. 4.16.

4.2.2.4 Nonlinear phase response curve

For the observation of so-called jittering regimes a PRC with a local slope less than -1 is necessary (please refer to section 3.1.1.2 for a numerical example on jittering bifurcations).[126,127] Considering just the basic relaxation type oscillator, which is used as a core in the following experiments, the observation of a nonlinear slope, or more specifically a slope with a magnitude less than -1, is not possible using constant discharges through gate to gate coupling schemes. Thus, an additional input terminal is necessary to shape the PRC as desired. The equivalent circuit of the oscillator which

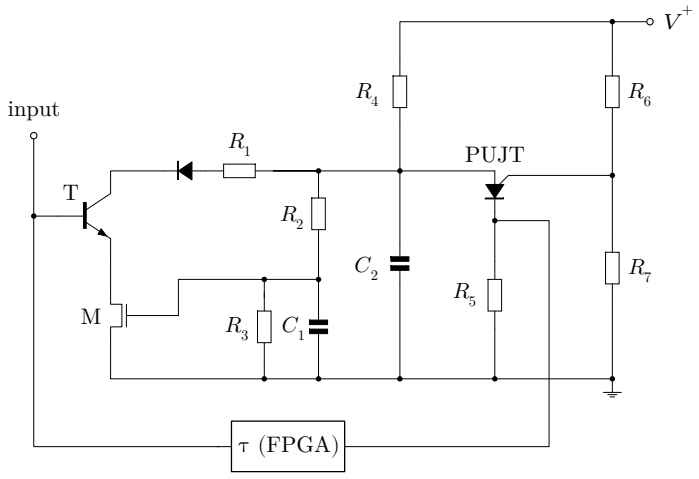

Fig. 4.17: Equivalent circuit of a relaxation type oscillator comprising a programmable signal delay. The oscillator is built using a PUJT. For the delay τ a FPGA is used, which can be programmed externally. Additionally to the signal delay, an input terminal is provided. Please refer to A.8 for an overview of the used parameters.

is used to generate sustained oscillations, as well as the input terminal necessary to generate the PRC, are depicted in Fig. 4.17. The core of the circuit is build based on a negative differential resistance based on a PUJT.

Essentially, this component is a four layer silicon diode, which consists of pnpn-doped silicon. The three terminals of the device are at the first p-region and the first and second n-region. Despite using the internal resistances of the silicon layers, the threshold is determined by external resistances, thus the term programmable.[195]
The working principle is based on the negative differential part of the I-V curve of these types of devices. For a certain range of input currents, the differential resistance of these devices is negative. This is exploited for the construction of sustained autonomous oscillations (please refer to 3.3.5 for further information about PUJT based relaxation type oscillators).
When the capacitor C_2 is charged, the voltage increases until the threshold is reached. This threshold can be changed by the voltage divider which is formed by R_6 and R_7. For the voltage evolution across the capacitor C_2 follows:

$$C_2\dot{v}_{C_2} = \frac{V^+ - v_{C_2}}{R_4} - \frac{v_{C_2}}{R_2 + R_3}. \tag{4.54}$$

The time needed to discharge the capacitor is much smaller than the time needed to charge the capacitor, thus the system approximates a leaky integrate and fire neuron as defined in chapter 4.1.2. Besides the charging term in equation (4.54), the leaky term models the current flow through the resistances R_2 and R_3. The second capacitance functions as a low pass filter for the voltage v_{C_2}. It is:

$$C_1\dot{v}_{C_1} = \frac{v_{C_2} - v_{C_1}}{R_2} - \frac{v_{C_1}}{R_3}. \tag{4.55}$$

Additional to the oscillatory subunit, the circuit has an input terminal. This terminal consists of a current regulating resistance R_1, a blocking diode, a bipolar transistor T and a MOSFET M. The voltage v_{C_1} is connected to the gate terminal of the MOSFET. Thus, the discharge current in response to an input stimuli is modulated, since the channel current of M is modified.
Due to the different values of the capacitors and resistances, the time constant R_2C_1 is larger than R_1C_2. As the perturbing pulse and the delayed feedback pulse is short in

time, the assumption is reasonable that only the capacitor C_2 is discharged. As the minimum of v_{C_1} is set to be below the onset voltage of the field effect transistor, the nonlinearity during the onset of conduction is exploited in the design.
Furthermore, the voltage v_{C_1} lags the voltage v_{C_2} due to the low pass characteristics of this part in the circuit. During the onset of conduction of the MOSFET this results in an increase in the conductivity with increasing oscillatory phase.

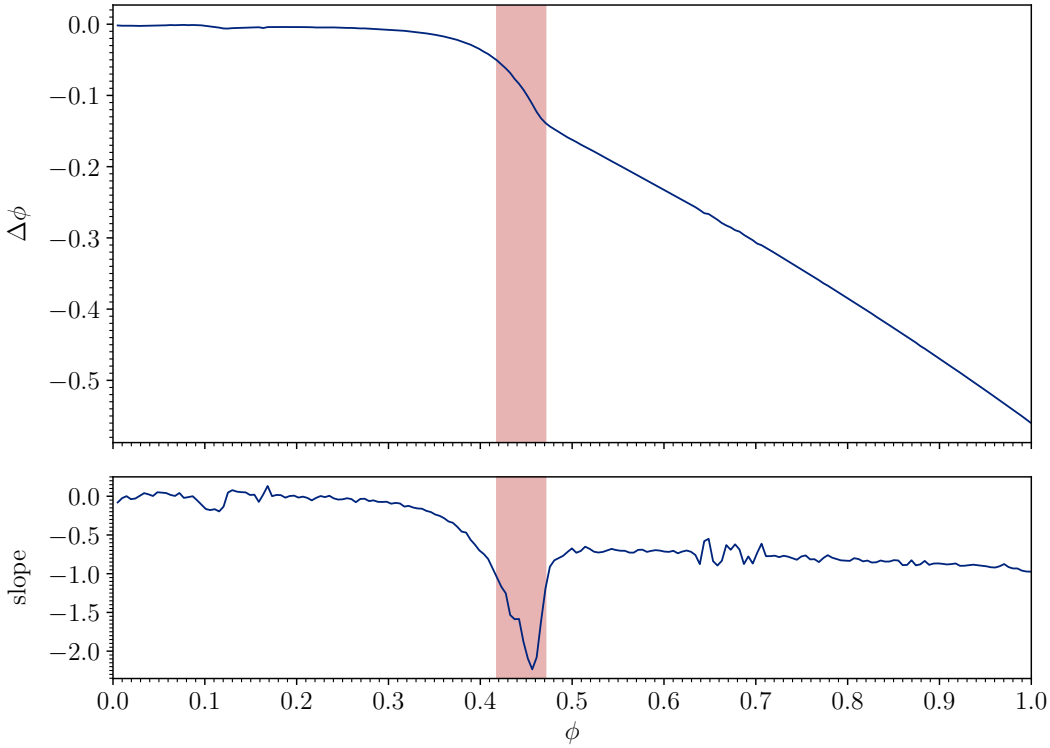

Fig. 4.18: Measured phase response curve and calculated slope are shown at the top and bottom trace, respectively. The phase response curve is shown as the change in phase $\Delta\phi$, which occurs in response to perturbations at different phases ϕ. The slope was calculated numerically using second order differences from the measured phase response curve. The part of the slope which is < -1 and its corresponding part in the phase response curve is highlighted in red.

The resulting PRC from the circuit is shown in Fig. 4.18. The presentation of an external perturbation to the circuit has nearly no influence, as long as $\phi < 0.3$. This part in the PRC is followed by a steep decrease, which refers to the part where the

slope is < -1, with its minimum around $\phi = 0.45$. This nonlinear increase is based on the onset of the conduction of the MOSFET, which is controlled by the low pass filtered voltage signal. After this steep decrease, the slope stabilizes at values near -1.

4.2.2.5 Jittering and regime switching

For the conduction of the experiments a set-up for the control of the delay time, the oscilloscope, and the perturbing pulse is necessary. As a basis, a general purpose computer as well as several micocontrollers were chosen. Python was used as a versatile and universal programming language to communicate between the general purpose computer and the controller as well as the oscilloscope. The microcontrollers were programmed with C++ and the development environment provided by the manufacturer. The resulting set-up is shown schematically in Fig. 4.19. To control the different parts of the experimental set-up, a general purpose personal computer is used. The relaxation type oscillator with a delayed feedback is depicted at the right. All signals which are

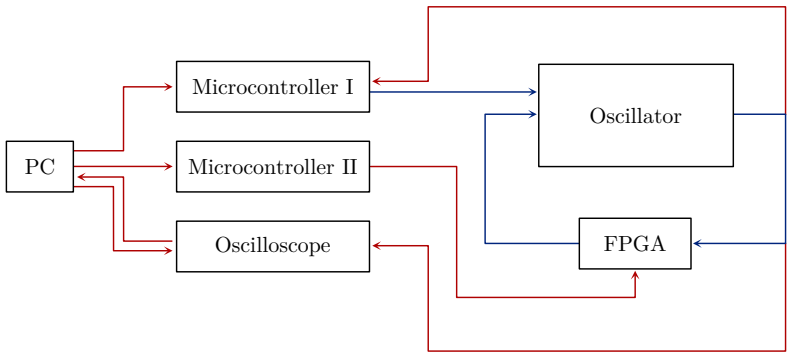

Fig. 4.19: Block diagram of the overall system used for the generation and manipulation of pulse patterns in a jittering relaxation type oscillator. A general purpose personal computer was used to control different microcontrollers and an oscilloscope. The oscilloscope gathers the raw data, which are analysed using the computer. Microcontroller I is used to apply defined perturbation pulses and microcontroller II for the definition of the delay time in operando. All signal paths for control and data acquisition are shown in red. The blue signal paths correspond to the oscillator with the delay feedback and external perturbation.

not used to either gather data or control subunits are depicted in blue, while the others are shown in red. The personal computer controls microcontroller I, which perturbs the oscillator at certain phases. Therefore, the microcontroller uses the output pulses of the oscillator to calculate the current phase. The microcontroller II controls the delay of the FPGA. To do so, the desired delay is converted into a 16-bit number and transferred to the general purpose input pins of the FPGA.
The data acquisition is done using a universal serial bus based oscilloscope. The start, stop, and duration of the measurement is controlled by the personal computer as well. Using this set-up, the delay can be changed in small steps. Additionally, pulses for the variation of certain inter spike intervals can be applied. Therefore, it is a versatile and reliable system for the investigation of a autonomous relaxation type oscillator comprising a finite time delay. In Fig. 4.20 (a) the occurring spike intervals are depicted under variation of the delay time. All values are normalized by the intrinsic period of the oscillator T_0. Here, intrinsic refers to the oscillator without an external perturbation or an delayed feedback. Each blue dot represents a certain measured ISI. The measured intrinsic period of the oscillator was 31.415 ms. The measurement was conducted by slowly increasing and decreasing the delay time of the delayed feedback loop with a step width of 600 µs.
For values of $\tau \leq 1$, the ISIs show the same shape as the mirrored phase response curve. This is, because the system does not have a memory, besides the delay line. Thus, the charging process starts again after each discharge of the capacitor voltage without information about the prior period. This also refers to a phase response curve of second order equal to 0, meaning a perturbation in one phase does not have an impact on the next phase and their related spike times.
In Fig. 4.20 (a), the jittering bifurcation points are clearly visible at the values $\frac{\tau}{T_0} = 1.5 + k$ with $k \in \mathbb{N}$. The subfigures 4.20 (b) and (c) show the observable dynamics of the system inside a regular spiking regime and inside a jittering regime. As (b) shows, a regular spiking regime refers to a situation where the periods are characterised by a constant period.
In contrast, the periods inside a jittering regime are not constant. In the example shown in Fig. 4.20 (c) two short periods and two long periods alternate. In the following, long periods are referred to as $'1'$ and short periods as $'0'$. It should be noted, that in a jittering regime more than one stable pattern can exist. In this sense, a pattern is

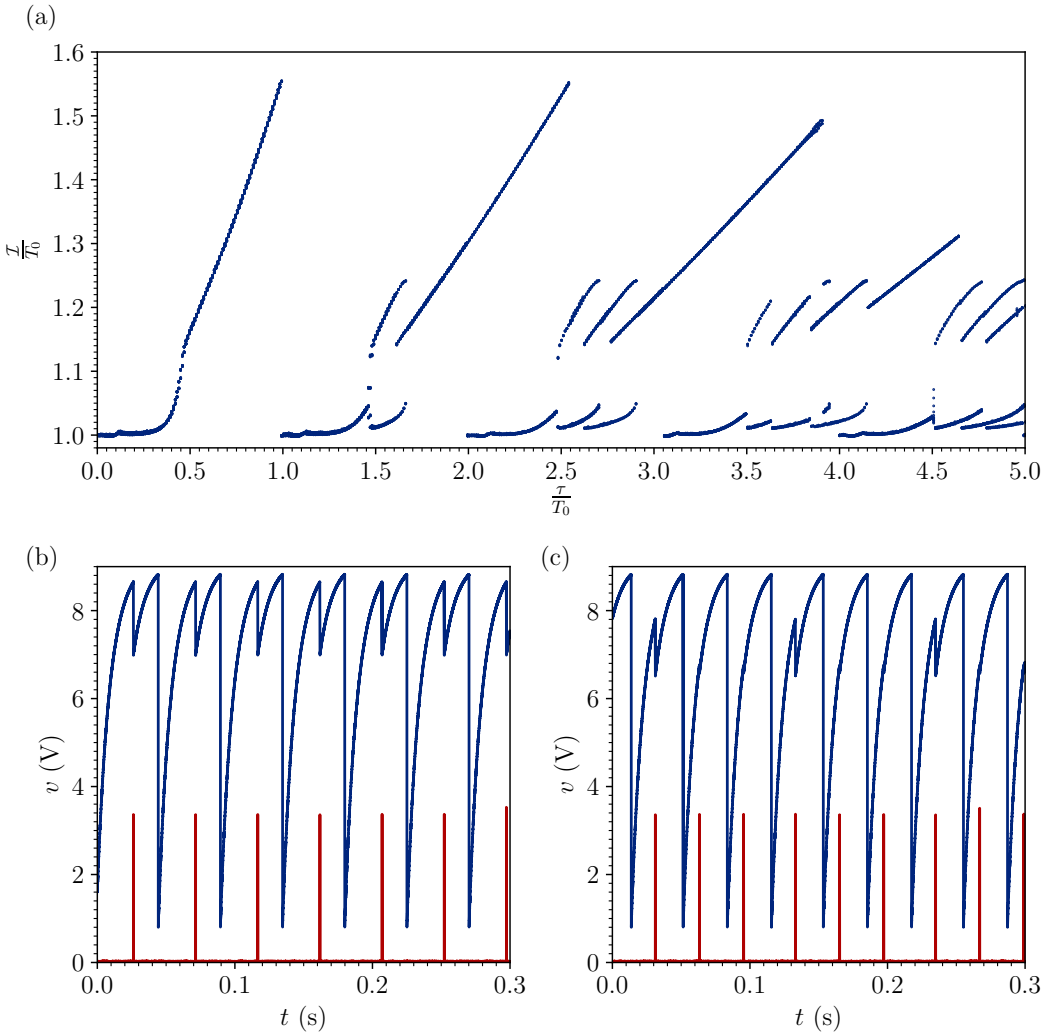

Fig. 4.20: Dynamics observed under varying time delay. (a) Bifurcation diagram of the ISI with the time delay as the control parameter. Each point refers to a measured interspike interval of the relaxation time oscillator. For values of $0 \leq \tau \leq 1$, the resulting curve has the shape of the measured phase response. For values of $\tau > 1$ jittering bifurcations occur at values $\frac{\tau}{T_0} = 1.5 + k, k \in \mathbb{N}$. T_0 refers to the unperturbed oscillator without a time delayed feedback. (b) The sustained oscillation represented by the voltage v_{C_2} is characterised by a constant period in the regular spiking regime ($\tau = 2.3 \cdot T_0$ (72.3 ms), delayed pulse in red). (c) The dynamics inside a jittering regime show different periods, which change between short and long intervals ($\tau = 2.6 \cdot T_0$ (81.7 ms), delayed pulse in red).

the sequence of periods of varying lengths. Furthermore, through the change of an ISI, it is possible to switch between different stable patterns.[235]

An example of switching between two patterns is shown in Fig. 4.21 (a) and (b). In (a) the voltage over the capacitor v_{C_2} is shown. At the beginning, the system shows a stable pulse pattern, which is characterised by a sequence of periods which reads to: $\overline{1100}$. Thus, the system shows a period 4 periodicity with a delay tuned to $\frac{\tau}{T_0} > 3$. After 0.5 s, two pulses were applied to the system. As a result, a short period changes to a long period. This is a pattern of $\overline{1010}$.

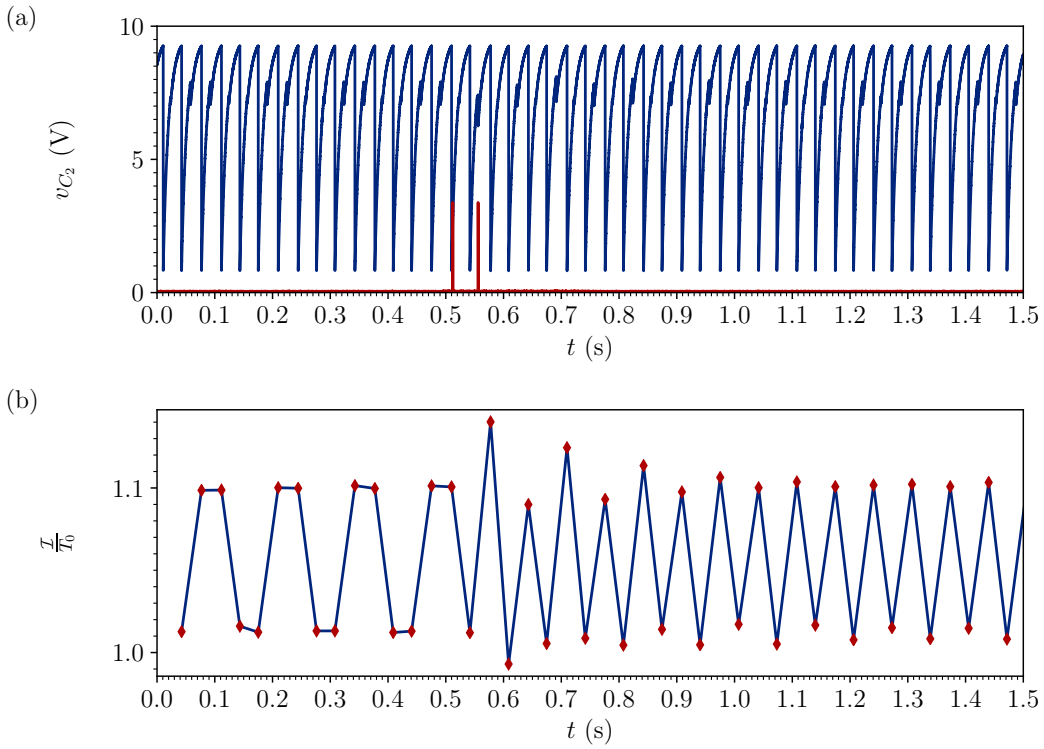

Fig. 4.21: Switching between different stable patterns. (a) The working point of the self-sustained oscillator with delayed feed was set to a period 4 periodicity ($\frac{\tau}{T_0} > 3$). The pulses depicted in red show the external perturbations, which perturb the base system. (b) ISIs obtained from the measurement shown in (a). The pattern at the beginning is set to two long and two short periods. After switching the dynamics change to one long and one short period.

4.3 Dynamic network

In the following, first steps are shown with regard to the possible implementation of growing and dynamically coupled networks. The first approach is based on the movement of nanoparticles in a liquid environment. Due to the influence of electric fields caused by the activity of the relaxation type oscillators, the network formed by the particles changes. The resulting structure is analysed using the metrics presented in chapter 3.2.
The second approach differs from the first approach in that no nanoparticles are used, but the potential difference presumably leads to the deposition of metal filaments. Here, the influence of dynamics on morphology is also considered by analysing the resulting change in the phase relationship between oscillators in the time varying network.*

4.3.1 Dimethylsulfoxid and zinc oxide colloid

The first experiments on dynamic network structures were conducted using equally spaced gold coated contacts. As a physical substrate of the network, a colloid based on dimethyl sulfoxid (DMSO) and ZnO particles was used. The gold coated contacts are the nodes of the network for further analysis (please see C.4 for additional information on the used setup). The resulting structure and labelling of the contacts is depicted in Fig. 4.22. For the comparison of the influence of changing potentials on the different contacts, relaxation type oscillators were connected to the contacts 14, 15, 20 and 21 (red).
The measurement of the single connections was carried out with the help of several multiplexers. This approach allowed for the controlled resistance measurement between each pair of contacts (please refer to chapter C.3 for more information on the layout and the PCB). To diminish the influence of the measurement, the selection of single contacts was randomized and the resultant weights are averaged over both measurements, which leads to $\omega_{ij} = \omega_{ji} = \frac{{\omega_{ij}^m}^1 + {\omega_{ji}^m}^2}{2}$.
In the following, the measured resistance values between all pairs of nodes are discussed

*In cooperation with M. Terasa, N. Carstens, A. Vahl, and O. Gronenberg

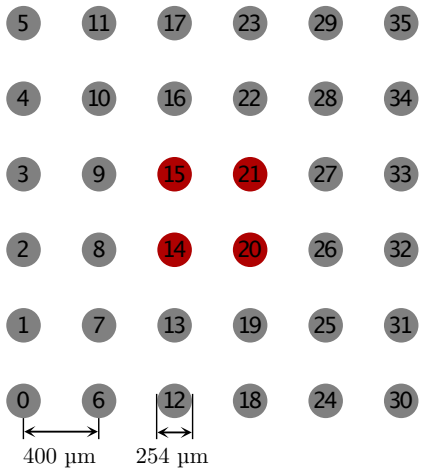

Fig. 4.22: Grid of nodes representing the contacts of the BGA adapter. From the 10 times 10 array, the central 36 contacts are used and depicted.

in more detail. It should be emphasised, however, that the resulting network is based on the resistance distance between two points. The measured resistance and the resistance of an equivalent circuit is not the same, as can be seen in the following short example. Imagine a network of three nodes, which are labelled with one, two, and three. For the sake of simplicity, there should be a resistance of $1\,\Omega$ between each node. Let the resistance between node one and two be R_1, between two and three be R_2, and between three and one be R_3. It is easy to show, that the measured resistance between each pair will be $\frac{2}{3}\,\Omega$, because exemplary for the measurable resistance between node one and two R_{12} the relation $R_{12} = \frac{R_1(R_2+R_3)}{R_1+R_2+R_3}$ holds.
In this regard the reader might refer to research based on two-point resistances in networks and resistance distance as a equivalent to information distance.[236–242] In Fig. 4.23, the connection strength of the contacts to each other before (Pre) and after (Post) the application of sustained oscillations are depicted. The partial image (a) shows the connectivity matrix in its original state, the partial image (b) in its changed state. The scales in both cases refer to nS. Already, a change can be detected with regard to the connection strength and distribution of the connections. This becomes more obvious when looking at the distribution of the network weights. Before and after the excitation of the middle contacts, the distributions change as shown in Fig. 4.24. The distribution

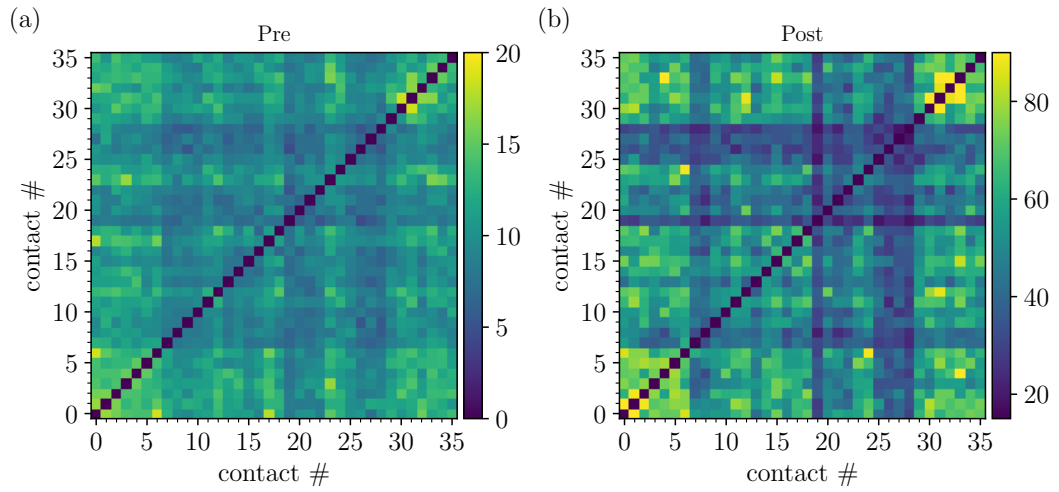

Fig. 4.23: Measured connection strength between each contact before (Pre) and after (Post) the influence of sustained oscillation. All weights are in nS. (a) Connectivity matrix before applying sustained oscillation to the network. (b) Connectivity matrix after the application of sustained oscillation. A general increase in connection strength is observable.

clearly shows, that the general conductivity of the network has increased. However, looking at the normalised weights $\hat{\omega}_{ij}$, the shape of the distribution is very similar. Only between approximately 0.2 and 0.375 higher counts are present. This indicates a higher proportion of weaker connections and thus a possible higher differentiation in the network.

In the following, the path lengths and clustering coefficients of the formed and unformed network are compared. The shortest paths and the clustering coefficients are shown in Fig. 4.25. In (a) the shortest paths between all node combinations $\hat{l}_{ij}$ are shown in ascending order. The paths are normalized to the respective longest path for better comparability. By comparing Pre and Post, it is noticeable that the path length has increased on average. This is consistent with a characteristic path length, which is 0.612 for the initial network and 0.687 for the formed network.

The maximum change of the normalised path lengths is about 20%. Besides the path length, the clustering coefficients change as well. Whereas the path lengths increase in the Post network in comparison to the Pre network, decrease the clustering coefficients for the single nodes. The coefficients are depicted in ascending order in Fig. 4.25 (b)

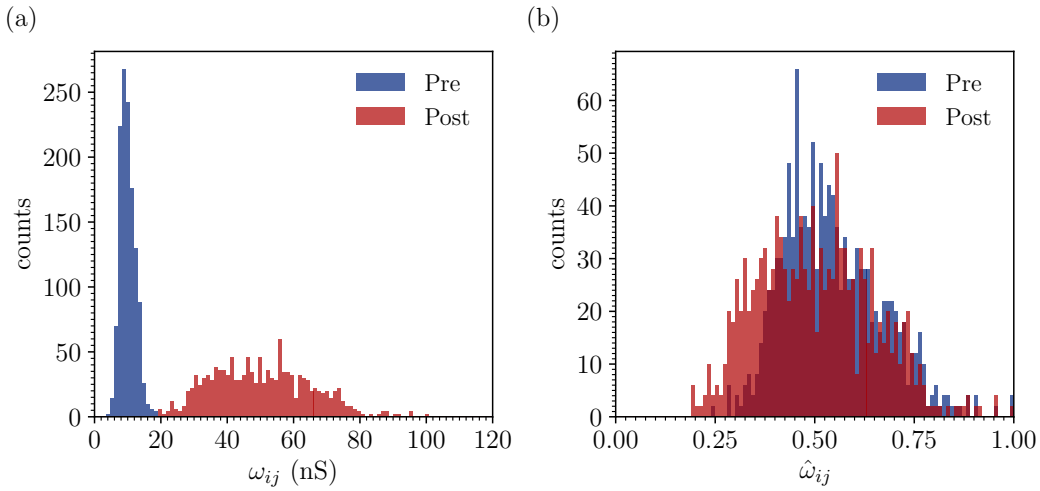

Fig. 4.24: Histogram of the measured connection strength between each contact before (Pre) and after (Post) the influence of sustained oscillation. (a) The weight distribution of both cases. The conductance and thus connection strength increases in the Post case. (b) Distribution of the weights normalized by the maximum weight in the Pre and Post case.

which leads to an average clustering coefficient of 0.538 and 0.493 for the Pre and Post network, respectively. Although the change varies from node to node, the clustering coefficient decreases by about 6% for about half of the nodes. The following takes a closer look at the most central nodes, determined by their betweenness centrality $\mathfrak{C}_B$. One characteristic of this type of network lies in the nature of the connections. As it is a resistance measurement, the network is fully connected, similar to a Hopfield neural network. This has a decisive impact on measured variables such as $\mathfrak{C}_B$, which is determined for the individual nodes with the help of the shortest paths through them. Since the resistance between the individual contacts varies less, it is often the case, that the shortest path length between two network points is the directly measured connection, rather than a path via another node.

This leads to many of the shortest paths running without the involvement of several nodes. In return is $\mathfrak{C}_B = 0$ for the majority of nodes. In Fig. 4.26, the nodes with a non zero betweenness centrality are highlighted before ((a)) and after ((b)) the application of external oscillations. Besides the single nodes, also the connections with a higher connection strength than 80% of all connections of the respective node are highlighted

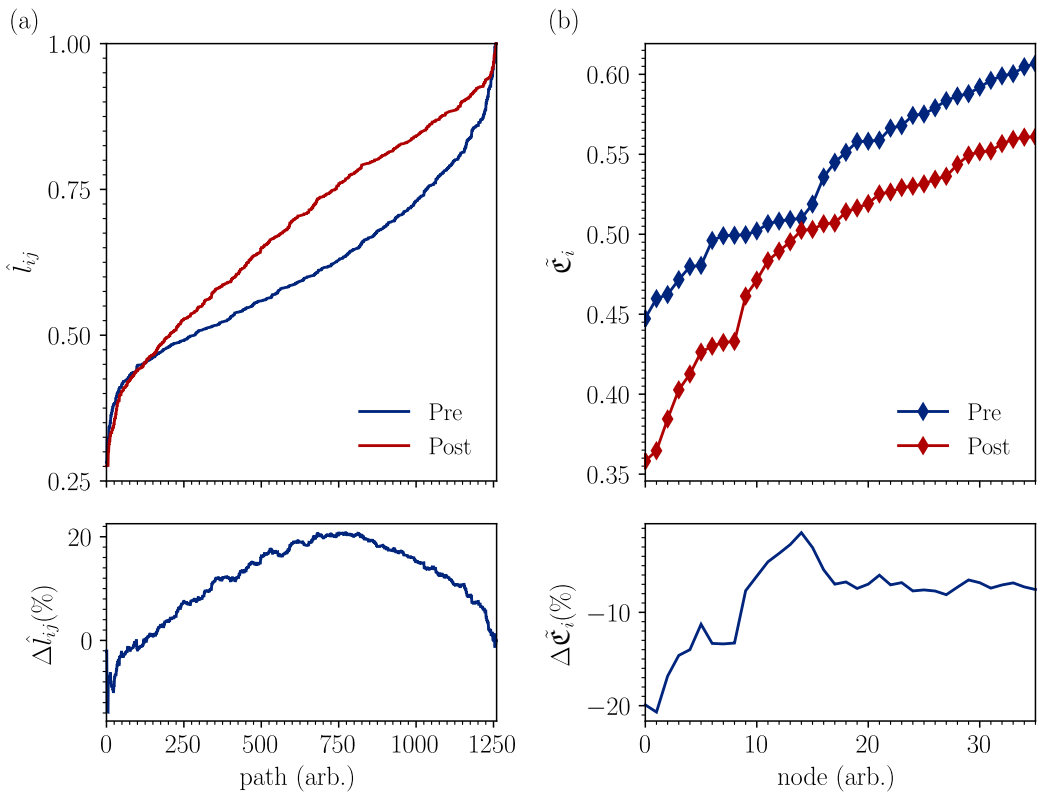

Fig. 4.25: Characteristic path length and clustering coefficient of the network, sorted in an ascending order. (a) All shortest path lengths between each pair of nodes are presented in an ascending order at top. The percentage change is depicted below. (b) shows the clustering coefficient for each node ordered in an ascending order as well at top and the percentage change below. The assigned nodes are arbitrary and do not refer to the nodes in the network.

as well. Although the nodes 27 and 28 remain in the set of nodes with $\mathfrak{C}_B > 0$, node 21 loses this property and the nodes 22 and 26 increase in centrality.

Furthermore, the strongest connections in each set of connections change considerably. This indicates, that the oscillators have significantly changed the state of the network. However, these considerations and measures are based on the resistance distance and not the equivalent circuit. The changes in the connection strength might be even more pronounced in this network. It also needs to be further clarified which physical mechanism has led to the large-scale change in resistance.

It is assumed, that the coating of the contacts was damaged during the tests, exposing

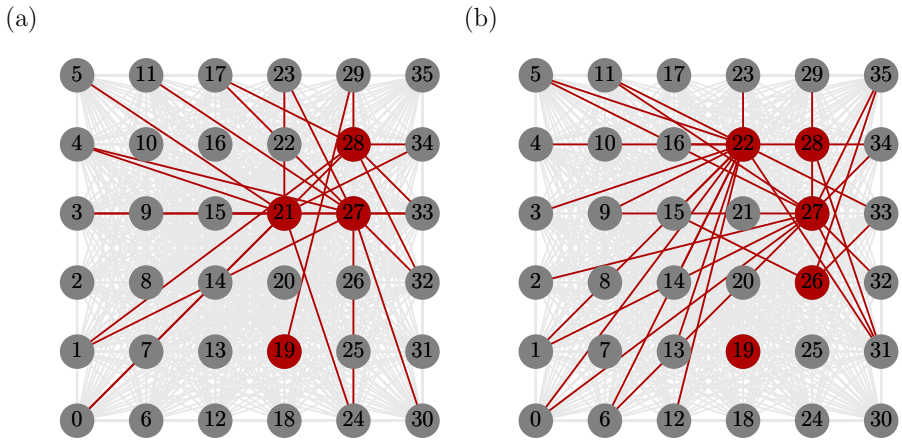

Fig. 4.26: Shown are the connections between all nodes of the Pre (a) and Post (b) network. The nodes with a betweenness centrality greater zero are highlighted red. The red connections refer to the connections with a connection strength above the 0.8 quantile $Q_{0,8}$.

the underlying nickel and copper. This would provide an explanation as to why irregularities in the connection matrix are already visible in the unformed state. Ultimately, this assumption led to the use of a solution of DMSO and $Zn(CH_3CO_2)_2$ (Zinc Acetate) for the coupling of oscillators. This will be further discussed in the following section.

4.3.2 Filamentary network growth

With the help of a solution of DMSO and Zinc Acetate, it is possible to employ a time varying coupling between dynamic systems, which will be shown in the following.
Here, an electric field will lead to the formation of metallic filaments, which can promote a connection between different contacts. For this purpose, three finger structures were deposited on a SiO_2 substrate. The contacts consist of sputter deposited 300 nm gold with a Ti adhesion promoter.
The dynamical system part consists of three separated autonomous relaxation oscillators as discussed earlier (please refer to 3.3.5 for more information about the basic circuit). They are coupled using the gate terminals of the circuits. Throughout the experiment evolution optical microscopy and electrical measurements lead to insights about the structural and dynamical changes of the system. In Fig. 4.27, still images

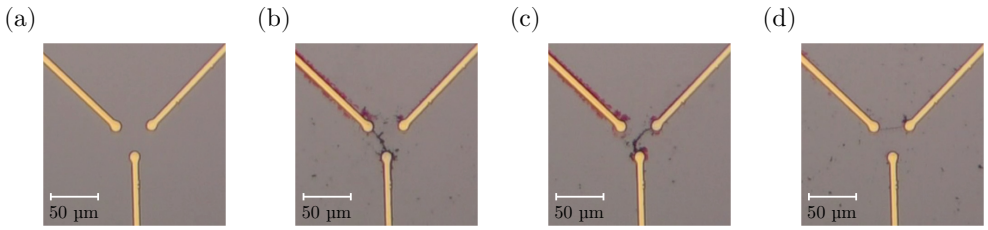

Fig. 4.27: Excerpts from the temporal course of the dynamic coupling. (a)-(d) show different states of the network. The unaffected initial state is shown in (a). The oscillatory activity leads to alternating strongly pronounced connections, as shown in (b)-(d).

from optical recording are shown. It is clear, that connections are both built up and broken down by the influence of the oscillators. Here, (a) refers to the contacts without any attached metal filaments. On the contrary, different filaments are present in Fig. 4.27 (b) to (d). By examining the signals of the relaxation type oscillators, the effect on the dynamics are revealed. In the upper part of Fig. 4.28, a rastergram of the activity of the individual oscillators is shown. Each vertical line corresponds to a capacitor discharge. Three different couplings are already recognisable in this picture.
They are even more obvious when the ISIs are considered, which are shown below. During the first 9 s, the oscillators are not synchronised and the ISIs fluctuate strongly,

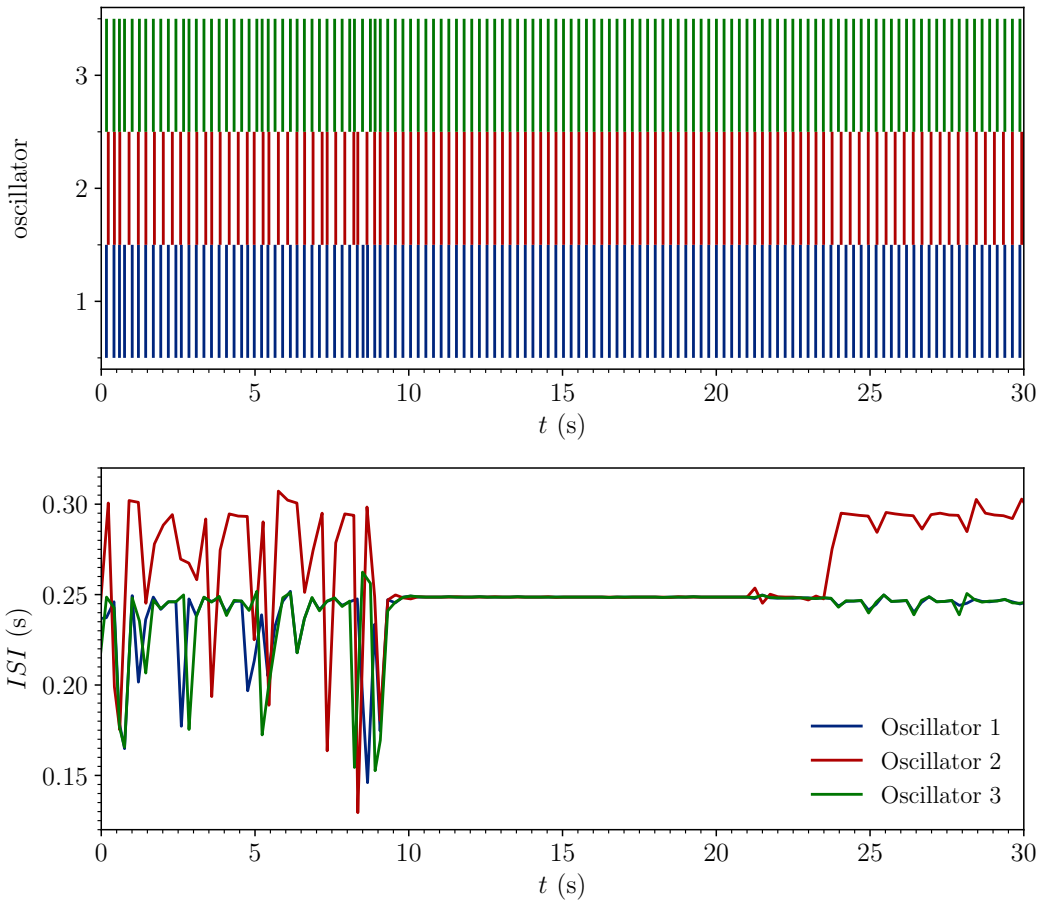

Fig. 4.28: Time transients from a system of three sustained oscillators coupled by a liquid electrolyte. Shown at the top is a rastergram of the oscillatory behaviour. Each vertical line refers to a discharge pulse at the cathode. The bottom shows the ISIs of the three oscillators. Clearly visible are three distinct states of no synchronisation, complete synchronisation and cluster synchronisation.

due to the non-constant coupling between the individual pairs. This is followed by a phase of synchronisation for $9\,\mathrm{s} \leq ISI \leq 23\,\mathrm{s}$. After this, a transition into a cluster synchronisation takes place, in which oscillators one and three are synchronised and oscillator two is not.

It should be noted, that the frequency distribution of the oscillators was completely random, due to the non-ideal components. This can lead to a more advantageous

synchronisation of individual oscillators if the distance between their frequencies is particularly small. This was especially observable for very small frequency differences, which led to synchronisation already taking place through the resistance of the electrolyte without a formed filament.
However, the time varying coupling can be exploited further to built a system with a directed flow of information, which is oriented on an associative learning rule as shown in the following. The circuit in use is shown in Fig. 4.29. Depicted are two

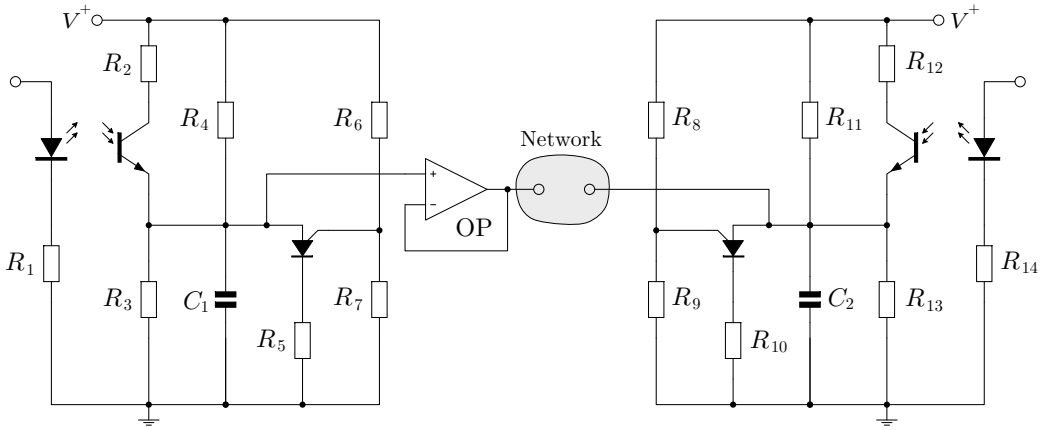

Fig. 4.29: Two oscillator feed forward circuit for the utilization of a liquid electrolyte. Both oscillators are in a silent state without sustained oscillations, due to the leakage resistances R_3 and R_{13}. However, they can be excited by optocouplers, which diminish the charging resistance and in return increase the capacitor voltages at C_1 and C_2. The liquid electrolyte is represented by the grey bubble as the basis for filamentary resistance change.

relaxation type oscillators. However, the circuit has some particularities. In addition to the structure presented in chapter 3.3.5, the capacitor is extended by a leakage resistor R_3 respective R_{13}. Due to this extension, the capacitor voltage is in equilibrium at v^{eq} below the threshold voltage, which is given by the voltage divider R_6 and R_7 or R_8 and R_9.
In order to excite the oscillator to sustained oscillation, the charging resistance can be reduced via an optocoupler. This makes it possible to increase the capacitor voltage in a controlled manner and thus to exceed the threshold voltage. In order to ensure a directional flow of information, the coupling between the oscillators is carried out with the aid of a unity gain amplifier OP, which maps the capacitor voltage over the

resistance of the network to a current and decouples both. The liquid electrolyte is represented by the grey bubble.
Since the second oscillator also does not oscillate in equilibrium, the voltage difference across the network reduces to $v_{C_1}^{p} - v_{C_2}^{eq}$. However, as soon as the second oscillator is also excited, the voltage difference increases depending on the phase relationship and the offset voltage of the single oscillator up to the maximum value of $v_{C_1}^{p}$. If the net formation of the filament requires a certain threshold voltage, or at least functions in a strongly non linear manner, a type of associative learning may be implemented. To map the current status of the link, only the first oscillator is excited for a short

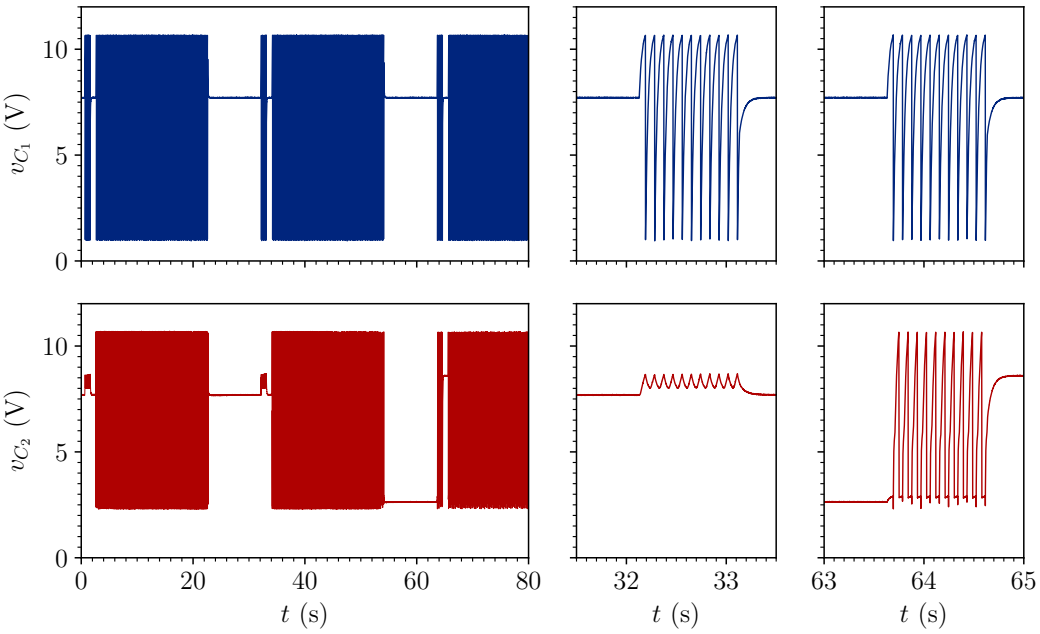

Fig. 4.30: Time curve of the capacitor voltage v_{C_1} at the top and v_{C_2} at the bottom. The oscillators were alternately excited to oscillation, either only oscillator one or both oscillator one and two. While the excitation of the first oscillator alone cannot initially excite the second oscillator to oscillate, as can be seen at approx. 1 s and 32.5 s, this is possible as soon as the filamentary connection has spread. The resulting excitation is shown at approximately 64 s.

time. As soon as the link is strong enough, the second oscillator should also start firing. Each short excitation of the first oscillator is followed by a prolonged and simultaneous excitation of the first and second oscillator. This pattern is repeated. After presenting a common excitation several times, it becomes apparent that the

connection has strengthened, so that now the single excitation of the first oscillator also leads to a continuous excitation of the second oscillator. This is shown in the time intervals around 32.5 s and 64 s. The excitation initially increases the capacitor voltage only minimally, which is not enough to exceed the threshold voltage, while the influence is strong enough.
In the longer term, the difficulty lies in bringing the different concepts together. On the one hand, a clever and application-oriented development on the circuit side is necessary, which can meet the target specifications in terms of size, voltages, currents and energy consumption. On the other hand, a physical substrate is crucial, which on the one hand should be robust enough to function over a longer period of time, and on the other hand variable enough to allow new connections to be created and forgotten. Possible systems are not limited to liquid electrolytes alone. It is well known, that resistive switching can also be observed in solid state systems.
However, the right interaction of both parts should allow the resulting network to have a self-organised criticality and a high complexity due to a balance of separation and integration.

4.4 Deterministic chaos

It is obvious, that the more complex the system, the more complex are the dynamics. This becomes impressively clear by looking at Fig. 3.1. Accordingly, it is hardly surprising that traces of chaotic dynamics also appear in neuronal systems.[41,42] However, the first reports and indications of low-dimensional chaos in the brain were apparently premature.[51]
Nevertheless, the system dynamics of the brain, similar to the structure, is at a self-organised point at the transition between periodic and thus easily predictable behaviour, to chaotic dynamics that can only be predicted with difficulty.[51]
For the design of the following experiment, this observations serve as a starting point to approach the question of what happens in a system that combines chaos and memory. In a sense, one approaches not from the periodic and easily predictable side, but from the direction of the chaotic dynamics.

4.4.1 Chaotic spiking in a driven relaxation oscillator

Chaotic dynamics can also exist in driven relaxation type oscillators, as shown in the following. The basis is built by a relaxation type oscillator, as it is used as a core for the spike based read out of the PiezoFET or the study of delayed feedback and jittering regimes. For the study of a chaotically spiking self sustained oscillator on the basis of a relaxation type oscillator, the circuit shown in Fig. 4.31 was used. The right hand side of the oscillator, this includes the resistances R_5, R_6 and R_7 as well as the transistors T_4 and T_5, forms the threshold and spike generation of the oscillator. The charging current of the capacitor C_1 is supplied by the pnp-type bipolar junction transistor T_3. The working point of this transistor is set by the voltage divider which consists of R_1 and R_2. Without the positive feedback this would result in a linearly increasing capacitor voltage. However, due to the feedback loop formed by T_1 and T_2, the voltage over R_2 decreases in result to the increase in capacitor voltage over C_1, which increases the charging current of the capacitor. Mathematically, this behaviour can be modelled as an integrate and fire neuron or relaxation type oscillator with an exponentially

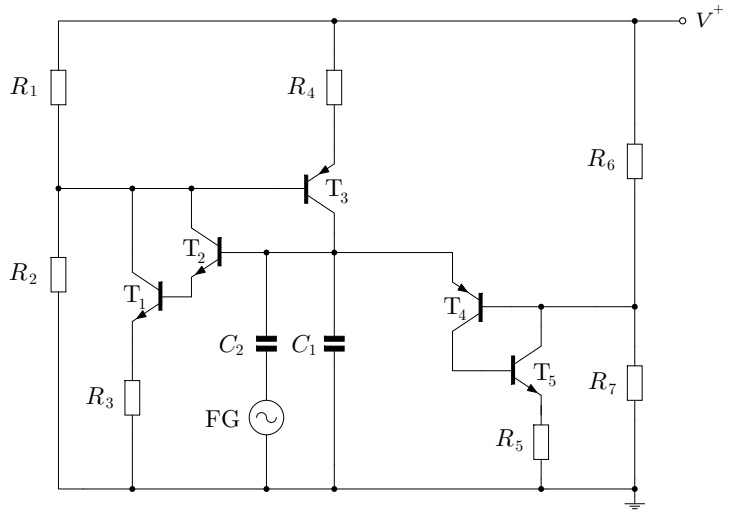

Fig. 4.31: Equivalent circuit of the autonomous oscillator with exponential increase in capacitor charge with periodic forcing. The increase in v_{C_1} leads to a drop in base voltage at T_3 which in return increases the loading current. Further, the capacitor voltage at C_1 is perturbed by a period signal. The parameters can be found in chapter A.9.

increasing state variable like membrane voltage. Thus it is:

$$\dot{\phi} = i + e^{\alpha\phi} + \beta \sin(2\pi f t)\,. \tag{4.56}$$

Here, ϕ refers to the phase of the oscillator and $\dot{\phi}$ to its time derivative. On the one hand, the change in phase is constant by i as well as self-dependent, due to the exponential function. This accelerates the development of the phase to a certain extent. In addition, however, a sine signal is superimposed, so that the phase dynamics are highly non-linear. As defined in 4.1 in course of the neuron model, if the system reaches the firing threshold ϕ_{theta}, the phase is reset to ϕ_{reset}. Thus, the spike times are defined as $t_s : \phi(t_s) = \phi_\vartheta$, and the ISIs as the difference between two successive spikes $\mathcal{I} = t_s^{n+1} - t_s^n$. Later the constants α, ϕ_ϑ, ϕ_{reset}, and i can be used to fit the model and the physical system. Both, the amplitude β and frequency f of the sinus can be used as bifurcation parameters for $\mathcal{I}$.

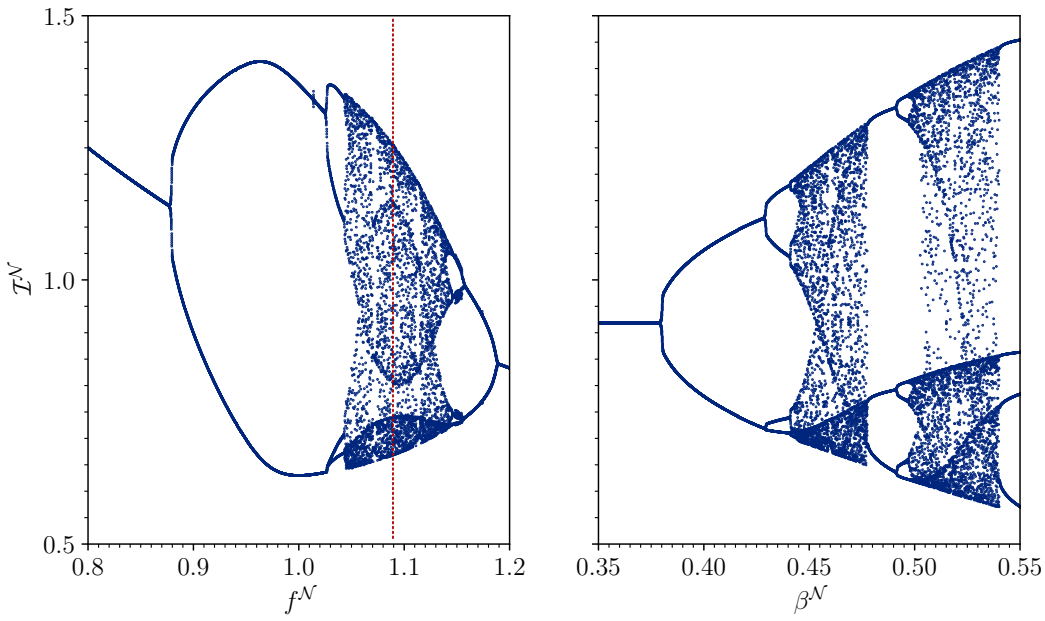

Fig. 4.32: Bifurcation diagram of the equilibrium point of the ISI $\mathcal{I}$ of an autonomous relaxation type oscillator with a superimpose sinusoidal signal.

In Fig. 4.32 a bifurcation diagram of the equilibria of the ISIs is shown. On the left-hand side, the frequency of the driving period signal is varying. In the diagram both the ISIs and frequencies are normalized to the intrinsic period of the unperturbed oscillator. The figure shows an overall decrease in $\mathcal{I}^{\mathcal{N}}$ which refers to an increase in firing frequency of the oscillator. However, at $f^{\mathcal{N}} = 0.88$ the first bifurcation takes place, which leads to a doubling in period. This behaviour continues and results in a chaotically spiking oscillator for $1.04 \leq f^{\mathcal{N}} \leq 1.14$.
On the right-hand side, a bifurcation diagram for the amplitude as the control parameter and a fixed frequency $f^{\mathcal{N}} = 1.09$ (red dotted line in the left diagram) is shown. The amplitude of the sinusoidal signal is normalized to the firing threshold of the oscillator, which leads to $\beta^{\mathcal{N}}$. The bifurcation diagram shows the well known period doubling route to chaos. The periodic windows are interrupted by periods of chaotically spiking of the oscillator.

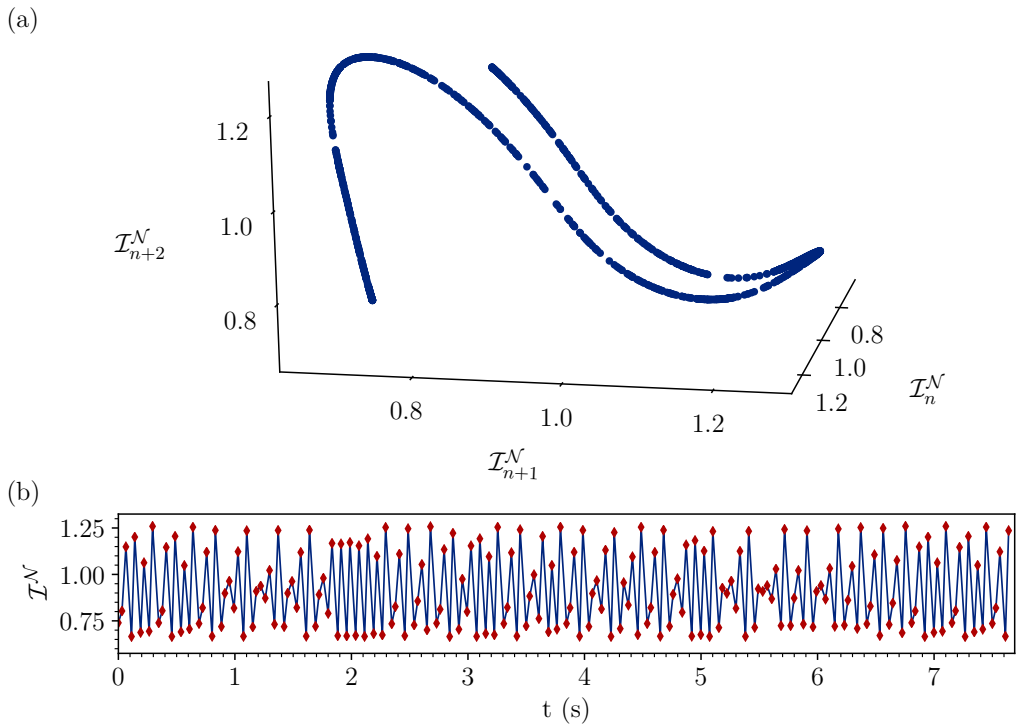

Fig. 4.33: Three dimensional diagram of the ISIs $\mathcal{I}$ of the chaotically spiking and driven relaxation type oscillator and time evolution of the ISIs. (a) Each point refers to a set of three successive ISIs. The geometrical shape of the attractor is apparent. (b) Time evolution of the ISIs of the driven system. A periodicity is not visible. The red diamonds refer to the measured ISI.

Looking at the measured ISIs visualised against each other, this is a diagram where each coordinate is determined by the values of three successive ISIs ($\mathcal{I}^{\mathcal{N}}_{n}$, $\mathcal{I}^{\mathcal{N}}_{n+1}$, $\mathcal{I}^{\mathcal{N}}_{n+2}$), a three dimensional curve forms as can be seen in Fig. 4.33 (a). Although the structure shows a clear geometric shape, the ISIs do not show a periodicity as the time evolution of the ISIs beneath the attractor underlines. However, the changes in the period duration as a result of the chaotic dynamics and the strong influence of the sinusoidal stimulation are clearly visible. From here on, the chaotic and global dynamics are focussed. For this purpose, a chaotically spiking system is no longer investigated, but an oscillator with a continuous but chaotic voltage characteristic - Chua's Oscillator.

4.4.2 Chua's Oscillator with memory - numerical results

For the investigation of the impact of memory on a chaotic circuit, the DBMD was built in parallel to the capacitance C_1 and Chua's Diode resulting in the state variable v_1 being the voltage which drives the current i_m through the memristive element. In

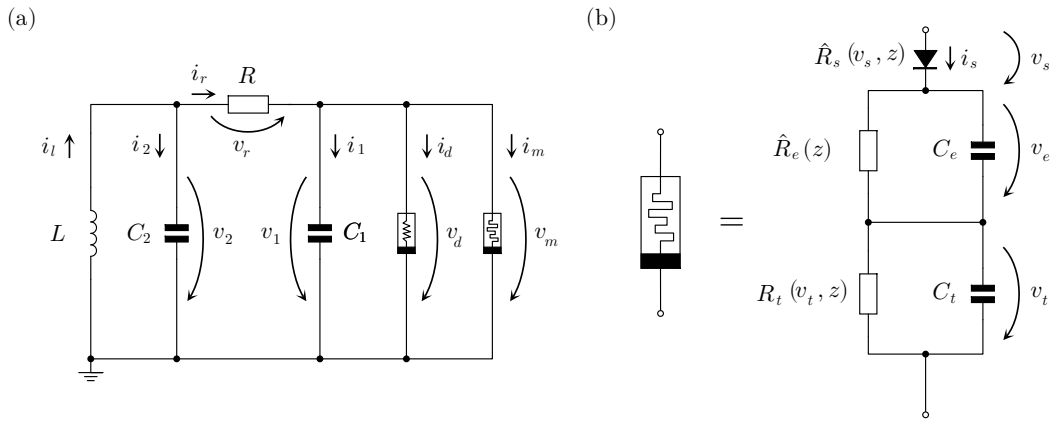

Fig. 4.34: Chua's Circuit and equivalent circuit of the memristive device. (a) The DBMD is located in parallel to Chua's Diode. The voltage drop across the device equals the first state variable v_1, which drives the current i_m through the memristive device. (b) Equivalent circuit, which was used to model the memristive device in use. The three regions of the physical device are the Schottky contact with the subsequent electrolyte and the tunnel barrier. The resistance modulation is a function of z which leads to a change in the tunnel current.

Fig. 4.34 (a) the equivalent circuit of the chaotic oscillator augmented with a memory element is shown. The strong asymmetric characteristic curve of the DBMD and the interplay with the chaotic yet symmetric dynamics of the state variables makes the orientation of the device in the circuit not crucial for the observation of the induced dynamics.
Nonetheless, the orientation of the component does change, which values either the positive or negative of the voltage v_1 are influenced. In the following, the orientation of the DBMD will be in parallel to C_1, i.e. the positive contact is connected to the capacitor and the negative contact to ground. As a result, positive values of v_1 will lead to significantly higher currents than negative voltages.

In Fig. 4.34 (b), the used equivalent circuit for the modelling of the DBMD is depicted. It can be divided into two main parts. The first is the Schottky contact, which consists of a diode and the resistance $\hat{R}_e(z)$, as well as the constant capacitance C_e. This is followed by a resistance $R_t(v_t, z)$ and a constant capacitance C_t as well. This last part represents the tunnel barrier of the device. The change in resistance is included into the equivalent circuit diagram through the variable z, which refers to the normalized average ion position in the component.
The position of the DBMD in the circuit and the changing resistance value give it the function of a time varying negative feedback for the state variable v_1. From the equivalent circuit of the memristive element in Fig. 4.34 (b), a set of differential equations, which describe the dynamics of the memristive device can be obtained. It needs to be noted, that the underlying equivalent circuit and formulas were derived by physical experiments and modeling of the DBMD.[190,243–245]
From the physical layers in the device and their equations, a set of differential equations can be obtained using the equivalent circuit in Fig. 4.34 (b). The layers are the Schottky contact, the electrolyte comprising the ion movement, and the tunnel barrier.[245] The Schottky current through the device reads to:

$$i_s(v_s, z) = I_s e^{\left(-\varphi_s(z) - \alpha_f \sqrt{\frac{|v_s| - v_s}{\alpha_s V_\vartheta}}\right)} \left(e^{\frac{v_s}{n(z) V_\vartheta}} - 1\right) \tag{4.57}$$

with the normalized and state dependent Schottky-barrier height $\varphi_s(z)$, an ideality factor $n(z)$, a fitting parameter α_f and the normalized Schottky-barrier thickness α_s. The magnitude of the current I_s scales to the temperature and device area (please see A.4 for more information about the overall model).[245] Following Kirchhoff's Voltage law the voltage v_s over the Schottky contact equals:

$$v_s = v_1 - v_e - v_t. \tag{4.58}$$

The voltage v_e refers to the voltage over the electrolyte layer and v_t to the voltage over the tunnel barrier. To incorporate the ion movement and thus the state dependence

of the resistance in this layer from z, a linear dependency is incorporated and reads to:[245]

$$\hat{R}_e(z) = R_{e0} + z\,(R_{e1} - R_{e0})\,. \tag{4.59}$$

This restricts the resistance $R_e(z)$ to a low resistance and a high resistance value. Using this dependency, for the voltage over this region follows:[245]

$$\dot{v}_e = \frac{1}{C_e}\left(i_s(v_s, z) - \frac{v_e}{\hat{R}_e(z)}\right). \tag{4.60}$$

The third region besides the electrolyte and the Schottky contact is the tunnel barrier. This part is modelled with Simmons equation, which leads to the current:[245,246]

$$i_t(v_t, z) = \frac{I_t g(-v_t, z) - g(v_t, z)}{a_t(z)^2}, \tag{4.61}$$

with:

$$g(v_t, z) = \varphi_t(v_t) e^{\left(-\alpha_t(z)\sqrt{\varphi_t(v_t)}\right)} \tag{4.62}$$

where

$$\varphi_t(v_t) = \varphi_{t0} + \frac{v_t}{2V_\vartheta}, \tag{4.63}$$

and

$$I_t = \frac{A k_b q_e \vartheta}{2\pi t D_t^2}. \tag{4.64}$$

Here, the tunnel barrier thickness $\alpha_t(z)$ accounts for the modulation of the current through the movement of ions in the electrolyte. Again, this function is implemented as linear, which leads to

$$\alpha_t(z) = a_{t0} + z\left(\alpha_{t1} - \alpha t0\right). \tag{4.65}$$

In all these equations, the key point is the movement of ions in the electrolyte, which is modelled as:[245]

$$\dot{z} = -\frac{\hat{Z}\omega(z)}{e^{\varphi_a(v_1,z)}} \sinh\left(\frac{v_r\left(v_1, v_s, z\right) + v_e - V_c}{V_e}\right). \tag{4.66}$$

Thus, the equations (3.18a) - (3.18c), (4.60), and (4.61) give rise to a system of differential equations describing the dynamics of Chua's Oscillator augmented with a

DBMD:[247]

$$\dot{v_1} = \frac{1}{C_1}\left(\frac{v_2 - v_1}{R} - i_d - i_s(v_s, z)\right) \tag{4.67a}$$

$$\dot{v_2} = \frac{1}{C_2}\left(\frac{v_1 - v_2}{R} - i_l\right) \tag{4.67b}$$

$$\dot{i_l} = \frac{v_2}{L} \tag{4.67c}$$

$$\dot{v_e} = \frac{1}{C_e}\left(i_s(v_s, z) - \frac{v_e}{R_e(z)}\right) \tag{4.67d}$$

$$\dot{v_t} = \frac{1}{C_t}\left(i_s(v_s, z) - i_t(v_t, z)\right) \tag{4.67e}$$

$$\dot{z} = -\frac{\hat{Z}\omega(z)}{e^{\varphi_a(v_1, z)}} \sinh\left(\frac{v_r(v_1, v_s, z) + v_e - V_c}{V_e}\right). \tag{4.67f}$$

The additional equations describing the dynamics of the used component are highlighted in red. Fig. 4.35 depicts the results of the augmented system obtained by numerical integration. Besides the chaotic oscillations, which are well known from the base system, the dynamics show a new feature.

These episodes of a decrease in local oscillation amplitudes are marked red. Due to the decrease in local oscillations of the overall system, these parts are called transient silent state (TSS). As the characteristics curve of the DBMD is strongly asymmetric, the TSS can be observed only during oscillations where $v_1 > 0$. If $v_1 < 0$, the current through the memristive device is not large enough to influence the base system dynamics.

However, voltages of $v_1 < 0$ are required to reset the state of the DBMD to values necessary for a new episode of a TSS. Although nearly all state variables seem to be attracted to a fixed point, the resistance and thus z does vary over time.

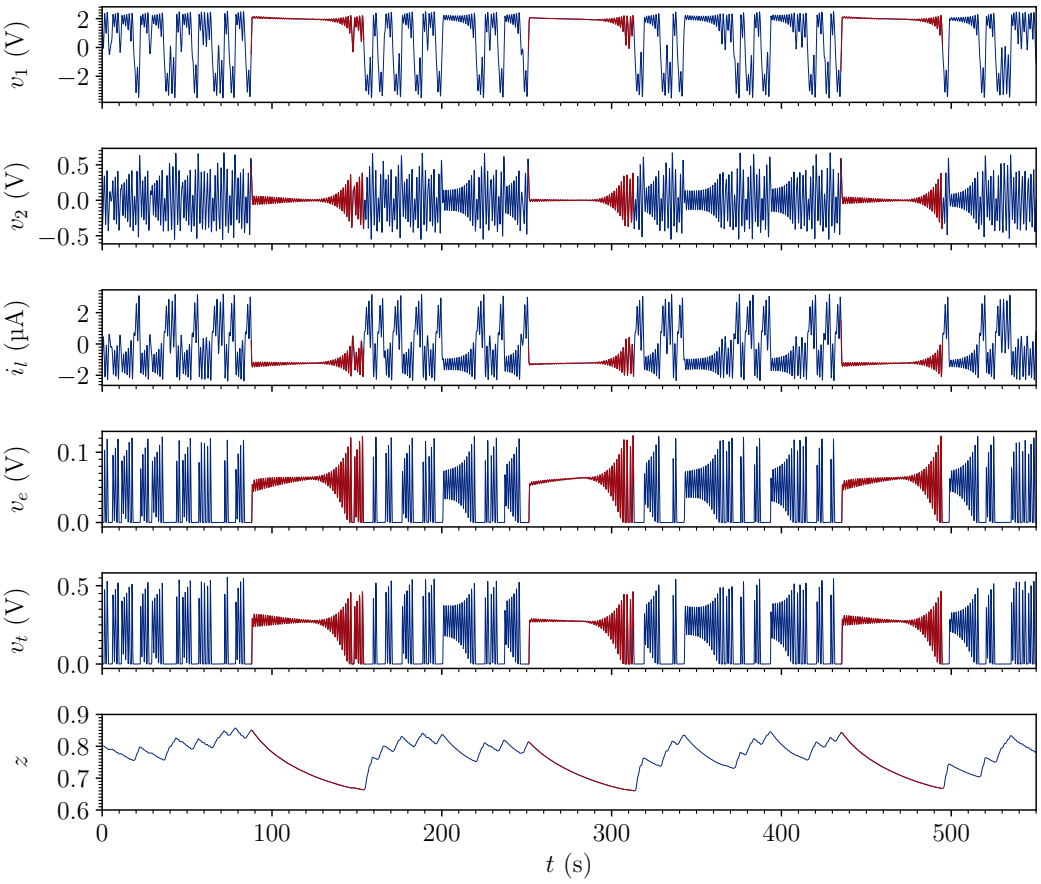

Fig. 4.35: Numerical results of Chua's system with DBMD model. Shown are the original state variables of Chua's Circuit (v_1, v_2, and i_l) as well as the additional variables of the DBMD (v_e, v_t, and z).

In Fig. 4.36 (a) and (b) the resulting attractor during one episode of TSS is shown using the (v_1, v_2) and (v_1, i_l) projections of the phase space.
The shown episode of the numerical results depicts the transient state between 80 s and 160 s (see Fig. 4.35). The additional part of the attractor gives the impression as if the original attractor is moved to the coordinate origin.
The way there is characterised by a funnel, which accounts for the transient damping of the signal over time. During the damping, the trajectory gains stability before losing stability again during amplification and following chaotic oscillations.

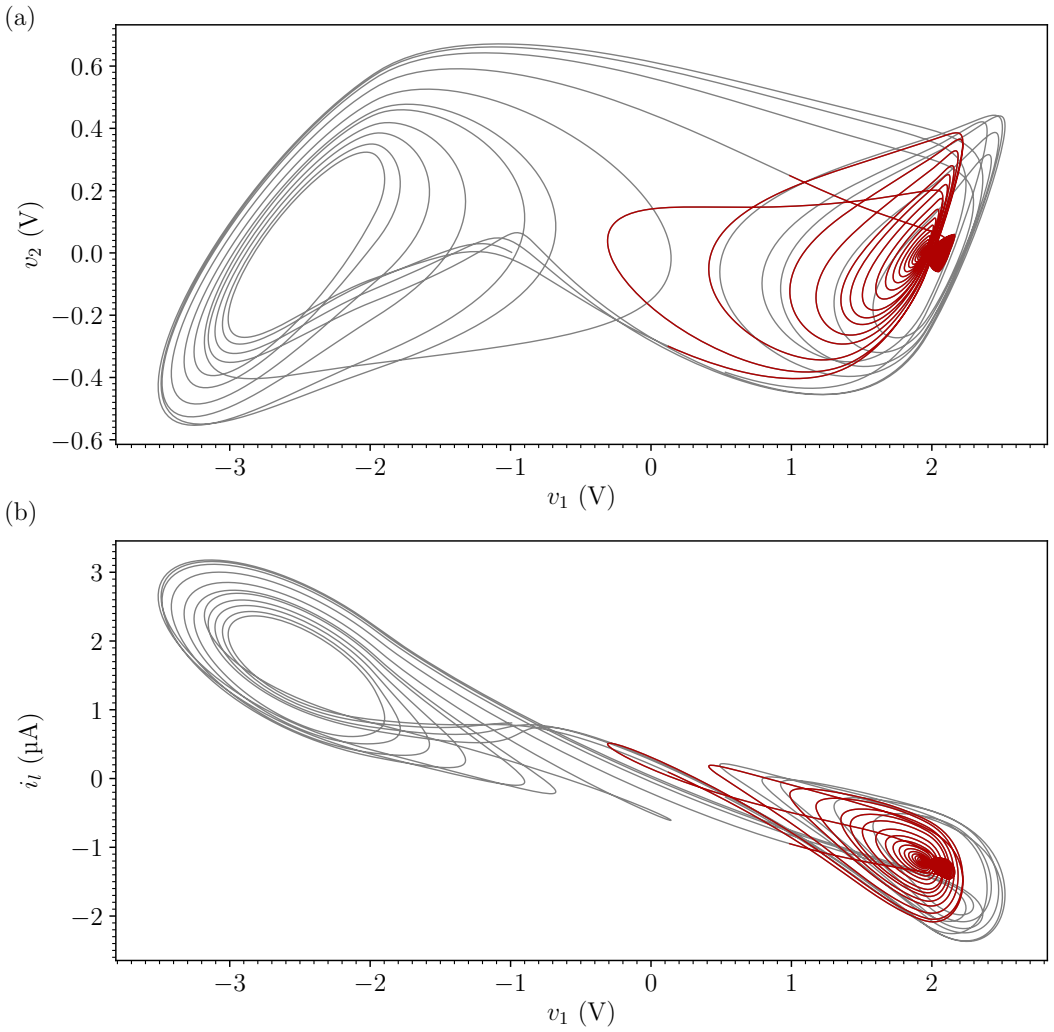

Fig. 4.36: Numerical results of Chua's system with DBMD model. (a) and (b) show that the new dynamics create an additional part of the attractor, which is traversed by the trajectories during TSSs (red).

During this process, the resistance of the DBMD changes and is depicted in Fig. 4.37. Shown is the (v_1, v_2, z) projection of the phase space in the same interval as in Fig. 4.36. The start point of the time evolution is marked by a blue diamond and the end point by a green diamond. First, the trajectory moves from positive voltage values of v_1 to negative values. However, during this, the resistance of the DBMD is nearly constant

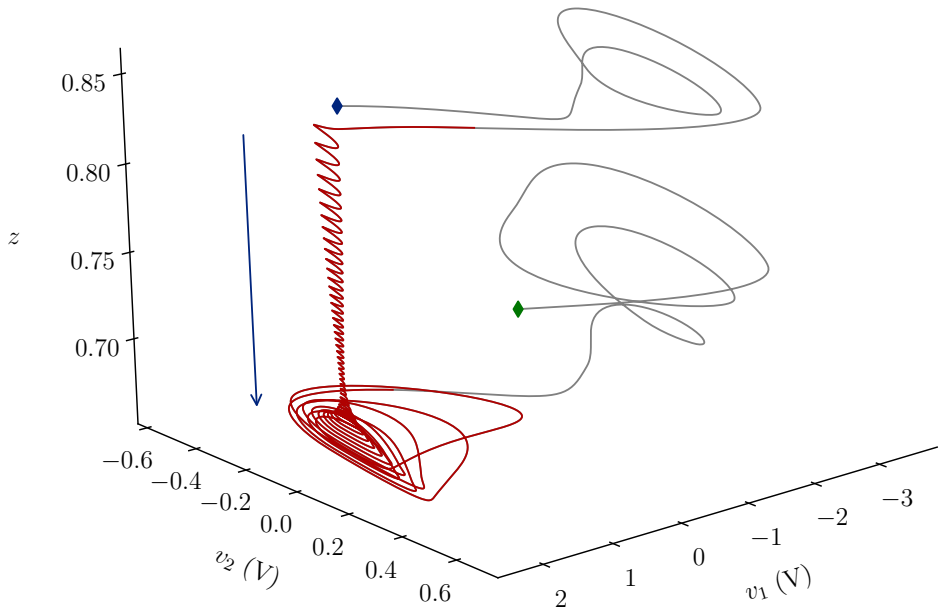

Fig. 4.37: Change in resistive state during an episode of a TSS obtained by simulation. During the the TSS the trajectory gets trapped in the funnel where the resistive state of the memristive device decreases until the the trajectory spirals out. Here, the blue and green diamond mark the start and end point of the section of the trajectory, respectively.

as suggested by z. Only with the change in polarity of v_1 back to positive values and the start of the TSS, a strong change occurs. During this, the local oscillations are damped (blue arrow).

After reaching a minimum in local oscillation amplitude, the dynamics get amplified and resume chaotic oscillations. After this, the polarity changes again and the resistance increases. Treating the variable z as a control parameter for the other faster variables a bifurcation diagram can be obtained (i.e. $\dot{z} = 0$).[248–250]

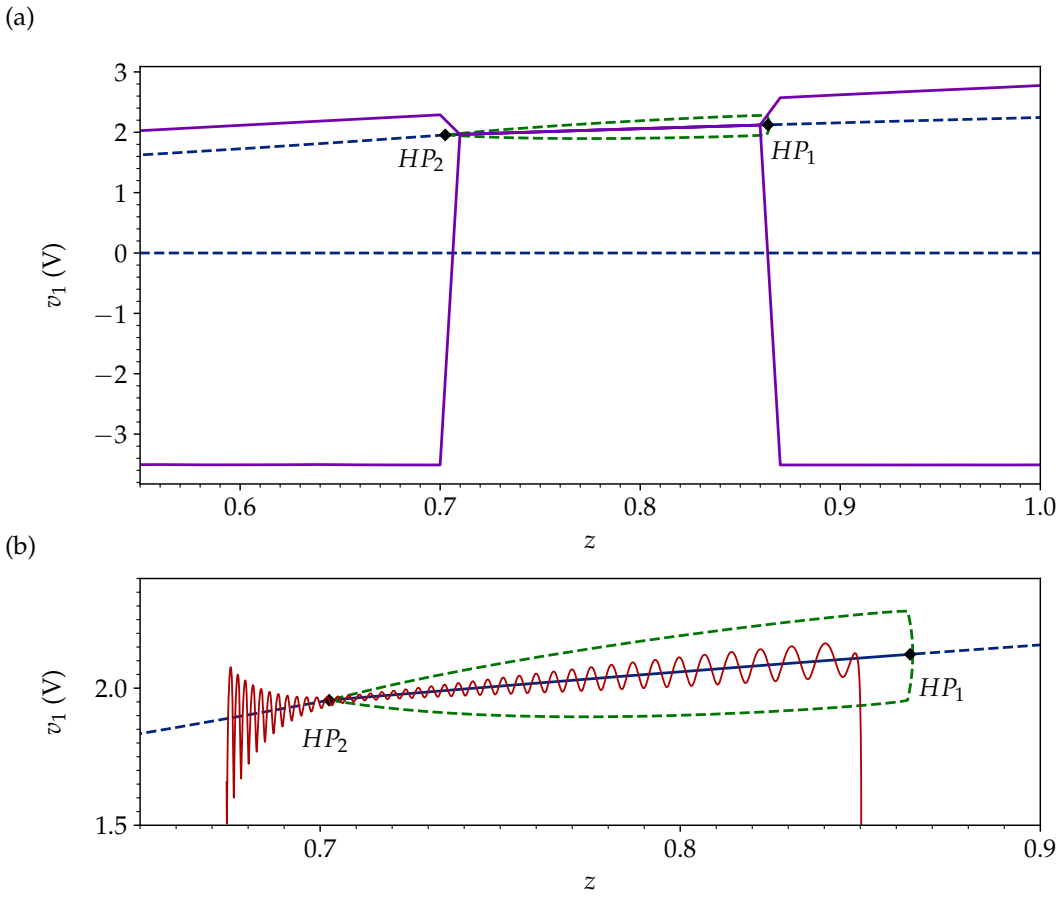

Fig. 4.38: Bifurcation diagram with z as the control parameter. (a) The stationary, periodic and chaotic solutions are marked blue, green and purple, respectively. A dashed line refers to unstable solutions, whereas a solid line shows stable ones. The Hopf bifurcation points are marked with diamonds (HP_1 and HP_2). (b) Close up of the bifurcation points with a superimposed trajectory during a TSS. The now solid blue line is the stable critical manifold where the trajectories of the full system are attracted to. During the TSS the state variable z decreases, which results in a stability change of the stable solution (HP_2).

The bifurcation diagram is depicted in Fig. 4.38. The solid lines in (a) and (b) depict the stable solutions, whereas unstable solutions are pictured with dashed lines. The stationary solutions are marked blue, the periodic solutions marked green, and the chaotic solutions are marked purple.

It can be seen, that the unstable stationary solution vanishes and stabilises into a stable stationary solution. This stable stationary state $(v_e(z), v_t(z), v_1(z), v_2 = 0$ and

$i_l(z)$) lays in the interval $0.71 < z < 0.86$ for all values of z. This change in stability at the boundaries of the stable branch ($z = 0.71$ and $z = 0.86$) takes place in subcritical Hopf bifurcations.

The stable set is called the stable critical manifold.[250] The trajectories of the system are attracted to this manifold. In Fig. 4.38 (b) one episode of TSS (red) is superimposed to the bifurcation diagram shown in (a). Depicted are just the critical manifold and the Hopf bifurcation points.

Once the trajectory gets close to the manifold, it gets attracted to it. Due to the steady change in the resistance state, the trajectory spirals and oscillates, although damped. As soon as the bifurcation point HP_2 is reached, the stability changes and the oscillations get amplified. The increasing local amplitude leads to chaotic oscillations and in return a change in polarity of v_1. Due to the polarity change, the resistance of the DBMD is reset, which allows for the process to restart if the trajectory comes close to the critical manifold.

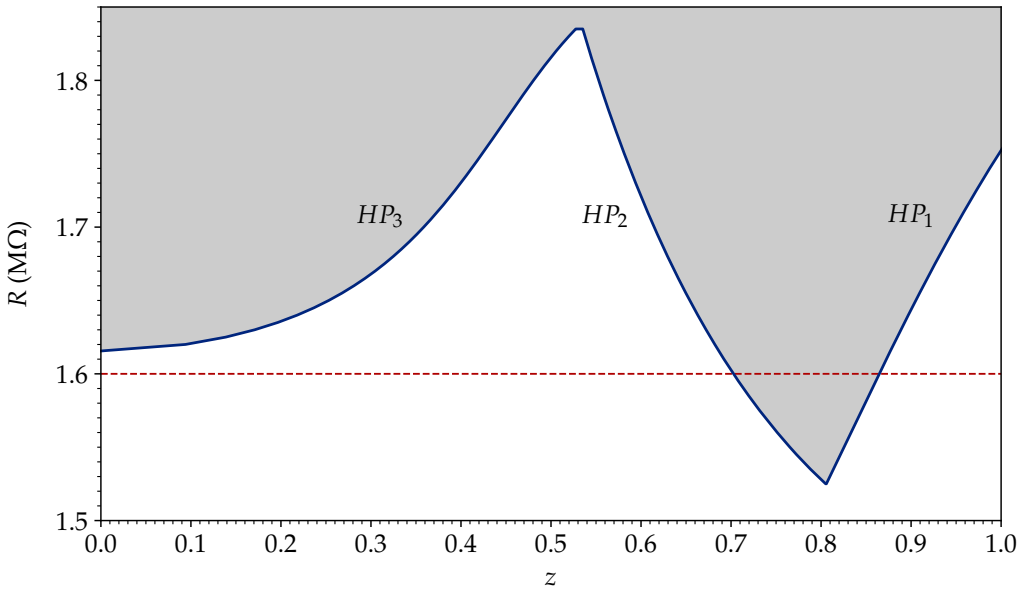

Fig. 4.39: Position and existence of the Hopf bifurcation points if z is varied as a control parameter. The grey area indicates the existence of a stable branch in the solution. The experimental value of the control resistance ($R = 1.6\,\mathrm{M\Omega}$) is shown as a dashed red line.

Instead of examining the state variables v_1, v_2 and i_l under variation of z, the existence of the stable branch with respect to the control parameter R can be investigated further. Fig. 4.39 shows a diagram where z is varied and the existence of a stable branch is depicted parametrised by R.
The grey area refers to an existing stable branch. The points of intersection with the horizontal dashed line refers to the Hopf bifurcation points shows in Fig. 4.38. Thus, R does not just control the overall dynamics of the base system (see Fig. 3.8), but also the duration of the TSS due to a change in the position of the Hopf bifurcation points. The here presented chaotic dynamics with TSS can be understood as slow-fast motion, with the slowest timescale determined by the memory component z of the system. As the TSS are only present when $v_1 > 0$ the equation (4.66) reduces to:

$$\dot{z} = -\frac{\hat{Z}\omega(z)}{e^{\varphi_{a1}+z(\varphi_{a0}-\varphi_{a1})}} \sinh\left(\frac{v_e - V_c}{V_e}\right), \tag{4.68}$$

because

$$v_r(v_1 > 0, v_s, z) = 0, \tag{4.69}$$

and

$$\varphi_a(v_1 > 0, z) = \varphi_{a1} + z\left(\varphi_{a0} - \varphi_{a1}\right). \tag{4.70}$$

From equation (4.68) the decrease in z for positives values of v_1 can be seen, because the derivative gets negative. This is the motion observed along the critical manifold to the left. Furthermore, the different velocities can be seen in Fig. 4.40. The values for $\dot{z}$ during the TSS episode are significant lower compared to values for $v_1 < 0$. The difference in set and reset are in the range of one order of magnitude. These multiscale arguments explain parts of the observed dynamics in the full system and underline the basal slow-fast dynamics.

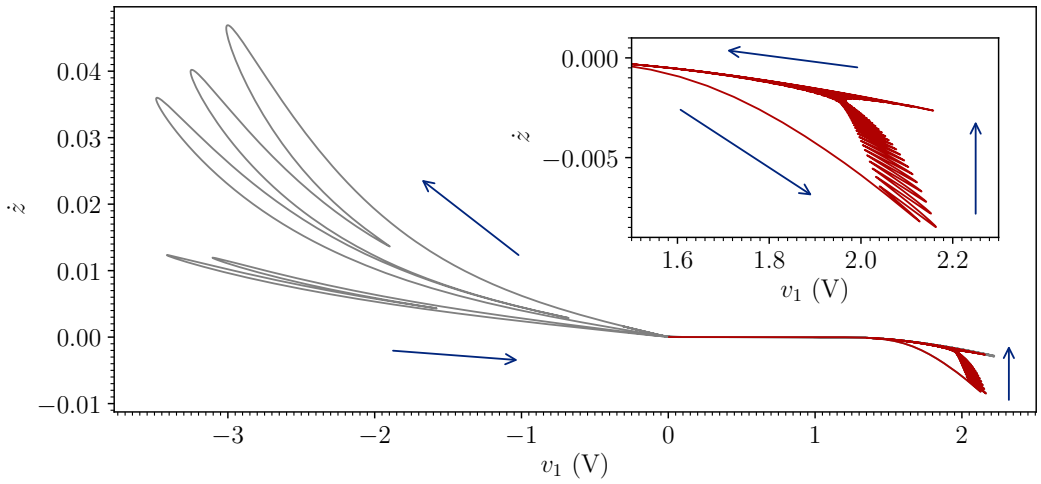

Fig. 4.40: Gradient of z obtained by central differences from the results of the numerical simulation of Chua's system augmented by a DBMD. The overall magnitudes differ by approximately one order of magnitude for the set ($v_1 > 0$) and reset process($v_1 < 0$).

4.4.3 Chua's Oscillator with memory - experimental results

To verify the numerical results obtained by simulation and modelling, Chua's system was built with discrete components. Although building the oscillator is straight forward, some changes have to me made. First, the current through the DBMD is small compared to most implementations of Chua's oscillator. Second, due to the slowly varying resistive state of the memristive device, the frequency has to be in the low Hz range. The first change in contrast to literature is easy to realize by scaling the used components. This is also true for the second requirement, which leads to a huge inductance. The use of a Gyrator allows the implementation of big inductances using active components without the need for big coils.

In Fig 4.41, the resulting equivalent circuit is depicted. A division into the chaotic oscillator and the signal acquisition stage can be made. It has to be noticed, that the circuit differs from the equivalent circuit in Fig. 4.34. On the one hand, this is the inductance which was built using Antoniou's inductance simulation circuit[251–254] and on the other, the nonlinear Chua's Diode, which is implemented using two INICs in

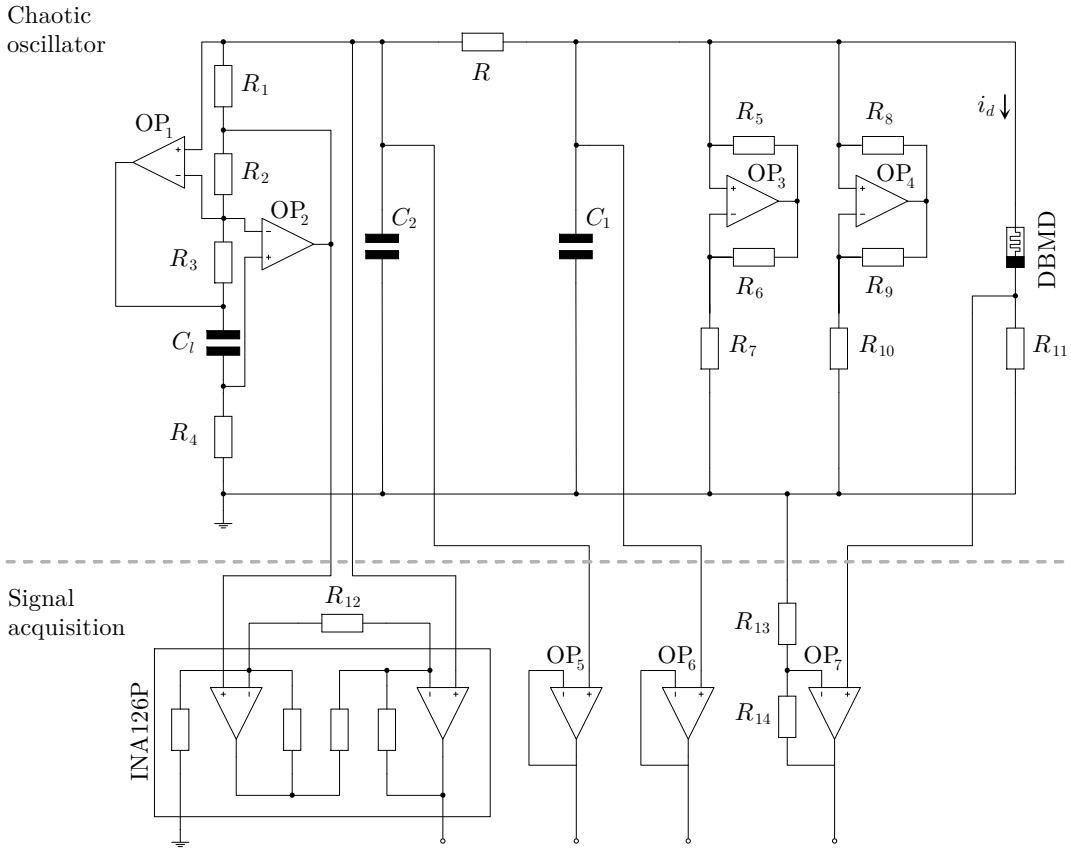

Fig. 4.41: Experimental set up of Chua's Oscillator with a DBMD in parallel to Chua's Diode. The experimental set up can be divided into the chaotic oscillator and the signal acquisition stage. The inductance is build with a gyrator (comprising the components: R_1, R_2, R_3, R_4, and C_l, as well as the operational amplifiers OP_1 and OP_2) and Chua's Diode using two negative impedance converter (INIC) in parallel (R_5, R_6, R_7, OP_3 and R_8, R_9, R_{10}, OP_4). The state variables and the current through the memristive device are measured as voltages, using instrumentation amplifier (INA126P and associated resistance R_{12}), non amplifying voltage follower (OP_5 and OP_5), and amplifier circuits (OP_7 with R_{13} and R_{14}).

parallel.[255] The working principles of the gyrator circuit can be found easily under the assumptions of ideal operational amplifiers.[254] This implies, that the voltage between both input terminals at each operational amplifier (OP_1 and OP_2) is equal and therefore no current flows into the terminals. Further, using the Laplace transformation for the

analysis allows a straight forward treatment of the circuit. For the description of the working principle, it is assumed, that the voltage V_{in} is applied to the gyrator circuit which leads to the input current I_{in}. Starting at the resistance R_4 the current through it is:

$$i_{R_4} = \frac{V_{in}}{R_4}, \tag{4.71}$$

because of the assumption of the ideal operational amplifiers. This implies also, that there are no input currents at the terminals. Using the Laplace relation of a current and voltage of a capacitance ($I(s) = sCV(s)$), the voltage over the capacitance C_l reads to:

$$v_{C_l} = \frac{V_{in}}{sR_4C_l}. \tag{4.72}$$

From this the voltage at the output of OP_1 can be determined as:

$$v_{\mathrm{OP}_1} = \frac{V_{in}}{sR_4C_l} + V_{in}. \tag{4.73}$$

From here, the voltage over R_3 reads to:

$$v_{R_3} = \left(\frac{V_{in}}{sR_4C_l} + V_{in}\right) - V_{in} = \frac{V_{in}}{sR_4C_l}, \tag{4.74}$$

and the current through this resistance is:

$$i_{R_3} = \frac{V_{in}}{sC_lR_3R_4}, \tag{4.75}$$

and equals the current through the resistance R_2. Therefore, the voltage at the output of OP_2 is:

$$v_{\mathrm{OP}_2} = V_{in} - \frac{V_{in} R_2}{s C_l R_3 R_4}. \tag{4.76}$$

From this the input current I_{in}, this is the current through the resistance R_1, can be determined as:

$$\begin{aligned} I_{in} &= \frac{V_{in} - \left(V_{in} - \frac{V_{in} R_2}{s C_l R - 3 R_4}\right)}{R_1} \\ &= \frac{V_{in} R_2}{s C_l R_1 R_3 R_4}. \end{aligned} \tag{4.77}$$

Because of the Laplace relation:

$$\frac{V(s)}{I(s)} = sL, \tag{4.78}$$

for the inductance of the gyrator circuit follows:

$$L = \frac{C_l R_1 R_3 R_4}{R_2}. \tag{4.79}$$

A derivation of equation (4.79) in a dense and compressed manner can be found in Sedra and Smith (2015).[254] The working principle of the INIC can be found analogue to the considerations above, whereby the use of Laplace transformation is not necessary. In the following, the resulting negative resistance for the first INIC (R_5, R_6, R_7, OP_3) shall be derived. Again an imaginary input voltage V_{in} and a resulting current I_{in} are applied. The operational amplifier is treated as ideal, this results in the voltage over

R_7 being equivalent to the input voltage V_{in}. Thus the current reads to:

$$i_{R_7} = \frac{V_{in}}{R_7}. \tag{4.80}$$

As no input currents are permitted to the ideal operational amplifier, the current through R_6 equals i_{R_7}. This results in the voltage:

$$v_{R_6} = V_{in}\frac{R_6}{R_7}. \tag{4.81}$$

From this, the voltage over the resistance R_5 can be determined. With $V_{R_5} = -V_{R_6}$ for the input current follows:

$$I_{in} = -\frac{V_{in}R_6}{R_5R_7}. \tag{4.82}$$

In result, for the input resistance follows:

$$\begin{aligned} R_{in} &= \frac{V_{in}}{I_{in}} \\ &= -\frac{R_5R_7}{R_6}. \end{aligned} \tag{4.83}$$

From here, it is clear that a favourable choice of the resistances ($R_5 = R_6$) leads to:

$$R_{in} = -R_7. \tag{4.84}$$

For the generation of the nonlinear I-V curve of Chua's Diode, a real word approximation

of the behaviour of the INICs is necessary and needs to be exploited.
Although the above considerations lead to the negative resistance obtained by the subcircuit, the real world device has a nearly constant output at sufficiently high and low voltages. These are called the negative V_{sat}^{-} and positive saturation region V_{sat}^{+}.[255] Starting from the breaking points, the slope of the I-V curves changes from positive to negative or reverse. These points can be calculated with the saturation voltage as follows:[255]

$$BP_1^{+/-} = \frac{R_7}{R_6 + R_7} V_{sat}^{+/-} \tag{4.85}$$

and

$$BP_2^{+/-} = \frac{R_{10}}{R_9 + R_{10}} V_{sat}^{+/-}. \tag{4.86}$$

For the piecewise linear function of Chua's Circuit only two symmetry breaking points are necessary. Therefore, during the design procedure one breaking point is near the saturation voltage and outside of the working point of the circuit. The resulting effective characteristic curve of the imitated Chua's Diode can be obtained by superposition of the single curves. For $BP_1^{+} > BP_2^{+}$ the resulting slopes are:[255]

$$m_0 = m_{11} + m_{02} \tag{4.87a}$$

$$m_1 = m_{11} + m_{12}. \tag{4.87b}$$

The first index indicates whether it is the slope before (0) or after (1) the breaking point and the second index whether it is the first (1) or second (2) INIC. The signal acquisition stage has the purpose to measure the signals of the chaotic oscillator and disturb its dynamics as little as possible. Therefore, unity gain circuits (OP_5 and

OP_6), inverting amplifier (OP_7), and an instrumentation amplifier for differential signal acquisition (INA126P) are used.

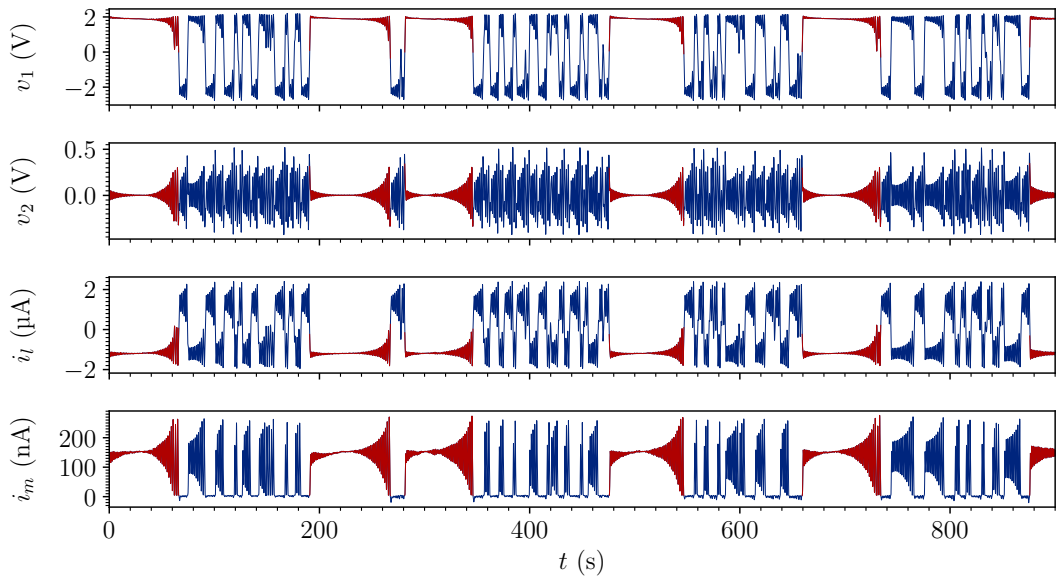

Fig. 4.42: Experimental results, obtained from the equivalent circuit shown in Fig. 4.41 (please refer to A.4 for further information about the used parameter of the circuit). The TSS episodes are marked red. In addition, to the basic state variables, the current through the DBMD is depicted as i_m.

In Fig. 4.42, the experimental results from the equivalent circuit shown in Fig. 4.41 are depicted.

Besides the basic state variables (v_1, v_2 and i_l), the current through the memristive device i_m is depicted. Again, the TSSs are highlighted in red. As obtained by numerical simulations, the experiment shows the same change in dynamics, which is a traverse of the funnel as shown by bifurcation analysis.

Additionally to the magnitudes of the signals, the time it takes to traverse a TSS is approximately 60 s, which fits well with the results obtained by simulation (see Fig. 4.35 for comparison).

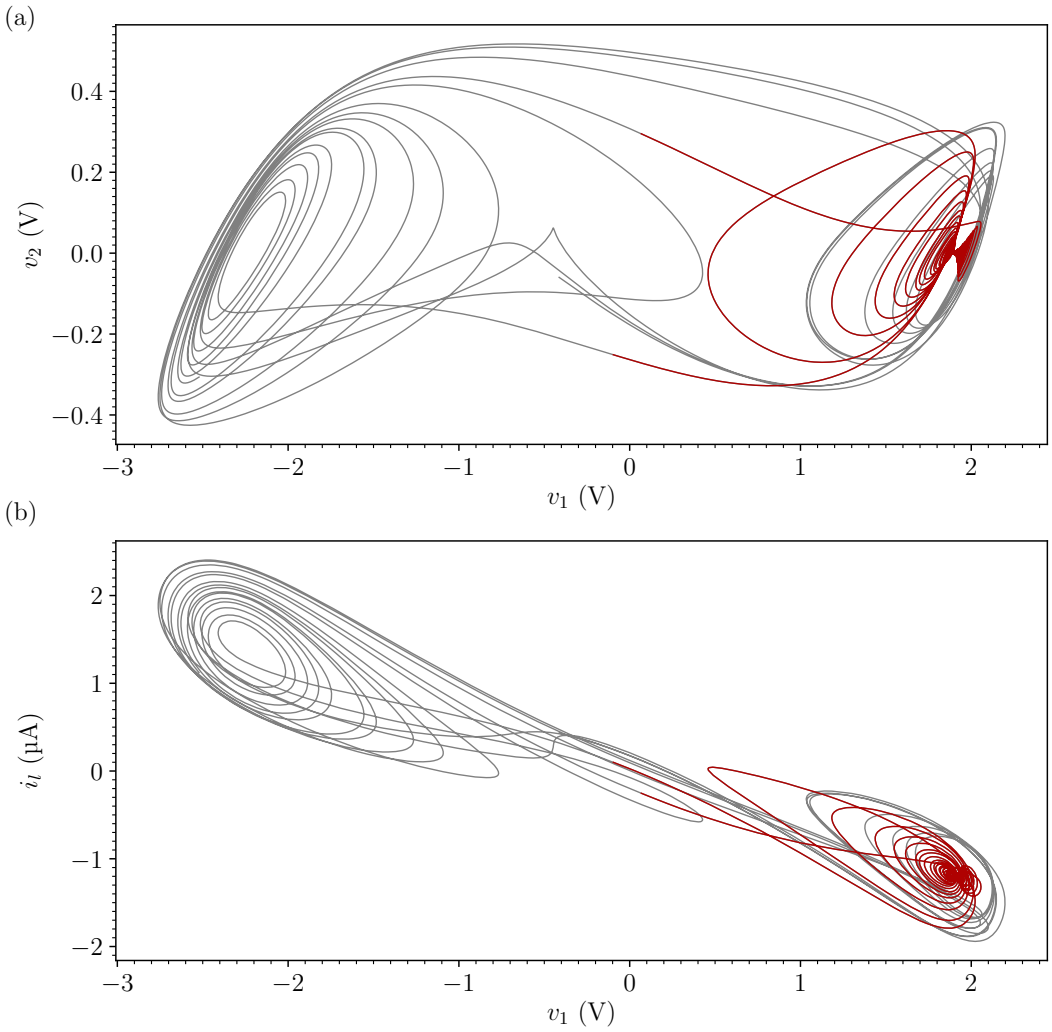

Fig. 4.43: Experimental results of Chua's system with a DBMD. (a) and (b) show the (v_1, v_2) and (v_1, i_l) projections of the phase space. The TSS is highlighted red. Again, the funnel and the strange attractor are visible.

The new part in the attractor is located in the same region as shown by simulations, as can be seen in Fig. 4.43. The chaotic oscillations and TSS are depicted grey and red, respectively. Together with Fig. 4.42, the (v_1, v_2) and (v_1, i_l) projections of the phase space show a good fit of the numerical and experimental results.

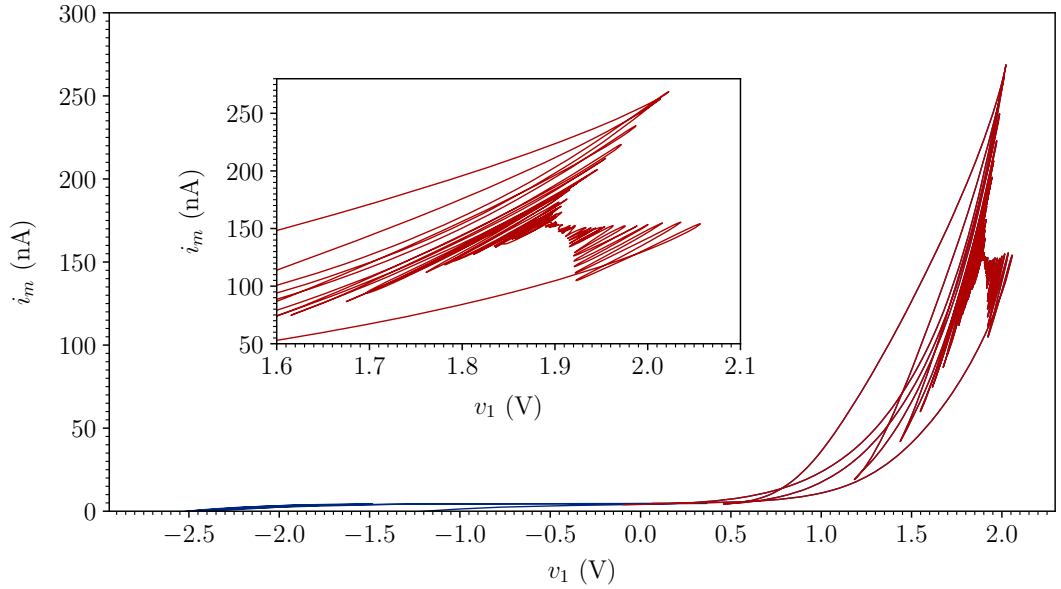

Fig. 4.44: Current through the DBMD during chaotic oscillations (blue) and a TSS (red). The inset shows a close up of the traverse of the funnel. The change in resistance is visible as varying currents for constant voltage values.

Unfortunately, a measurement of the ion distribution inside the DBMD as well as the voltages of the interfaces was not possible during the experiment.
Nonetheless, to examine the state change of the DBMD the resulting current during chaotic oscillations and therefore varying voltages can be measured. This is depicted in Fig. 4.44. The red part in the diagram refers to TSS between 475 s and 545 s. The traverse of the TSS is visible as a quenching in the diagram as well as the state change. Considering the same voltages, the resulting current through the DBMD is not constant but changes with time.

5 Conclusion

The brain differs from modern silicon-based computers in many ways. These include not only the structure of information processing, but also the unification of binary and analogue mechanisms. Certainly, the performance of today's artificial neural systems is already impressive, but it is still not fully known how exactly the human brain achieves its superiority. It appears, however, that the interwoven structure of morphology and dynamics makes a decisive contribution. Taking this as the inspiration, individual aspects, such as delay, chaos, and time varying networks, that are presumably important for cognitive performance were examined in more detail within the framework of neuromorphic engineering.

In the course of this work a spiking and adapting tactile sensory unit was presented. The core of this unit is built by the PiezoFET, which is an acronym for a piezoelectrically augmented MOSFET. Located in the gate stack of this device is a piezoelectric material, which translates mechanical stress into voltages. As a result, the gate voltage changes in response to a mechanical deformation of the transistor. The piezoelectric material used is AlScN, although other piezoelectric materials could be used as well, as for example PVDF-TrFE. Nonetheless, an advantage of AlScN over PVDF-TrFE is its CMOS compatibility and the omission of usually necessary forming steps in PVDF-TrFE based devices.

The PiezoFET was embedded in a relaxation type oscillator. Nevertheless, the working point of the circuit allows an interpretation as a leaky integrate and fire neuron as well. This circuit, which is used to translate the current response of the device into a series of pulses, is based on the positive feedback connection of a npn and pnp bipolar junction transistor.

All in all, the sensory unit is able to convert applied forces to a series of pulses, based on the change of the gate voltage of the PiezoFET due to the piezoelectric effect. These

pulses are correlated to the magnitude and duration of the applied force in terms of frequency. Furthermore, the sensory unit adapts to the applied force with regard to the frequency of the oscillator, a mechanism which is presumably based on the leakage current that depolarises the piezoelectric layer.
The presented results are based on simulations as well as experiments. The experimental set-up is based on a cantilever, on which the PiezoFET is located and a PCB with the integrate and fire circuit to generate the voltage pulses. The experimental set-up allows the application of forces in both directions by exploiting a magnetic coupling based on a constant magnetic field of a permanent magnet and the controllable magnetic field of an electric coil with an iron core.
Besides this sensory unit, a system consisting of a relaxation type oscillator with a delayed pulsatile feedback was investigated. Due to the design of the input terminal, the oscillator has a PRC with a steep negative slope. This forms the basis for observing a series of jittering bifurcations, which mark the transition from a regular spiking regime to a regime with multiple stable solutions regarding the pulse pattern of the oscillator.
In this jittering regimes, the number of existing stable solutions increases exponentially with an increase in the time delay. It is possible to switch between these stable solutions, due to the manipulation of single ISIs. Both of these phenomena, this is the observation of jittering bifurcations and the switching between them, were observed experimentally utilising microcontrollers and a FPGA for real time delay adjustments.
In the brain, the basis for temporal delays is the transmission of information via axons and the transformation of electrical to chemical signals and back again. This illustrates the fundamental influence of structure on the dynamics of neuronal systems once more. However, the structure is not rigid and not fixed from the beginning, but develops and changes over time. The goal of mapping the development of neural structures in hardware has led to initial considerations and experiments, in which the dynamics of oscillators have changed the structure of a physical substrate. One of these was a colloid of DMSO and ZnO, in which a change in network measures was caused by the dynamics of connected oscillators. This first approach was further developed, so that a dynamic and short-term synchronisation of oscillators could be demonstrated. This is due to the build-up and degradation of metallic filaments within a solution consisting of DMSO and Zinc Acetate.

Interestingly, there was not only a sole synchronisation and desynchronisation of the oscillators, but also a phase with high variability in the ISIs, as well as a phase of cluster synchronisation, in which two oscillators synchronise, but the third does not.
Inspired by chaotic dynamics that can occur in complex networks, the last part of the work investigates a chaotic oscillator that has been extended with a memory element. The model system, which provides intrinsic and tunable chaotic dynamics, is Chua's Oscillator. This system offers several advantages, such as the good adjustability of the period of the underlying oscillations, a robust experimental realisation and a well understood mathematical model. Especially the latter is important, so that the newly added dynamics can be distinguished from the dynamics of the base system.
Furthermore, a memristive device serves as a memory element. The device used is based on an interface-based switching mechanism and provides an analogue type of resistance change in response to an applied voltage. In the system expanded in this way, additional dynamics are observable. They are characterised as a strong reduction of the oscillation amplitudes. By modelling the entire system, it could be shown, that these TSSs can be explained by a bifurcation without parameters. Although the oscillations vanish, the state of the memristive element continues to change due to a constantly applied voltage. This drives the change in the state of the DBMD, which leads to a renewed increase in the magnitude of the oscillations. The different time durations required to reduce or increase the resistance of the DBMD lead to a slow-fast dynamic behind the TSS.
All in all, certain aspects of neuronal systems such as transmission delay, sensory coding, complex dynamics, and network development were used as an inspiration for the design of experiments and systems within the framework of neuromorphic engineering and the utilization of oscillator circuits. In these systems interesting dynamics such as the switching between stable pulse patterns, transient silent states and frequency adaptation in a sensory unit are observable as well as structural changes in response to oscillatory signals.
The phenomena observed might encourage further research. For example, a question which might arise from the concept of the touch sensor is, if an integration of many sensory units in a system for the detection of static and dynamic forces is feasible. Additionally, it would certainly be interesting to connect the individual sensory units and to be able to achieve pre-processing through the interaction of these oscillators

and the adaptation of the single unit. This might be beneficial for the amount of data to be transmitted and the associated reduction of the necessary capacity for data transmission and processing in the following.
Regarding the temporal delay and its influence on the occurrences of stable pulse patterns, it might be worthwhile to investigate the storage possibilities of this system for external inputs as observable patterns. The rich dynamics which can be observed already by a single oscillator with time delay feedback could serve as a basis for possible applications regarding the storage of an input which is temporally correlated to the phase of the oscillator as well as its processing.
With respect to time varying network formation, the question arises, if it is possible to use the dynamic formation of connections between individual structures not only to create functionality but also to increase the system performance. Maybe this would also allow the dynamic connection and disconnection of structures which are needed for the respective tasks. Thus, only the necessary structures would participate in the information processing. In addition, the functionality of the entire system could constantly be adapted to changes in the environment, which might result in an increased performance. Furthermore, a control of the formation of new connections as well as the pruning of old connections might be promising regarding the development of a self-organised electrical circuit with a certain set of parameters. In this case, the variability of the connection strength and hence of the network topology could be an interesting approach to limit the parameter space, although the individual dynamic units are rigid in their properties.
Never before has more been known about the human brain than today, and yet it remains exciting which future discoveries and phenomena can be used for the further development of current technical systems.

Appendices

A Parameters

A.1 Hodgkin-Huxley membrane model

The values of the parameters used in chapter 2.2.1 to simulate the membrane voltage, ion conduction and ion currents are listed in table A.1. The values are from Izhikevich (2006).[53] The solution was obtained by forward integration with a stepsize of 1 ms. The equations for $\alpha_i(v)$ and $\beta_i(v)$ which are used for the description of the gating variable are shown in (A.1a) - (A.1f). For more information about the used model, the reader can refer to Izhikevich (2006).[53]

Parameter	Value
C	$1\,\mu\mathrm{F\,m^{-2}}$
g_{Na}	$120\,\mathrm{mS\,cm^{-2}}$
g_{K}	$36\,\mathrm{mS\,cm^{-2}}$
g_{l}	$0.3\,\mathrm{mS\,cm^{-2}}$
V_{Na}	$120\,\mathrm{mV}$
V_{K}	$-12\,\mathrm{mV}$
V_{l}	$10.6\,\mathrm{mV}$

Table A.1: Parameters used for Hodgkin-Huxley model. Values from Izhikevich (2006)[53]

$$\alpha_m(v) = 0.1\frac{25-v}{e^{\left(\frac{25-v}{10}\right)}-1} \tag{A.1a}$$

$$\beta_m(v) = 4e^{\left(-\frac{v}{18}\right)} \tag{A.1b}$$

$$\alpha_h(v) = 0.07e^{\left(-\frac{v}{20}\right)} \tag{A.1c}$$

$$\beta_h(v) = \frac{1}{e^{\left(\frac{30-v}{10}\right)}+1} \tag{A.1d}$$

$$\alpha_n(v) = 0.01\frac{10-v}{e^{\left(\frac{10-v}{10}\right)}-1} \tag{A.1e}$$

$$\beta_n(v) = 0.125e^{\left(-\frac{v}{80}\right)}. \tag{A.1f}$$

A.2 Curve fit spike timing depend plasticity

The data from Bi and Poo (1998)[91] were fitted using a least square algorithm to the following equations:

$$f(t^{post} - t^{pre}) = \alpha e^{-\frac{t^{post}-t^{pre}}{\beta}} \tag{A.2}$$

for values of $t^{post} - t^{pre} > 0$, and:

$$f(t^{post} - t^{pre}) = -\gamma e^{-\frac{t^{post}-t^{pre}}{\delta}} \tag{A.3}$$

for values of $t^{post} - t^{pre} < 0$. The parameters can be found in table A.2.

Parameter	Value
α	78.135
β	16.818
γ	27.18
δ	33.635

Table A.2: Parameters used to fit the changes in the evoked EPSC, which were recorded by Bi and Poo (1998)[91] rounded to three decimal places.

A.3 Curve fit phase response curve

A sixth order polynomial of the following form:

$$f(x) = \alpha x^6 + \beta x^5 + \gamma x^4 + \delta x^3 + \epsilon x^2 + \zeta x + \eta \tag{A.4}$$

was used to fit the data from Netoff *et al.* 2005[124] by a least square algorithm.
Prior to curve fitting the data are normalized by the specified period, followed by calculating the PRC using equation (3.9). The used values are listed in table A.3.

Parameter	Value
α	14.601
β	−41.310
γ	44.639
δ	−24.171
ϵ	6.753
ζ	−0.518
η	−0.005

Table A.3: Curve fit parameters for PRC

A.4 Parameters Chua's Circuit

Variable	Value	Variable	Value
R	$1.6\,\mathrm{M\Omega}$	R_9	$22\,\mathrm{M\Omega}$
R_1	$1\,\mathrm{k\Omega}$	R_G	$100\,\mathrm{k\Omega}$
R_2	$100\,\Omega$	R_m	$1\,\mathrm{k\Omega}$
R_3	$10\,\mathrm{k\Omega}$	R_{10}	$3.3\,\mathrm{M\Omega}$
R_4	$1.82\,\mathrm{M\Omega}$	R_{11}	$100\,\Omega$
R_5	$250\,\mathrm{k\Omega}$	R_{12}	$100\,\mathrm{k\Omega}$
R_6	$250\,\mathrm{k\Omega}$	C	$470\,\mathrm{nF}$
R_7	$2.5\,\mathrm{M\Omega}$	C_1	$47\,\mathrm{nF}$
R_8	$22\,\mathrm{M\Omega}$	C_2	$470\,\mathrm{nF}$

Table A.4: Parameters of Chua's Circuit.

Variable	Value	Variable	Value
L	$85\,540\,\mathrm{H}$	φ_{a0}	26.305
m_0	$-3.545 \cdot 10^{-7}\,\mathrm{A\,V^{-1}}$	φ_{ar}	30.173
m_1	$-7.03 \cdot 10^{-7}\,\mathrm{A\,V^{-1}}$	ω_0	$1 \cdot 10^{-4}$
B_P	1.957	φ_{s0}	27.079
C_e	$1.74 \cdot 10^{-13}\,\mathrm{F}$	φ_{s1}	34.815
C_t	$2.07 \cdot 10^{-13}\,\mathrm{F}$	n_0	2.9
V_c	$1 \cdot 10^{-4}\,\mathrm{V}$	n_1	4.1
V_e	$0.323\,\mathrm{V}$	R_{e0}	$200\,\mathrm{k\Omega}$
I_s	$1.081\,\mathrm{A}$	R_{e1}	$510\,\mathrm{k\Omega}$
I_t	$4.326\,\mathrm{A}$	φ_{t0}	108.314
α_f	-1.25	V_ϑ	$0.026\,\mathrm{V}$
α_s	3.77	p	12
$\hat{Z}$	$0.64\,\mathrm{THz}$	α_{t0}	1.812
φ_{a1}	36.749	α_{t1}	2.026

Table A.5: Parameters and constants used for the simulation of Chua's Circuit, rounded on three digits.

Equations which describe the ion motions inside the DBMD as well as the increase and decrease of the interfacial energy barrier heights:

$$\omega(z) = (1 - 2\omega_0)\left[1 - (2z - 1)^p\right] + \omega_0 \tag{A.5a}$$

$$\varphi_a(v_1, z) = \sigma(v_1)\left[\varphi_{a1} + z\left(\varphi_{a0} - \varphi_{a1}\right) - \varphi_{ar}\right] + \varphi_{ar} \tag{A.5b}$$

$$v_r(v_1, v_s, z) = \sigma(-v_1)v_s(1 - z) \tag{A.5c}$$

$$\varphi_s(z) = \varphi_{s0} + z\left(\varphi_1 - \varphi_0\right) \tag{A.5d}$$

$$n(z) = n_0 + z(n_1 - n_0) \tag{A.5e}$$

$$R_e(z) = R_{e0} + z\left(R_{e1} - R_{e0}\right) \tag{A.5f}$$

$$i_t(v_t, z) = \frac{I_t g(-v_t, z) - g(v_t, z)}{\alpha_t(z)^2} \tag{A.5g}$$

$$g(v_t, z) = \varphi_t(v_t) e^{-\alpha_t(z)\sqrt{\varphi_t(v_t)}} \tag{A.5h}$$

$$\varphi_t(v_t) = \varphi_{t0} + \frac{v_t}{2V_\vartheta} \tag{A.5i}$$

$$\alpha_t(z) = \alpha_{t0} + z\left(\alpha_{t1} - \alpha_{t0}\right) \tag{A.5j}$$

$$\sigma(x) = \begin{cases} 1 & \text{for } x > 0 \\ 0 & \text{otherwise .} \end{cases} \tag{A.5k}$$

A.5 Parameters used for the simulation of a basic relaxation oscillator

The circuit was simulated in LTSpice. The circuit values shown in table A.6 were used.

Parameter	Value
V^+	10 V
$PUJT$	2N6027, ON Semiconductor
C	0.1 µF
R_1	500 kΩ
R_2	1 kΩ
R_3	100 kΩ
R_4	100 kΩ

Table A.6: Parameters used for simulation of a basic relaxation type oscillator based on a PUJT

A.6 Parameters touch sensor

Variable	Value	Variable	Value
I_s	1.216 pA	R_1	9.58 MΩ
V_{GS}	1.4 V	R_2	100 MΩ
m	5.646	R_3	100 MΩ
V_T	25 mV	R_l	500 MΩ
g_{31}	0.039 V m N^{-1}	R_k	10 kΩ
h_{AlScN}	500 nm	C_1	680 pF
L	7.7 mm	C_2	150 pF
a	2 mm	V_{th}	3.213 V
b	475 µm	B_1	0.163 T
d	1.8 mm	A_1	$2.827 \cdot 10^{-5}$ m
τ_{AlScN}	8.69 s	A_2	$2.25 \cdot 10^{-3}$ m
V_s	5 V		

Table A.7: Parameters and values used for the simulation and experimental set-up of the touch sensor.

A.7 Simulation phase response curve and charge response curve

The parameters for visualizing the concept of a PRC and QRC in section 4.2.1 are listed in table A.8.

Parameter	Value
V^+	7 V
V_{th}	5 V
V_r	0.7 V
C	0.1 µF
R_1	500 kΩ
R_2	5 MΩ
τ	10 ms

Table A.8: Parameters used for simulation of charging as well as for PRC and QRC calculations

A.8 Parameters delay circuit

Variable	Value	Variable	Value
R_1	31.6 kΩ	C_1	1.5 nF
R_2	11.8 MΩ	C_2	4.7 nF
R_3	5 MΩ	Diode	1N4148
R_4	2 MΩ	T	2N3904
R_5	500 Ω	M	2N7000
R_6	68 kΩ	PUJT	2N6027
R_7	200 kΩ	FPGA	Cyclon V

Table A.9: Parameters of the components used for the delayed feedback experiment.

The FPGA was programmed using Quartus Prime from Intel and VHDL. The code can be found in D.

A.9 Parameters of driven exponential integrate relaxation oscillator

Parameters used for the driven exponential integrate relaxation oscillator.

Variable	Value	Variable	Value
R_1	470 kΩ	C_1	1.4 nF
R_2	20 MΩ	C_2	600 pF
R_3	20 MΩ	T_1	BC547A
R_4	440 kΩ	T_2	BC547A
R_5	1 kΩ	T_3	BC557A
R_6	100 kΩ	T_4	BC557A
R_7	100 kΩ	T_5	BC547A

Table A.10: Parameters of the exponential integrate and fire oscillator

B Mathematical derivations

B.1 Derivation of a charge response curve

In the following the derivation of a QRC is repeated with additional steps. From Kirchhoffs current law follows:

$$i_1 = i_c + i_2. \tag{B.1}$$

Thus:

$$i_c = \frac{V^+ - V_c}{R_1} - \frac{V_c}{R_2}. \tag{B.2}$$

Because $Q = CV$:

$$\frac{dQ_c}{dt} = \frac{CR_2V^+ - Q_cR_1 - Q_cR_2}{R_1R_2C}. \tag{B.3}$$

This equation can be solved by integration:

$$\int_0^{Q_c(t)} \frac{1}{Q_c(R_1 + R_2) - CR_2V^+} dQ_c = \int_0^t -\frac{1}{R_1R_2C} dt. \tag{B.4}$$

It is:

$$\int \frac{1}{ax-b}dx = \frac{\ln(ax-b)}{a} + constant. \tag{B.5}$$

Therefore, equation (B.4) solves to

$$\frac{\ln\left(Q_c(t)(R_1+R_2) - R_2CV^+\right)}{R_1+R_2} - \frac{\ln\left(-R_2CV^+\right)}{R_1+R_2} = -\frac{t}{R_1R_2C}. \tag{B.6}$$

This is:

$$\ln\left(\frac{Q_c(t)(R_1+R_2) - R_2CV^+}{-R_2CV^+}\right) = -\frac{t\,(R_1+R_2)}{R_1R_2C}. \tag{B.7}$$

By resolving the logarithm follows:

$$V_c(t)\,(R_1+R_2) = R_2V^+\left(1 - e^{-\frac{t(R_1+R_2}{R_1R_2C}}\right). \tag{B.8}$$

With eta as the ratio between leakage resistance and series resistance, this is $\eta = \frac{R_2}{R_1+R2}$, follows:

$$V_c(t) = \eta V^+\left(1 - e^{-\frac{t}{\eta R_1C}}\right). \tag{B.9}$$

The time t can be expressed as:

$$t = -\eta R_1C\ln\left(\frac{\eta V^+ - V_c}{\eta V^+}\right). \tag{B.10}$$

As shown in Fig. 4.12, the interesting time points during a charging period lead to:

$$t^p - t^r + t^{th} - t^* = T'(\phi). \tag{B.11}$$

With the definition of the PRC:

$$P(\phi) = 1 - \frac{T'(\phi)}{T_0}, \tag{B.12}$$

the duration of the changed period $T'(\phi)$ can be calculated as:

$$T'(\phi) = T_0 \left(1 - P(\phi)\right). \tag{B.13}$$

The intrinsic period can be expressed with the same time points used in equation (B.11). This is:

$$T_0 = t^{th} - t^r. \tag{B.14}$$

By inserting (B.14) in (B.13) the influenced period in dependence on the time points from Fig. 4.12 reads to:

$$T'(\phi) = t^{th} - t^{th} P(\phi) - t^r + t^r P(\phi). \tag{B.15}$$

Inserting (B.15) in (B.11) leads to:

$$t^* = t^p + t^{th} P(\phi) - t^r P(\phi). \tag{B.16}$$

From the equation (B.10) the time needed for the capacitor to charge to a certain voltage V_c can be calculated. Together with equation (B.16) follows for the time t^*:

$$t^* = -\eta RC \ln\left(\frac{\eta V^+ - V_p}{\eta V^+}\right) + P(\phi)\eta RC\left(\ln\left(\frac{\eta V^+ - V_r}{\eta V^+}\right) - \ln\left(\frac{\eta V^+ - V_{th}}{\eta V^+}\right)\right). \tag{B.17}$$

By expansion this is:

$$\begin{aligned} t^* = &- \eta RC \ln\left(\frac{\eta V^+ - V_p}{\eta V^+}\right) \\ &+ P(\phi)\eta RC\left(\ln\left(\eta V^+ - V_r\right) - \ln\left(\eta V^+\right) - \left(\ln\left(\eta V^+ - V_{th}\right) - \ln\left(\eta V^+\right)\right)\right), \end{aligned} \tag{B.18}$$

and thus:

$$t^* = P(\phi)\eta RC \ln\left(\frac{\eta V^+ - V_r}{\eta V^+ - V_{th}}\right) - \eta RC \ln\left(\frac{\eta V^+ - V_p}{\eta V^+}\right). \tag{B.19}$$

From the definition of t^* the corresponding voltage V_* can be expressed as:

$$V_* = \eta V^+\left(1 - e^{\ln\left(\frac{\eta V^+ - V_p}{\eta V^+}\right) - P(\phi)\ln\left(\frac{\eta V^+ - V_r}{\eta V^+ - V_{th}}\right)}\right). \tag{B.20}$$

Alternatively, instead of calculating the new voltage by V_p, one can express the actual voltage by its phase. Because:

$$\phi = \frac{t^p - t^r}{t^{th} - t^r} \tag{B.21}$$

one can write:

$$\phi = \frac{\ln\left(\frac{\eta V^+ - V_p}{\eta V^+}\right) - \ln\left(\frac{\eta V^+ - V_r}{\eta V^+}\right)}{\ln\left(\frac{\eta V^+ - V_{th}}{\eta V^+}\right) - \ln\left(\frac{\eta V^+ - V_r}{\eta V^+}\right)}. \tag{B.22}$$

By expanding (B.22) it follows:

$$\begin{aligned}\ln\left(\frac{\eta V^+ - V_p}{\eta V^+}\right) =& \phi\left(\ln\left(\eta V^+ - V_{th}\right) - \ln\left(\eta V^+\right) - \ln\left(\eta V^+ - V_r\right) + \ln\left(\eta V^+\right)\right) \\ &+ \ln\left(\frac{\eta V^+ - V_r}{\eta V^+}\right).\end{aligned} \tag{B.23}$$

Therefore,

$$e^{\left(\phi \ln\left(\frac{\eta V^+ - V_{th}}{\eta V^+ - V_r}\right) + \ln\left(\frac{\eta V^+ - V_r}{\eta V^+}\right)\right)} = \frac{\eta V^+ - V_p}{\eta V^+}, \tag{B.24}$$

which leads to an expression for V_p as a function of the phase:

$$V_p = \eta V^+ \left(1 - e^{\left(\phi \ln\left(\frac{\eta V^+ - V_{th}}{\eta V^+ - V_r}\right) + \ln\left(\frac{\eta V^+ - V_r}{\eta V^+}\right)\right)}\right). \tag{B.25}$$

By defining the QRC $\Delta Q(\phi)$ as the difference between the actual charge on the capacitor $Q_c(\phi)$ and the charge Q^* the capacitor is transferred to depending on the phase ϕ:

$$\Delta Q(\phi) = Q_* - Q_c(\phi) \tag{B.26}$$

it follows from (B.20) and (B.25), with $Q = VC$:

$$\frac{\Delta Q(\phi)}{C} = \eta V^+ \left(1 - e^{\left(\ln\left(\frac{\eta V^+ - \eta V^+ \left(1 - e^{\left(\phi \ln\left(\frac{\eta V^+ - V_{th}}{\eta V^+ - V_r} \right) + \ln\left(\frac{\eta V^+ - V_r}{\eta V^+} \right) \right)} \right)}{\eta V^+} \right) - P(\phi) \ln\left(\frac{\eta V^+ - V_r}{\eta V^+ - V_{th}} \right) \right)} \right) - \eta V^+ \left(1 - e^{\left(\phi \ln\left(\frac{\eta V^+ - V_{th}}{\eta V^+ - V_r} \right) + \ln\left(\frac{\eta V^+ - V_r}{\eta V^+} \right) \right)} \right). \tag{B.27}$$

This equation can be reduced. For the first part of the exponent of the first exponential function in equation (B.27) it is:

$$\begin{aligned} \ln\left(\frac{\eta V^+ - \eta V^+ \left(1 - e^{\left(\phi \ln\left(\frac{\eta V^+ - V_{th}}{\eta V^+ - V_r} \right) + \ln\left(\frac{\eta V^+ - V_r}{\eta V^+} \right) \right)} \right)}{\eta V^+} \right) &= \ln\left(e^{\left(\phi \ln\left(\frac{\eta V^+ - V_{th}}{\eta V^+ - V_r} \right) \right) + \ln\left(\frac{\eta V^+ - V_r}{\eta V^+} \right)} \right) \\ &= \phi \ln\left(\frac{\eta V^+ - V_{th}}{\eta V^+ - V_r} \right) + \ln\left(\frac{\eta V^+ - V_r}{\eta V^+} \right). \end{aligned} \tag{B.28}$$

Thus, the complete exponent of the first exponential function reads to:

$$\phi \ln\left(\frac{\eta V^+ - V_{th}}{\eta V^+ - V_r} \right) - P(\phi) \ln\left(\frac{\eta V^+ - V_r}{\eta V^+ - V_{th}} \right) + \ln\left(\frac{\eta V^+ - V_r}{\eta V^+} \right). \tag{B.29}$$

This can be expanded, leading to:

$$\begin{aligned}(\phi + P(\phi))\left(\ln\left(\eta V^+ - V_{th}\right) - \ln\left(\eta V^+ - V_r\right)\right) + \ln\left(\frac{\eta V^+ - V_r}{\eta V^+}\right) \\ = (\phi + P(\phi))\ln\left(\frac{\eta V^+ - V_{th}}{\eta V^+ - V_r}\right) + \ln\left(\frac{\eta V^+ - V_r}{\eta V^+}\right).\end{aligned} \tag{B.30}$$

By rewriting equation (B.27) with equation (B.30), the function for the charge reads to:

$$\Delta Q(\phi) = C\eta V^+\left(e^{\phi\ln\left(\frac{\eta V^+ - V_{th}}{\eta V^+ - V_r}\right)+\ln\left(\frac{\eta V^+ - V_r}{\eta V^+}\right)} - e^{(\phi+P(\phi))\ln\left(\frac{\eta V^+ - V_{th}}{\eta V^+ - V_r}\right)+\ln\left(\frac{\eta V^+ - V_r}{\eta V^+}\right)}\right). \tag{B.31}$$

Because the logarithm is defined as $a^x = b^{x\log_b(a)}$ equation (B.31) equals:

$$\frac{\Delta Q(\phi)}{\eta C V^+} = \left(\frac{\eta V^+ - V_r}{\eta V^+}\right)\left(\frac{\eta V^+ - V_{th}}{\eta V^+ - V_r}\right)^{\phi} - \left(\frac{\eta V^+ - V_r}{\eta V^+}\right)\left(\frac{\eta V^+ - V_{th}}{\eta V^+ - V_r}\right)^{\phi+P(\phi)}. \tag{B.32}$$

As a result, the QRC can be written in a more compact form as follows:

$$\Delta Q(\phi) = C\left(\eta V^+ - V_r\right)\left(k^{\phi} - k^{\phi+P(\phi)}\right) \tag{B.33}$$

with

$$k = \frac{\eta V^+ - V_{th}}{\eta V^+ - V_r}. \tag{B.34}$$

B.2 Calculation of spike times based on data

The calculation of the times at which the oscillator fires is essentially based on determining the zero points of the cathode voltage V_K shifted by a threshold value V_{th}. Sampling the time-continuous cathode signal produces a time-discrete measurement signal. This is shifted by a fixed threshold value on the y-axis. After using the sign function, the cathode voltage equals 1 during the discharge and -1 in all other time points. Thus, the zero crossing can be easily calculated numerically using $V_K^0 = V_K[i+1] - V_K[i]$. It is $V_K^0 = 2$ at the positive crossing, which refers to the increase of the discharge pulse, and $V_K^0 = -2$ at the negative crossing which is the decrease of the discharge pulse. From this, the time points can be determined easily. The error in time is mostly based on the sampling rate and rise time of the discharge pulse at the cathode, if the onset of the pulse is considered, which is normally the case. The threshold value should be selected carefully in order to diminish the possible influence of noise.

C Printed circuit boards

C.1 Touch sensor

The PCB used to conduct the experiments on the touch sensor is depicted in Fig. C.1. The prolonged metal contacts on the left hand side of the board are used to connect the PCB to the PiezoFET via wire bonding.

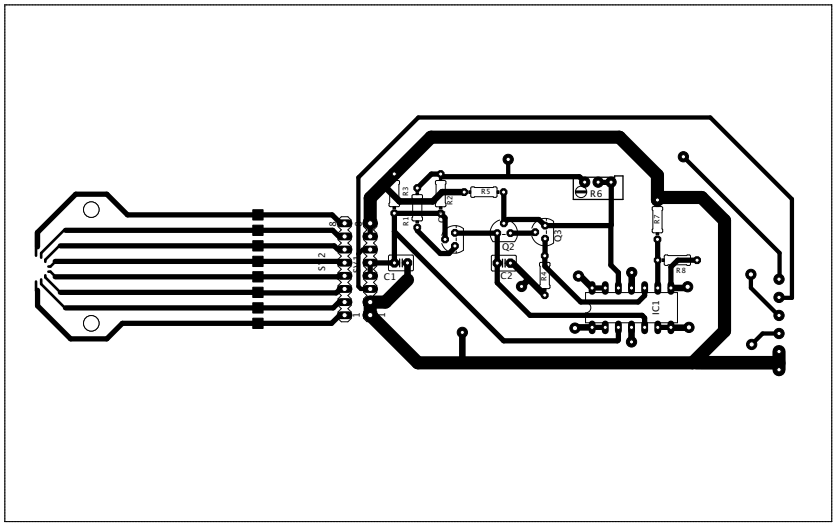

Fig. C.1: The picture shows the tracks and positions of the components of the PCB, which was used for the touch sensor. The GND-Plate is faded out for clarity. The missing ground connection of C_2 and R_4 was established using an isolated wire.

C.2 Chua's Oscillator

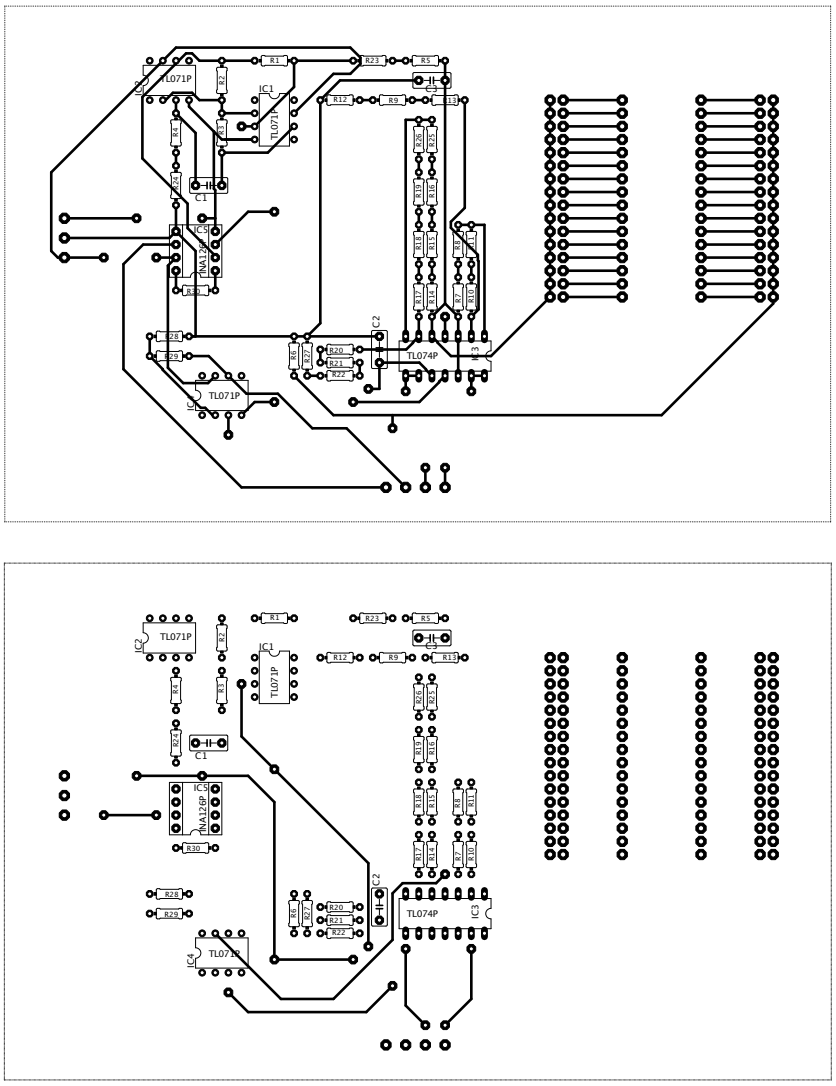

Fig. C.2: The picture shows the tracks and positions of the components of the PCB, which was used for the Chua Oscillator including DBMD. The GND-Plate is faded out for clarity. The pin row on the right side of the board was used to mount a zero force test socket for dual inline packages.

C.3 Custom circuit for network measurements

C.3.1 Schematic diagram of the circuit for network measurements

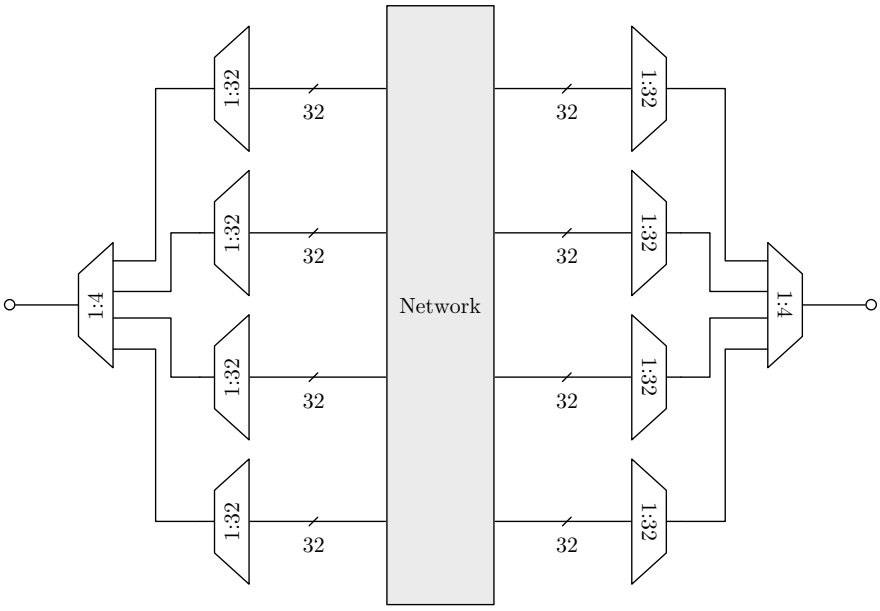

Fig. C.3: Block diagram of the circuit used to measure the network. Each multiplexer is controlled by serial peripheral interface and controlled by an microcontroller which converts the commands send by PC.

Fig. C.3 shows the structure of the system for choosing any node of a network. It consists of a series of multiplexers controlled by a microcontroller via a serial peripheral interface (SPI). The structure shown allows the analysis of a network with a maximum of 128 nodes, where any pair of nodes can be selected by the multiplexers. The measurement of the resistance can be done by using an external device connected to the input and output of the system.

C.3.2 Multiplexer board

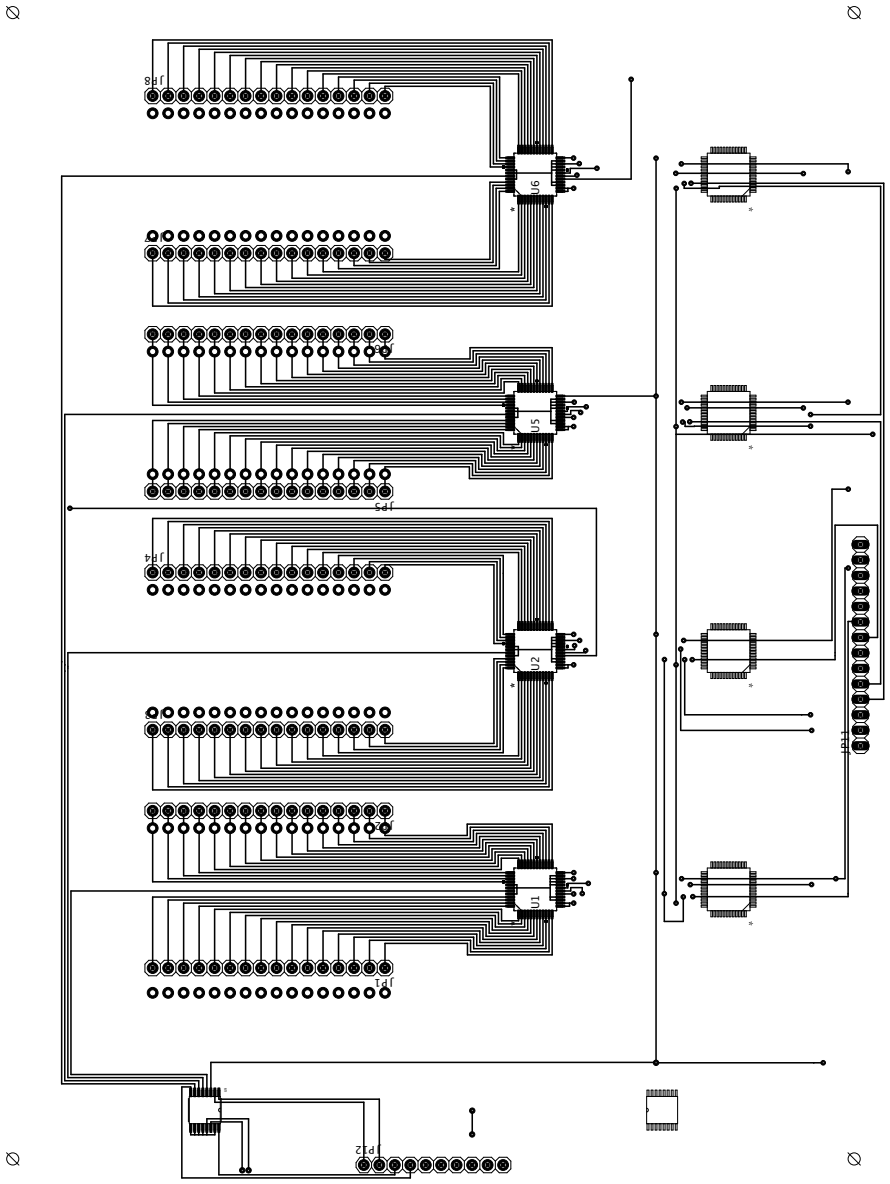

Fig. C.4: Layout of top side of the PCB used to measure the colloid network.

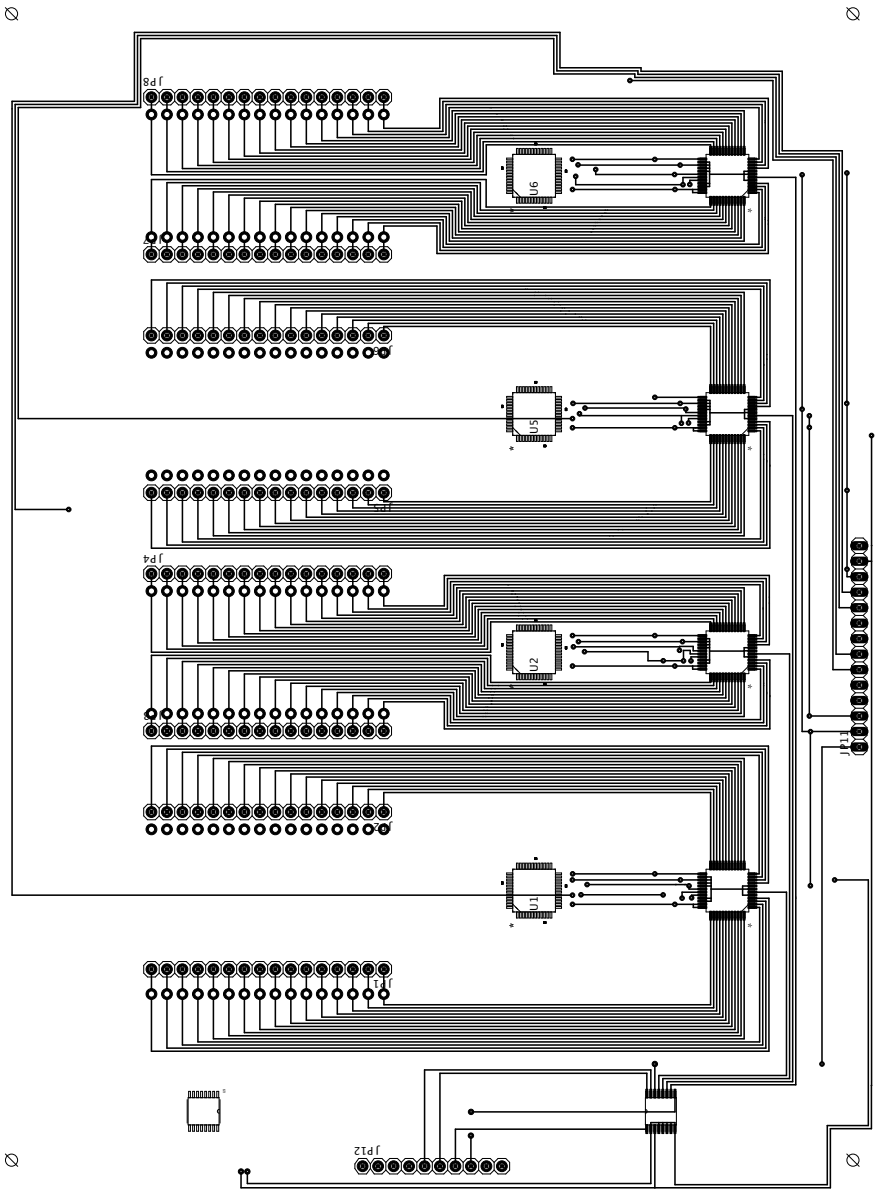

Fig. C.5: Layout of bottom side of the PCB used to measure the colloid network.

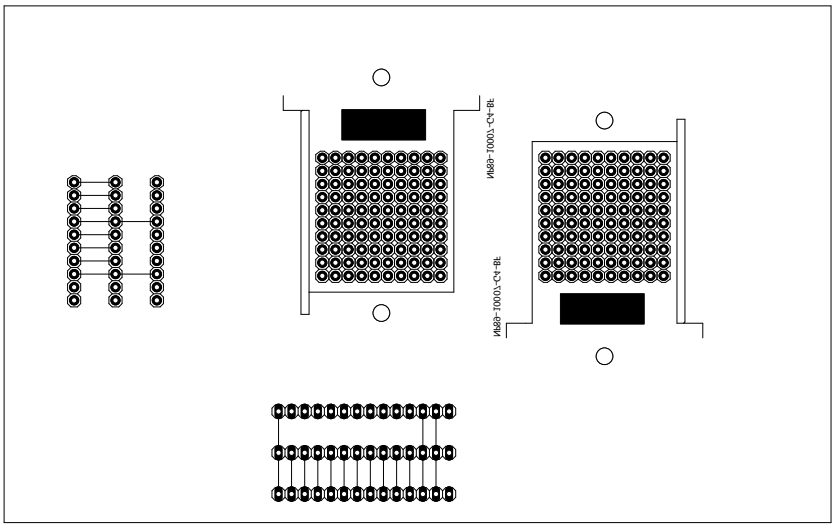

Fig. C.6: Layout of the adapter PCB used to access the contacts of the adapter on which the colloid network was applied.

C.4 Experimental set-up for experiments on time varying network

The first experiments on dynamic network structures were done exploiting an adapter which is normally used for contacting a ball grid array (BGA). For this purpose, the adapter has round contacts at regular intervals. The adapter used is a conventional product from Proto Advantage. The type is specified by the manufacturer as BGA0023. It is a 10 times 10 adapter with a pitch of 0.4 mm. The diameter of the contacts is typically 0.254 mm. The surface finishing of the adapter was created with a electroless nickel immersion gold (ENIG) process.

D Programme code delay line

D.1 Entity Ad1

```
1  library ieee;
2  use ieee.std_logic_1164.all;
3
4  entity Ad1 is
5  generic(N: integer := 50000);
6  port(
7    clock_in: in std_logic;
8    enable: in std_logic;
9    flag_out: out std_logic);
10 end;
11
12 architecture behavioral of Ad1 is
13 signal flag_temp: std_logic := '0';
14
15 begin
16 flag_out <= flag_temp;
17
18 process(clock_in, enable)
19 variable temp: integer:= 0;
20 variable count_e: integer:= 0;
21
22 begin
23 if(rising_edge(clock_in) AND
```

```
24  (enable = '1' OR count_e = 1)) then
25          count_e := 1;
26          temp := temp + 1;
27          flag_temp <= '0';
28
29          if(temp = 1) then
30                  flag_temp <= '1';
31          else
32                  flag_temp <= '0';
33          end if;
34
35          if(temp = N) then
36                  temp := 0;
37                  count_e := 0;
38          end if;
39  end if;
40  end process;
41  end behavioral;
```

D.2 Entity Ad2

```
1  library ieee;
2  use ieee.std_logic_1164.all;
3  use ieee.std_logic_unsigned.all;
4  use ieee.numeric_std.all;
5
6  entity Ad2 is
7  port(
8    N_con: std_logic_vector (31 downto 0);
9    clock_in: in std_logic;
10   enable: in std_logic;
11   flag_out: out std_logic;
```

```
12    count_e: out std_logic);
13  end;
14
15  architecture behavioral of Ad2 is
16  signal flag_temp: std_logic := '0';
17  signal flag_count:       std_logic := '0';
18
19  begin
20  flag_out <= flag_temp;
21  count_e <= flag_count;
22
23  process(clock_in, enable)
24  variable temp: integer := 0;
25
26  begin
27  if(rising_edge(clock_in) AND
28  (enable = '1' OR flag_count = '1')) then
29          flag_count <= '1';
30          temp := temp +1;
31
32          if(temp = N_con) then
33                  temp := 0;
34                  flag_count <= '0';
35                  flag_temp <= '1';
36          else
37                  flag_temp <= '0';
38          end if;
39  end if;
40
41  if(rising_edge(clock_in) AND
42  enable = '0' AND
43  flag_count = '0') then
44          flag_temp <= '0';
```

```
45 end if;
46 end process;
47 end behavioral;
```

D.3 Entity Ad3

```
1  library ieee;
2  use ieee.std_logic_1164.all;
3
4  entity Ad3 is
5  generic(N: integer := 25000);
6  port(
7    clock_in: in std_logic;
8    enable: in std_logic;
9    flag_out: out std_logic);
10 end;
11
12 architecture behavioral of Ad3 is
13 signal flag_temp: std_logic := '0';
14
15 begin
16 flag_out <= flag_temp;
17 process(clock_in, enable)
18 variable temp: integer:= 0;
19 variable count_e: integer:= 0;
20 begin
21 if(rising_edge(clock_in) AND (enable = '1' OR count_e = 1))
22 then
23          count_e := 1;
24          temp := temp +1;
25          flag_temp <='1';
26
```

```
27          if(temp = N) then
28                  temp := 0;
29                  count_e := 0;
30                  flag_temp <='0';
31          else
32                  flag_temp <= '1';
33          end if;
34  end if;
35
36  if(rising_edge(clock_in) AND enable = '0' AND count_e = 0) then
37                  flag_temp <= '0';
38  end if;
39  end process;
40  end behavioral;
```

D.4 Entity delayControl

```
1  library ieee;
2  use ieee.std_logic_1164.all;
3
4  entity delayControl is
5  port(
6    GPIO_0: in std_logic ;
7    GPIO_1: in std_logic ;
8    GPIO_2: in std_logic ;
9    GPIO_3: in std_logic ;
10   GPIO_4: in std_logic ;
11   GPIO_5: in std_logic ;
12   GPIO_6: in std_logic ;
13   GPIO_7: in std_logic ;
14   GPIO_8: in std_logic ;
15   GPIO_9: in std_logic ;
```

```
16    GPIO_10: in std_logic ;
17    GPIO_11: in std_logic ;
18    GPIO_12: in std_logic ;
19    GPIO_13: in std_logic ;
20    GPIO_14: in std_logic ;
21    GPIO_15: in std_logic ;
22    clock_in: in std_logic;
23    N: out std_logic_vector (15 downto 0));
24  end;
25  architecture behavioral of delayControl is
26  signal N_temp: std_logic_vector (15 downto 0) := (others => '0');
27  begin
28  N <= N_temp;
29  process(clock_in)
30  begin
31  if(rising_edge(clock_in)) then
32    N_temp (0) <= GPIO_0;
33    N_temp (1) <= GPIO_1;
34    N_temp (2) <= GPIO_2;
35    N_temp (3) <= GPIO_3;
36    N_temp (4) <= GPIO_4;
37    N_temp (5) <= GPIO_5;
38    N_temp (6) <= GPIO_6;
39    N_temp (7) <= GPIO_7;
40    N_temp (8) <= GPIO_8;
41    N_temp (9) <= GPIO_9;
42    N_temp (10) <= GPIO_10;
43    N_temp (11) <= GPIO_11;
44    N_temp (12) <= GPIO_12;
45    N_temp (13) <= GPIO_13;
46    N_temp (14) <= GPIO_14;
47    N_temp (15) <= GPIO_15;
48  end if;
```

```
49 end process;
50 end behavioral;
```

D.5 Entity convert

```
1  library ieee;
2  use ieee.std_logic_1164.all;
3  use ieee.numeric_std.all;
4
5  entity convert is
6  Port (
7    N_in: in std_logic_vector (15 downto 0);
8    N_con: out integer);
9  end convert;
10 architecture behavioral of convert is
11 signal b: integer := 0;
12 signal x: integer := 500;
13 begin
14 b <= to_integer(unsigned(N_in));
15 N_con <= (b*x);
16 end behavioral;
```

List of Figures

List of Tables

Bibliography

[1] S. Ramon y Cajal. The Croonian lecture.—La fine structure des centres nerveux. *Proceedings of the Royal Society of London*, 55(331-335):444–468, January 1894.

[2] C. Sherrington. *The Integrative Action of the Nervous System.* Yale University Press, 1906.

[3] K. Brodmann. *Vergleichende Lokalisationslehre der Grosshirnrinde in ihren Prinzipien dargestellt auf Grund des Zellenbaues.* Barth, Leipzig, 1909.

[4] J. A. De Carlos and J. Borrell. A historical reflection of the contributions of Cajal and Golgi to the foundations of neuroscience. *Brain Research Reviews*, 55(1):8–16, August 2007.

[5] D. S. Bassett and O. Sporns. Network neuroscience. *Nature Neuroscience*, 20(3):353–364, March 2017.

[6] N. Kriegeskorte and P. K. Douglas. Cognitive computational neuroscience. *Nature Neuroscience*, 21(9):1148–1160, September 2018.

[7] D. Purves, G. Augustine, D. Fitzpatrick, W. Hall, A.-S. LaMantia, J. O. McNamara, and S. M. Williams. *Neuroscience.* Sinauer Associates, Publishers, Sunderland, Mass, 3rd ed edition, 2004.

[8] E. R. Kandel, J. H. Schwartz, T. M. Jessell, S. A. Siegelbaum, and A. J. Hudspeth. *Principles of Neural Science, Fifth Edition.* McGraw Hill Professional, 2013.

[9] P. Broca. Sur le siège de la faculté du langage articulé. *Bulletins et Mémoires de la Société d'Anthropologie de Paris*, 6(1):377–393, 1865.

[10] C. Wernicke. The Symptom Complex of Aphasia. In R. S. Cohen and M. W. Wartofsky, editors, *Proceedings of the Boston Colloquium for the Philosophy of Science 1966/1968*, Boston Studies in the Philosophy of Science, pages 34–97. Springer Netherlands, Dordrecht, 1969.

[11] W. B. Scoville and B. Milner. Loss of recent memory after bilateral hippocampal lesions. *Journal of Neurology, Neurosurgery, and Psychiatry*, 20(1):11–21, February 1957.

[12] J. von Neumann. First draft of a report on the EDVAC. *IEEE Annals of the History of Computing*, 15(4):27–75, 1993.

[13] W. S. McCulloch and W. Pitts. A logical calculus of the ideas immanent in nervous activity. *The bulletin of mathematical biophysics*, 5(4):115–133, December 1943.

[14] D. O. Hebb. *The Organization of Behavior: A Neuropsychological Theory*. John Wiley & Sons, Inc., New York, 1949.

[15] M. A. Sivilotti, M. R. Emerling, and C. A. Mead. VLSI architectures for implementation of neural networks. *AIP Conference Proceedings*, 151(1):408–413, August 1986.

[16] C. Mead and M. A. Mahowald. A silicon model of early visual processing. *Neural Networks*, 1(1):91–97, January 1988.

[17] C. Mead. Neuromorphic electronic systems. *Proceedings of the IEEE*, 78(10):1629–1636, October 1990.

[18] C. Diorio, P. Hasler, B. A. Minch, and C. Mead. Floating-Gate MOS Synapse Transistors. In T. S. Lande, editor, *Neuromorphic Systems Engineering: Neural*

Networks in Silicon, The Springer International Series in Engineering and Computer Science, pages 315–337. Springer US, Boston, MA, 1998.

[19] J. J. Hopfield and D. W. Tank. "Neural" computation of decisions in optimization problems. *Biological Cybernetics*, 52(3):141–152, July 1985.

[20] J. J. Hopfield and D. W. Tank. Computing with neural circuits: A model. *Science*, 233(4764):625–633, August 1986.

[21] G. E. Moore. Cramming more components onto integrated circuits. *Electronics*, 38(8):4, 1965.

[22] D. A. Ferrucci. Introduction to "This is Watson". *IBM Journal of Research and Development*, 56(3.4):1:1–1:15, May 2012.

[23] D. Silver, A. Huang, C. J. Maddison, A. Guez, L. Sifre, G. van den Driessche, J. Schrittwieser, I. Antonoglou, V. Panneershelvam, M. Lanctot, S. Dieleman, D. Grewe, J. Nham, N. Kalchbrenner, I. Sutskever, T. Lillicrap, M. Leach, K. Kavukcuoglu, T. Graepel, and D. Hassabis. Mastering the game of Go with deep neural networks and tree search. *Nature*, 529(7587):484–489, January 2016.

[24] F. H. Sinz, X. Pitkow, J. Reimer, M. Bethge, and A. S. Tolias. Engineering a Less Artificial Intelligence. *Neuron*, 103(6):967–979, September 2019.

[25] A. M. Zador. A critique of pure learning and what artificial neural networks can learn from animal brains. *Nature Communications*, 10(1):3770, December 2019.

[26] D. Attwell and S. B. Laughlin. An Energy Budget for Signaling in the Grey Matter of the Brain. *Journal of Cerebral Blood Flow & Metabolism*, 21(10):1133–1145, October 2001.

[27] S. B. Laughlin and T. J. Sejnowski. Communication in Neuronal Networks. *Science*, 301(5641):1870–1874, September 2003.

[28] P. Lennie. The Cost of Cortical Computation. *Current Biology*, 13(6):493–497, March 2003.

[29] C.-S. Poon and K. Zhou. Neuromorphic Silicon Neurons and Large-Scale Neural Networks: Challenges and Opportunities. *Frontiers in Neuroscience*, 5, 2011.

[30] A. Moujahid, A. D'Anjou, and M. Graña. Energy demands of diverse spiking cells from the neocortex, hippocampus, and thalamus. *Frontiers in Computational Neuroscience*, 8, April 2014.

[31] E. D. Adrian and Y. Zotterman. The impulses produced by sensory nerve endings. *The Journal of Physiology*, 61(4):465–483, 1926.

[32] E. D. Adrian and Y. Zotterman. The impulses produced by sensory nerve endings: Part 3. Impulses set up by Touch and Pressure. *The Journal of Physiology*, 61(4):465–483, August 1926.

[33] D. Kaplan and L. Glass. *Understanding Nonlinear Dynamics*. Textbooks in Mathematical Sciences. Springer-Verlag, New York, 1995.

[34] A. Pikovsky, M. Rosenblum, and J. Kurths. *Synchronization: A Universal Concept in Nonlinear Sciences*, volume 12. Cambridge university press, 2003.

[35] R. V. Solé and S. Valverde. Information Theory of Complex Networks: On Evolution and Architectural Constraints. In E. Ben-Naim, H. Frauenfelder, and Z. Toroczkai, editors, *Complex Networks*, Lecture Notes in Physics, pages 189–207. Springer, Berlin, Heidelberg, 2004.

[36] O. Sporns. *Networks of the Brain*. MIT Press, Cambridge, Mass, 2011.

[37] A.-L. Barabási and R. Albert. Emergence of Scaling in Random Networks. *Science*, 286(5439):509–512, October 1999.

[38] C.-W. Shin and S. Kim. Self-organized criticality and scale-free properties in emergent functional neural networks. *Physical Review E*, 74(4):045101, October 2006.

[39] B. J. He. Scale-free brain activity: Past, present, and future. *Trends in Cognitive Sciences*, 18(9):480–487, September 2014.

[40] A. Fornito, A. Zalesky, and E. T. Bullmore. *Fundamentals of Brain Network Analysis*. Elsevier/Academic Press, Amsterdam ; Boston, 2016.

[41] C. A. Skarda and W. J. Freeman. How brains make chaos in order to make sense of the world. *Behavioral and brain sciences*, 10(2):161–173, 1987.

[42] W. J. Freeman III. The physiology of perception. *Scientific American*, 264(2), 1991.

[43] D. Plenz. Criticality in Cortex: Neuronal Avalanches and Coherence Potentials. In *Criticality in Neural Systems*, pages 5–42. John Wiley & Sons, Ltd, 2014.

[44] R. Kozma, M. Puljic, and W. J. Freeman. Thermodynamic Model of Criticality in the Cortex Based on EEG/ECoG Data. In *Criticality in Neural Systems*, pages 153–176. John Wiley & Sons, Ltd, 2014.

[45] M. Rybarsch and S. Bornholdt. Self-Organized Criticality in Neural Network Models. In *Criticality in Neural Systems*, pages 227–254. John Wiley & Sons, Ltd, 2014.

[46] R. R. Schaller. Moore's law: Past, present and future. *IEEE Spectrum*, 34(6):52–59, June 1997.

[47] R. Merritt. EETimes - Moore's Law Dead by 2022, Expert Says -, August 2013.

[48] M. M. Waldrop. The chips are down for Moore's law. *Nature News*, 530(7589):144, February 2016.

[49] W. Singer and C. M. Gray. Visual Feature Integration and the Temporal Correlation Hypothesis. *Annu. Rev. Neurosci.*, (18):555–86, 1995.

[50] O. Bertrand and C. Tallon-Baudry. Oscillatory gamma activity in humans: A possible role for object representation. *International Journal of Psychophysiology*, 38(3):211–223, December 2000.

[51] G. Buzsáki. *Rhythms of the Brain.* Oxford University Press, Oxford; New York, 2006.

[52] P. Uhlhaas. Neural synchrony in cortical networks: History, concept and current status. *Frontiers in Integrative Neuroscience*, 3, 2009.

[53] E. Izhikevich. *Dynamical Systems in Neuroscience: The Geometry of Excitability and Bursting.* The MIT Press, 2007.

[54] W. Singer. Neuronal oscillations: Unavoidable and useful? *European Journal of Neuroscience*, 48(7):2389–2398, 2018.

[55] F. C. Hoppensteadt and E. Izhikevich. Oscillatory neurocomputers with dynamic connectivity. *Physical Review Letters*, 82(14):2983, 1999.

[56] F. C. Hoppensteadt and E. Izhikevich. Pattern recognition via synchronization in phase-locked loop neural networks. *IEEE Transactions on Neural Networks*, 11(3):734–738, 2000.

[57] T. Nishikawa, F. C. Hoppensteadt, and Y.-C. Lai. Oscillatory associative memory network with perfect retrieval. *Physica D: Nonlinear Phenomena*, 197(1-2):134–148, October 2004.

[58] T. Nishikawa, Y.-C. Lai, and F. C. Hoppensteadt. Capacity of Oscillatory Associative-Memory Networks with Error-Free Retrieval. *Physical Review Letters*, 92(10), March 2004.

[59] D. Malagarriga, M. A. García-Vellisca, A. E. P. Villa, J. M. Buldú, J. García-Ojalvo, and A. J. Pons. Synchronization-based computation through networks of coupled oscillators. *Frontiers in Computational Neuroscience*, 9, August 2015.

[60] D. E. Nikonov, G. Csaba, W. Porod, T. Shibata, D. Voils, D. Hammerstrom, I. A. Young, and G. I. Bourianoff. Coupled-Oscillator Associative Memory Array Operation for Pattern Recognition. *IEEE Journal on Exploratory Solid-State Computational Devices and Circuits*, 1:85–93, December 2015.

[61] D. Vodenicarevic, N. Locatelli, F. Abreu Araujo, J. Grollier, and D. Querlioz. A Nanotechnology-Ready Computing Scheme based on a Weakly Coupled Oscillator Network. *Scientific Reports*, 7:44772, March 2017.

[62] J. Torrejon, M. Riou, F. A. Araujo, S. Tsunegi, G. Khalsa, D. Querlioz, P. Bortolotti, V. Cros, K. Yakushiji, A. Fukushima, H. Kubota, S. Yuasa, M. D. Stiles, and J. Grollier. Neuromorphic computing with nanoscale spintronic oscillators. *Nature*, 547(7664):428–431, July 2017.

[63] J. C. Coulombe, M. C. A. York, and J. Sylvestre. Computing with networks of nonlinear mechanical oscillators. *PloS one*, 12(6):e0178663, 2017.

[64] A. Raychowdhury, A. Parihar, G. H. Smith, V. Narayanan, G. Csaba, M. Jerry, W. Porod, and S. Datta. Computing With Networks of Oscillatory Dynamical Systems. *Proceedings of the IEEE*, 107(1):73–89, January 2019.

[65] R. D. Beer. Dynamical approaches to cognitive science. *Trends in Cognitive Sciences*, 4(3):9, 2000.

[66] P. Mazzarello. Camillo Golgi's Scientific Biography. *Journal of the History of the Neurosciences*, 8(2):121–131, August 1999.

[67] P. Dayan and L. F. Abbott. *Theoretical Neuroscience*, volume 10. Cambridge, MA: MIT Press, 2001.

[68] W. Gerstner, W. M. Kistler, R. Naud, and L. Paninski. *Neuronal Dynamics: From Single Neurons to Networks and Models of Cognition*. Cambridge University Press, Cambridge, 2014.

[69] W. Nernst. *Reasoning of Theoretical Chemistry: Nine Papers (1889–1921)*. Verlag Harri Deutsch, Frankfurt am Main, 2003.

[70] D. E. Goldman. Potential, impedance, and rectification in membranes. *The Journal of General Physiology*, 27(1):37–60, September 1943.

[71] G. L. Fain and T. O'Dell. *Molecular and Cellular Physiology of Neurons*. Harvard University Press, Cambridge, Massachusetts, second edition edition, 2014.

[72] K. Cole. Dynamic electrical characteristics of the squid axon membrane. *Archives des sciences physiologiques*, 253(3), 1949.

[73] A. L. Hodgkin and A. F. Huxley. A quantitative description of membrane current and its application to conduction and excitation in nerve. *The Journal of Physiology*, 117(4):500–544, August 1952.

[74] A. L. Hodgkin. The Croonian Lecture - Ionic movements and electrical activity in giant nerve fibres. *Proceedings of the Royal Society of London. Series B - Biological Sciences*, 148(930):1–37, January 1958.

[75] W. Ulbricht. Sodium Channel Inactivation: Molecular Determinants and Modulation. *Physiological Reviews*, 85(4):1271–1301, October 2005.

[76] M. Pospischil, M. Toledo-Rodriguez, C. Monier, Z. Piwkowska, T. Bal, Y. Frégnac, H. Markram, and A. Destexhe. Minimal Hodgkin–Huxley type models for different classes of cortical and thalamic neurons. *Biological Cybernetics*, 99(4-5):427–441, November 2008.

[77] H. Haken. *Brain Dynamics*. Springer Series in Synergetics. Springer Berlin Heidel-

berg, Berlin, Heidelberg, 2008.

[78] M. A. Lynch. Long-Term Potentiation and Memory. *Physiol Rev*, 84:50, 2004.

[79] L. R. Squire. Memory and the hippocampus: A synthesis from findings with rats, monkeys, and humans. *Psychological Review*, 99(2):195–231, April 1992.

[80] D. O. Hebb. The organization of behavior: A neuropsychological theory. *New York: John Wiley and Sons, Inc.,*, 34(5):335, 1949.

[81] T. Lømo. Frequency potentiation of excitatory synaptic activity in the dentate area of the hippocampal formation. *Acta Physiologica Scandinavica*, 68(suppl. 277):128, 1966.

[82] T. Lømo. Potentiation of monosynaptic EPSPs in the perforant path-dentate granule cell synapse. *Experimental Brain Research*, 12(1), January 1971.

[83] T. Bliss and T. Lømo. Long-lasting potentiation of synaptic transmission in the dentate area of the anaesthetized rabbit following stimulation of the perforant path. *The Journal of physiology*, 232(2):331–356, 1973.

[84] L. F. Abbott and S. B. Nelson. Synaptic plasticity: Taming the beast. *Nature Neuroscience*, 3(S11):1178–1183, November 2000.

[85] R. A. Nicoll, J. A. Kauer, and R. C. Malenka. The current excitement in long term potentiation. *Neuron*, 1(2):97–103, April 1988.

[86] R. M. Mulkey and R. C. Malenka. Mechanisms underlying induction of homosynaptic long-term depression in area CA1 of the hippocampus. *Neuron*, 9(5):967–975, November 1992.

[87] S. M. Dudek and M. F. Bear. Homosynaptic long-term depression in area CA1 of hippocampus and effects of N-methyl-D-aspartate receptor blockade. In *How*

We Learn; How We Remember: Toward an Understanding of Brain and Neural Systems, volume Volume 10 of *World Scientific Series in 20th Century Physics*, pages 200–204. World Scientific, September 1995.

[88] R. G. M. Morris, P. Garrud, J. N. P. Rawlins, and J. O'Keefe. Place navigation impaired in rats with hippocampal lesions. *Nature*, 297(5868):681–683, June 1982.

[89] H. Markram and W. Gerstner, editors. *Spike-Timing Dependent Plasticity*. Frontiers Research Topics. Frontiers Media SA, 2012.

[90] H. Markram, J. Lübke, M. Frotscher, and B. Sakmann. Regulation of Synaptic Efficacy by Coincidence of Postsynaptic APs and EPSPs. *Science*, 275(5297):213–215, January 1997.

[91] G.-Q. Bi and M.-M. Poo. Synaptic Modifications in Cultured Hippocampal Neurons: Dependence on Spike Timing, Synaptic Strength, and Postsynaptic Cell Type. *Journal of Neuroscience*, 18(24):10464–10472, December 1998.

[92] P. J. Sjöström, G. G. Turrigiano, and S. B. Nelson. Rate, Timing, and Cooperativity Jointly Determine Cortical Synaptic Plasticity. *Neuron*, 32(6):1149–1164, December 2001.

[93] E. L. Bienenstock, L. N. Cooper, and P. W. Munro. Theory for the development of neuron selectivity: Orientation specificity and binocular interaction in visual cortex. *Journal of Neuroscience*, 2(1):32–48, January 1982.

[94] E. Izhikevich and N. S. Desai. Relating stdp to bcm. *Neural computation*, 15(7):1511–1523, 2003.

[95] V. E. Abraira and D. D. Ginty. The Sensory Neurons of Touch. *Neuron*, 79(4):618–639, August 2013.

[96] E. D. Adrian. *The Basis of Sensation*. The Basis of Sensation. W W Norton & Co,

New York, NY, US, 1928.

[97] B. Ermentrout. Linearization of F-I curves by adaptation. *Neural Computation*, 10(7):1721–1729, October 1998.

[98] V. Booth and A. Bose. Neural Mechanisms for Generating Rate and Temporal Codes in Model CA3 Pyramidal Cells. *Journal of Neurophysiology*, 85(6):2432–2445, June 2001.

[99] J. Benda and Andreas V. M. Herz. A Universal Model for Spike-Frequency Adaptation. *Neural Computation*, 15(11):2523–2564, November 2003.

[100] J. Benda, L. Maler, and A. Longtin. Linear Versus Nonlinear Signal Transmission in Neuron Models With Adaptation Currents or Dynamic Thresholds. *Journal of Neurophysiology*, 104(5):2806–2820, November 2010.

[101] F. Zeldenrust and W. J. Wadman. Modulation of spike and burst rate in a minimal neuronal circuit with feed-forward inhibition. *Neural Networks*, 40:1–17, April 2013.

[102] F. A. C. Azevedo, L. R. B. Carvalho, L. T. Grinberg, J. M. Farfel, R. E. L. Ferretti, R. E. P. Leite, W. J. Filho, R. Lent, and S. Herculano-Houzel. Equal numbers of neuronal and nonneuronal cells make the human brain an isometrically scaled-up primate brain. *Journal of Comparative Neurology*, 513(5):532–541, 2009.

[103] J. M. Beggs and D. Plenz. Neuronal Avalanches in Neocortical Circuits. *Journal of Neuroscience*, 23(35):11167–11177, December 2003.

[104] D. R. Chialvo. Emergent complex neural dynamics. *Nature Physics*, 6(10):744–750, October 2010.

[105] V. Priesemann, M. Valderrama, M. Wibral, and M. Quyen. Neuronal Avalanches Differ from Wakefulness to Deep Sleep – Evidence from Intracranial Depth Recordings in Humans. *PLOS Computational Biology*, 9(3):e1002985, March 2013.

[106] L. Cocchi, L. L. Gollo, A. Zalesky, and M. Breakspear. Criticality in the brain: A synthesis of neurobiology, models and cognition. *Progress in Neurobiology*, 158:132–152, November 2017.

[107] P. Bak, C. Tang, and K. Wiesenfeld. Self-organized criticality. *Physical Review A*, 38(1):364–374, July 1988.

[108] P. Bak and K. Chen. Self-Organized Criticality. *Scientific American*, 264(1):46–53, 1991.

[109] E. Ising. Beitrag zur Theorie des Ferromagnetismus. *Zeitschrift für Physik*, 31(1):253–258, February 1925.

[110] W. Maass, T. Natschläger, and H. Markram. Real-Time Computing Without Stable States: A New Framework for Neural Computation Based on Perturbations. *Neural Computation*, 14(11):2531–2560, November 2002.

[111] H. Jaeger. Adaptive nonlinear system identification with Echo state networks. In *Proceedings of the 15th International Conference on Neural Information Processing Systems*, NIPS'02, pages 609–616, Cambridge, MA, USA, January 2002. MIT Press.

[112] N. Bertschinger and T. Natschläger. Real-Time Computation at the Edge of Chaos in Recurrent Neural Networks. *Neural Computation*, 16(7):1413–1436, July 2004.

[113] J. Boedecker, O. Obst, J. T. Lizier, N. M. Mayer, and M. Asada. Information processing in echo state networks at the edge of chaos. *Theory in Biosciences*, 131(3):205–213, September 2012.

[114] S. Strogatz. *Nonlinear Dynamics and Chaos*. Perseus Books, 1994.

[115] H. K. Khalil. *Nonlinear Systems*. Prentice Hall, 2002.

[116] L. Glass and M. C. Mackey. *From Clocks to Chaos*. Princeton University Press, New Jersey, 1988.

[117] A. A. Andronov, A. A. Vitt, and S. E. Khaikin. *Theory of Oscillators*. Elsevier, 1966.

[118] B. van der Pol. LXXXVIII. On "relaxation-oscillations". *The London, Edinburgh, and Dublin Philosophical Magazine and Journal of Science*, 2(11):978–992, November 1926.

[119] A. N. Zaikin and A. M. Zhabotinsky. Concentration Wave Propagation in Two-dimensional Liquid-phase Self-oscillating System. *Nature*, 225(5232):535–537, February 1970.

[120] R. M. Goodwin. The Nonlinear Accelerator and the Persistence of Business Cycles. *Econometrica*, 19(1):1–17, 1951.

[121] K. Sasakura. The business cycle model with a unique stable limit cycle. *Journal of Economic Dynamics and Control*, 20(9):1763–1773, September 1996.

[122] C. L. Partch, C. B. Green, and J. S. Takahashi. Molecular architecture of the mammalian circadian clock. *Trends in Cell Biology*, 24(2):90–99, February 2014.

[123] R. M. Smeal, G. B. Ermentrout, and J. A. White. Phase-response curves and synchronized neural networks. *Philosophical Transactions of the Royal Society B: Biological Sciences*, 365(1551):2407–2422, August 2010.

[124] T. I. Netoff, M. I. Banks, A. D. Dorval, C. D. Acker, J. S. Haas, N. Kopell, and J. A. White. Synchronization in Hybrid Neuronal Networks of the Hippocampal Formation. *Journal of Neurophysiology*, 93(3):1197–1208, March 2005.

[125] D. Hansel, G. Mato, and C. Meunier. Synchrony in Excitatory Neural Networks. *Neural Computation*, 7(2):307–337, March 1995.

[126] V. Klinshov, L. Lücken, D. Shchapin, V. Nekorkin, and S. Yanchuk. Multistable Jittering in Oscillators with Pulsatile Delayed Feedback. *Physical Review Letters*, 114(17):178103, April 2015.

[127] V. Klinshov, L. Lücken, D. Shchapin, V. Nekorkin, and S. Yanchuk. Emergence and combinatorial accumulation of jittering regimes in spiking oscillators with delayed feedback. *Physical Review E*, 92(4), October 2015.

[128] S. H. Strogatz. Nonlinear dynamics: Death by delay. *Nature*, 394(6691):316–317, 1998.

[129] J. Foss and J. Milton. Multistability in recurrent neural loops arising from delay. *Journal of Neurophysiology*, 84(2):975–985, 2000.

[130] G. B. Ermentrout and N. Kopell. Fine structure of neural spiking and synchronization in the presence of conduction delays. *Proceedings of the National Academy of Sciences*, 95(3):1259–1264, 1998.

[131] E. Scholl, G. Hiller, P. Hovel, and M. A Dahlem. Time-delayed feedback in neurosystems. *Philosophical Transactions of the Royal Society A: Mathematical, Physical and Engineering Sciences*, 367(1891):1079–1096, March 2009.

[132] V. V. Klinshov and V. I. Nekorkin. Synchronization of time-delay coupled pulse oscillators. *Chaos, Solitons & Fractals*, 44(1-3):98–107, January 2011.

[133] K. Blaha, J. Lehnert, A. Keane, T. Dahms, P. Hövel, E. Schöll, and J. L. Hudson. Clustering in delay-coupled smooth and relaxational chemical oscillators. *Physical Review E*, 88(6), December 2013.

[134] D. V. Ramana Reddy, A. Sen, and G. L. Johnston. Time Delay Induced Death in Coupled Limit Cycle Oscillators. *Physical Review Letters*, 80(23):5109–5112, June 1998.

[135] M. Kantner, E. Schöll, and S. Yanchuk. Delay-induced patterns in a two-dimensional lattice of coupled oscillators. *Scientific Reports*, 5:8522, February 2015.

[136] T. Matsumoto. A chaotic attractor from Chua's circuit. *IEEE Transactions on Circuits and Systems*, 31(12):1055–1058, 1984.

[137] L. O. Chua, C. W. Wu, A. Huang, and G.-Q. Zhong. A universal circuit for studying and generating chaos. I. Routes to chaos. *IEEE Transactions on Circuits and Systems I: Fundamental Theory and Applications*, 40(10):732–744, 1993.

[138] Z. Guo-Qun. Implementation of Chua's circuit with a cubic nonlinearity. *IEEE Transactions on Circuits and Systems I: Fundamental Theory and Applications*, 41(12):934–941, December 1994.

[139] J. Kengne. On the Dynamics of Chua's oscillator with a smooth cubic nonlinearity: Occurrence of multiple attractors. *Nonlinear Dynamics*, 87(1):363–375, January 2017.

[140] A. C. Hindmarsh. ODEPACK, A Systematized Collection of ODE Solvers. *Scientific Computing, R. S. Stepleman et al. (Eds.)*, 1:55–64, 1983.

[141] L. Petzold. Automatic Selection of Methods for Solving Stiff and Nonstiff Systems of Ordinary Differential Equations. *SIAM Journal on Scientific and Statistical Computing*, 4(1):136–148, March 1983.

[142] E. N. Lorenz. Deterministic Nonperiodic Flow. *Journal of the Atmospheric Sciences*, 20(2):130–141, March 1963.

[143] O. E. Rössler. An equation for continuous chaos. *Physics Letters A*, 57(5):397–398, July 1976.

[144] M. Hénon. A Two-dimensional Mapping with a Strange Attractor. *Communications in Methematical Physics*, 50:69–77, 1976.

[145] M. Newman. *Networks*, volume 1. Oxford University Press, October 2018.

[146] O. Sporns, G. Tononi, and R. Kötter. The Human Connectome: A Structural Description of the Human Brain. *PLOS Computational Biology*, 1(4):e42, September 2005.

[147] O. Sporns. *Discovering the Human Connectome*. MIT Press, Cambridge, Mass, 2012.

[148] M. Rubinov and O. Sporns. Complex network measures of brain connectivity: Uses and interpretations. *NeuroImage*, 52(3):1059–1069, September 2010.

[149] A. Levina, J. M. Herrmann, and T. Geisel. Dynamical synapses causing self-organized criticality in neural networks. *Nature Physics*, 3(12):857–860, December 2007.

[150] M. G. Kitzbichler, R. N. A. Henson, M. L. Smith, P. J. Nathan, and E. T. Bullmore. Cognitive Effort Drives Workspace Configuration of Human Brain Functional Networks. *Journal of Neuroscience*, 31(22):8259–8270, June 2011.

[151] F. Harary and E. Palmer. *Graphical Enumeration*. Academic Press, New York and London, 1973.

[152] R. Milo, S. Shen-Orr, S. Itzkovitz, N. Kashtan, D. Chklovskii, and U. Alon. Network Motifs: Simple Building Blocks of Complex Networks. *Science*, 298(5594):824–827, October 2002.

[153] D. J. Watts and S. H. Strogatz. Collective dynamics of 'small-world' networks. *Nature*, 393(6684):440–442, June 1998.

[154] J.-P. Onnela, J. Saramäki, J. Kertész, and K. Kaski. Intensity and coherence of motifs in weighted complex networks. *Physical Review E*, 71(6):065103, June 2005.

[155] V. Latora and M. Marchiori. Efficient Behavior of Small-World Networks. *Physical Review Letters*, 87(19):198701, October 2001.

[156] M. P. van den Heuvel, R. C. W. Mandl, C. J. Stam, R. S. Kahn, and H. E. H. Pol. Aberrant Frontal and Temporal Complex Network Structure in Schizophrenia: A Graph Theoretical Analysis. *Journal of Neuroscience*, 30(47):15915–15926, November 2010.

[157] J. M. Anthonisse. The rush in a directed graph. *Stichting Mathematisch Centrum*, January 1971.

[158] L. C. Freeman. A Set of Measures of Centrality Based on Betweenness. *Sociometry*, 40(1):35–41, 1977.

[159] A. A. Barlian, W.-T. Park, J. R. Mallon, A. J. Rastegar, and B. L. Pruitt. Review: Semiconductor Piezoresistance for Microsystems. *Proceedings of the IEEE*, 97(3):513–552, March 2009.

[160] C. Herring and E. Vogt. Transport and Deformation-Potential Theory for Many-Valley Semiconductors with Anisotropic Scattering. *Physical Review*, 101(3):944–961, February 1956.

[161] S. M. Sze. *Semiconductor Sensors*. John Wiley & Sons, Inc., 1994.

[162] R. Waser, editor. *Nanoelectronics and Information Technology Advanced Electronic Materials and Novel Devices*. Wiley-VCH Verlag GmbH & Co. KGaA, 2003.

[163] S. M. Sze and K. K. Ng. *Physics of Semiconductor Devices*. John Wiley & Sons, 2006.

[164] C. S. Smith. Piezoresistance Effect in Germanium and Silicon. *Physical Review*, 94(1):42–49, April 1954.

[165] Y. Kanda. A graphical representation of the piezoresistance coefficients in silicon. *IEEE Transactions on Electron Devices*, 29(1):64–70, January 1982.

[166] J. F. Creemer, F. Fruett, G. C. M. Meijer, and P. J. French. The piezojunction effect in silicon sensors and circuits and its relation to piezoresistance. *IEEE Sensors Journal*, 1(2):98, 2001.

[167] K. Matsuda. Strain-Dependent Hole Masses and Piezoresistive Properties of Silicon. *Journal of Computational Electronics*, 3(3):273–276, October 2004.

[168] Y. Sun, S. E. Thompson, and T. Nishida. Physics of strain effects in semiconductors and metal-oxide-semiconductor field-effect transistors. *Journal of Applied Physics*, 101(10):104503, May 2007.

[169] J. Curie and P. Curie. Développement par compression de l'électricité polaire dans les cristaux hémièdres à faces inclinées. *Bulletin de Minéralogie*, 3(4):90–93, 1880.

[170] H.-R. Tränkler and E. Obermeier, editors. *Sensortechnik Handbuch für Praxis und wissenschaft*. Springer, 1998.

[171] G. H. Haertling. Ferroelectric Ceramics: History and Technology. *Journal of the American Ceramic Society*, 82(4):797–818, 1999.

[172] B. V. Mill and Y. V. Pisarevsky. Langasite-type materials: From discovery to present state. In *Proceedings of the 2000 IEEE/EIA International Frequency Control Symposium and Exhibition (Cat. No.00CH37052)*, pages 133–144, June 2000.

[173] Z. Wang, R. Yu, C. Pan, Z. Li, J. Yang, F. Yi, and Z. L. Wang. Light-induced pyroelectric effect as an effective approach for ultrafast ultraviolet nanosensing. *Nature Communications*, 6(1):8401, September 2015.

[174] G. E. Stan, M. Botea, G. A. Boni, I. Pintilie, and L. Pintilie. Electric and pyroelectric

properties of AlN thin films deposited by reactive magnetron sputtering on Si substrate. *Applied Surface Science*, 353:1195–1202, October 2015.

[175] B. Jaffe. *Piezoelectric Ceramics*. Elsevier, December 2012.

[176] R. S. Dahiya and M. Valle. *Robotic Tactile Sensing: Technologies and System*. Springer Netherlands, 2013.

[177] Y. B. Jeon, R. Sood, J.-h. Jeong, and S.-G. Kim. MEMS power generator with transverse mode thin film PZT. *Sensors and Actuators A: Physical*, 122(1):16–22, July 2005.

[178] L. Chua. Memristor-The missing circuit element. *IEEE Transactions on Circuit Theory*, 18(5):507–519, September 1971.

[179] D. B. Strukov, G. S. Snider, D. R. Stewart, and R. S. Williams. The missing memristor found. *Nature*, 453(7191):80–83, May 2008.

[180] J. F. Gibbons and W. E. Beadle. Switching properties of thin Nio films. *Solid-State Electronics*, 7(11):785–790, November 1964.

[181] J. G. Simmons and R. R. Verderber. New conduction and reversible memory phenomena in thin insulating films. *Proceedings of the Royal Society of London. Series A. Mathematical and Physical Sciences*, 301(1464):77–102, October 1967.

[182] S. Q. Liu, N. J. Wu, and A. Ignatiev. Electric-pulse-induced reversible resistance change effect in magnetoresistive films. *Applied Physics Letters*, 76(19):2749–2751, May 2000.

[183] S. Seo, M. J. Lee, D. H. Seo, E. J. Jeoung, D.-S. Suh, Y. S. Joung, I. K. Yoo, I. R. Hwang, S. H. Kim, I. S. Byun, J.-S. Kim, J. S. Choi, and B. H. Park. Reproducible resistance switching in polycrystalline NiO films. *Applied Physics Letters*, 85(23):5655–5657, December 2004.

[184] M. D. Ventra and Y. V. Pershin. On the physical properties of memristive, memcapacitive and meminductive systems. *Nanotechnology*, 24(25):255201, May 2013.

[185] S. Vongehr and X. Meng. The Missing Memristor has Not been Found. *Scientific Reports*, 5(1):11657, June 2015.

[186] I. Abraham. The case for rejecting the memristor as a fundamental circuit element. *Scientific Reports*, 8(1):10972, July 2018.

[187] L. Chua. If it's pinched it's a memristor. *Semiconductor Science and Technology*, 29(10):104001, September 2014.

[188] R. Tetzlaff, editor. *Memristors and Memristive Systems*. Springer New York, New York, NY, 2014.

[189] L. Chua. Resistance switching memories are memristors. *Applied Physics A*, 102(4):765–783, March 2011.

[190] M. Hansen, M. Ziegler, L. Kolberg, R. Soni, S. Dirkmann, T. Mussenbrock, and H. Kohlstedt. A double barrier memristive device. *Scientific Reports*, 5(1), November 2015.

[191] R. Meyer, L. Schloss, J. Brewer, R. Lambertson, W. Kinney, J. Sanchez, and D. Rinerson. Oxide dual-layer memory element for scalable non-volatile cross-point memory technology. In *2008 9th Annual Non-Volatile Memory Technology Symposium (NVMTS)*, pages 1–5, November 2008.

[192] T. P. Sylvan. *The Unijunction Transistor Characteristics and Applications*. Semiconductor Products Department, General Electric, 1965.

[193] M. J. Callahan. Programmable Unijunction Transistor for Integrated circuits. *IEEE Journal of Solid-State Circuits*, 7(2):204–206, 1972.

[194] A. Alvarez, editor. *BiCMOS Technology and Applications*. The Springer International Series in Engineering and Computer Science. Springer US, second edition, 1993.

[195] T. L. Floyd. *Electronic Devices: Electron Flow Version*. Prentice Hall, Boston, 9th ed edition, 2012.

[196] H. Winterfeld, L. Thormählen, H. Lewitz, E. Yarar, T. Birkoben, N. Niethe, N. Preinl, H. Hanssen, E. Quandt, and H. Kohlstedt. A stress sensor based on a silicon field effect transistor comprising a piezoelectric AlN gate dielectric. *Journal of Materials Science: Materials in Electronics*, May 2019.

[197] T. Birkoben, H. Winterfeld, S. Fichtner, A. Petraru, and H. Kohlstedt. A spiking and adapting tactile sensor for neuromorphic applications. *Scientific Reports*, 10(1):17260, October 2020.

[198] N. Yogeswaran, W. T. Navaraj, S. Gupta, F. Liu, V. Vinciguerra, L. Lorenzelli, and R. Dahiya. Piezoelectric graphene field effect transistor pressure sensors for tactile sensing. *Applied Physics Letters*, 113(1):014102, July 2018.

[199] Y.-R. Wu and J. Singh. Metal piezoelectric semiconductor field effect transistors for piezoelectric strain sensors. *Applied Physics Letters*, 85(7):1223–1225, August 2004.

[200] H.-B. Yao, J. Ge, C.-F. Wang, X. Wang, W. Hu, Z.-J. Zheng, Y. Ni, and S.-H. Yu. A Flexible and Highly Pressure-Sensitive Graphene–Polyurethane Sponge Based on Fractured Microstructure Design. *Advanced Materials*, 25(46):6692–6698, 2013.

[201] B. Zhu, Z. Niu, H. Wang, W. R. Leow, H. Wang, Y. Li, L. Zheng, J. Wei, F. Huo, and X. Chen. Microstructured Graphene Arrays for Highly Sensitive Flexible Tactile Sensors. *Small*, 10(18):3625–3631, 2014.

[202] S. Chun, Y. Kim, H. Jung, and W. Park. A flexible graphene touch sensor in the general human touch range. *Applied Physics Letters*, 105(4):041907, July 2014.

[203] H. Tian, Y. Shu, X.-F. Wang, M. A. Mohammad, Z. Bie, Q.-Y. Xie, C. Li, W.-T. Mi, Y. Yang, and T.-L. Ren. A Graphene-Based Resistive Pressure Sensor with Record-High Sensitivity in a Wide Pressure Range. *Scientific Reports*, 5:8603, February 2015.

[204] C. Li, P. Wu, S. Lee, A. Gorton, M. J. Schulz, and C. H. Ahn. Flexible Dome and Bump Shape Piezoelectric Tactile Sensors Using PVDF-TrFE Copolymer. *Journal of Microelectromechanical Systems*, 17(2):334–341, April 2008.

[205] R. Dahiya, G. Metta, M. Valle, A. Adami, and L. Lorenzelli. Piezoelectric oxide semiconductor field effect transistor touch sensing devices. *Applied Physics Letters*, 95(3):034105, July 2009.

[206] C. M. Boutry, M. Negre, M. Jorda, O. Vardoulis, A. Chortos, O. Khatib, and Z. Bao. A hierarchically patterned, bioinspired e-skin able to detect the direction of applied pressure for robotics. *Science Robotics*, 3(24):eaau6914, November 2018.

[207] Y. Zhengkun and Z. Yilei. Recognizing tactile surface roughness with a biomimetic fingertip: A soft neuromorphic approach. *Neurocomputing*, 244:102–111, June 2017.

[208] J.-Y. Yoo, M.-H. Seo, J.-S. Lee, K.-W. Choi, M.-N. Jo, and J.-B. Yoon. Industrial Grade, Bending-Insensitive, Transparent Nanoforce Touch Sensor via Enhanced Percolation Effect in a Hierarchical Nanocomposite Film. *Advanced Functional Materials*, 28(42):1804721, October 2018.

[209] K. Takei, T. Takahashi, J. C. Ho, H. Ko, A. G. Gillies, P. W. Leu, R. S. Fearing, and A. Javey. Nanowire active-matrix circuitry for low-voltage macroscale artificial skin. *Nature Materials*, 9(10):821–826, October 2010.

[210] W. Taube Navaraj, C. García Núñez, D. Shakthivel, V. Vinciguerra, F. Labeau, D. H. Gregory, and R. Dahiya. Nanowire FET Based Neural Element for Robotic Tactile Sensing Skin. *Frontiers in Neuroscience*, 11, 2017.

[211] W.-Y. Tseng, J. S. Fisher, J. L. Prieto, K. Rinaldi, G. Alapati, and A. P. Lee. A slow-adapting microfluidic-based tactile sensor. *Journal of Micromechanics and Microengineering*, 19(8):085002, July 2009.

[212] R. S. Dahiya, D. Cattin, A. Adami, C. Collini, L. Barboni, M. Valle, L. Lorenzelli, R. Oboe, G. Metta, and F. Brunetti. Towards Tactile Sensing System on Chip for Robotic Applications. *IEEE Sensors Journal*, 11(12):3216–3226, December 2011.

[213] A. Adami, R. S. Dahiya, C. Collini, D. Cattin, and L. Lorenzelli. POSFET touch sensor with CMOS integrated signal conditioning electronics. *SENSORS AND ACTUATORS A-PHYSICAL*, 188(SI):75–81, December 2012.

[214] S. Caviglia, L. Pinna, M. Valle, and C. Bartolozzi. Spike-Based Readout of POSFET Tactile Sensors. *IEEE Transactions on Circuits and Systems I: Regular Papers*, 64(6):1421–1431, June 2017.

[215] G. Indiveri. A low-power adaptive integrate-and-fire neuron circuit. In *Proceedings of the 2003 International Symposium on Circuits and Systems, 2003. ISCAS '03.*, volume 4, pages IV–IV, May 2003.

[216] E. Chicca, F. Stefanini, C. Bartolozzi, and G. Indiveri. Neuromorphic electronic circuits for building autonomous cognitive systems. *Proceedings of the IEEE*, 102(9):1367–1388, 2014.

[217] L. Camunas-Mesa, C. Zamarreno-Ramos, A. Linares-Barranco, A. J. Acosta-Jimenez, T. Serrano-Gotarredona, and B. Linares-Barranco. An Event-Driven Multi-Kernel Convolution Processor Module for Event-Driven Vision Sensors. *IEEE Journal of Solid-State Circuits*, 47(2):504–517, February 2012.

[218] J. A. Pérez-Carrasco, B. Zhao, C. Serrano, B. Acha, T. Serrano-Gotarredona, S. Chen, and B. Linares-Barranco. Mapping from Frame-Driven to Frame-Free Event-Driven Vision Systems by Low-Rate Rate Coding and Coincidence Process-

ing–Application to Feedforward ConvNets. *IEEE Transactions on Pattern Analysis and Machine Intelligence*, 35(11):2706–2719, November 2013.

[219] C. Posch, T. Serrano-Gotarredona, B. Linares-Barranco, and T. Delbruck. Retinomorphic Event-Based Vision Sensors: Bioinspired Cameras With Spiking Output. *Proceedings of the IEEE*, 102(10):1470–1484, October 2014.

[220] A. Linares-Barranco, H. Liu, A. Rios-Navarro, F. Gomez-Rodriguez, D. P. Moeys, and T. Delbruck. Approaching Retinal Ganglion Cell Modeling and FPGA Implementation for Robotics. *Entropy*, 20(6):475, June 2018.

[221] R. C. Jaeger, J. C. Suhling, R. Ramani, A. T. Bradley, and X. Jianping. CMOS stress sensors on [100] silicon. *IEEE Journal of Solid-State Circuits*, 35(1):85–95, January 2000.

[222] A. T. Bradley, R. C. Jaeger, J. C. Suhling, and K. J. O'Connor. Piezoresistive characteristics of short-channel MOSFETs on (100) silicon. *IEEE Transactions on Electron Devices*, 48(9):2009–2015, Sept./2001.

[223] M. Akiyama, T. Kamohara, K. Kano, A. Teshigahara, Y. Takeuchi, and N. Kawahara. Enhancement of Piezoelectric Response in Scandium Aluminum Nitride Alloy Thin Films Prepared by Dual Reactive Cosputtering. *Advanced Materials*, 21(5):593–596, 2009.

[224] S. Fichtner, N. Wolff, G. Krishnamurthy, A. Petraru, S. Bohse, F. Lofink, S. Chemnitz, H. Kohlstedt, L. Kienle, and B. Wagner. Identifying and overcoming the interface originating c-axis instability in highly Sc enhanced AlN for piezoelectric micro-electromechanical systems. *Journal of Applied Physics*, 122(3):035301, July 2017.

[225] S. Fichtner, N. Wolff, F. Lofink, L. Kienle, and B. Wagner. AlScN: A III-V semiconductor based ferroelectric. *Journal of Applied Physics*, 125(11):114103, March 2019.

[226] V. Kaajakari. *Practical MEMS*. Small Gear Pub., Las Vegas, 2009.

[227] K. Roy, A. Jaiswal, and P. Panda. Towards spike-based machine intelligence with neuromorphic computing. *Nature*, 575(7784):607–617, November 2019.

[228] T. Kreuz, F. Mormann, R. G. Andrzejak, A. Kraskov, K. Lehnertz, and P. Grassberger. Measuring synchronization in coupled model systems: A comparison of different approaches. *Physica D: Nonlinear Phenomena*, 225(1):29–42, January 2007.

[229] T. Kreuz, J. S. Haas, A. Morelli, H. D. I. Abarbanel, and A. Politi. Measuring spike train synchrony. *Journal of Neuroscience Methods*, 165(1):151–161, September 2007.

[230] T. Kreuz, D. Chicharro, C. Houghton, R. G. Andrzejak, and F. Mormann. Monitoring spike train synchrony. *Journal of Neurophysiology*, 109(5):1457–1472, March 2013.

[231] P. Sterling and S. Laughlin. *Principles of Neural Design*. The MIT Press, 2015.

[232] G. M. Edelman. Neural Darwinism: Selection and reentrant signaling in higher brain function. *Neuron*, 10(2):115–125, February 1993.

[233] G. Tononi, O. Sporns, and G. M. Edelman. A measure for brain complexity: Relating functional segregation and integration in the nervous system. *Proceedings of the National Academy of Sciences*, 91(11):5033–5037, 1994.

[234] E. Bullmore and O. Sporns. Complex brain networks: Graph theoretical analysis of structural and functional systems. *Nature Reviews Neuroscience*, 10(3):186–198, March 2009.

[235] V. Klinshov and V. Nekorkin. Switching thresholds for multistable systems under strong external perturbation. *Communications in Nonlinear Science and Numerical Simulation*, 83:105067, April 2020.

[236] K. Stephenson and M. Zelen. Rethinking centrality: Methods and examples. *Social Networks*, 11(1):1–37, March 1989.

[237] D. J. Klein and M. Randi. Resistance distance. *Journal of Mathematical Chemistry*, 12:81–95, 1993.

[238] F. Y. Wu. Theory of resistor networks: The two-point resistance. *Journal of Physics A: Mathematical and General*, 37(26):6653–6673, July 2004.

[239] E. Bozzo and M. Franceschet. Resistance distance, closeness, and betweenness. *Social Networks*, 35(3):460–469, July 2013.

[240] V. Čerňanová, J. Brenkuŝ, and V. Stopjaková. Non–Symmetric Finite Networks: The Two–Point Resistance. *Journal of Electrical Engineering*, 65(5):283–288, September 2014.

[241] N. S. Izmailian, R. Kenna, and F. Y. Wu. The two-point resistance of a resistor network: A new formulation and application to the cobweb network. *Journal of Physics A: Mathematical and Theoretical*, 47(3):035003, January 2014.

[242] J. W. Essam, N.-S. Izmailyan, R. Kenna, and Z.-Z. Tan. Comparison of methods to determine point-to-point resistance in nearly rectangular networks with application to a 'hammock' network. *Royal Society Open Science*, 2(4), April 2015.

[243] S. Dirkmann, M. Hansen, M. Ziegler, H. Kohlstedt, and T. Mussenbrock. The role of ion transport phenomena in memristive double barrier devices. *Scientific Reports*, 6(1), December 2016.

[244] E. Solan and K. Ochs. Parameter Identification of a Double Barrier Memristive Device. *Boston: IEEE MWSCAS*, 2017.

[245] E. Solan, S. Dirkmann, M. Hansen, D. Schroeder, H. Kohlstedt, M. Ziegler, T. Mussenbrock, and K. Ochs. An enhanced lumped element electrical model

of a double barrier memristive device. *Journal of Physics D: Applied Physics*, 50(19):195102, May 2017.

[246] J. G. Simmons. Generalized Formula for the Electric Tunnel Effect between Similar Electrodes Separated by a Thin Insulating Film. *Journal of Applied Physics*, 34(6):1793–1803, June 1963.

[247] T. Birkoben, M. Drangmeister, F. Zahari, S. Yanchuk, P. Hövel, and H. Kohlstedt. Slow–Fast Dynamics in a Chaotic System with Strongly Asymmetric Memristive Element. *International Journal of Bifurcation and Chaos*, 30(08):2050125, June 2020.

[248] F. Dumortier and R. Roussarie. *Canard Cycles and Center Manifolds*. American Mathematical Soc., 1996.

[249] M. Krupa, B. Sandstede, and P. Szmolyan. Fast and Slow Waves in the FitzHugh–Nagumo Equation. *Journal of Differential Equations*, 133(1):49–97, January 1997.

[250] C. Kuehn. *Multiple Time Scale Dynamics*. Applied Mathematical Sciences. Springer International Publishing, 2015.

[251] A. Antoniou. Gyrators using operational amplifiers. *Electronics Letters*, 3(8):350–352, August 1967.

[252] A. Antoniou. Realisation of gyrators using operational amplifiers, and their use in RC-active-network synthesis. *Proceedings of the Institution of Electrical Engineers*, 116(11):1838–1850, November 1969.

[253] A. Antoniou and K. Naidu. Modeling of a gyrator circuit. *IEEE Transactions on Circuit Theory*, 20(5):533–540, September 1973.

[254] A. S. Sedra and K. C. Smith. *Microelectronic Circuits*. The Oxford Series in

Electrical and Computer Engineering. Oxford University Press, New York ; Oxford, seventh edition edition, 2015.

[255] M. P. Kennedy. Robust Op Amp realization of Chua's Circuit. *Frequenz*, 46(3-4):66–80, 1992.